THÈSE

En vue de l'obtention du

DOCTORAT DE L'UNIVERSITÉ DE TOULOUSE

Délivré par :

Institut National Polytechnique de Toulouse (INP Toulouse)

Discipline ou spécialité :

Energétique et Transferts

Présentée et soutenue par :

M. THOMAS JARAVEL

le jeudi 28 avril 2016

Titre :

PREDICTION OF POLLUTANTS IN GAS TURBINES USING LARGE EDDY SIMULATION

Ecole doctorale :

Mécanique, Energétique, Génie civil, Procédés (MEGeP)

Unité de recherche :

Centre Européen de Recherche et Formation Avancées en Calcul Scientifique (CERFACS)

Directeur(s) de Thèse :

MME BENEDICTE CUENOT

MME ELEONORE RIBER

Rapporteurs :

M. DENIS VEYNANTE, ECOLE CENTRALE PARIS

M. HEINZ PITSCH, RHEINISCH-WESTFALISCHE TECH. HOCH.AACHEN

Membre(s) du jury :

Mme FREDERIQUE BATTIN-LECLERC, UNIVERSITE DE LORRAINE, Président

Mme BENEDICTE CUENOT, CERFACS, Membre

Mme PERRINE PEPIOT-DESJARDINS, CORNELL UNIVERSITY EU, Membre

M. OLIVIER COLIN, INSTITUT FRANCAIS DU PETROLE (IFP), Membre

Abstract

Stringent regulations of pollutant emissions now apply to new-generation combustion devices. To achieve low nitrogen oxides (NOx) and carbon monoxide (CO) emissions simultaneously, a complex optimisation process is required in the development of new concepts for engines. Already efficient for the prediction of turbulent combustion, Large Eddy Simulation (LES) is also a promising tool to better understand the processes of pollutant formation in gas turbine conditions and to provide their quantitative prediction at the design stage. In this work, a new methodology for the prediction with LES of NOx and CO in realistic industrial configurations is developed. It is based on a new strategy for the description of chemistry, using Analytically Reduced Chemistry (ARC) combined with the Thickened Flame model (TFLES). An ARC with accurate CO and NO prediction is derived, validated on canonical laminar flames and implemented in the LES solver. The accuracy of this approach is demonstrated with a highly resolved simulation of the academic turbulent Sandia flame D, for which excellent prediction of NO and CO is obtained. The methodology is then applied to two industrial configurations. The first one is the SGT-100, a lean partially-premixed gas turbine model combustor studied experimentally at DLR. LES of this configuration highlights the chemical processes of pollutant formation and provides qualitative and quantitative understanding of the impact of the operating conditions. The second target configuration corresponds to a mono-sector prototype of an ultra-low NOx, staged multipoint injection aeronautical combustor developed in the framework of the LEMCOTEC European project and studied experimentally at ONERA. An ARC for the combustion of a representative jet fuel surrogate is derived and used in the LES of the combustor with an Eulerian formalism to describe the liquid dispersed phase. Results show the excellent performances of the ARC, for both the flame characteristics and the prediction of pollutants.

Résumé

Les réglementations en termes d émission de polluants qui s appliquent aux chambres de combustion de nouvelle génération nécessitent de nouvelles approches de conception. Afin d atteindre simultanément des objectifs de faibles émissions d oxydes d azote (NOx) et de monoxyde de carbone (CO), un processus d optimisation complexe est nécessaire au développement de nouveaux concepts de moteur. La simulation aux grandes échelles (SGE) a déjà fait ses preuves pour la prédiction de la combustion turbulente. C est aussi un outil prometteur pour mieux comprendre la formation des polluants dans les turbines à gaz, ainsi que pour en fournir une prédiction quantitative. Dans ces travaux, une nouvelle méthodologie pour la prédiction du NOx et du CO dans des configurations réalistes est développée. La méthode est basée sur une description du système chimique par des schémas réduits fidèles dits analytiques (ARC) combinés au modèle de flamme épaissie (TFLES). En particulier, un ARC ayant des capacités de prédiction précise du CO et du NO est développé, validé sur des cas laminaires canoniques et implémenté dans le solveur SGE. Le potentiel de l approche est démontré par une simulation haute résolution de la flamme académique turbulente Sandia D, pour laquelle une excellente prédiction du CO et du NO est obtenue. La méthodologie est ensuite appliquée à deux configurations industrielles. La configuration SGT-100 est un bruleur commercial partiellement prémélangé de turbine à gaz terrestre pour la production d énergie, étudié expérimentalement au DLR. La SGE de cette configuration permet de mettre en évidence les processus chimiques de formation des polluants et fournit une compréhension qualitative et quantitative de l effet des conditions de fonctionnement. La seconde application correspond à un prototype monosecteur de système d injection aéronautique multipoint à très faibles émissions de NOx développé dans le cadre du projet européen LEMCOTEC et étudié expérimentalement à l ONERA. Un ARC représentant la cinétique chimique d un carburant aéronautique modèle est dérivé et employé dans la SGE de la chambre de combustion avec un formalisme eulérien pour décrire la phase dispersée. Les résultats obtenus montrent l excellente capacité de prédiction de l ARC en termes de propriétés de flamme et de prédiction des polluants.

If you want a happy ending, that depends, of course, on where you stop your story.

Orson Welles

Acknowledgements

I would like to thank SNECMA for offering this PhD thesis opportunity and for the four months I have spent there, in particular Michel Cazalens, Matthieu Rullaud and Sébastien Bourgois who successively followed my work during these three years. I also would like to thank Ghenadie Bulat from Siemens for providing data and the fruitful discussions about the SGT-100 configuration, which is central in this thesis. I also would like to thank Heinz Pitsch and Denis Veynante for examining my work and the other members of the jury, Olivier Colin, Frédérique Battin-Leclerc, Alain Cayre and Stéphane Richard for their very positive comments, with a special thank to Perrine Pepiot-Desjardins who directly contributed to this work with the YARC tool.

Ce travail a été possible grace à mes encadrantes, l hydre à deux tetes Bénéle (ou Elebéné ??), qui m a embarqué dans cette aventure du cote obscur de la chimie. Leur conseils ont permis à mon "esprit libre" de garder la bonne direction tout au long de la thèse. Ils ont le plus souvent été d ordre scientifique, mais aussi esthétique, avec mes choix de couleurs douteux pour les graphs, et parfois memes capillaires, pileux ou vestimentaires... Il a aussi fallu faire face avec courage à mon addiction aux heures de calcul, et comprendre qu il valait mieux ne pas me déranger avant la première pause café du matin. Merci également aux autres seniors, notamment gab qui nous permet faire tourner le code sur toutes les machines de la planète (et aussi pour sa puissance au quizz), et Thierry pour son énergie permanente et son oeil toujours aiguisé. Pour le travail au quotidien, l équipe CSG a fait en sorte que tout marche tout le temps, ne nous laissant jamais d excuse pour ne pas bosser, et toujours avec le sourire, et merci également à Chantal, Michelle, Marie et Nicole pour le support administratif dans la bonne humeur.

Ces quatre années passées au CERFACS, c est aussi un long défilé de collègues qui contribuent largement à la bonne ambiance de travail. Il y a d abord les très très vieux un peu barges qui étaient là au début, David (3 ans de bureau commun, l invicibilité du duo au foot, et la longévité en soirée..), Guigz (qui m a dégoté ce magnifique surnom que je me traine encore...), Ptit Ju, Gilou & Happy Moff, le Dr Salas, Herr Franseeeen, TomTom le trimard, Greg, qui ont été synonymes de guerre de fruit/ticket de café, de discussions hautement philosophiques et de soirées improbables.

Il y a aussi les moins vieux qui m ont accompagné au cours des ses années, notamment Herr Ghani (j ai une question Tommy..), Laure (mème si j en veux beaucoup à la

Section Paloise d avoir piqué notre place dans l élite...), Yannis (et sa fascination pour Silvère Tian) et la LEMCOTeam (Lucas/Mika) qui m a mis le pied à l étrier.

Et puis les générations se succèdent, et vous font gentiment comprendre que maintenant c est vous le vieux. Sans rancune, on va quand mème leur souhaiter bonne chance: Majd & Romain (le ptit couple bobo barbu bio), Laura (Traam, Traaam, Traaaam), Dario (l ersatz d Inzaghi), jamais loin Mélissa, Pierre (What string color ?), Kelu (et les afters douteux..), Francis (qui nous a sauvés de l humiliation sur l épreuve des poteaux à l école de combu), Grosnick (imbattable aux 25 mètres malgré mon style fluide et aérien), Omar (Merci poulet), Mowgli, Luis, Franchine, Carlos, Anne qui doit poursuivre le boulot, et aux plus nouveaux qui ont plus de temps devant eux, Valentin (inratable sur l autoroute) et Félix (l insidieux mangeur de paille) et au tout jeune comme Lulu (aka la matraque). En plus de ça on ajoute l arrivée en cours de route des post-docs égarés, Nico (le bouffeur d huıtre, #IlestLaJarJar) et Lola (qui par miracle n a pas encore étranglé Romain).

C en est fini pour la partie CERFACS, mais il y aussi tous les autres. Merci aux anciens d école ou d ailleurs, notamment ceux qui ont eu l inconscience d etre présents à la soutenance: Geoffrey (remets nous des glaçons), Emilien (Roll in the Benz with me), Otti & Julien, et Camille. Merci à mes parents grace à qui j ai parcouru ce chemin et qui on fait le déplacement de nos contrées oyonnaxiennes pour etre de la partie. Au-delà de la soutenance, il y aussi tous les gens croisés à Toulouse au cours de ces années, notamment ceux de la rue Fieux, et surtout mes colocs qui m ont supporté, et qui ont pu assister à mon élévation spirituelle (ou spiritueuse ?) et la dégradation progressive de mon état mental. Par d ordre d apparition à la coloc (et non pas par ordre de préférence Marie...), Guillaume, Gwen, Marie, Anaelle, Astrid, Alex, Élodie. Vos tentatives désespérées de vous enfuir en Amérique du Sud, en Angleterre, à Nantes, Grenoble ou ailleurs sont vaines, je vous retrouverai... Je n oublierai pas non plus Ze Bec pour les fat restos et Dédé pour les mises au vert dans les Cévennes. Et pour conclure, ma dernière décla au CERFACS Football Club:

I came like a king, left like a legend.
Zlatan Ibrahimović

Contents

List of symbols

Roman characters

Symbol	Description	Unit
a	Strain rate	$[\mathrm{s}^{-1}]$
c	Flame progress variable	[-]
d_l	Liquid droplet diameter	[m]
D_k	Diffusion coefficient of species k	$[-]$
E	Gaseous total energy per unit mass	[J/kg]
$\mathcal{E}$	Efficiency function	[-]
EICO	CO emission index	[g/kg]
EINO	NO emission index	[g/kg]
$F_{d,i}$	Volumetric force vector of particle drag	$[\mathrm{N/m}^3]$
$F_{p,i}$	Drag force vector of a Lagrangian particle	[N]
$\mathcal{F}$	Thickening factor	[-]
h_s	Sensible enthalpy	[J/kg]
HRR	Heat Release Rate	$[\mathrm{W/m}^3]$
$J_{j,k}$	Diffusive flux vector of species k	$[\mathrm{kg/m}^2\mathrm{/s}]$
$\mathcal{K}$	Flame curvature	$[\mathrm{m}^{-1}]$
L_v	Latent heat of evaporation	[J/kg]
m_p	Mass of a Lagrangian particle	[kg]
m_p	Rate of change of droplet mass	[kg/s]
m_p	Mass flux of gaseous fuel from a droplet	[kg/s]
m	Mass flux	[kg/s]
$n_{\mathcal{F}}$	Number of points in the flame front	[-]
n_l	Number of droplet density	$[\mathrm{m}^{-3}]$
P	Pressure	[Pa]
P	Probability density function	$[-]$
q	Momentum flux ratio	$[-]$
r	Mixture gas constant	[J/kg/K]
r_j	Rate of reaction j	$[\mathrm{mol\,s}^{-1}]$
$\mathcal{R}$	Universal gas constant (mass)	$[\mathrm{J\,mol}^{-1}\ \mathrm{K}^{-1}]$
S_{ij}	Strain rate tensor	$[\mathrm{s}^{-1}]$
t	Time	[s]
T	Gaseous temperature	[K]
u_i	Gaseous velocity vector	[m/s]
u_l	Eulerian liquid phase velocity	[m/s]
$u_{p,i}$	Velocity vector of a Lagrangian particle	[m/s]
W	Molecular weight	[kg/mol]
x_i	Spatial coordinate (vector)	[m]
$\mathbf{x}$	Spatial coordinate (vector)	[m]
x	Spatial coordinate	[m]
$x_{p,i}$	Position vector of a Lagrangian particle	[m]
X_k	Molar fraction of species k	$[-]$
y	Spatial coordinate	[m]
Y_k	Mass fraction of species k	$[-]$
z	Spatial coordinate	[m]
Z	Mixture fraction	$[-]$

Greek characters

Symbol	Description	Unit
α_l	Liquid volume fraction	$[-]$
χ	Scalar dissipation rate	$[\mathrm{s}^{-1}]$
δ_{ij}	Kronecker symbol	$[-]$
η_κ	Kolmogorov scale	$[\mathrm{m}]$
Γ_l	Rate of change per unit volume of the liquid phase mass	$[\mathrm{kg/m^3/s}]$
Γ	Rate of mass change per unit vol. in the gas phase by evap.	$[\mathrm{kg/m^3/s}]$
$\Gamma_{u,i}$	Momentum exchange through mass exchange	$[\mathrm{kg/m^2/s^2}]$
κ	Flame stretch	$[\mathrm{s}^{-1}]$
λ	Heat conduction coefficient	$[\mathrm{W/m/K}]$
μ	Molecular viscosity	$[\mathrm{Pa\,s}]$
μ_t	Turbulent viscosity	$[\mathrm{Pa\,s}]$
ϕ	Equivalence ratio	[-]
Π_g	Sensible enth. rate of ch. per unit vol. in the gas phase by evap.	$[\mathrm{W/m^3}]$
Π_l	Sensible enth. rate of ch. per unit vol. in the liq. phase by evap.	$[\mathrm{W/m^3}]$
ρ	Gaseous density	$[\mathrm{kg/m^3}]$
ρ_k	Density of the gaseous species k	$[\mathrm{kg/m^3}]$
ρ_l	Liquid phase density	$[\mathrm{kg/m^3}]$
τ_{ij}	Stress tensor	$[\mathrm{N/m^2}]$
τ_{ij}^t	Turbulent tress tensor	$[\mathrm{N/m^2}]$
τ_p	Particle relaxation timescale	$[\mathrm{s}]$
Φ_g^c	Sensible enth. rate of change in the gas due to conduction	$[\mathrm{W}]$
Φ_g^{ev}	Sensible enth. rate of change in the gas due to evaporation	$[\mathrm{W}]$
Φ_l^{ev}	Sensible enth. rate of change in the liq. due to evaporation	$[\mathrm{W}]$
Φ_l^c	Sensible enth. rate of change in the liq. due to conduction	$[\mathrm{W}]$
Φ_l	Liquid volume flux	$[\mathrm{m^3/s/m^2}]$
ω_k	Species source term (in mass) of species k	$[\mathrm{kg/m^3/s}]$
ω_{Y_k}	Species source term (divided by density) of species k	$[\mathrm{s}^{-1}]$

Dimensionless numbers

Symbol	Description
B_M	Spalding number for mass transfer
B_T	Spalding number for heat transfer
Da	Damkohler number
Le	Lewis number
Nu	Nusselt number
Pr	Prandtl number
Pr_t	Turbulent Prandtl number
Re	Reynolds number
Re_t	Turbulent Reynolds number
Re_p	Particle Reynolds number
Sc	Schmidt number
Sh	Sherwood number
St	Stokes number
We	Weber number

Indices and superscripts

Symbol	Description
g	Index of a gaseous phase quantity
l	Index of a liquid phase quantity
F	Index of a fuel quantity
$glob$	Index of a quantity at global equivalence ratio
O	Index of an oxidiser quantity
st	Index of a quantity at stoichiometric equivalence ratio
tot	Superscript of an integrated quantity

Acronyms

Acronym	Definition
ARC	Analytically Reduced Chemistry
CFD	Computational Fluid Dynamics
CFL	Courant-Friedrichs-Lewy
CMC	Conditional Moment Closure
CRZ	Central Recirculation Zone
DNS	Direct Numerical Simulation
DOM	Discrete Ordinate Method
DRG	Directed Relation Graph method
DRGEP	DRG with Error Propagation
DTFLES	Dynamically Thickened Flame model for LES
EVC	Exit Vortex Core
FGM	Flame Generated Manifold
FIM-UR	Fuel Injection Method by Upstream Reconstruction
FPI	Flame Prolongation of Intrinsic Low-Dimensional Manifold
GRC	Globally Reduced Chemistry
HIT	Homogeneous Isotropic Turbulence
IRZ	Inner Recirculation Zone
LDV	Laser Doppler Velocimetry
LEMCOTEC	Low Emissions Core-Engine Technologies
LES	Large Eddy Simulation
LOI	Level Of Importance
LPP	Lean-Premixed Prevaporized
LW	Lax-Wendroff
NOMAGT	NOMAni with Grc and Tfles
NOMANI	Nitrogen Oxide emission model with one-dimensional MANIfold
NORA	NO Relaxation Approach
NSCBC	Navier-Stokes Characteristic Boundary Conditions
OPR	Overall Pressure Ratio
ORZ	Outer Recirculation Zone
PCM	Presumed Conditional Moments
PDF	Probability Distribution Function
PEA	Pre-Exponential Adjustment
PIV	Particle Image Velocimetry
PLIF	Planar Laser-Induced Fluorescence
PRZ	Primary Recirculation zone
PSR	Perfectly Stirred Reactor
PVC	Precessing Vortex Core
QSS	Quasi-Steady State
QSSA	QSS Approximation
RANS	Reynolds Average Navier-Stokes
RMS	Root-Mean-Square
RQL	Rich-burn, Quick-Quench, Lean-Burn
SRZ	Separator Recirculation Zone
TF	Thickened Flame
TFLES	Thickened Flame model for LES
TLC	Towards Lean Combustion
TTGC	Two-step Taylor-Galerkin scheme version C
UHC	Unburnt HydroCarbons

1

Introduction

Contents

1.1 Industrial context

Gas turbines are one of the most widely-used technology for power generation. They are used for electricity production, rotorcraft and aircraft propulsion, with high reliability and performance for various operating ranges. They were introduced in the aircraft industry to achieve better level of thrust at high altitude. For mid and long-range aircraft applications, the turbofan is the most common architecture. It consists of a gas turbine which generates the mechanical energy and a ducted fan which uses this energy to generate most of the thrust.

1.1.1 Fuel efficiency

Since the eighties, driven by increasing fuel prices, fuel consumption became a great concern. The aircraft industry was forced to explore fuel efficient engine concepts, which resulted in major changes in the global architecture of engines. This effort has been maintained in the last decades, thanks to innovations in materials and the architecture of the different stages of the engine. It is still pursued, since conventional jet fuel remains the main source of energy for aircraft propulsion due to its easy storage, safety and high energy density.

1.1.2 Environmental regulations

Since the nineties, the rapid growth of air traffic focused the attention on the environmental impact of civil aviation, although it remains a small contributor to global emissions (around 2 % of global CO_2 emissions). However air traffic is expected to grow even faster in the next decades (Fig. 1.1): fuel for aviation represents three percent of all combustion sources, and it is forecasted to reach 5 percent by 2050 (Intergovernmental Panel on Climate Change forecast). Moreover, air traffic is the major contributor to high altitudes emissions, which induce strong impact on atmospheric chemistry [1]. Therefore it has a significant impact both on local air quality and global atmospheric changes, which leads to the introduction of more drastic regulations of pollutant emissions.

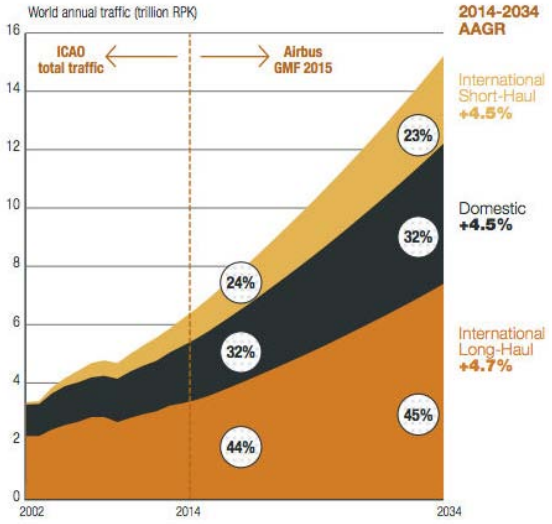

Figure 1.1: ICAO air traffic data and Airbus traffic forecast in revenue passenger kilometers. From [5].

The main pollutants emitted by aircraft engines are the following:

- **Carbon dioxide** (CO_2) is the direct product of combustion process. Thus the amount of carbon dioxide emitted is directly linked to the fuel efficiency of the engine. It is a major greenhouse gas.

- **Carbon monoxide** (CO) is mainly an issue at reduced power. It is colourless and highly toxic.

- **Nitrogen oxide and dioxide** (NO_x) contribute to ozone depletion, acid rains and directly affect local air quality.

- **Smoke** is composed of solid particles made of long hydrocarbon chains resulting from incomplete combustion process. It has a global warming effect and causes severe air pollution.

- **Unburnt hydrocarbons** (UHC) are a blend of fuel derivatives, resulting from incomplete combustion, that leave the combustion chamber. They consist of large to light hydrocarbons and are highly toxic.

The Committee on Aviation Environmental Protection (CAEP) and the Advisory Council for Aviation Research and Innovation in Europe (ACARE) have set up ambitious targets for 2020 [3]. There are multiple objectives:

- ACARE has a target of 20% reduction of CO_2 emissions and fuel consumption for the engine alone (and 50% for the overall aircraft) compared to the reference of 2000, which requires the development of engines with very high efficiency.

- New environmental standards require mitigation of pollutant emissions (smoke, CO, UHC) with great effort towards NO_x. The CAEP has a midterm goal of 45% and a long term goal of 60% NO_x reduction compared to the standard of 2008 [1]. Comparison of current engine emissions with CAEP regulations is shown in Fig. 1.2. Today, most engines on the market are 20 % below CAEP 6 regulations. However, for engines with high overall pressure ratio (OPR) (such as GE90 engine, with OPR $\simeq$ 45), this margin is reduced. The ACARE has an overall target of 80% NO_x reduction compared to the reference of 2000, with 60% for the combustor only.

The dual objectives of fuel-efficiency and low emissions raise a challenge from the combustor design point of view that will be addressed in Sec. 1.3.

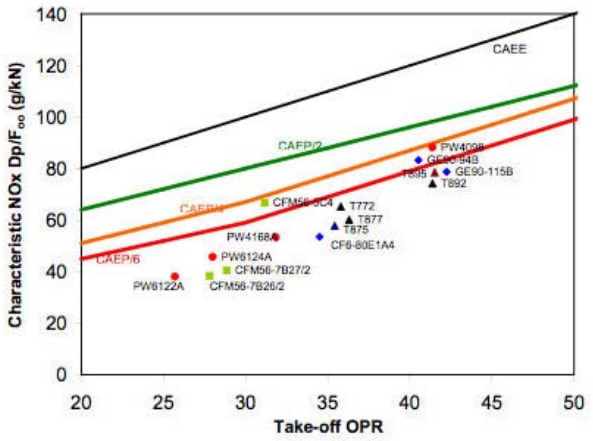

Figure 1.2: NO_x vs OPR for various engines and comparison with regulatory levels from CAEP. From [1].

1.2 Overview of CO and NO_x formation in gas turbine conditions

The design of modern gas turbine combustors requires an optimum compromise between NO_x and CO emissions at the different engine regimes. In this section, a concise review of the underlying chemical processes of NO_x and CO formation is provided. In particular, the impact of high temperature and pressure conditions and fuel-air stratification typically encountered in gas turbine configurations is discussed.

1.2.1 CO formation

CO is an intermediate product of the reaction between fuel and air. It is formed in the flame region, through highly reactive precursors such as HCO. The oxidation of CO into CO_2 is a slower process, initiated in the flame zone and continuing in the post-flame region. Thus, CO concentrations at the combustor exit are generally above equilibrium values and are linked to the combustor residence time.

For gas turbine applications, high CO levels at the combustor exit result from several factors:

- High CO concentrations are found in fuel-rich conditions because of the lack of oxygen to be recombined into CO_2. Fuel-rich combustion typically occurs in RQL concepts (see Sec. 1.3.3), non-premixed and complex two-phase flow flame structures. In this situation, the rich mixture is generally diluted prior to the combustor exit to burn the remaining fuel. However insufficient residence time and the quenching of the CO recombination reactions may lead to concentrations at the combustor exit much higher than the equilibrium value.

- High CO levels are also related to flame quenching that occurs due to flame-wall interactions or inappropriate design of air cooling [111]. All these effects may lead to overall CO values significantly higher than equilibrium values at the combustor exit.

- In addition, conditions close to lean blow-off combined with short residence time in the combustor can lead to incomplete oxidation of CO [73]. This situation is generally associated with poor combustion efficiency.

Impact of the operating conditions

Increased pressure tends to shift the CO-CO_2 equilibrium towards recombination in CO_2. *Bhargava et al.* [17] reported a $P^{-0.5}$ pressure dependence. On the contrary, higher inlet temperature which results in higher flame temperature promotes chemical dissociations that shift CO-CO_2 equilibrium towards CO. However no clear correlation is found between the operating conditions and the CO emissions because the non-equilibrium level at the combustor exit is highly dependent on the exact design of the combustor. Thanks to high combustion efficiency, CO levels are generally far below regulatory levels at high power conditions, but they generally peak and become a design issue at low-power conditions.

1.2.2 NO_x formation

NO_x is the generic term for nitric oxide (NO) and nitrogen dioxide (NO_2). The NO_x chemistry is governed by hundreds of elementary reactions which can be decomposed in several major chemical pathways that are detailed thereafter.

Thermal NO [212] is essentially formed in the hot product region of the flame where the reaction between the fuel and the air is already completed. It is formed from the oxidation of nitrogen and is described by the Zeldovich mechanism,

$$O + N_2 \rightleftharpoons NO + N\,, \tag{1.1}$$

$$N + O_2 \rightleftharpoons NO + O\,, \tag{1.2}$$

$$N + OH \rightleftharpoons NO + H\,. \tag{1.3}$$

Because of its high activation energy, the first reaction (Eq. 1.1) is rate limiting. In addition, the O species concentration is exponentially dependent on the temperature, so that the NO formation rate becomes significant only for temperatures above 1800 K, i.e. mostly in the burnt gases. Compared to carbon oxidation reactions, thermal NO formation occurs on slower time scales. Depending on temperature and pressure conditions and on the residence time, this slow post-flame process generally represents 35

to 70% of the total NO formation [117]. Given that it is a slow chemical process and that gas turbines have small residence times, the exhaust concentrations remain significantly below equilibrium values and strongly depend on the residence time. Note that thermal NO formation is also promoted by the super-equilibrium concentrations of O and OH radicals [40] occurring in the flame front.

The **prompt NO route** was initially suggested by *Fenimore* [53, 54], who observed that high NO concentrations were found close to the flame region that could not be attributed to the slow thermal route alone. The prompt NO production is a rapid process that occurs in the reaction zone from the interaction of N_2 with radicals generated by fuel oxidation. This interaction was initially attributed to a reaction with CH to form HCN intermediate:

$$N_2 + CH \rightleftharpoons HCN + N\,. \tag{1.4}$$

HCN further reacts through various reactions to lead to the formation of NO, while the N radical directly promotes the thermal NO formation. Thus the thermal and prompt pathways are highly coupled in the flame reaction zone. This description of prompt NO via HCN has been retained in many detailed mechanisms [22, 128, 207] and yields satisfactory prediction of NO levels in several reference flames for which this pathway is significant [11]. However, it was argued that the reaction between N_2 and CH violates the quantum mechanics principle of spin conservation, and thus cannot represent the true chemical process of prompt NO initiation. It is now accepted that the correct intermediate species is rather NCN [132] via the reaction

$$N_2 + CH \rightleftharpoons NCN + H\,, \tag{1.5}$$

which conserves electron spin, and is now implemented in recently built detailed mechanisms [103].

The prompt NO process peaks at stoichiometric or slightly rich conditions, because it is enhanced by high flame temperature and large quantities of available hydrocarbon radicals. It plays also a significant role in the rich region of diffusion flames. Its contribution is generally negligible in the post-flame region where hydrocarbon radicals are no longer available.

In the **N_2O route**, N_2O intermediate is formed via the reaction of N_2 and O that

leads to NO formation via the following reactions:

$$N_2 + O + M \rightleftharpoons N_2O + M\,, \tag{1.6}$$

$$N_2O + O \rightleftharpoons NO + NO\,, \tag{1.7}$$

$$N_2O + H \rightleftharpoons NO + NH\,. \tag{1.8}$$

It is one of the major contributor to NO_x formation under lean premixed, high pressure conditions, that are typically found in modern gas turbine combustors [47]. It is also promoted by O superequilibrium concentrations in the flame region.

In the **NNH pathway** [25], N_2 and H react to form NNH intermediate, which is then oxidised by the O atom to form NO:

$$N_2 + H \rightleftharpoons NNH\,, \tag{1.9}$$

$$NNH + O \rightleftharpoons NO + NH\,. \tag{1.10}$$

This process is significant for low flame temperatures. Similarly to the thermal pathway, it is promoted by possible superequilibrium O concentration in the flame front.

NO conversion in NO_2 is promoted by high pressure conditions. NO is also rapidly oxidised into NO_2 at moderate temperatures. However, NO_2 concentrations are generally small in the hot exhaust gases of gas turbine chambers.

Fuel NO [151] is relevant for fuels containing chemically bound nitrogen, which is typically the case for coal and biomass that are not considered in this work.

Decomposition of NO_x formation into slow and fast processes

Fenimore [53] observed that the NO profile in burnt gases had a non-zero intercept when extrapolated to the flame front for rich mixtures. As exemplified in Fig. 1.3 on a rich premixed methane-air flame computation, rapid NO formation occurs in the reaction of zone, which was given the name "prompt NO" by Fenimore. To analyse NO_x formation in combustors, it is interesting to separate the overall NO_x production into the fast flame processes that are related to the fuel consumption and the local combustion regime, and the slower post-flame processes that are related to residence time and essentially driven by thermal NO pathway. This can be done in several manners:

- **By chemical pathways:**

- The total NO source term can be decomposed into the contributions of the different pathways. However, as mentioned above, prompt and thermal pathways are highly coupled via N radical, so that there is no clear separation.
- The subtraction method consists in removing one pathway from the mechanism to obtain an evaluation of its impact on NO production. However it requires to perform several computations which can be too costly in the context of LES.

- **By separating flame and post-flame processes:**
  As suggested by *Biagioli et al.* [18], the decomposition can be based on the analysis of chemical time scales. Another possibility is to measure NO concentration at a given arbitrary distance from the flame front to separate flame and post-flame processes. However, this definition is not applicable to turbulent flows. Instead, a threshold value of the progress variable can be used to separate flame and post-flame zones.

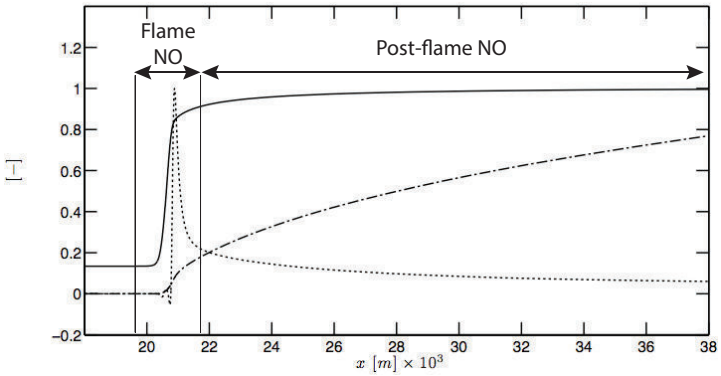

Figure 1.3: One-dimensional premixed methane-air flame at atmospheric conditions and equivalence ratio $\phi = 1.15$ with GRI 2.11. Normalised temperature (—), NO mass fraction $(\cdot - \cdot -)$ and NO source term $(\cdots)$.

Impact of operating conditions

The temperature has a strong impact on NO_x formation rate. Increased combustor inlet temperature results in a higher flame and post-flame temperature, and in turns increased NO_x emissions mostly because of thermal NO. Prompt NO formation is also promoted by increased temperature, but to a smaller extent.

The influence of pressure on NO_x formation is more complex, because it differs for the different pathways. It is case dependent, and influenced by the combustion regime, the fuel-air stratification and the relevant NO_x chemical pathways. As a result, available data from the literature sometimes exhibit contradictory trends. A square root dependence on pressure ($P^{0.5}$) of thermal NO is generally accepted [40], but the situation

is less clear for the other pathways. Using laminar flame calculations with natural gas mixtures, *Biagioli et al.* [18] analysed the effect of pressure (in a range from 0.1 to 3 MPa), equivalence ratio and unmixedness on the production of NO, decomposed into a rapid flame contribution and a slower post-flame one. They found that the rapid flame contribution decreases as $P^{-0.45}$ and that the post-flame contribution increases as $P^{0.67}$. They also reported a stronger sensitivity of post-flame NO to fuel-air unmixedness. Since post-flame NO_x driven by the thermal route is a significant mechanism in gas turbines, NO_x emissions are expected to increase with pressure. However this trend could be reversed with lean, low temperature flames in combustor having efficient mixing between fuel and air, for which the fast flame contribution to NO formation can be dominant. In particular, in the review of *Correa et al.* [40], a positive pressure exponent is found for lean premixed combustion, which decreases to 0 for very low equivalence ratio. *Leonard and Stegmaier* [113] reported NO_x emissions to be independent of pressure in perfectly-premixed conditions with temperature below 1900 K and lean equivalence ratio ($\phi = 0.7$). Also *Bhargava et al.* [17] conducted experiments in the range 0.7 to 2.7 MPa. They reported a pressure exponent dependency between -0.77 and 1.6 depending on the fuel injection type, highlighting the impact of local mixing quality, which is also in agreement with the experimental and numerical findings of *Mongia et al.* [133] who also reported the high sensitivity of NO_x levels to incomplete mixing at lean conditions. *Gokulakrishnan et al.* [73] reported a positive dependence of NO_x to pressure for a lean premixed combustor, with both gaseous and liquid fuels. To summarise, the impact of pressure on NO_x depends on various parameters including combustor design and fuel considered. However, the clear global trend is that low flame temperature and efficient mixing of fuel and air prior to combustion always tend to decrease NO_x production.

1.2.3 Impact of liquid fuel

Spray combustion can play a significant role in CO and NO_x emissions. Because of the formation of rich pockets of fuel-air mixture due to local droplet evaporation and droplet segregation processes [171], near stoichiometric burning regions appear even in lean global conditions, and the fuel-air mixing is reduced. *Baessler et al.* [8] studied the influence of the pre-vaporization rate of aeronautical fuel on NO_x formation. At stoichiometric conditions, NO_x emissions were high and insensitive to the pre-vaporization rate. For lean conditions, the emissions were comparable to the stoichiometric case at low pre-vaporization rate, but they strongly decreased beyond a pre-vaporization rate threshold. It indicates that NO_x formation is sensitive to the flame combustion regime which is strongly driven by the spray characteristics.

1.3 Challenge for the development of low emission aeronautical burners

From the combustor design point of view, the dual objectives of fuel efficiency and low environmental impact are contradictory. Indeed, higher core engine thermal efficiency requires higher operating pressure and temperature of the combustor, which directly promotes NO_x emissions. Thus innovative architectures are required to achieve low emissions. As shown in Fig. 1.4, the design of aeronautical combustion chambers is constrained by high safety and operability requirements over the whole flight envelope, as well as drastic weight and size constraints compared to land gas turbines. Thus the development of low emission innovative design must result from a global optimisation process.

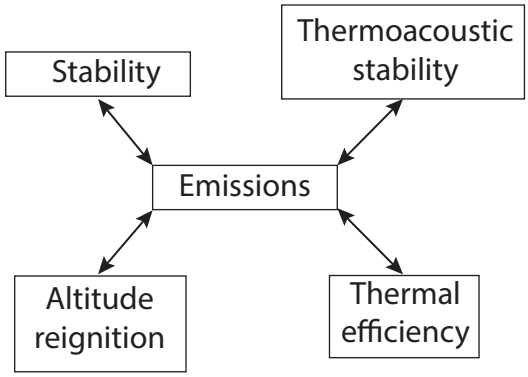

Figure 1.4: Design constraints applying to aeronautical burners.

1.3.1 Towards higher thermal efficiency

The global efficiency η of a turbofan engine can be decomposed into a propulsive efficiency η_{prop} and a thermal efficiency $\eta_{thermal}$

$$\eta = \eta_{prop} \times \eta_{th} \,, \tag{1.11}$$

thus both must be improved to achieve higher global efficiency.

The **propulsive efficiency** is essentially related to the bypass ratio, which is the ratio between the mass flow that bypasses the engine core (compressor stages, combustor and turbine stages) to the mass flow passing through the engine core. To reduce fuel consumption, the bypass ratio has been dramatically increased over the last decades, typically from 1-2 in the sixties to 10-15 for the most recent engines. Because of weight and drag limitations, further increasing the bypass ratio requires the development of

new architectures, such as open rotor engines, for which the bypass ratio reaches values up to 30. However this type of architecture raises many other issues (integration, acoustics) that still need to be addressed.

On the other side, the **thermal efficiency** is the efficiency of the thermodynamic cycle of the core engine. It corresponds to an ideal Brayton cycle, whose efficiency is directly related to the OPR, which is the total pressure ratio between the combustor entrance and the compressor inlet. Its expression reads [24]

$$\eta_{th} = 1 - \frac{T_2}{T_3} = 1 - (1/\mathrm{OPR})^{(\gamma-1)\ \gamma}\ , \tag{1.12}$$

where T_2 and T_3 are respectively the total temperature at the compressor inlet and the combustor entrance and γ is the heat capacity ratio. Thus, high thermal efficiency is achieved by increasing the OPR. In modern core engine architectures, such as the LEAP-X, the typical OPR is 40:1.

1.3.2 The LEMCOTEC project

This thesis is part of the European project LEMCOTEC (Low Emissions Core-Engine Technologies). This industrial and academic research project aims at developing technologies for core engines with ultra high OPR up to 70, that allows to improve the thermal efficiency of the engine. The project includes the development of innovative high pressure ratio compressors, advanced materials and thermal management for the core engine architecture.

For the combustor part, the effort is focused on the development of ultra-low NO_x combustion systems adapted to high temperature and pressure conditions of high OPR core engines. In this purpose, SNECMA is currently developing a prototype of ultra-low NO_x combustor that will be introduced in Sec. 1.3.4. The final objective is to demonstrate the technological readiness of the prototype regarding the design constraints of Fig. 1.4: the light-around capability, the thermo-acoustic stability and the pollutant emission levels of the prototype will be assessed on a full annular test-rig.
In this purpose, a comprehensive numerical methodology for the design and understanding of ultra-low NO_x combustion chambers has been developed, based on the solver AVBP co-developed by CERFACS and IPFEN. *Bauerheim* [13] focused on the development of numerical and analytical models to predict azimuthal thermo-acoustic instabilities. The ignition process, including light-around phase was studied in the thesis of *Esclapez* [52]. The aim of this thesis is to build a methodology for the numerical

prediction of NO_x and CO that is able to tackle the complexity of aeronautical configurations.

.

1.3.3 Towards lower pollutant emissions: ultra low emission combustor design

In terms of combustor design, the need for higher OPR leads to higher inlet temperature and pressure as well as higher outlet temperature. As shown in Sec. 1.2.2, these conditions strongly promote the formation of NO_x. Thus, innovative combustor design is required to meet current and future NO_x emission requirements, without being detrimental to other pollutant emission levels and the global performances of the core engine in terms of safety, operability and efficiency. The main low-emission concepts used in modern aircraft combustors are summarised in this section. Whereas combustion in conventional combustors is done at near-stoichiometric conditions, in most innovative concepts, the combustion process occurs away from stoichiometry. As shown in Fig. 1.5, strong NO_x reduction is achievable on both the lean and rich sides of stoichiometry. Conversely, CO concentrations are generally high in rich conditions or close to lean-blow off conditions, where the NO_x emissions are the lowest. The residence time of the combustor must be sufficient so that CO can be fully burnt out into CO_2, but this will promote NO_x in the post-flame region that is directly related to the residence time. Therefore a strong compromise must be found to obtain satisfactory emission levels at all regimes.

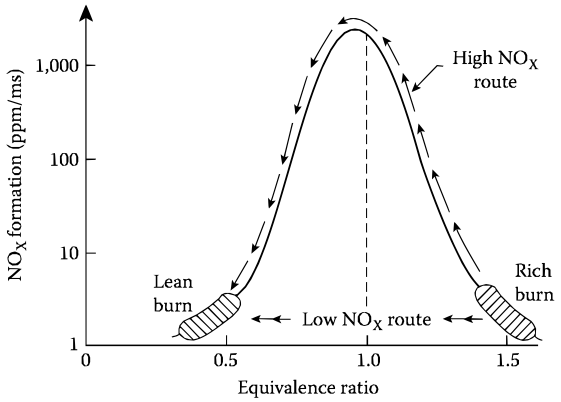

Figure 1.5: Typical NOx levels vs equivalence ratio and illustration of the RQL principle. From [111].

In **Lean premixed pre-vaporized (LPP) concepts** [6], a premixing zone between air and fuel prior to combustion enables a reduction of NO_x thanks to low flame temperature. However this concept is generally not applicable to aeronautical engines because

the premixing zone increases the combustor size and the risk of autoignition of the mixture.

The **Lean Direct Injection (LDI)** concept consists of a reduced-size series of lean direct injectors. The fuel is directly injected without staging or premixing zone and the reduced size of the multiple injection systems allow to improve spray properties and fuel-air mixing [79, 193] leading to flame temperature below the critical value of 1800 K for thermal NO formation.

In **Rich-burn, Quick-Quench, Lean-Burn (RQL)** concepts, the combustion process is initiated in rich conditions in the primary zone. Then rapid dilution and mixing of the hot products with fresh gases occur and the remaining fuel burns in lean conditions. This allows to avoid fuel burning at near-stoichiometric conditions which are favourable to NO_x production. The low-NO_x route of the RQL concept is shown in Fig. 1.5. It is still successfully applied in commercial engine combustor design. However, considering the future trend of extreme pressure and temperature conditions, it will become increasingly difficult to keep satisfactory emission levels with this concept, because of high NO production even with limited residence time in stoichiometric conditions at high pressure and temperature. Also, the rich combustion significantly promotes the formation of smoke.

The **multipoint injection concept** (also known as premixing swirler concept) is the concept retained by SNECMA in the framework of the LEMCOTEC project to demonstrate the performance of an ultra-low NO_x combustion chamber in a full-annular test rig. More details about this concept are provided hereafter.

1.3.4 Multipoint injection system: design and optimisation

A schematic of the multipoint injection concept is shown in Fig. 1.6, and a typical configuration designed by SNECMA is shown in Fig. 1.7. The injection system is radially staged, and leads to two distinct flame regions: a pilot flame close to the centerline, and a main (multipoint) flame in the outer region. The key idea of the concept is to inject the main fuel through small holes in the vanes of the main swirler. The highly swirling environment promotes a fine atomisation of the liquid jets, thus enabling a rapid evaporation and mixing between fuel and air to obtain a lean, homogeneous mixture. It results in a lean, well-premixed flame achieving low NO_x formation.

The pilot flame is stabilised in the central region where the fuel is injected via a pilot atomiser: its main role is to provide hot products to help stabilising the main flame.

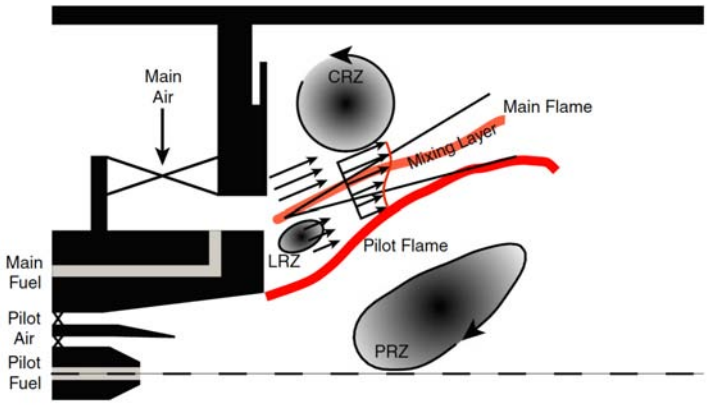

Figure 1.6: Schematic view of the multipoint injection system and flame structure. From [44]. PRZ: primary recirculation zone. CRZ: corner recirculation zone. LRZ: lip recirculation zone.

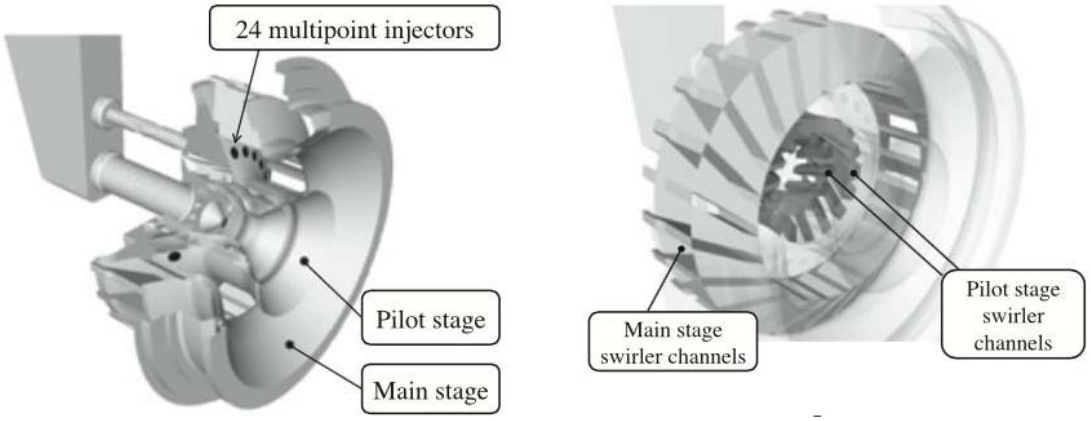

Figure 1.7: SNECMA multipoint injector design (TLC project). From [91].

It also provides most of the energy at low-power conditions. This type of design has been successfully implemented in the combustor of the LEAP-X core engine with a 50% margin from CAEP 6 regulations for NO_x emissions despite a design OPR of 40.

Design trade-off to achieve low emissions

To achieve low NO_x emissions, the strategy is to minimise the residence time in the combustor to limit the thermal NO_x contribution. However a sufficient residence time is required to fully burn out CO, and a compromise must be found. Efficient staging strategy is also mandatory to achieve pollutant emissions targets for the wide range of operating conditions while maintaining sufficient stability margins. In particular, the compromise between NO_x and CO emissions at low and intermediate power strongly depends on the staging strategy. At low power conditions, only the pilot flame is burning and fresh air from the main swirler can freeze the combustion process if the spatial separation between stages is not sufficient, which typically promotes CO emissions. At

higher power, interactions between the two flames can also occur [9], affecting the local flame structure and pollutant formation.

The lean multipoint flame may be subject to strong dynamics and interactions with acoustics [83]. For instance, periodic instability related to flashback in lean staged injection system was identified and investigated experimentally by *Dhanuka et al.* [43, 44], the main steps of the instability being shown in Fig. 1.8. After an initial perturbation, local extinction occurs in the outward flame region. It is subsequently filled with unburnt reactants, until the flame abruptly propagates into these region and flashes back to the injector wall, which generates a pressure wave sustaining the process loop, leading to high amplitude and low-frequency ($\simeq 15Hz$) pressure oscillations. In addition,

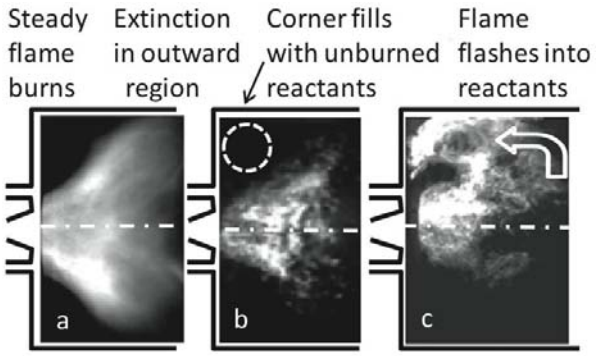

Figure 1.8: High speed imaging of periodic flashback sequence in a lean staged model combustor. From [43].

because of the strong sensitivity of heat release to equivalence ratio fluctuation in the lean domain [116], the multipoint flame is more sensitive to strong coupling with the acoustics, which can potentially lead to thermo-acoustic instabilities.

1.4 Objectives and organisation of the thesis

1.4.1 Challenges of accurate pollutant prediction in gas turbine configurations

Given the important optimisation process associated with innovative combustor designs, numerical tools like Large Eddy Simulation (LES) are of great help for a better understanding of the combustor behaviour and underlying mechanisms, since it can correctly capture most unsteady features, such as fuel-air mixing and flame dynamics [69]. It can be a valuable complement to experimental campaigns for which diagnostics inside the combustor are costly and limited. LES is also capable of predicting unstable behaviour of the combustor [209], as well as ignition and re-ignition capabilities [12].

Therefore it can cover many aspects of the design of ultra low emission combustors.

Even though chemical processes of CO and NO_x formation are rather well understood, their accurate prediction in real aeronautical geometries remains a challenge because they are strongly impacted by multiple effects such as multiphase combustion, turbulence, air cooling and dilution, or radiative and wall heat transfer. The high temperature environment and limited optical access of combustors make the measurement of species very difficult inside the combustion chamber, thus experimental data in real gas turbine burners are often limited to exhaust gas composition. This limitation does not allow a thorough validation of models for pollutant formation and emissions, and it is necessary to consider first academic configurations, where more detailed measurements are available, but the variety of phenomena occurring in real industrial chambers is only partially represented.

In the last years, most of the modelling effort for pollutant prediction relied on the tabulated chemistry approach, as it is able to include detailed chemistry effects needed to predict pollutant formation while remaining computationally efficient: academic configurations such as the Sandia flame D were extensively used as a validation case, and a fair agreement was generally obtained between measurements and simulations [85, 122, 148, 201, 213]. However the standard flamelet formulation is not appropriate for the slow processes of NO_x and CO formation and thus requires additional modelling [85, 148, 213]. These extended models lead to reasonable NO_x prediction in academic configurations but less effort was made towards accurate CO prediction. Moreover, their application to real configurations with complex flow and flame structures and multiphysics phenomena is not straightforward.

A promising alternative to tabulated chemistry is to use reduced chemical mechanisms. If globally fitted, 1- to 4-step mechanisms are not well suited to describe pollutant formation, as they contain few intermediate species involved in pollutant formation. More advanced reduction techniques lead to larger, but still reduced mechanisms that preserve a faithful description of the combustion and pollutant formation processes, and are therefore able to handle multiple and complex combustion regimes in real configurations at varying pressure and temperature conditions. Compared to tabulated methods, there is no *a priori* assumption made on the local flame structure. Moreover, the chemical impact of wall heat transfer and thermal radiation is intrinsically taken into account in the chemical description. Such schemes, named analytically reduced chemistries (ARCs) comprise for example about ten to twenty species for methane-air combustion [126, 191].

1.4.2 Organisation of the thesis

ARCs have shown their capability to accurately predict NO formation in canonical configurations such as perfectly stirred reactors (PSRs), freely propagating flames and diffusion flames. They have been recently applied in the context of LES to turbulent flames by *Jones and Prasad* [94] on the Sandia flame series (D-F). However, complex industrial configurations are tackled in very few studies. They were employed by *Bulat et al.* [27] on an industrial gas turbine configuration, which is also studied in this thesis. In addition, *Franzelli et al.* [62] showed the capability to accurately predict the flame structure in a partially premixed swirled gas turbine model combustion with a 13-species ARC [176].

The main objective of this work is to build a methodology for pollutant prediction in aeronautical gas turbine configurations based on ARCs that include accurate CO and NO_x prediction. One of the novel aspects of this work is that the ARCs are specifically derived for the intended applications, whereas available mechanisms from the literature are generally used in most previous studies. This enables to have a direct control of their cost, accuracy, and range of validity. This was made possible by the contribution of the thesis of *Felden*, which is currently going on, and is specifically oriented towards the reduction of complex chemistries. Another novel aspect is that the ARC is combined with the artificial thickened flame model which has largely proven its capability to predict the combustion features in complex configurations [12, 69] The thesis is organised as follows:

- In the first part, the theoretical backgrounds of computational fluid dynamics, combustion and two-phase flow description are introduced.
- In the second part, two methodologies for pollutant prediction are developed and validated on canonical cases. The first one is based on a tabulated approach, and is an extension of the model of *Pecquery et al.* [148], who derived a model for NO_x prediction with application to academic and industrial configurations. The second, which is the major novelty of this thesis, is based on the combination of reduced mechanism (ARC) having an accurate flame structure and pollutant description with the artificially thickened flame model.
- Finally, the methodology is applied in the LES of three turbulent configurations with increasing complexity:
  - The Sandia D turbulent flame, a reference academic case for pollutant emission modelling.

- A gas turbine model combustor derived from the commercial Siemens SGT-100 burner studied experimentally at DLR Stuttgart.
- A prototype of multipoint aeronautical injection system developed by SNECMA in the framework of the LEMCOTEC project and studied experimentally at ONERA.

This wide range of configurations allows to demonstrate the prediction capability of the methodology and the analysis of local flow conditions, flame structure and turbulence-chemistry interaction provides a better understanding of the driving mechanisms of pollutant formation in such configurations.

1.4.3 Brief introduction of the target configurations

The conditions corresponding to two of the three target configurations will be widely employed throughout the first chapters of the thesis to build and validate the different models. For the clarity of the reader, they are briefly introduced at this early stage:

- The **Sandia flame D** is a turbulent non-premixed jet flame. The burner consists of three coaxial jets. The main central jet is a rich methane-air mixture, with an equivalence ratio $\phi = 3.17$, at ambient conditions. The flame is stabilised via a pilot encompassing the main jet. It consists of burnt gases at an equivalence ratio $\phi = 0.77$. A coflow of air at ambient conditions surrounds the pilot jet.
- The **SGT-100 burner** is gas turbine combustor configuration operated with natural gas. The combustor burns in a lean, partially-premixed regime. Two operating points are considered: SGT-100/Case A with a fresh gas temperature $T_{in} = 680\,\mathrm{K}$ and combustor pressure $P = 3\,\mathrm{bars}$ and SGT-100/Case B with the same fresh gas temperature and combustor pressure $P = 6\,\mathrm{bars}$.

Part I

Theoretical concepts and modelling of turbulent reacting flows for Large Eddy Simulation

2

Governing equations for Large Eddy Simulation

Contents

2.1 Introduction

In this chapter, the governing equations and the physical modelling are presented for the gaseous phase. The fundamental concepts of LES are introduced along with the resulting filtered equations that are at the basis of the numerical implementation in the AVBP solver, which is briefly introduced thereafter.

2.2 Governing equations for the Gaseous Phase

Note: The Einstein s rule of summation is employed except when explicitly stated otherwise and at the exception of the index k which is employed to refer to the k^{th} species without summation rule.

2.2.1 The Navier-Stokes equations

The Navier-Stokes equations arise from conservation principles of mass, momentum and energy. For multi-species reacting flows, they can be written in conservative form as follows:

- Mass conservation
$$\frac{\partial \rho}{\partial t} + \frac{\partial}{\partial x_j}\left(\rho u_j\right) = 0\,, \tag{2.1}$$
- Momentum conservation
$$\frac{\partial \rho u_i}{\partial t} + \frac{\partial \rho u_i u_j}{\partial x_j} = -\frac{\partial}{\partial x_j}\left(P\delta_{ij} - \tau_{ij}\right)\,, \quad \text{for } i = 1,2,3\,, \tag{2.2}$$
- Energy conservation
$$\frac{\partial \rho E}{\partial t} + \frac{\partial}{\partial x_j}\left(\rho E u_j\right) = -\frac{\partial}{\partial x_j}\left(u_i\left(P\delta_{ij} - \tau_{ij}\right) + q_j\right) + \omega_T\,, \tag{2.3}$$
- Species conservation
$$\frac{\partial \rho Y_k}{\partial t} + \frac{\partial \rho Y_k u_j}{\partial x_j} = -\frac{\partial}{\partial x_j} J_{jk} + \omega_k\,, \quad \text{for } k = 1, n_{spec}\,. \tag{2.4}$$

The left-hand side (LHS) of these equations correspond to the unsteady and convective terms for the density ρ , the i^{th} component of the velocity u_i, the total energy E and the k^{th} species. The right-hand side (RHS) comprises the viscous momentum flux tensor $-\tau_{ij}$, the pressure flux tensor $P\delta_{ij}$, the energy flux q_i and the species diffusive flux J_{ik}. The species source terms ω_k and heat release rate (energy source term) ω_T due to the chemical reactions also appear on the RHS of the equations.

To close the equations, an equation of state that relates pressure, temperature and density is needed. Considering an ideal gas mixture, it reads

$$r = \frac{\mathcal{R}}{W}\,, \tag{2.5}$$
$$P = \rho r T\,, \tag{2.6}$$

where $\mathcal{R} = 8.3143\,\mathrm{J/mol/K}$ is the universal gas constant and r is the gas constant that depends on the local gas composition through the mean molecular weight W, whose expression reads

$$\frac{1}{W} = \sum_{k=1}^{n_{spec}} \frac{Y_k}{W_k}\,. \tag{2.7}$$

2.2.2 Viscous momentum flux

The viscous momentum flux tensor (or viscous stress tensor) for Newtonian fluid is given by

$$\tau_{ij} = 2\mu \left(S_{ij} - \frac{1}{3}\delta_{ij} S_{ll} \right) , \tag{2.8}$$

where S_{ij} is the strain rate tensor

$$S_{ij} = \frac{1}{2} \left(g_{ij} + g_{ji} \right) , \tag{2.9}$$

and is defined as the symmetric part of the velocity gradient tensor g_{ij}

$$g_{ij} = \frac{\partial u_i}{\partial x_j} , \tag{2.10}$$

and μ is the molecular viscosity, whose modelling is presented in Sec. 2.2.5.

2.2.3 Species diffusion flux

Using the *Hirschfelder Curtis* [82] approximation, the species diffusion flux can be expressed as

$$J_{ik} = -\rho Y_k V_i^k = -D_k \frac{W_k}{W} \frac{\partial X_k}{\partial x_i} , \tag{2.11}$$

where D_k is the mixture diffusion coefficient for the k^{th} species and $X_k = Y_k W / W_k$ is the k^{th} species mole fraction. To ensure mass conservation ($\sum_{k=1}^{n_{spec}} J_{ik} = 0$), a correction diffusion velocity

$$V_i^c = \sum_{k=1}^{n_{spec}} D_k \frac{W_k}{W} \frac{\partial X_k}{\partial x_i} \tag{2.12}$$

is introduced. With this correction, the species diffusion flux finally reads

$$J_{ik} = -\rho \left(D_k \frac{W_k}{W} \frac{\partial X_k}{\partial x_i} - Y_k V_i^c \right) . \tag{2.13}$$

The expression of D_k, depending on the transport model retained is presented in Sec. 2.2.5.

2.2.4 Energy flux

The energy flux is decomposed into a diffusive term (heat conduction) and an additional term due to the transport of energy by the species diffusion. The total energy flux can be expressed as

$$q_i = \underbrace{-\lambda \frac{\partial T}{\partial x_i}}_{\text{Conduction}} \underbrace{-\rho \sum_{k=1}^{N} \left(D_k \frac{W_k}{W} \frac{\partial X_k}{\partial x_i} - Y_k V_i^c \right) h_{s,k}}_{\text{Energy transport through species diffusion}} = -\lambda \frac{\partial T}{\partial x_i} + \sum_{k=1}^{N} J_{ik} h_{s,k} , \tag{2.14}$$

where λ is the heat conduction coefficient (see Sec. 2.2.5) of the mixture and $h_{s,k}$ is the sensible enthalpy of the k^{th} species.

2.2.5 Modelling transport coefficients

Advanced models for transport coefficients employed in kinetics solver such as Cantera [74] remain expensive for LES computations. Therefore a simplified approach presented in this subsection is retained.

The molecular viscosity μ is assumed to be independent of the gas composition and to be close to that of air. Thus the classical Sutherland law can be used

$$\mu = c_1 \frac{T^{3\ 2}}{T + c_2} \frac{T_{ref} + c_2}{T_{ref}^{3\ 2}}, \tag{2.15}$$

Alternatively, a second law is available, called power law, for which the expression of the molecular viscosity reads

$$\mu = c_1 \left(\frac{T}{T_{ref}} \right)^b, \tag{2.16}$$

with b typically ranging between 0.5 and 1.0. For example $b = 0.76$ for air.

Assuming a constant molecular Prandtl number Pr, the heat conduction coefficient of the gas mixture is simply related to the molecular viscosity as

$$\lambda = \frac{\mu C_p}{Pr}, \tag{2.17}$$

where $C_p = \sum_{k=1}^{n_{spec}} C_{p,k} Y_k$ is the heat capacity of the mixture.

The computation of the species diffusion coefficients D_k is a specific issue. These coefficients should be expressed as a function of the binary coefficients D_{ij} obtained from kinetic theory (*Hirschfelder et al.* [82]). Following *Bird et al.* [20], the mixture diffusion coefficient of species k can be expressed as

$$D_k = \frac{1 - Y_k}{\sum_{j \neq k} X_j / D_{jk}}. \tag{2.18}$$

To reduce the numerical costs associated with the binary coefficients computation, a simplified approximation is used in AVBP for D_k. Similarly to thermal diffusion, the Schmidt numbers Sc_k of the species are supposed to be constant so that the diffusion coefficient for each species is expressed as

$$D_k = \frac{\mu}{\rho\, S_{c,k}}. \tag{2.19}$$

The impact of this assumption will be highlighted in Chapter 7.

2.3 The Large Eddy Simulation concept

2.3.1 The energy cascade

Big whorls have little whorls, which feed on their velocity, And little whorls have lesser whorls, and so on to viscosity - Lewis Richardson

The transition from a laminar flow to a turbulent flow is characterised by the Reynolds number comparing inertia forces with viscous forces

$$Re = \frac{\rho u L}{\mu}\,, \tag{2.20}$$

where u and L are characteristic velocity and length scales of the flow and μ is the molecular viscosity. For large Reynolds number, inertia forces are dominant and the turbulent flow is characterised by a wide variety of scales, from the largest eddies at the integral length scale l_t to the smallest dissipative scales at the so-called Kolmogorov scale η_κ. For isotropic turbulence, the ratio of the largest to the smallest eddies can be expressed as

$$\frac{l_t}{\eta_\kappa} = Re_t^{3\ 4} = \left(\frac{\rho u' l_t}{\mu}\right)^{3\ 4}\,, \tag{2.21}$$

where u' are the turbulent velocity fluctuations at the integral length scale and

$$Re_t = \frac{\rho u' l_t}{\mu} \tag{2.22}$$

is the turbulent Reynolds number. In practical applications, this ratio is of the order of one thousand. In-between, the inertial zone is an intermediate range of scale in which the energy is transferred from the largest scales to the smaller scales. This concept of direct energy cascade was first formalised by *Kolmogorov* [102] for homogeneous isotropic turbulence. A schematic view of this cascade is shown in Fig. 2.1. The length scales are characterised in terms of wavelength k, with high wavelengths corresponds to the smaller turbulent scales. The inertial range is characterised by a constant slope (in log-log scale) $E(k) \quad k^{-5\ 3}$ where $E(k)$ is the kinetic energy at wavenumber k. These pioneering findings are at the basis of the different strategies for simulation of turbulent flows.

2.3.2 Strategies for simulation of turbulent flows

Direct Numerical Simulation (DNS) is a brute force approach, in which all the scales of the turbulent motion are explicitly resolved. The grid resolution must be of the order of the Kolmogorov scale $\Delta x = O(\eta_\kappa)$ [165]. Given that the integral length

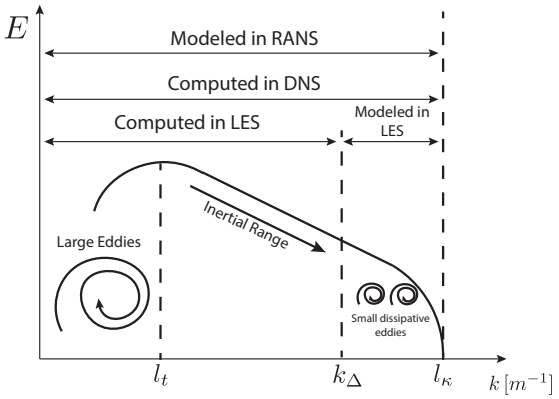

Figure 2.1: Sketch of energy density E vs wavelength k in an homogeneous isotropic turbulence (log-log scale).

scale l_t and the computational size are of the same order, the number of grid points needed to correctly resolve all the turbulent scales scales as

$$N_{points} \quad \left(\frac{l_t}{\eta_\kappa}\right)^3 = Re_t^{9\ 4} \tag{2.23}$$

Therefore for high Reynolds number practical applications, this number rapidly becomes out of reach of today s and tomorrow s computational power. To circumvent these limitations, two approaches have been extensively used in the last decades in CFD.

The fundamental idea of the **Reynolds-Averaged Navier Stokes (RANS)** approach is to decompose the turbulent flow into two contributions, a mean flow and its fluctuations. Formally, an averaging operator is applied to each quantity $\mathcal{Q}$ leading to the Reynolds decomposition

$$\mathcal{Q} =< \mathcal{Q} > +\mathcal{Q}' \quad \text{with } < \mathcal{Q}' >= 0\,, \tag{2.24}$$

where $< \mathcal{Q} >$ is the mean of the quantity and $\mathcal{Q}'$ is the deviation from the mean. The RANS equations are obtained by applying this averaging operator to the whole set of Navier-Stokes equations. Thus only the mean quantities are solved. Because of the non-linear terms of the Navier-Stokes equations, unclosed higher order terms appear in the transport equations of the mean quantities. They can be modelled or resolved through additional transport equations in which even higher order unclosed terms will appear. First or second order closures are generally employed in practice. Closure models were designed to be suitable for specific configurations (e.g. isotropic turbulence, flow on a flat plate) but the largest scales of turbulence are largely dependent on the configuration geometry. Since the whole turbulent spectrum is modelled in RANS, it might limit the prediction capability of this approach, especially in turbulent combustion applications where interactions between the flow and the flame lead to complex

structure and strong unsteadiness at various scales.

The **Large Eddy Simulation (LES)** appears as an intermediate between RANS and DNS. In this approach, the largest scales of the turbulent motion are resolved whereas the smallest universal scales are modelled. The LES prediction capability of complex turbulent flows is expected to be higher than RANS since a large part of physics is related to large scale and mid-scale phenomena which are resolved in LES, whereas they were fully modelled in RANS. In LES, a filter scale Δ is introduced to separate the resolved scales and the modelled scales. Similarly to the RANS averaging operator, the filtering operator is applied to the governing equations. Conservations equations are obtained for filtered quantities with unclosed terms that relate to the behaviour of the smallest scales which are above the cut-off wavelength k_Δ. The formal derivation of the filtered equations is the object of the next section (Sec. 2.3.3).

The computed and modelled part of the turbulent energy spectrum for DNS, RANS and LES approaches are summarised in Fig. 2.1.

2.3.3 Governing equations for LES

The LES approach can be seen formally as a filtering operation (denoted by $\overline{\cdot}$ in the following. When applied on a general quantity $\mathcal{Q}$, the resulting expression of the filtered quantity $\overline{\mathcal{Q}}$ reads

$$\overline{\mathcal{Q}}(\mathbf{x}) = \int \mathcal{Q}(\mathbf{y}) F_\Delta(\mathbf{x}-\mathbf{y})\,\mathbf{dy}\,, \tag{2.25}$$

where F_Δ is the filter kernel and Δ is the filter width. For variable density flows, a Favre-filtering operation (weighted by the density) is preferred, and the expression of the Favre-filtered quantity $\mathcal{Q}$ reads

$$\overline{\rho}\widetilde{\mathcal{Q}}(\mathbf{x}) = \int \rho\mathcal{Q}(\mathbf{y}) F_\Delta(\mathbf{x}-\mathbf{y})\,\mathbf{dy} = \overline{\rho\mathcal{Q}}\,, \tag{2.26}$$

The filtering operator is applied to the full set of Navier-Stokes to obtain the filtered Navier Stokes equations:

- **Filtered Mass conservation**

$$\frac{\partial\overline{\rho}}{\partial t} + \frac{\partial}{\partial x_j}\left(\overline{\rho}\widetilde{u}_j\right) = 0\,, \tag{2.27}$$

- **Filtered Momentum conservation**

$$\frac{\partial\overline{\rho}\widetilde{u}_i}{\partial t} + \frac{\partial\overline{\rho}\widetilde{u}_j\widetilde{u}_i}{\partial x_j} = -\frac{\partial}{\partial x_j}\left(\overline{P}\delta_{ij} - \overline{\tau}_{ij} - \overline{\tau}^t_{ij}\right) + \overline{F_i}\,, \quad \text{for } i = 1,2,3\,, \tag{2.28}$$

- **Filtered Energy conservation**

$$\frac{\partial \overline{\rho}\widetilde{E}}{\partial t} + \frac{\partial}{\partial x_j}\left(\overline{\rho}\widetilde{E}\widetilde{u}_j\right) = -\frac{\partial}{\partial x_j}\left(\overline{u_i(P\delta_{ij} - \tau_{ij})} + \overline{q_j} + \overline{q_j}^t\right) + \overline{\omega_T}\,, \tag{2.29}$$

- **Filtered Species conservation**

$$\frac{\partial \overline{\rho}\widetilde{Y}_k}{\partial t} + \frac{\partial \overline{\rho}Y_k\widetilde{u_j}}{\partial x_j} = -\frac{\partial}{\partial x_j}\left(\overline{J}_{j,k} + \overline{J}^t_{j,k}\right) + \overline{\omega}_k\,, \quad \text{for } k = 1, n_{spec}\,. \tag{2.30}$$

In these equations, $\overline{\tau}^t_{ij}$, $\overline{q}^t_j$ and $\overline{J}^t_{j,k}$ are unclosed subgrid terms arising from convective terms, for which closures need to be supplied. Closure is also required for filtered viscous terms.

2.3.4 Filtered viscous terms closures

- The **laminar viscous tensor** $\overline{\tau}_{ij}$ reads

$$\overline{\tau}_{ij} = \overline{2\mu\left(S_{ij} - \frac{1}{3}\delta_{ij}S_{ll}\right)}\,, \tag{2.31}$$

  which is approximated when neglecting high order cross terms as

$$\overline{\tau}_{ij} \simeq 2\overline{\mu}\left(\widetilde{S}_{ij} - \frac{1}{3}\delta_{ij}\widetilde{S}_{ll}\right)\,, \tag{2.32}$$

$$\text{with } \widetilde{S}_{ij} = \frac{1}{2}\left(\frac{\partial}{\partial x_i} + \frac{\partial}{\partial x_j}\right) \text{ and } \overline{\mu} \simeq \mu(\widetilde{T})\,. \tag{2.33}$$

- For **filtered laminar diffusion fluxes** the cross terms are also neglected, thus the fluxes are directly expressed based on the filtered quantities. The **laminar species diffusion flux** reads

$$\overline{J}_{ik} = -\overline{\rho\left(D_k\frac{W_k}{W}\frac{\partial X_k}{\partial x_i} - Y_k V_i^c\right)} \simeq -\overline{\rho}\left(\overline{D}_k\frac{W_k}{W}\frac{\partial X_k}{\partial x_i} - \widetilde{Y}_k\widetilde{V}_i^c\right)\,, \tag{2.34}$$

$$\text{with } \widetilde{V}_i^c = \sum_{k=1}^{n_{spec}} \overline{D}_k\frac{W_k}{W}\frac{\partial X_k}{\partial x_i} \text{ and } \overline{D}_k \simeq \frac{\overline{\mu}}{\overline{\rho}Sc_k}\,. \tag{2.35}$$

  Similarly the **laminar energy flux** is expressed as

$$\overline{q}_i = -\overline{\lambda\frac{\partial T}{\partial x_i}} + \sum_{k=1}^{n_{spec}}\overline{J_{ik}h_{sk}} \simeq -\overline{\lambda}\frac{\partial \widetilde{T}}{\partial x_i} + \sum_{k=1}^{n_{spec}}\overline{J}_{ik}h_{sk}\,, \tag{2.36}$$

$$\text{with } \overline{\lambda} = \frac{\overline{\mu}\overline{C_p}(\widetilde{T})}{Pr}\,. \tag{2.37}$$

2.3.5 Subgrid terms closures

- The **subgrid Reynolds stress tensor** $\overline{\tau}^t = -\overline{\rho}\left(u_i u_j - \widetilde{u_i}\widetilde{u_j}\right)$ is generally represented by an eddy-viscosity model, as a diffusive contribution with an associated turbulent viscosity μ_t and similar in form to the laminar contribution. It can be written as

$$\overline{\tau}^t = 2\mu_t\left(\widetilde{S}_{ij} - \frac{1}{3}\delta_{ij}S_{ll}\right) . \tag{2.38}$$

  The turbulent viscosity μ_t is evaluated based on the turbulence subgrid model. Available models are detailed in Sec. 2.3.6.

- In a similar manner, **subgrid species and enthalpy fluxes** are modelled with a diffusive contribution based on a turbulent diffusivity,

$$\overline{J}^{sgs}_{i,k} = \overline{\rho}\left(u_i Y_k - \widetilde{u_i}Y_k\right) = -\overline{\rho}\left(D^t_k\frac{W_k}{W}\frac{\partial X_k}{\partial x_i} - Y_k V_i^{c,t}\right) , \tag{2.39}$$

  where D^t_k is the turbulent species diffusivity that is based on a turbulent Schmidt number Sc^T_k as

$$D^t_k = \frac{\mu_t}{\overline{\rho}Sc^t_k} \tag{2.40}$$

  which relates the species turbulent diffusivities to the turbulent viscosity. Sc^t_k is chosen equal to 0.65 is the present study. A turbulent correction velocity

$$\widetilde{V}_i^{c,t} = \sum_k D^t_k\frac{W_k}{W}\frac{\partial X_k}{\partial x_i} \tag{2.41}$$

  is also introduced similarly to the laminar one to ensure mass conservation.

- Similarly, a turbulent viscosity is also introduced for the **subgrid heat flux vector**

$$\overline{q}^t_i = \overline{\rho}\left(u_i E - \widetilde{u_i}\widetilde{E}\right) , \tag{2.42}$$

  which is related to the turbulent viscosity μ_t by the turbulent Prandtl number

$$\lambda_t = \frac{\mu_t\overline{C_p}}{Pr^t} , \tag{2.43}$$

  which has a fixed value $Pr^t = 0.65$ in this work.

- Since the combustion processes occur at small scale, the modelling of the **filtered chemical source terms** $\overline{\omega}_k$ and $\overline{\omega}_T$ is of key importance and is the object of Sec. 4.5.

2.3.6 Turbulent viscosity models

The role of the turbulent subgrid model is to correctly account for the interaction between the resolved and the unresolved scales. The subgrid scales are assumed to have a universal behaviour, their contribution is generally represented as purely dissipative, which is a valid hypothesis in the frame of the Kolmogorov cascade theory [102]. In complex turbulent flow, energy transfer from small residual scales to the largest scale is also possible through backscatter [115]. In all the models describe below, an eddy-viscosity model of the form given in Eq. 2.38 is employed. In this form, the energy is transferred only from the filtered motions to the residual motions, with no backscatter [165]. The main subgrid model available in AVBP are described below:

- The **Smagorinksy model** was initially proposed by *Smagorinsky* [184]. The expression of the turbulent viscosity based on a mixing-length analogy reads

$$\nu_t = \frac{\mu_t}{\rho} = (C_S\Delta) \quad \overline{2\widetilde{S}_{ij}\widetilde{S}_{ij}}\,, \tag{2.44}$$

  where Δ is the characteristic filter width (linked to the cube-root of the cell volume), C_S is the model constant with a typical value $C_S = 0.17$ estimated from the Kolmogorov spectrum [118]. This model is able to correctly predict the decay of turbulence in homogeneous isotropic turbulence. However, the model is non-vanishing in pure shear, it is therefore generally not suitable for wall-bounded flows [174] and is generally too dissipative [67].

- An extension of the Smagorinksy model is the **dynamic Smagorinsky model**. In this approach, the constant C_S is no longer a user-defined constant. Instead, it is evaluated dynamically in the computation based on the Germano identity, as done in Lilly s procedure [119] using a test-filter scale.

- The **WALE model** was initially proposed by *Ducros* [48]. The turbulent viscosity reads

$$\nu_t = (C_w\Delta)^2 \frac{(s^d_{ij}s^d_{ij})^{3\ 2}}{(\widetilde{S}_{ij}\widetilde{S}_{ij})^{5\ 2} + (s^d_{ij}s^d_{ij})^{5\ 4}}\,, \tag{2.45}$$

  with

$$s^d_{ij} = \frac{1}{2}\,(\widetilde{g}^2_{ij} + \widetilde{g}^2_{ji}) - \frac{1}{3}\,\widetilde{g}^2_{kk}\,\delta_{ij}\,, \tag{2.46}$$

  where $C_w = 0.4929$ is the model constant and and $\widetilde{g}_{ij}$ denotes the resolved velocity gradient. It was developed to obtain correct scaling laws in near wall regions for wall bounded flows.

	Smagorinsky	WALE	SIGMA
Correct asymptotic behaviour at walls	**No**	**Yes**	**Yes**
No subgrid viscosity for solid rotation	**Yes**	**No**	**Yes**
No subgrid viscosity for pure shear	**No**	**Yes**	**Yes**
No subgrid viscosity for axisymmetric expansion	**No**	**No**	**Yes**
No subgrid viscosity for isotropic expansion	**No**	**Yes**	**Yes**

Figure 2.2: Comparison of the properties of the different subgrid scale models. Adapted from [144].

- The **SIGMA model** was proposed by *Nicoud et al.* [144]. The singular values $\sigma_1 \geq \sigma_2 \geq \sigma_3$ of the velocity gradient tensor g_{ij} are use to build the turbulent viscosity

$$\nu_t = (C_\sigma \Delta)^2 \frac{\sigma_3(\sigma_1 - \sigma_2)(\sigma_2 - \sigma_3)}{\sigma_1^2}, \tag{2.47}$$

  where $C_\sigma = 1.35$ is the constant of the model. Like the WALE model, the SIGMA model has the correct asymptotic behaviour at the wall but has an improved behaviour for rotating flows, as detailed below.

A summary of the properties of the different model (Table. 2.2). In this work, the SIGMA model is preferred in most cases: it has a the correct asymptotic behaviour for wall-bounded flows, and induces no subgrid viscosity for solid rotation. This last property is important for swirling flows which tends to exhibit large rotational structures. The correct treatment of axisymmetric expansion might also be important when considering jet flames.

2.4 Numerical aspects

2.4.1 The AVBP solver

The AVBP solver is a massively-parallel code for the simulation of compressible reacting flows [173], developed by CERFACS and IFPEN, that solves the Navier-Stokes equations explicitly on unstructured and hybrid grids. It relies on the cell-vertex discretisation method and treats boundaries according to the Navier Stokes Characteristic Boundary Conditions (NSCBCs) formalism [158]. The code handles multi-component reacting flows [138].

2.4.2 Numerical schemes

To solve the equations presented in Sec. 2.3.3, numerical schemes are employed. Their dissipation and dispersion properties is of paramount importance for accurate flow and flame structure prediction. An overview of the schemes available in AVBP can be found

in the thesis of Lamarque [105]. The convective numerical schemes employed in this work are briefly summarised:

- **The Lax-Wendroff (LW) scheme** [108] is a finite volume centered scheme, with an explicit single step time integration. It is second order accurate in both space and time. It has a low computational cost and is therefore employed to establish the flow when starting simulations.
- **The Two-step Taylor Galerkin scheme (TTGC)** [39] is a finite element centered scheme, with an explicit two-step integration in time. It has very good dispersion and dissipation properties, it is therefore well-suited for LES application. However it is approximately 2.5 times more expensive than the LW scheme.

2.4.3 Artificial viscosity

The numerical schemes employed in AVBP are spatially centered, and are therefore prone to point-to-point oscillations (also named wiggles) close to regions of steep gradients. An artificial viscosity (AV) term is added to the discrete equations in order to limit these spurious oscillations. This is done in practice by the introduction of two artificial viscosity terms:

- A background dissipation term (4^{th} order hyperviscosity) limits the amplitude of wiggles.
- A 2^{nd} order viscosity term smooths local gradients, and introduces artificial dissipation. To preserve global dissipation properties of the scheme, it is applied only in regions where a sensor is triggered. The sensor employed is similar to shock capturing sensors, it is linear preserving and detects strong deviations of variables from linear behaviour.

2.4.4 Chemical source term evaluation

In AVBP, the chemical source terms evaluation procedure normally depends on the numerical scheme:

- Source terms **@ nodes**: for finite volume schemes (e.g. Lax-Wendroff scheme), the chemical source terms are directly evaluated at the grid vertices (also called grid nodes) from nodal temperature and species composition.
- Source terms **@ cells**: for finite element schemes (e.g. TTGC), a cell-vertex formulation is employed. The chemical source term is evaluated at the cell center. The procedure is depicted in Fig. 2.3. First, a so-called "Gather" operation is used to evaluate the quantities at the cell centers from nodal values (temperature

and species composition). Based on these cell quantities, the source term at the cell center ω_k^{cell} is evaluated. It is further redistributed back and stored at the grid nodes via a "Scatter" operation.

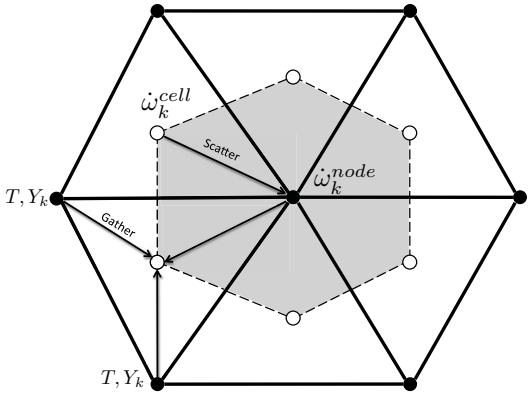

Figure 2.3: Illustration of the procedure for the evaluation of the source terms at the cell center. The black circles correspond to grid nodes and the white circles to the cell centers.

The evaluation of the source terms at the cell vertices might improve the accuracy, as will be further discussed in Sec. 7.3. However, it is computationally more expensive that nodal source term evaluation. The Gather-Scatter operations are costly, especially when a large number of species is considered. In addition, there is statistically 6 times more cell centers than cell vertices for tetrahedral meshes, thus more chemical source terms computations are required when evaluated at the cell centers, which can also significantly increase the cost if kinetics schemes containing a large number of reactions are employed. This difference in terms of cost will be further illustrated in Sec. 9.8.

3

Governing equations for the dispersed liquid phase

Contents

3.1 Introduction

Whereas the flow description is based on continuum mechanics with an Eulerian point of view, spray dynamics may be described with different theoretical approaches. In the Lagrangian approach, the dispersed phase is considered as a set of discrete particles on which laws of point mechanics are applied. In the Eulerian approach (denoted EE), the spray is viewed as a continuum (similarly to the Navier-Stokes equations being the continuum description of an ensemble of molecules), with local mean properties that correspond to the considered set of particles. In this work, the Eulerian approach is retained because of its high scalability for applications to complex industrial configurations with large numerical grids.

The chapter is organised as follows:

- Firstly, the modelling assumptions and the derivation of the equations for the mesoscopic statistical approach are presented (Sec. 3.2), and extended to the LES formalism.

- Secondly, the modelling of the exchanges terms between the phase (through momentum, mass and heat transfers) are presented (Sec. 3.3).

3.2 Derivation of the mesoscopic Eulerian equations

3.2.1 Description of the dispersed phase

The following assumptions are made for the liquid phase:

- The density of the particles ρ_l is constant.
- The particles are spherical and not subject to breakup mechanisms.
- The temperature is uniform inside the droplets (infinitely fast conductivity).

Under these assumptions, the state of a single particle is described by its position $x_{p,i}$, its mass m_p (or equivalently its diameter d_p) and its temperature T_p (or equivalently its sensible enthalpy $h_{s,p}$).

An additional assumption of **diluted** dispersed phase is made. This hypothesis is valid if the local liquid volume fraction α_l (ratio of the liquid volume to the total volume) is small, typically $\alpha_l < 0.01$. Under this hypothesis, the gaseous volumes is $1 - \alpha_l \simeq 1$ and the interactions between droplets can be neglected.

3.2.2 The Eulerian mesoscopic approach

Principle

In the Euler-Euler approach, the description of the history of each particle is replaced by the description of their mean properties, the spray is viewed as a continuous fluid. A statistical average is performed to transform the Boltzmann equations that describe the dispersed phase into transport equations for mean properties of the dispersed phase.

For any quantity Ψ, the mass-weighted statistical average operator reads

$$\breve{\Psi} = \ \Psi\ _l = \frac{1}{\rho_l \breve{\alpha}_l} \int m_p \Psi\left(u_p, T_p, m_p\right) f_p\left(u_p, T_p, m_p \middle| \mathcal{H}_f\right)\ du_p\, dT_p\, dm_p\,. \tag{3.1}$$

Here, $f_p(u_p, T_p, m_p|\mathcal{H}_f)$ is a probability density function, where u_p, T_p and m_p are the phase parameters. This function is conditioned on a flow realisation $\mathcal{H}_f$. ρ_l is the liquid density and $\breve{\alpha}_l$ is the volume fraction of the dispersed phase defined by

$$\rho_l \breve{\alpha}_l = \int m_p f_p\left(u_p, T_p, m_p \middle| \mathcal{H}_f\right)\ du_p\, dT_p\, dm_p\,. \tag{3.2}$$

General method: the Enskog equations

The general methods to obtain the mesoscopic conversation equations is to multiply

the Boltzmann equations for the dispersed phase issued from the kinetic theory gases [33, 96, 135] by a particle function Ψ and to apply the statistical average operator to obtain the general Enskog equation.

Additional assumptions are made in the derivation process of the mesoscopic equations are:

- The spray is **locally monodisperse** and has **locally a statistically uniform temperature**.
- The dispersed phase is assumed to have low impact on the carrying phase, allowing to condition the dispersed phase statistics on only **one realisation of the carrying phase**.

The Enskog equation

When multiplying the Boltzmann equation with any particle function Ψ and integrating in the phase space ($\cdot\, du_p\, dT_p\, dm_p$), one obtains *the general form of the Enskog equation*:

$$\begin{aligned}\frac{\partial}{\partial t}\rho_l \breve{\alpha}_l \ \Psi\ _l + \frac{\partial}{\partial x_i}\rho_l \breve{\alpha}_l \ u_{p,i}\Psi\ _l &= \mathbf{C}\left(m_p\Psi\right) \\ &+ \rho_l \breve{\alpha}_l \left\langle \frac{du_{p,j}}{dt}\frac{\partial \Psi}{\partial u_{p,j}} \right\rangle_l + \rho_l \breve{\alpha}_l \left\langle \frac{dT_p}{dt}\frac{\partial \Psi}{\partial T_p} \right\rangle_l \\ &+ \rho_l \breve{\alpha}_l \left\langle \frac{dm_p}{dt}\left(\frac{\partial \Psi}{\partial m_p} + \frac{\Psi}{m_p}\right) \right\rangle_l \end{aligned} \tag{3.3}$$

where $\mathbf{C}\left(m_p\Psi\right)$ is the variation of $\rho_l \breve{\alpha}_l \breve{\Psi}$ due to interactions between particles and is therefore neglected in the diluted approximation.

Velocity of the dispersed phase: mesoscopic and Random Uncorrelated Motion (RUM)

The RUM approach relies on the decomposition of the dispersed phase velocity $\mathbf{u}_p$ into the statistical average $\breve{\mathbf{u}}_l$ and the deviation from this mean $\mathbf{u}_p''$:

$$\mathbf{u}_p = \breve{\mathbf{u}}_l + \mathbf{u}_p'', \qquad \text{with } \breve{\mathbf{u}}_l = \ \mathbf{u}_p\ _l \qquad \text{and } \left\langle \mathbf{u}_p'' \right\rangle_l = 0\,. \tag{3.4}$$

This velocity decomposition allows to see the spray as a set of particles with the same *mesoscopic motion* while each individual particle deviates from this global mesoscopic motion because of the *uncorrelated velocity* contribution (cf. Fig. 3.1).

In the RUM formalism, this uncorrelated motion leads to additional transport equations for relevant quantities such as the uncorrelated kinetic energy, with additional closure terms. The detailed equations and closures can be found in the work of *Sierra Sanchez* [181] and *Masi* [131]. However in the present work, RUM and more generally statistical

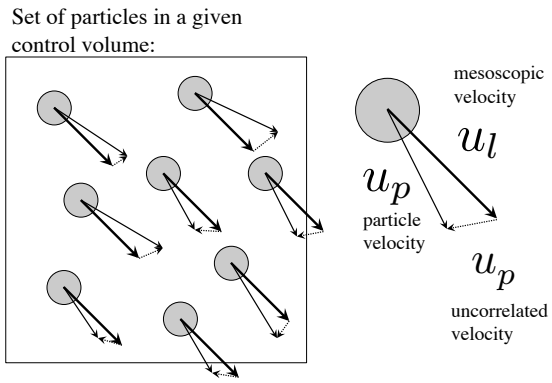

Figure 3.1: Decomposition of the particle velocity $\mathbf{u}_p$ into a mesoscopic part $\breve{\mathbf{u}}_l$ and an uncorrelated part $\mathbf{u}_p''$.

variation of velocity are assumed to have a negligible effect on the spray dynamics: the individual particle velocity $\mathbf{u}_p$ is thus taken equal to its mesoscopic value $\breve{\mathbf{u}}_l$.

3.2.3 Conservation equations

The conservation equations are obtained by choosing the appropriate quantities for Ψ. Note that all the collisional source terms are neglected because of the diluted phase assumption .

Number density

Taking $\Psi = \frac{1}{m_p}$, the conservation equation for number of droplets density is obtained

$$\frac{\partial}{\partial t}\breve{n}_l + \frac{\partial}{\partial x_i}\breve{n}_l\breve{u}_{l,i} = 0\,. \tag{3.5}$$

.

Volume fraction

Taking $\Psi = 1$ the conservation equation for the volume fraction is obtained

$$\frac{\partial}{\partial t}\rho_l\breve{\alpha}_l + \frac{\partial}{\partial x_i}\rho_l\breve{\alpha}_l\breve{u}_{l,i} = \Gamma_l\,, \tag{3.6}$$

where $\Gamma_l = -\Gamma = \rho_l\breve{\alpha}_l \quad \frac{1}{m_p}\frac{dm_p}{dt} \quad _l$ is the rate of change of mass through phase exchange (evaporation).

Momentum

Taking $\Psi = \mathbf{u}_p$, the momentum conservation equation is obtained

$$\frac{\partial}{\partial t}\rho_l\breve{\alpha}_l\breve{u}_{l,i} + \frac{\partial}{\partial x_j}\rho_l\breve{\alpha}_l\breve{u}_{l,i}\breve{u}_{l,j} = F_{d,i} + \Gamma_{u,i}\ . \tag{3.7}$$

$F_{d,i} = \rho_l \breve{\alpha}_l \left\langle \frac{F_{p,i}}{m_p} \right\rangle_l$ is the exchange of momentum with the gaseous phase via the drag force $\mathbf{F}_p$ exerted on each particle. $\Gamma_{u,i} = \rho_l \breve{\alpha}_l \left\langle \frac{u_{p,i}}{m_p} \frac{dm_p}{dt} \right\rangle_l = \Gamma_l \breve{u}_{l,i}$ is the exchange of momentum with the gaseous phase through mass exchange.

Sensible enthalpy

Taking $\Psi = h_{s,p}$, the energy equation is obtained

$$\frac{\partial}{\partial t} \rho_l \breve{\alpha}_l \breve{h}_{s,l} + \frac{\partial}{\partial x_j} \rho_l \breve{\alpha}_l \breve{u}_{l,j} \breve{h}_{s,l} = \Pi_l \,. \tag{3.8}$$

Π_l represents the sensible enthalpy rate of change per unit volume due to evaporation.

The modelling and closure of the source terms of Eq. 3.5 to Eq. 3.8 is presented in Sec. 3.3. Similarly to gaseous phase equations, the mesoscopic equations in conservative form must now be spatially filtered to be applied in LES computations.

3.2.4 LES equations for the dispersed phase

3.2.4.1 LES Filtering

The LES filtering is identical to the filtering procedure used for the gaseous phase equations. The Favre average for the dispersed phase is similar to the Favre average of the gaseous phase and is obtained by using the mesoscopic volume fraction $\breve{\alpha}_l$ instead of the gaseous density ρ:

$$\overline{\alpha}_l \widehat{f}_l = \overline{\breve{\alpha}_l \breve{f}_l} \,, \tag{3.9}$$

where $\overline{\alpha}_l$ is the filtered volume fraction of the liquid. If the spray is monodisperse at the filter size, the liquid Favre average may be equivalently defined with the number density as:

$$\overline{\breve{n}_l \breve{f}_l} = \overline{\frac{6\breve{\alpha}_l}{\pi \breve{d}^3} \breve{f}_l} = \frac{6}{\pi \breve{d}^3} \overline{\alpha}_l \widehat{f}_l = \overline{n}_l \widehat{f}_l \tag{3.10}$$

where $\overline{n}_l$ is the filtered number density and $\breve{d}$ is the mesoscopic diameter for which it is supposed that $\overline{\breve{d}} = \breve{d}$, or: $\breve{d}'' = 0$. The filtering of the conservation equations of the dispersed phase derived in the previous section gives the LES equations. The final LES equations are shown in Sec. 3.4.

Similarly to the gaseous phase, subgrid terms and unclosed source terms appear in the filtered equations. In the present implementation, the subgrid effects are taken into account only for the momentum equation. The closure of the subgrid scale mesoscopic velocity tensor $\overline{\tau}_l^t$, which is analogue to the subgrid stress velocity tensor of the gaseous phase, is presented in Sec. 3.2.5. In addition, all source terms are approximated by their unfiltered form. The terms are detailed in Sec. 3.3. More details about this simplification can be found in the thesis of *Boileau* [21].

3.2.5 Sub-grid scale models for the dispersed phase

By analogy with the LES modelling of gaseous flows, *Riber et al.* [172] propose a viscous-type model for the sub-grid scale mesoscopic velocity tensor $\overline{\tau}_l^t$. The deviatoric part is evaluated with the compressible Smagorinsky model [184] whereas the diagonal part is calculated with the Yoshizawa model [211]:

$$\overline{\tau}_{l,ij}^t = -\rho_l \overline{\alpha}_l \left(\widehat{u_{l,i} u_{l,j}} - \widehat{u}_{l,i} \widehat{u}_{l,j} \right) \tag{3.11}$$

$$\textit{model:} \quad \overline{\tau}_{l,ij}^t = 2\rho_l \overline{\alpha}_l \nu_{l,t} \left(\widehat{S}_{l,ij} - \frac{1}{3} \widehat{S}_{l,kk} \delta_{ij} \right) \tag{3.12}$$

$$+2\rho_l \overline{\alpha}_l \kappa_{l,t} \widehat{S}_{l,ij} \delta_{ij} \tag{3.13}$$

$$\text{with:} \quad \widehat{S}_{l,ij} = \frac{1}{2} \left(\frac{\partial \widehat{u}_{l,i}}{\partial x_j} + \frac{\partial \widehat{u}_{l,j}}{\partial x_i} \right) - \frac{1}{3} \frac{\partial \widehat{u}_{l,k}}{\partial x_k} \delta_{ij} \tag{3.14}$$

$$\textit{Smagorinsky model:} \quad \nu_{l,t} = (C_{S,l} \Delta)^2 \sqrt{2 \widehat{S}_{l,ij} \widehat{S}_{l,ij}} \tag{3.15}$$

$$\textit{Yoshizawa model:} \quad \kappa_{l,t} = 2 (C_{V,l} \Delta)^2 \widehat{S}_{l,ij} \tag{3.16}$$

The model constants are fixed from *a priori* tests [134]: $C_{S,l} = 0.14$ et $C_{V,l} = 0.11$.

3.3 Modelling of the exchanges between phases

The purpose of this section is to give an overview of the physics behind the source terms related to the exchange between the gas and the liquid phase. The main assumptions and derivation procedure regarding mass and heat transfer between phases are presented. Note that two-way coupling is considered, the impact of the liquid phase on the gaseous phase is fully taken into account.

3.3.1 Drag

3.3.1.1 Expression for a single droplet

The particles are assumed to be spherical and isolated. Under these assumptions, the drag force exerted by the gas with the velocity u on a particle of mass m_p and velocity u_p is obtained by a simplification of the Basset-Boussinesq-Oseen equation [36]

$$\frac{F_{p,i}}{m_p} = \frac{1}{\tau_p} \left(u_i - u_{p,i} \right) , \tag{3.17}$$

where τ_p is the relaxation time of the particle expressed as

$$\tau_p = \frac{\tau_p'}{1 + 0.15 Re_p^{0.687}} \quad \text{with} \qquad \tau_p' = \frac{\rho_l d_p^2}{18\mu} , \tag{3.18}$$

and Re_p is the Reynolds number of the particle:

$$Re_p = \frac{|u_i - u_{p,i}| \, d_p}{\nu} . \tag{3.19}$$

Equation 3.18 includes an empirical correlation proposed by *Schiller and Naumann* [177] to take into account Reynolds number effects. For low particle Reynolds numbers, Eq. 3.18 yields $\tau_p = \tau_p'$, which is actually the well-known drag coefficient proposed by *Stokes* [187]. The effects of drag on the dispersed phase dynamics depend on the Stokes number comparing the characteristic time of the drag τ_p to the flow characteristic time

$$St = \frac{\tau_p}{\tau_L}\,, \tag{3.20}$$

where τ_L is a characteristic time scale of the gaseous flow. The Stokes number is an indicator of the response of the particle to the variations of the flow velocity. For $St \ll 1$, the particle behaves like a tracer of the gaseous flow. For $St \gg 1$, the particle has an inertial trajectory and is insensitive to the gaseous flow perturbations. Finally, for Stokes numbers of order unity, the effects of preferential concentration are maximum [55, 56, 205].

3.3.1.2 Resulting source term in mesoscopic equations

Two-way coupling terms model the drag forces exerted by the droplet onto the surrounding gas. Starting from the model for drag (Eq. 3.17), the source term $F_{d,i}$ corresponds to the statistical mescoscopic mean

$$F_{d,i} = \rho_l \breve{\alpha}_l \left\langle \frac{F_{p,i}}{m_p} \right\rangle_l = \frac{\rho_l \breve{\alpha}_l}{\tau_p} \left(u_i - \breve{u}_{l,i}\right)\,. \tag{3.21}$$

The second equality is valid because of the locally monodisperse assumption.

3.3.2 Evaporation model

The evaporation model used in the present is based on the Spalding mass-transfer model. The following assumptions are made:

- Interaction between droplets are neglected, a droplet is considered to be isolated and spherical.
- The droplet has a uniform temperature (infinite conductivity).
- The droplet is assumed to be at equilibrium with the surrounding gas phase (in a quasi-steady state sense).

The derivations of the evaporation model and the notation follow the outlines given by *Kuo* [104], *Sirignano* [182] and *Boileau* [21].
The gas flow is also assumed to be quasi steady, which means that equations are independent of time. Furthermore, the position of the liquid surface is considered constant. This reflects the fact that $\rho_l >> \rho$ resulting in a velocity of the receding

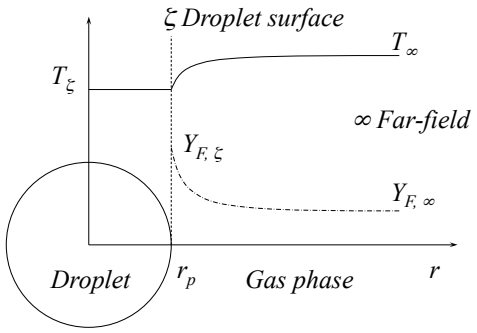

Figure 3.2: ***Qualitative profiles of temperature*** T ***and fuel mass fraction*** Y_F ***vs radial distance from a spherical single droplet with constant temperature*** T_ζ**.**

liquid surface that is small compared to the evaporated fuel moving away from the surface. The problem is formulated in spherical coordinates (illustrated in Fig. 3.2) for radii between the droplet surface (index ζ) and the far-field (index). The following set of equations of the gaseous flow field for $r > r_\zeta$ is obtained:

$$\text{Mass conservation:} \qquad \rho u r^2 = const = \left(\rho u r^2\right)_\zeta = \frac{m_F}{4\pi} \,. \tag{3.22}$$

$$\text{Fuel species conservation:} \qquad \rho u r^2 \, \frac{dY_F}{dr} = \frac{d}{dr}\left(r^2 \, [\rho D_F] \, \frac{dY_F}{dr} \right) \,. \tag{3.23}$$

$$\text{Energy equation:} \qquad \rho u r^2 \, \frac{dC_P T}{dr} = \frac{d}{dr}\left(\frac{\lambda}{C_P} r^2 \, \frac{dC_P T}{dr} \right) \,. \tag{3.24}$$

The expression $[\rho\, D_F]$ in Eq. 3.23 contains the diffusion coefficient of the species representing the fuel, D_F, and the density of the mixture in the gas phase ρ. It can be expressed as a function of the gas viscosity μ and the Schmidt number of the gaseous fuel Sc_F

$$[\rho D_F] = \frac{\mu}{Sc_F} \,. \tag{3.25}$$

The thermal conductivity λ in Eq. 3.24 is related to the gas viscosity by the Prandtl number

$$\lambda = \frac{\mu \, \overline{C}_P}{Pr} \,, \tag{3.26}$$

where $\overline{C}_P$ is the average heat capacity at constant pressure of the gaseous mixture. It is important to note that there are several definitions regarding the mass exchange between liquid and gaseous phase. In the equation of mass conservation (3.22), the

gaseous fuel mass flux m_F through a spherical surface at the radius r appears. Its sign is determined by the formulation in spherical coordinates. In this case, a mass flux away from the droplet centre is considered positive.

The derivation or the evaporation model is divided into two steps. First the temporal evolution of the mass of a single droplet is derived. Then, the model for heat transfer is obtained.

3.3.2.1 Mass transfer

The model for the mass transfer between a single, isolated droplet and the surrounding gas is derived using the equation of species conservation (Eq. 3.23), with two boundary conditions, one at the droplet surface (ζ) and the other at the far-field ( ). The integration of Eq. 3.23 yields

$$\rho u r^2 \, Y_F = r^2 \, [\rho D_F] \, \frac{dY_F}{dr} + c_1 \, . \tag{3.27}$$

It can be observed that $\rho u r^2 \, Y_F - r^2 \, [\rho D_F] \, \frac{dY_F}{dr}$ is the fuel flux. Since only the fuel is moving, this flux corresponds to the total flux $\rho u r^2$ and c_1 can be determined as $c_1 = \rho u r^2 = m_F / 4\pi$. The equation for Y_F becomes

$$\rho u r^2 \, \left(Y_F - 1 \right) = r^2 \, [\rho D_F] \, \frac{dY_F}{dr} \, . \tag{3.28}$$

Under the assumption of constant $[\rho D_F]$, Eq. 3.28 can be integrated between r and to obtain

$$\frac{m_F}{4\pi r \, [\rho D_F]} = \ln \left(\frac{Y_{F,\infty} - 1}{Y_F - 1} \right) \, . \tag{3.29}$$

Applying the boundary conditions at $r = r_\zeta$ leads to

$$m_F = 4\pi r_\zeta \, [\rho D_F] \ln \left(B_M + 1 \right) \quad \text{where} \quad B_M = \frac{Y_{F,\zeta} - Y_{F,\infty}}{1 - Y_{F,\zeta}} \, . \tag{3.30}$$

This condition imposes m_F and the speed at which the evaporated fuel leaves the droplet surface, u_ζ

$$r_\zeta \rho_\zeta u_\zeta = \frac{m_F}{4\pi r_\zeta} = [\rho D_F] \ln \left(1 + B_M \right) \, . \tag{3.31}$$

The global droplet mass m_p evolution has an opposite sign

$$m_p = -\pi d_p \, Sh \, [\rho D_F] \ln \left(1 + B_M \right) \, , \tag{3.32}$$

where d_p is the particle diameter. The Sherwood number Sh, obtained above in the case of a droplet in a quiescent atmosphere is

$$Sh = 2\,. \tag{3.33}$$

This value is not exact in the general case where droplets may have a non-zero velocity relative to the surrounding gas. This can be taken into account by correlations like the one proposed by *Ranz and Marshall* [170], which is based on the particle Reynolds number Re_p and the Schmidt number of the fuel species Sc_F

$$Sh = 2 + 0.55\, Re_p^{\frac{1}{2}}\, Sc_F^{\frac{1}{3}}\,. \tag{3.34}$$

The *Spalding* number B_M uses the fuel mass fractions at the surface and the far-field, $Y_{F,\zeta}$ and $Y_{F,\infty}$. An expression for $Y_{F,\zeta}$ must be obtained by stating that the flow at the droplet surface is saturated. Using the molar fraction of the fuel vapour at the surface $X_{F,\zeta}$, the molar weight of the fuel W_F, and the molar weight of the mixture of all species *other* than the fuel $\overline{W}_{nF,\zeta}$, calculated at the surface, one obtain

$$Y_{F,\zeta} = \frac{X_{F,\zeta} W_F}{X_{F,\zeta} W_F + (1 - X_{F,\zeta})\,\overline{W}_{nF,\zeta}}\,. \tag{3.35}$$

Assuming that the mixture composition does not change between the droplet surface (ζ) and the far-field (∞), $\overline{W}_{nF,\zeta}$ only depends on known variables of the far-field namely $Y_{F,\infty}$ and $\overline{W}$, the molar weight of the mixture of *all* species in the gas-phase

$$\overline{W}_{nF,\zeta} = \overline{W}_{nF,\infty} = \frac{1 - Y_{F,\infty}}{1 - Y_{F,\infty}\frac{\overline{W}}{W_F}}\overline{W}\,. \tag{3.36}$$

The fuel molar fraction, $X_{F,\zeta}$ is obtained using the partial pressure of the fuel species, $P_{F,\zeta}$

$$X_{F,\zeta} = \frac{P_{F.\zeta}}{P}\,, \tag{3.37}$$

where $P_{F,\zeta}$ is calculated by the *Clausius-Clapeyron* law

$$P_{F,\zeta} = P_{cc}\, \exp\left(\frac{W_F L_v(T_{ref})}{\mathcal{R}}\left(\frac{1}{T_{cc}} - \frac{1}{T_\zeta}\right)\right)\,, \tag{3.38}$$

where T_{cc} and p_{cc} correspond to an arbitrary reference point on the saturation curve. $L_v(T)$ is the latent heat given by

$$L_v(T) = h_{s,F}(T) - h_{s,p}(T)\,. \tag{3.39}$$

where $h_{s,F}(T)$ and $h_{s,p}(T)$ are respectively the gaseous and liquid fuel sensible enthalpy.

3.3.2.2 Statistical source terms for mass transfer

In the Eulerian approach, the mean statistical mass source term Γ_l applied on the conservation equations is taken equal to the expression obtained for a single droplet

$$\Gamma_l = \rho_l \breve{\alpha}_l \left\langle \frac{1}{m_p} \frac{d\, m_p}{dt} \right\rangle = -\rho_l \breve{\alpha}_l \, m_F \, . \tag{3.40}$$

Consistently, a mass source term $\Gamma = -\Gamma_l$ is applied to the LES equations.

3.3.2.3 Heat transfer

The fuel mass flux from a single droplet was evaluated in the previous section. It must now be combined with a model describing the heat exchange between the droplet and its surroundings. This is done in two steps:

- The different contributions to the global enthalpy balance are first defined and analytical relations are derived.
- They are further combined to form the model for droplet heat transfer.

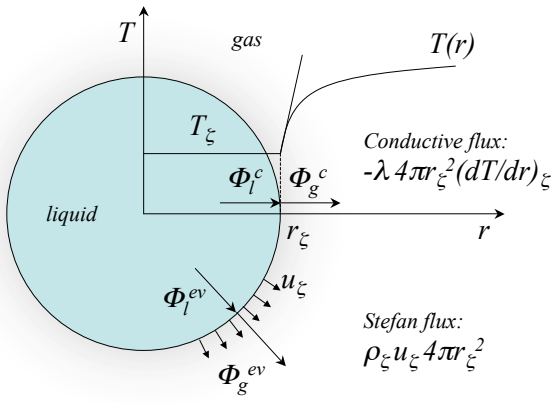

Figure 3.3: ***Contributions to the enthalpy balance at the liquid-gaseous interface***

3.3.2.4 Enthalpy conservation at the gas/liquid interface

The derivation of a law for the temporal evolution of a droplet s temperature involves the enthalpy conservation equation (Eq. 3.24) with boundary conditions at the far-field ( ) and the droplet surface (ζ). Furthermore, for the enthalpy fluxes at the interface,

a conservation law at the liquid/gas interface can be stated. Figure 3.3 shows the decomposition into four contributions

$$\Phi_l^{ev} + \Phi_l^c + \Phi_g^{ev} + \Phi_g^c = 0\,. \tag{3.41}$$

On the gaseous side, there is a convective part, denoted Φ_g^{ev}, which represents the sensible enthalpy of the fuel species $h_{s,F}$ that is transported by the *Stefan* flux m_F, i.e. the evaporated mass moving away from the surface at the velocity u_ζ. Φ_g^{ev} is defined as

$$\Phi_g^{ev} = m_F\, h_{s,F}(T_\zeta)\,. \tag{3.42}$$

The other contribution on the gaseous side is the conductive heat transfer Φ_g^c which is proportional to the temperature gradient at the surface

$$\Phi_g^c = \left(-4\pi r^2 \lambda \frac{dT}{dr}\right)_\zeta\,. \tag{3.43}$$

Similarly, there also is a convective and a conductive contribution on the liquid side. Mass conservation at the interface (Eq. 3.22) imposes that the mass flux in the liquid and gas phase are equal, namely $m_F = -m_p$. A liquid convective flux Φ_l^{ev} arises from this mass flux and is defined as

$$\Phi_l^{ev} = -m_F\, h_{s,p}(T_\zeta)\,. \tag{3.44}$$

The liquid conductive flux Φ_l^c depends on the temperature gradient at the surface inside the droplet

$$\Phi_l^c = \left(4\pi r^2 \lambda_l \frac{dT_l}{dr}\right)_\zeta\,. \tag{3.45}$$

Given that the temperature is assumed constant inside the droplet, this expression can not be evaluated directly. Evaporation models that are presented in the following either neglect Φ_l^c or substitute it when necessary. Eq. 3.41 can be rewritten as

$$\underbrace{-m_F h_{s,p}(T_\zeta)}_{\text{liquid conv. flux}} + \underbrace{\Phi_l^c}_{\text{liquid cond. flux}} + \underbrace{m_F h_{s,F}(T_\zeta)}_{\text{gaseous conv. flux}} + \underbrace{\left(-4\pi r^2 \lambda \frac{dT}{dr}\right)_\zeta}_{\text{gaseous cond. flux}} = 0\,. \tag{3.46}$$

Using the definition of the latent heat L_v (Eq. 3.39), Eq. 3.46 can be rewritten as

$$m_F L_v(T_\zeta) + \Phi_l^c + \Phi_g^c = 0\,, \tag{3.47}$$

where $L_v(T_\zeta)$ is the heat of evaporation at the temperature T_ζ. Note that, while L_v is a constant in the Clausius-Clapeyron law, (Eq. 3.38), it changes with T_ζ in the context of Eq. 3.47. $L_v(T_{l,ref})$ is provided by literature at the reference temperature $T_{l,ref}$ for

the liquid phase enthalpy $h_{s,p}$. To compute $L_v(T_\zeta)$, the definition of $L_v(T)$ (eq. 3.39) must be recast as:

$$L_v(T_\zeta) = h_{s,F}(T_\zeta) - h_{s,p}(T_\zeta) - h_{s,corr}\,, \tag{3.48}$$

where $h_{s,corr}$ is a correction enthalpy that, if necessary, accounts for different reference temperatures for the gaseous and the liquid enthalpy.
The remaining term in Eq. 3.47 to be evaluated is the gaseous conductive enthalpy flux Φ_g^c. There are differences between early models of the literature about how this term is handled. The derivations presented in the following subsection (Sec. 3.3.2.5 and Sec. 3.3.2.6) are only valid in the case of a quiescent atmosphere (i.e. $u_p - u_g = 0$), which makes corrections necessary if cases with a slip velocity are considered.

3.3.2.5 The d^2-law

The simplest form of an evaporation law was originally introduced by *Spalding* [186] and *Godsave* [72] in 1953 and is commonly known as Spalding law or d^2-law. It considers only effects on the gaseous side of the droplet surface while neglecting all effects on the liquid side. Consequently, the unknown term for the liquid conductive heat transfer Φ_l^c that contributes to the energy balance is neglected. Equation 3.47 then reduces to

$$m_F L_v(T_\zeta) = -\Phi_g^c\,. \tag{3.49}$$

This corresponds to an equilibrium state characterised by the so-called equilibrium- or "wet bulb temperature", T_{wb}. This temperature is a function of the gaseous conditions near the droplet. This is a plateau temperature for which the gaseous conductive flux cancels the heat flux related to evaporation. Combining Eq. 3.49 and Eq. 3.65 yields

$$B_T = \frac{(T_\infty - T_\zeta)\, C_P}{L_v(T_\zeta)}\,. \tag{3.50}$$

Considering this simplified form of the temperature Spalding number B_T, combined with the mass transfer number B_M (Eq. 3.31) and the Clausius-Clapeyron relation (Eq. 3.38), the wet-bulb temperature T_{wb} for given ambient conditions can be obtained iteratively.

3.3.2.6 The infinite conductivity model

This model is the most commonly used for spray simulations. It meets the concerns raised by studies of *Law* [106] or *Hubbart et al.* [84] that transient droplet heating cannot be neglected in combustion applications. It assumes a uniform droplet temperature, and is therefore often referred to as the infinite conductivity model (*Aggarwal et al. [4]*). The assumption of quasi-steadiness is employed, i.e. a rate of change of

global droplet quantities that is sufficiently low to consider the system as stationary at a given instant in time. In the case of droplet heat transfer, the enthalpy fluxes are evaluated for a steady state while the droplet temperature is allowed to vary over time. Again, quasi-steadiness translates to a the condition of a time scales sufficiently short to keep variation of global quantities negligibly small.

If the temporal evolution of the enthalpy $m_p\, h_{s,p}(T_p)$ of a given droplet is considered, only the heat fluxes on the liquid side contribute to the equation

$$\frac{d}{dt}\left(m_p\, h_{s,p}(T_p)\right) = \Phi_l^{ev} + \Phi_l^c\,. \tag{3.51}$$

Splitting up the temporal derivative on the left hand side and substituting Φ_l^{ev} according to Eq. 3.44 gives

$$\frac{d\, m_p}{dt}\, h_{s,p}(T_p) + \frac{d\left(h_{s,p}(T_p)\right)}{dt}\, m_p = -m_F\, h_{s,p}(T_\zeta) + \Phi_l^c\,. \tag{3.52}$$

The droplet temperature is constant over r, so that $T_\zeta = T_p$. Furthermore, under the assumption of quasi-steadiness, the gaseous fuel mass flux m_F can be substituted by the evolution of the droplet mass m_p which results in the terms describing the enthalpy transport by the *Stefan* flux on both sides of Eq. 3.52 becoming identical

$$\frac{d\, m_p}{dt}\, h_{s,p}(T_p) = m_p\, h_{s,p}(T_\zeta)\,. \tag{3.53}$$

Moreover, the variation of the liquid sensible enthalpy, $d\left(h_{s,p}(T_p)\right)$, can be expressed as

$$d\left(h_{s,p}(T_p)\right) = C_{p,l}\, dT_p\,. \tag{3.54}$$

Injecting Eq. 3.54 and Eq. 3.53 into Eq. 3.52 finally yields a law for the Lagrangian temporal derivative of the droplet temperature

$$\frac{dT_p}{dt} = \frac{1}{m_p\, C_{p,l}}\, \Phi_l^c\,. \tag{3.55}$$

Using Eq.3.47, Φ_l^c can be substituted and one obtains

$$\frac{dT_p}{dt} = \frac{1}{m_p\, C_{p,l}}\, \left(-\Phi_g^c + m_p L_v(T_\zeta)\right)\,. \tag{3.56}$$

Note that the evolution of the droplet temperature given by Eq. 3.55 depends on the liquid conductive heat exchange Φ_l^c which, in most cases, only plays a role during the droplet heat-up phase at the onset of evaporation. After a transient regime, the terms $-\Phi_g^c$ and $m_p L_v(T_\zeta)$ cancel each other out so that Φ_l^c becomes negligible. This corresponds to the steady state situation considered in the d^2-law with Eq. 3.49 being satisfied. With $dT_p\,/\,dt \to 0$ for $\Phi_l^c \to 0$, the droplet temperature tends towards the wet bulb plateau temperature T_{wb}. In Eq. 3.56, the remaining unknown is Φ_g^c for which the analytical expression is further derived.

3.3.2.7 Heat transfer of an evaporating droplet

To evaluate the heat transfer, the thermal conductivity λ is assumed to be constant over the radial distance r. The mass conservation equation (Eq. 3.22) is employed to rewrite the energy conservation equation (Eq. 3.24)

$$m_F\, C_P \frac{dT}{dr} = 4\pi \frac{d}{dr}\left(\lambda r^2 \frac{dT}{dr}\right) , \tag{3.57}$$

where $r^2\rho u$ on the left hand side is replaced by $r_\zeta^2 \rho_\zeta u_\zeta = m_F/4\pi$, and $m_F = 4\pi\rho u r^2$ is the *Stefan* flux at the droplet surface. The integration of this equation yields

$$m_F\, C_P T = 4\pi r^2 \lambda \frac{dT}{dr} + c_1 , \tag{3.58}$$

where c_1 is a constant determined by applying the boundary condition at the surface ζ

$$m_F\, C_P T_\zeta = 4\pi r_\zeta^2 \lambda \left[\frac{dT}{dr}\right]_\zeta + c_1 . \tag{3.59}$$

The term $4\pi r_\zeta^2 \lambda \left[\frac{dT}{dr}\right]_\zeta$ can directly be replaced using Eq. 3.43 and taking into account that the thermal conductivity λ has been assumed to be constant

$$4\pi r_\zeta^2 \lambda \left[\frac{dT}{dr}\right]_\zeta = -\Phi_g^c . \tag{3.60}$$

Injecting this expression in the integrated conservation law (Eq. 3.58) via c_1, one obtains

$$m_F \left(C_P T - C_P T_\zeta - \frac{\Phi_g^c}{m_F}\right) = 4\pi r^2 \lambda \frac{dT}{dr} . \tag{3.61}$$

The separation of the variables r and T and a second integration yields

$$-\frac{1}{r} = \frac{4\pi\lambda}{m_F C_P} \ln\left(T - T_\zeta - \frac{\Phi_g^c}{m_F C_P}\right) + c_2 . \tag{3.62}$$

Applying the far-field boundary condition allows to determine c_2 to finally obtain

$$\frac{1}{r} = \frac{4\pi\lambda}{m_F C_P} \ln \quad \frac{T_\infty - T_\zeta - \frac{\Phi_g^c}{m_F C_P}}{T - T_\zeta - \frac{\Phi_g^c}{m_F C_P}} \quad . \tag{3.63}$$

This equation relates the gaseous temperature as a function of the radial distance and the conductive enthalpy flux at the liquid side. When evaluated at the droplet surface, an additional expression for the mass flux m_F is obtained that is different from Eq. 3.32

$$m_F = \frac{4\pi\lambda r_\zeta}{C_P} \ln\left(B_T + 1\right) . \tag{3.64}$$

In this case, m_F depends on the *Spalding* number for the temperature, B_T

$$B_T = \frac{\left(T_\infty - T_\zeta\right) m_F C_P}{-\Phi_g^c} . \tag{3.65}$$

These two expressions for the mass flux can be equalised to obtain a relation between B_M and B_T

$$B_T = (1 + B_M)^{\frac{Sh}{Nu\, Le_F}} - 1\,, \tag{3.66}$$

with the Lewis number of the fuel species $Le_F = Sc_F/Pr = \mu/[\rho D_F] \cdot \lambda/(\mu C_P)$. After rearrangement, Eq. 3.65 yields

$$\Phi_g^c = \frac{m_F C_P}{B_T} \left(T_\zeta - T_\infty\right) . \tag{3.67}$$

By replacing the mass flux m_F using Eq. 3.64, one obtains the final expression for Φ_g^c as a function of the known temperatures T_ζ and T_∞ as well as of B_T

$$\Phi_g^c = \lambda 4\pi r_\zeta \left(T_\zeta - T_\infty\right) \frac{\ln(B_T + 1)}{B_T} = \lambda \pi d_p Nu \left(T_\zeta - T_\infty\right) \frac{\ln(B_T + 1)}{B_T} . \tag{3.68}$$

3.3.2.8 Advanced evaporation models

The model used in the scope of this work is of the infinite conductivity type. Note that there are more advanced models available in literature. An example is the one proposed by *Abramzon and Sirignano* [2], which takes into account the finite thickness of the fuel mass fraction and thermal boundary layers, resulting in modified expressions for the Nusselt and Sherwood numbers. This model is also available in AVBP but was not employed in the present work.

3.3.2.9 Statistical source terms for heat transfer

The fluxes Φ_g^c, Φ_g^{ev}, Φ_l^c and Φ_l^{ev} previously derived are relevant for the temporal evolutions of a single droplet enthalpy. The enthalpy transfer that is passed to the energy equation of the gaseous phase Π_g is per unit volume. Conversely, Π_l is the volumic source term in the energy equation of the liquid phase. Both are defined as the statistical average over a single droplet s heat transfer contributions and their expression finally reads

$$\begin{aligned}
\Pi_g &= \rho_l \breve{\alpha}_l \left\langle \frac{1}{m_p} \left(\Phi_g^c + \Phi_g^{ev}\right) \right\rangle_l , \qquad (3.69)\\
&= \lambda \pi \breve{n}_l \breve{d}\, Nu \left(\breve{T}_l - T\right) \frac{\ln(B_T + 1)}{B_T} + \Gamma h_{s,F}(\breve{T}_l) \,,\\
\Pi_l &= \rho_l \breve{\alpha}_l \left\langle \frac{1}{m_p} \left(\Phi_l^c + \Phi_l^{ev}\right) \right\rangle_l , \qquad (3.70)\\
&= -\Pi_g - \rho_l \breve{\alpha}_l \left\langle \frac{1}{m_p} \left(m_p\, h_{s,corr}\right) \right\rangle_l ,\\
&= -\Pi_g - \Gamma\, h_{s,corr} \,.
\end{aligned}$$

3.4 Summary of the governing equations for the liquid phase

The governing equations for the liquid dispersed phase in the Eulerian formalism with source terms due to mass, heat and momentum transfers finally reads:

- **Number density**

$$\frac{\partial}{\partial t}\breve{n}_l + \frac{\partial}{\partial x_j}\breve{n}_l\breve{u}_{l,j} = 0\,, \tag{3.71}$$

- **Volume fraction**

$$\frac{\partial}{\partial t}\rho_l\breve{\alpha}_l + \frac{\partial}{\partial x_j}\rho_l\breve{\alpha}_l\breve{u}_{l,j} = -\Gamma\,, \tag{3.72}$$

- **Momentum**

$$\frac{\partial}{\partial t}\rho_l\breve{\alpha}_l\breve{u}_{l,i} + \frac{\partial}{\partial x_j}\rho_l\breve{\alpha}_l\breve{u}_{l,i}\breve{u}_{l,j} = -\Gamma\breve{u}_{l,i} + \frac{\rho_l\breve{\alpha}_l}{\tau_p}\left(u_i - \breve{u}_{l,i}\right)\,, \tag{3.73}$$

- **Sensible enthalpy**

$$\frac{\partial}{\partial t}\rho_l\breve{\alpha}_l\breve{h}_{s,l} + \frac{\partial}{\partial x_i}\rho_l\breve{\alpha}_l\breve{u}_{l,i}\breve{h}_{s,l} = -\Gamma\left(h_{s,F}(\breve{T}_l) + h_{s,corr}\right) - \lambda\pi\breve{n}_l\breve{d}\,Nu\left(\breve{T}_l - T\right)\frac{\ln(B_T+1)}{B_T}\,. \tag{3.74}$$

These governing equations will be employed in Chapter 10 for the LES study of the LEMCOTEC aeronautical combustion chamber.

4

Theoretical concepts of combustion

Contents

4.1 Introduction

The goal of this chapter is to provide some theoretical aspects of turbulent combustion. First, general aspects of premixed and non-premixed combustion and their interaction with turbulence are presented. Then the most common descriptions of combustion chemistry are compared and their potential use and limitations in LES computations is discussed. Finally, several approaches for subgrid turbulence-chemistry interaction closure able to handle pollutant formation are described.

4.2 Premixed combustion

4.2.1 Unstretched premixed flame

The unstretched premixed flame is a fundamental canonical case to understand combustion processes. It corresponds to a situation where the fuel and the oxidiser are mixed prior to combustion. In the flow, the premixed flame corresponds to a localised region of strong temperature gradient, generally of the order of 0.1 mm.

Spatial structure

The flame region can be decomposed in three layers [154] as illustrated in Fig. 4.1:

- A **preflame zone**, which is chemically inert. In this region, fresh gases are preheated due to thermal fluxes.
- An **inner reaction layer** of thickness δ_r (reaction thickness) where the fuel decomposes into smaller intermediate fuels like CH_3 or H_2 to react with radicals such as H or OH.
- A **post-flame zone**, where the intermediates are converted into products like CO_2 and H_2O, and where slow NO_x reactions continue to occur.

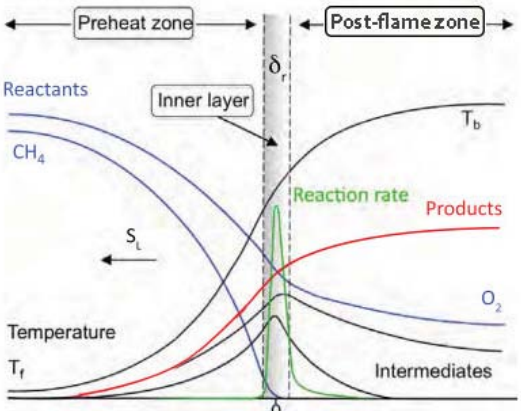

Figure 4.1: Schematic of a one-dimensional premixed CH4/air flame.

Governing equations

When the flame is steady (the reference frame is the flame), the simplified balance equations reads

$$\frac{\partial \rho u}{\partial x} = 0 \text{ or equivalently } \rho u = cst = \rho_f S_l \,, \tag{4.1}$$

$$\frac{\partial}{\partial x}\left(\rho(u+V_k)Y_k\right) = \dot{\omega}_k = \rho\dot{\omega}_{Y_k} \,, \tag{4.2}$$

$$\rho C_p u \frac{\partial T}{\partial x} = \dot{\omega}_T + \frac{\partial}{\partial x}\left(\lambda\frac{\partial T}{\partial x}\right) - \frac{\partial T}{\partial x}\left(\rho\sum_{k=1}^{n_{spec}} C_{p,k}Y_kV_k\right) \,. \tag{4.3}$$

Control variables for a premixed flame: equivalence ratio and progress variable

The initial conditions of a premixed flame are controlled by the pressure, fresh gas temperature and the fresh gas composition. The latter is parametrised by the **equivalence ratio** ϕ, which is defined as

$$\phi = s\frac{Y_F}{Y_O} = \left(\frac{Y_F}{Y_O}\right) \Big/ \left(\frac{Y_F}{Y_O}\right)_{st}, \tag{4.4}$$

where Y_F and Y_O are respectively the fuel and oxidiser mass fractions at the inlet (fresh gas side). s is the mass stoichiometric ratio which reads

$$s = \left(\frac{Y_O}{Y_F}\right)_{st} = \frac{\nu'_O W_O}{\nu'_F W_F}. \tag{4.5}$$

where ν'_O and ν'_F are the oxidiser and fuel stoichiometric molar coefficients of the global reaction. At stoichiometric conditions ($\phi = 1.0$), the fuel and oxidiser are completely converted into products. When $\phi < 1$, the mixture is lean corresponding to an excess of oxidant, and when $\phi > 1$ the mixture is rich, the oxidiser becomes the limiting reactant. Alternatively to the equivalence ratio, the composition of the fresh gases can also be characterised by the mixture fraction Z which is introduced in Sec. 4.3.1.

Another important control variable is the **progress variable** c which quantifies the evolution of the mixture from fresh gases ($c = 0$) to burnt gases ($c = 1$). It can be based on the temperature

$$c = \frac{T - T_f}{T_b - T_f} \tag{4.6}$$

where the subscripts $_f$ and $_b$ corresponds respectively to fresh gases and burnt gases conditions. Another typical choice is to use major products of combustion to build up the progress variable as

$$c = \frac{Y_c}{Y_c^{eq}}, \tag{4.7}$$

where typically $Y_c = Y_{\mathrm{CO}} + Y_{\mathrm{CO_2}} + Y_{\mathrm{H_2O}}$ and the superscript ^{eq} denotes the equilibrium value. Under unity Lewis assumptions, a balance equation for the progress variable can be derived as

$$\frac{\partial \rho u c}{\partial x} = \frac{\partial}{\partial x}\left(\rho D \frac{\partial c}{\partial x}\right) + \omega_c. \tag{4.8}$$

The progress variable c is convenient to analyse the flame structure. In particular comparisons between laminar and turbulent cases are simpler in c-space and an iso-surface of c is convenient to localise the flame front and also to define the normal to the flame front (pointed towards fresh gases) as

$$\mathbf{n} = -\frac{\nabla c}{|\nabla c|}. \tag{4.9}$$

Intrinsic properties: flame speed and thickness

In the premixed regime, the flame has a characteristic propagation speed, which is the laminar flame speed S_l. It depends on the fresh gas composition, the fresh gas temperature and the pressure. For a one-step chemistry, it can be shown from asymptotic analysis of the governing equations [206] that the laminar flame speed is related to the thermal diffusivity $D_{th} = \lambda/(\rho C_p)$ and the Arrhenius pre-exponential constant A of the reaction step as

$$S_l \qquad \overline{D_{th} A}\,. \tag{4.10}$$

The laminar flame speed usually falls in the range $S_l = 0.1 - 2\,\mathrm{m/s}$ for hydrocarbons at gas turbine conditions. In addition, the laminar flame is characterised by an intrinsic thickness δ_l. It can be estimated from the temperature profiles as

$$\delta_l = \frac{T_b - T_f}{\max\left(\mid \frac{\partial T}{\partial x} \mid \right)}\,, \tag{4.11}$$

where T_f and T_b are respectively the fresh and burnt gas temperature. From asymptotic theory, the flame thickness is related to thermal diffusivity and laminar flame speed as

$$\delta_l \quad \frac{D_{th}}{S_l} \qquad \overline{\frac{D_{th}}{A}}\,. \tag{4.12}$$

The flame may also be characterised by its **reaction zone thickness** δ_r [107] which is smaller than the thermal thickness δ_l.

Other relevant speeds

Several speeds might be of interest for kinematic interpretation of the propagation of premixed flames. The absolute velocity of the flame in the reference frame $\mathbf{w}$ can be decomposed following Fig 4.2:

- The **absolute speed** $S_a = \mathbf{w} \cdot \mathbf{n}$, which is the flame front speed in the absolute reference frame.
- The **displacement speed** $S_d = (\mathbf{w} - \mathbf{u}) \cdot \mathbf{n} = S_a - \mathbf{u} \cdot \mathbf{n}$, which is the flame front speed relative to the local flow velocity u. S_d is useful for a kinematic interpretation of the flame as an interface. Because of its local nature, its interpretation is however not always straightforward.
- The **consumption speed** S_c is the speed at which reactants are consumed, and is equal to the integral of fuel consumption in the direction normal to the flame.

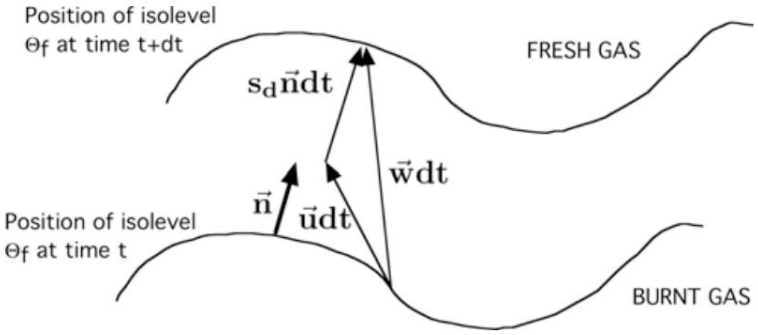

Figure 4.2: Flame speed definitions. From [159].

The expression of S_c reads

$$S_c = -\frac{1}{\rho_f \left(Y_F^f - Y_F^b\right)} \int_{-\infty}^{\infty} \dot{\omega}_F \mathbf{dn} \,. \tag{4.13}$$

Contrarily to the displacement speed, the consumption speed is a global quantity. Its interpretation is simpler than the displacement speed, but this quantity can only be evaluated globally.

For a laminar steady premixed flames, the following relations can be obtained

$$S_a = 0 \,, \tag{4.14}$$

$$S_l = S_c = S_d^* = \frac{\rho}{\rho_f} S_d \,, \tag{4.15}$$

$$\tag{4.16}$$

where S_d^* is a the density weighted displacement speed [88] introduced to take into account flow dilatation. For more complex cases, these quantities might strongly differ under the effect of turbulence, unsteadiness and stretch (curvature and strain). The latter effect is described in the next subsection (Sec. 4.2.2).

4.2.2 Strain and curvature effects

The total flame stretch κ is defined as the temporal variation of a flame surface element [206]

$$\kappa = \frac{1}{A} \frac{dA}{dt} \,. \tag{4.17}$$

Following [31] it can be expressed and decompose as

$$\kappa = \underbrace{\left(\delta_{ij} - n_i n_j\right) \frac{\partial u_i}{\partial x_j}}_{\text{Tangential strain rate}} + \underbrace{S_d \frac{\partial n_i}{\partial x_i}}_{\text{Curvature effect}} = a_t + 2 S_d \mathcal{K} \,, \tag{4.18}$$

where S_d is the flame displacement speed, a_t is the tangential strain rate, $\mathbf{n}$ is the vector normal to the flame (pointing towards fresh gases) and

$$\mathcal{K} = \frac{1}{2} \nabla . \mathbf{n} \tag{4.19}$$

is the flame front curvature. The first term contributing to κ in Eq. 4.18 is the strain rate, which is related to the non-uniformity of the flow. This non-uniformity can be caused by the mean flow (typically in shear layers) and by turbulent velocity fluctuations (turbulent strain). The second term is related to the flame front curvature [159].

Impact of stretch

Under some assumptions (low stretch level, single step chemistry etc.), it can be shown that the local flame structure is controlled only by the stretch κ [26, 29, 35]. It corresponds to a linear regime in which the flame displacement speed S_d and the flame consumption are linearly related to the flame stretch by the following expressions

$$\frac{S_d}{S_l} = 1 - Ma^d \frac{\delta_{th}}{S_l}\kappa\,, \tag{4.20}$$

$$\frac{S_c}{S_l} = 1 - Ma^c \frac{\delta_{th}}{S_l}\kappa\,, \tag{4.21}$$

where Ma^d and Ma^c are Markstein number respectively for the displacement and the consumption speed. These numbers are proportional to the fuel Lewis number $(Le_{fuel} - 1)$.

- For fuels with $Le_{fuel} \simeq 1$ (e.g CH_4), species and temperature gradients increase in the same proportion with increasing stretch. The flame becomes thinner but its overall consumption is not affected.
- When $Le_{fuel} < 1$ the Markstein number is negative and the consumption speed increases linearly when the stretch increases.
- When $Le_{fuel} > 1$ the Markstein number is positive, the consumption speed decreases when stretch increases.

This analysis is performed for a one-step irreversible chemistry but might not be valid for complex chemistry with varying Lewis number. However, strain and curvature effects for flame with complex chemistry can be evaluated on canonical configurations presented hereafter, and compared with theoretical responses.

Strain effect evaluation

The canonical case to evaluate the effect of strain is presented in Fig. 4.3. A fresh premixed methane/air mixture is injected on the left side with a velocity u_f, whereas combustion products are injected on the right side with a velocity u_b. By varying the injection velocities, the global strain rate a

$$a = \frac{u_f + u_b}{d} \tag{4.22}$$

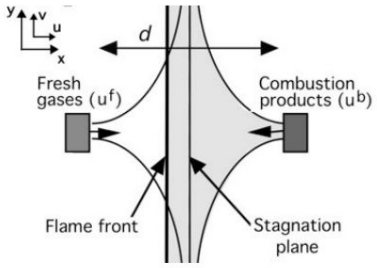

Figure 4.3: Schematic of a canonical counterflow strained premixed flame. From [159].

is varied. The flame front stabilises in the vicinity of the stagnation plane and the impact of the strain rate on the flame consumption speed defined in Eq. 4.13 can be assessed along with its impact on pollutant species formation. Global quantities based on consumption speed of Eq. 4.13 are preferred to kinematic interpretations because of the non-uniformity of the velocity field in this type of configuration.

Curvature effect evaluation

There is no simple one-dimensional configuration to evaluate the impact of curvature because it is (at least) a two-dimensional effect. Its impact might be evaluated from two-dimensional or three dimensional flame vortex interactions [161].

Impact on pollutant formation

Since stretch modifies the residence time inside the flame (the flame becomes thinner with increasing stretch), slow chemical processes as NO_x formation and CO recombination in CO_2 can be strongly impacted, compared to fuel oxidation process which are least an order of magnitude faster. This increased sensitivity to stretch will be illustrated for methane-air mixture in Sec. 9.4.2.1.

4.2.3 Flame-turbulence interaction

The interaction between the turbulent flame and the flow can be assessed by the comparison of the flow and the flame turbulent scales. From these scales, two essential dimensionless numbers characterise the flame-turbulence interaction.

- The **Damköhler number** is defined as the ratio between the largest turbulent time scale and a chemical time scale

$$Da = \frac{\tau_t}{\tau_c} = \frac{l_t}{\delta_l}\frac{S_l}{u'_t} \tag{4.23}$$

  When $Da >> 1$, the flame surface is wrinkled and stretched by the turbulent flow. However its internal structure is not directly impacted by the turbulent

motions. In this **flamelet regime**, the structure of the reaction zone corresponds locally to the one of a laminar flame. When $Da << 1$ reactants and products are strongly mixed by turbulence and react through slow reactions. In practical application, the first regime corresponding to $Da >> 1$ is generally found for the fuel oxidation, but slower process like NO formation or CO oxidation may fall in other regimes.

- The **Karlovitz number** characterises the interaction between the reactive scales and the smallest (Kolmogorov) flow scales

$$Ka = \frac{1}{Da(\eta_\kappa)} = \frac{\delta_l}{\eta_\kappa} \frac{u_{\eta_\kappa}}{S_l} . \tag{4.24}$$

  and the turbulent Reynolds number of Eq. 2.22 can be rewritten as

$$Re_t = Da^2 Ka^2 . \tag{4.25}$$

Since the turbulent Reynolds is linked to the two dimensionless numbers, they can be employed to qualitatively estimate the combustion regime. The combustion regimes can be decomposed following the combustion diagram of Fig. 4.4. The following regimes are identified and illustrated in Fig. 4.5:

- **Laminar flame regime** ($Re_t < 1$): the flow is quasi-laminar, thus the flame is only slightly wrinkled.
- **Thin flame regime** ($Re_t < 1$, $Ka < 1$). Depending on the velocity ratio $\frac{u'}{S_l}$ it may be decomposed into two regimes:
  - **Wrinkled flamelet regime** ($Ka < 1$, $u'/S_l < 1$) The flame thickness remains smaller than the Kolmogorov scale and is therefore in the flamelet regime. Due to the moderate intensity of the turbulent fluctuations, the flame surface is only slightly wrinkled and stretched by the turbulent structures.
  - **Corrugated flamelet regime** ($Ka < 1$, $u'/S_l > 1$) The turbulent intensity is higher, the flame surface is highly wrinkled and stretched by turbulent motions. Isolated burning pockets of the eddy size may form.
- **Thickened wrinkled flame or reaction-sheet regime** ($Re_t > 1$, $Ka > 1$, $Ka_r < 1$, $Da > 1$) The smallest eddies are smaller than the flame thickness. They are able to interact with the preheating zone, thus enhancing mass and heat transfer. Because the reaction zone remains thinner than the smallest turbulent scales ($Ka_r < 1$), it keeps its laminar structure.

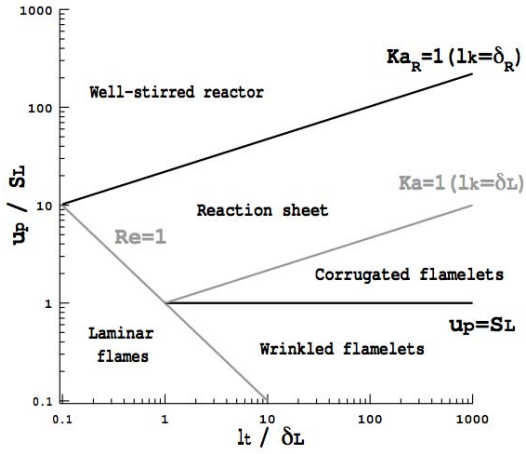

Figure 4.4: Turbulent combustion regime decomposed in terms of length scales (l_t/δ_l) and velocity scales u'/S_l. From [155].

- **Well-stirred reactor** ($Re_t > 1$, $Ka > 1$, $Ka_r > 1$, $Da < 1$) The smaller turbulent scale can penetrate the reaction zone, thus increasing diffusion and heat transfer in both preheat and reaction zone. The flame has no distinct laminar structure.

4.3 Non-premixed combustion

4.3.1 Laminar diffusion flames

In the case of diffusion flames, fuel and oxidiser are not mixed before combustion. Thus, diffusion flames are largely controlled by mixing, which must bring the reactants into the reaction zone localised around stoichiometry, which is the region where fuel and oxidiser are mixed adequately to burn. A schematic of this type of flame structure is given in Fig. 4.6. The temperature peak is located in the reaction zone and diffuses towards the fresh fuel and oxidiser streams. Contrarily to premixed flames, diffusion flames **do not propagate** and have **no intrinsic thickness**. The inner structure of a diffusion flame is imposed by the external conditions, which depend on the local stretch.

The local mixing state is adequately described by the mixture fraction Z. It may be defined using Bilger definition [19] based on atomic mass fraction

$$\beta = \sum_{i=1}^{N_a} \gamma_i Z_i = \sum_{i=1}^{n_{spec}} \gamma_i \sum_{j=1}^{N_a} n_{ij} \frac{W_i Y_j}{W_j}\,, \tag{4.26}$$

where n_{ij} is the number of atoms of the i^{th} element in the j^{th} specie and N_a is the total number of atoms. γ_i are weighting factors, with values $\gamma_C = 2/W_C$, $\gamma_H = 1/(2W_H)$

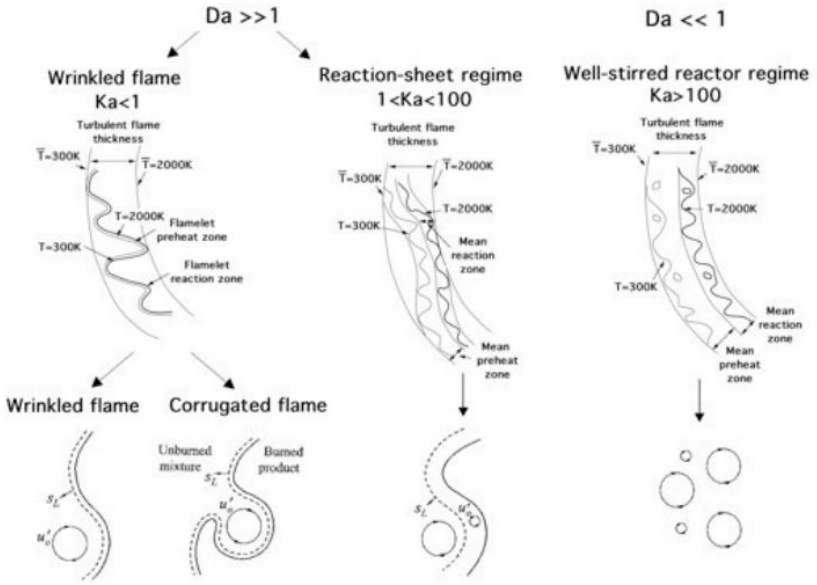

Figure 4.5: Illustration of turbulent combustion regimes (*Poinsot and Veynante* [159], *Law et al.* [107]).

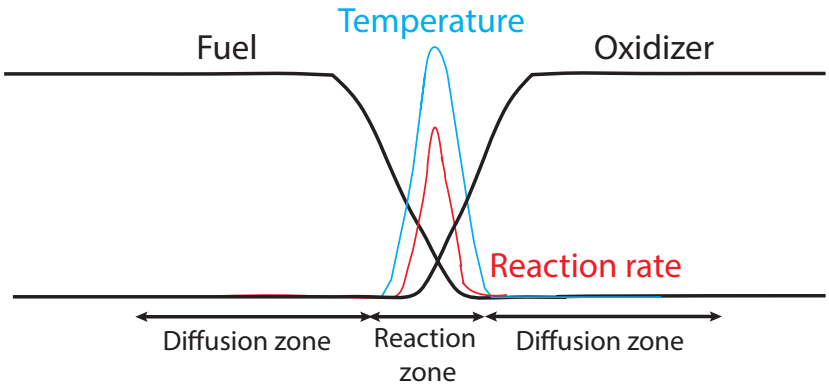

Figure 4.6: Diffusion flame structure.

and $\gamma_O = -1/W_O$ according to Bilger. β is then rescaled by the oxidiser value β_o and the fuel value β_f to obtained the normalised mixture fraction

$$Z = \frac{\beta - \beta_o}{\beta_f - \beta_o} \,. \tag{4.27}$$

By definition, the mixture fraction is invariant with respect to chemical reactions. Under the assumption of equal species Schmidt numbers, it behaves like a passive scalar and its transport equation reads

$$\frac{\partial \rho Z}{\partial t} + \frac{\partial}{\partial x_j}\left(\rho Z u_j\right) = \frac{\partial}{\partial x_l}\left[\rho D \frac{\partial Z}{\partial x_l}\right] \,. \tag{4.28}$$

This equation allows to decompose the resolution of the flame into a mixing problem and a flame structure problem in the phase space. If the Lewis number is equal to unity, the species and temperature equations can be rewritten in Z-space as a function of Z and the scalar dissipation rate $\chi = 2D\left|\nabla Z\right|^2$ [28]

$$\rho\frac{\partial Y_k}{\partial t} = \frac{1}{2}\rho\chi\frac{\partial^2 Y_k}{\partial Z^2} + w_k\,, \tag{4.29}$$

$$\rho\frac{\partial T}{\partial t} = \frac{1}{2}\rho\chi\frac{\partial^2 T}{\partial Z^2} + w_T\,. \tag{4.30}$$

In Eq. 4.29 and Eq. 4.30, the scalar dissipation rate χ is the only parameter depending on space. Thus once the scalar dissipation rate χ is known, it parametrises the two equations and they can be directly resolved in Z-space. The scalar dissipation characterises the intensity of the gradients and thus molecular fluxes towards the flame, and is directly linked to velocity strain. The **mixing layer thickness** can be estimated as

$$l_Z = \quad \overline{\frac{D}{\chi}} = \frac{1}{\mid \nabla Z \mid}\,. \tag{4.31}$$

This parameter directly controls the flame structure, and in turns the flame consumption speed and pollutant formation rates. A **reaction layer thickness** l_{reac} characterising the width of the reaction zone can also be defined. From asymptotic theory [120], it is proportional to the mixing layer thickness

$$l_{reac} \quad l_Z\left(Da^{fl}\right)^{-1\ b}\,, \tag{4.32}$$

where $b = 1 + \nu'_O + \nu'_F$. An important canonical case representative of practical applications is the steady strained one-dimensional diffusion flame, and is at the basis of numerous tabulated chemistry models for non-premixed flames. A schematic of this type of flame is given in Fig. 4.7. The strain rate might not be exactly constant in this

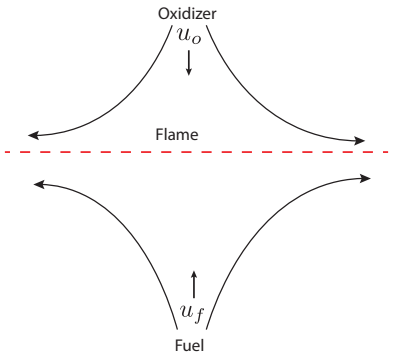

Figure 4.7: Steady strained one-dimensional diffusion flame.

situation along the flame normal, but it can estimated from global quantity as

$$a \simeq \frac{u_f + u_o}{L} \tag{4.33}$$

where u_f and u_o are respectively the fuel and oxidiser injection velocity and L is the distance between the two inlets. Under the assumption of asymptotically infinitely fast chemistry, it can be shown that the flame consumption speed (integrated fuel reaction rate along the flame normal) is linked to the strain rate a and the diffusivity D as [159]

$$\Omega_{fuel} \qquad \overline{aD} \tag{4.34}$$

$$\tag{4.35}$$

and that the scalar dissipation rate is directly proportional to the strain rate

$$\chi \qquad a\,. \tag{4.36}$$

Compared to premixed flame for which the stretch rate only introduces a small linear correction to the flame consumption speed, which remains essentially piloted by the intrinsic properties of the premixed flame, the scalar dissipation rate directly controls the diffusion flame consumption speed

$$\Omega_{fuel} \qquad \overline{aD}\,, \tag{4.37}$$

thus diffusion flames are much more sensitive to local flow conditions for which the scalar dissipation rate results.

Finite rate chemistry effect

For finite rate chemistry, similarly to premixed combustion, a Damkohler number comparing flow and chemistry time scales can be defined as

$$Da^{fl} = \frac{\tau_f}{\tau_c} \simeq \frac{1}{\chi_{st}\tau_c}\,, \tag{4.38}$$

where τ_c is the chemical time and χ_{st} is the stoichiometric scalar dissipation rate. The previous findings were derived assuming infinitely fast chemistry. However they remain valid for finite rate chemistry in the high Damkohler limit, corresponding to low strain values. As shown in Fig. 4.8, the response of finite rate chemistry deviates when the strain rate (or equivalently the scalar dissipation rate) increases. The maximum temperature of the flame decreases and beyond a certain threshold value, quenching occurs.

Impact of scalar dissipation rate on pollutant formation

Similarly to stretch in the premixed flame, the scalar dissipation rate can be interpreted as an inverse of the residence time in the flame, thus impacting slow CO oxidation in CO_2 and NO_x formation processes. Illustration of this behaviour will be provided for methane-air cases corresponding to the Sandia Flame D conditions in Sec. 7.4.1.

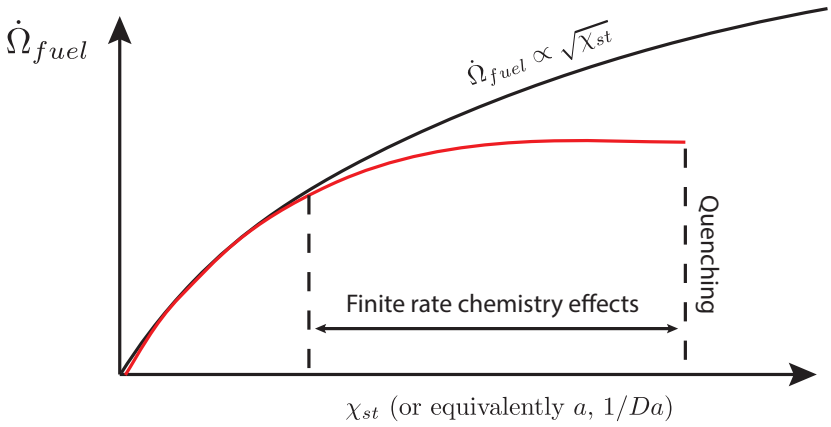

Figure 4.8: Diffusion flame consumption speed vs scalar dissipation (or equivalently strain rate a or inverse of Damköhler $1/Da$) for infinitely fast chemistry (black) and finite rate chemistry (red).

4.3.2 Turbulent diffusion flames

Whereas premixed flames have intrinsic properties, the structure of diffusion flames is governed by the scalar dissipation rate which is directly linked to the turbulent strain rate. Because of this strong coupling between flow and flame scales, establishing a universal combustion diagram in this situation is not straightforward. Flow and flame scales are summarised in Fig. 4.9. Similarly to the premixed case, combustion regimes

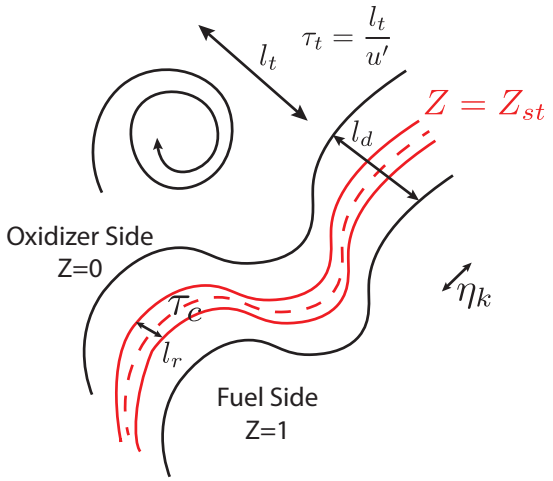

Figure 4.9: Spatial scales in turbulent diffusion flames. Turbulent scales: Integral length scale l_t, integral time scale τ_t and Kolmogorov scale η_k. Flame scales: diffusive thickness l_d, reaction zone thickness l_r and chemical time τ_c.

can be roughly estimated for diffusion flames by comparison of these scales. As shown in [41], several regimes can be identified in a log-log diagram based on the turbulent Reynolds number Re_t and the Damkohler number $Da = \tau_t/\tau_c$ (Fig. 4.10).

- In the **flamelet regime** correspond into Da^{fl} lower than a critical value Da^{LFA} (LFA: laminar flamelet assumption), the inner flame structure is not affected by turbulence.
- When Da^{fl} is higher than a critical value referred to as Da_{ext}, **quenching** occurs because chemical times are too large compared to flow scales.
- In-between, there is an intermediate situation with strong unsteady effects.

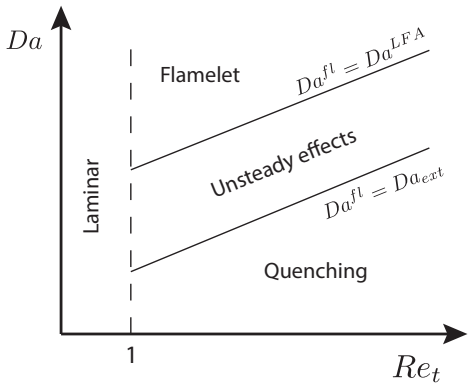

Figure 4.10: Regimes for turbulent non-premixed combustion as a function of the Damköhler number Da and the turbulent Reynolds number Re_t [41].

4.4 Chemical description

The chemical description is of critical importance for LES oriented towards pollutant prediction, and results from a compromise between cost and accuracy. To correctly describe the flame structure and pollutant formation, the retained modelling should be able to capture complex flow/flame interactions previously describe and to correctly handle multiple chemical time scales, while keeping the numerical cost and stiffness reasonable for three-dimensional computations of realistic configurations. The main approaches available in the literature are presented in the next subsections.

4.4.1 Detailed chemistry

The most direct and brute-force approach is to employ detailed chemistry. Detailed mechanisms contain a thorough description of the chemical system. They can contain up to hundreds of species and thousands of elementary reactions and are constructed to reproduce experimental data for a large variety of phenomena: auto-ignition, extinction, shock tube experiments, premixed and non-premixed planar flames etc. Such mechanisms are available for small hydrocarbon (e.g. GRI mechanisms [22, 23] for natural gas combustion) to large hydrocarbon chains (e.g. the Dagaut mechanism [42]

for jet fuel combustion). These mechanisms contain a large set of elementary reactions, generally involving two or three species that represents from a mesoscopic point of view the interactions occuring at the molecular level. The reaction rate of a given reaction j of the form

$$\mathrm{A} + \mathrm{B} \longrightarrow \mathrm{C} + \mathrm{D}\,, \tag{4.39}$$

involving species A, B, C and D is expressed in an Arrhenius form as

$$r_j = k_j [A][B] T^{\beta_i} \exp\left(\frac{-E_{a,i}}{RT}\right)\,, \tag{4.40}$$

where $[X] = \dfrac{\rho Y_X}{W_X}$ is the activity concentration of the species X, k_j and $E_{a,i}$ are respectively the pre-exponential constant and the activation energy of the reaction and β_i is a temperature exponent. Slightly modified expressions are employed for reactions involving a third-body or pressure dependent (typically fall-off) reactions.

However, detailed mechanisms are generally out of scope for LES computations and barely employed in DNS computations for two essential reasons:

1. These mechanisms contain highly reacting radicals essential to describe the fuel oxidation. These highly reacting radicals have a life-span of the order of $10^{-10} - 10^{-8}$ s and are associated with very small length scales as well. Therefore their correct prediction requires a tremendous grid resolution which might not be achieved even with grid size sufficiently small to fully resolved the turbulent spectrum, and a costly implicit temporal integration of the stiff source terms might be required [127].

2. The number of transported species rapidly becomes higher than one hundred for large hydrocarbons, which strongly increases the CPU, memory and storage cost.

Therefore such detailed mechanisms are only marginally applicable in LES computations. For methane/air mixture however, the numerical cost might remain acceptable in some situations: a full detailed mechanism was employed by *Navarro-Martinez et al.* [142] in the LES of a lifted methane-air jet flame.

4.4.2 Tabulated chemistry

The central idea of the model is based on the **flamelet hypothesis**: the chemical timescales are short so that the the structure of the reaction zone remains laminar and corresponds locally to a canonical laminar problem identified *a priori*. Flamelet models were introduced by *Peters* [152, 153] for non-premixed combustion. They can also be employed for partially-premixed and premixed combustion regimes.

- For **premixed or partially-premixed** (or stratified) applications, laminar premixed flames are generally chosen as the reference flame. The mixture fraction Z is employed to describe the initial mixing state of the gas and a progress variable c introduced in Eq. 4.7 is used to parametrise the spatial evolution of the flame. This approach is for example employed in the FPI (Flame Prolongation of Intrinsic Low-Dimensional Manifold) model proposed by *Gicquel et al.* [70] and the FGM (Flame Generated Manifold) model proposed by *van Oijen et al.* [197]. Additional variables might be employed to include effects such as enthalpy losses [58] or multi-stream problems [59]. Based on these control variables, the relevant chemical source terms such as the progress variable source term are stored in a look-up table as a function of the control parameters

$$\omega_X = \omega_X \left(Z, c, ...\right) . \tag{4.41}$$

  and intermediate species concentrations can also be directly extracted from the table. In the LES computations, transport equations are solved for the control variables (typically $Y_c = c \times Y_c^{eq}$ and Z) with the relevant source terms extracted from the look-up table.

- For **non-premixed regimes**, counterflow diffusion flames introduced in Sec. 4.3 can be employed alternatively, leading to a table generally parametrised by the mixture fraction Z and the scalar dissipation rate χ_Z [157], and unsteady flamelet modelling can be used to better describe slow processes such as the formation of pollutants and radiative heat transfer [157].

Tabulated models have been extensively used for the prediction of complex turbulent flow and pollutants [58, 59, 85, 148], thanks to their capability to reproduce at least partially detailed chemistry effects while keeping the numerical cost very reasonable because of the small number of scalars to transport. An hybrid model combining this approach with globally reduced chemistry will be derived in Chapter 5. However they suffer some limitations when applied to practical combustion systems:

- To promote mixing, practical combustion system are generally swirled, leading to high turbulence intensity. This results in strong interactions through strain and curvature effects, along with dilution by burnt gases that are generally not taken into account in a tabulated approach.

- Multiple combustion regimes are generally found because of partial-premixing or two-phase flow flame structures. Therefore there might be no proper reference flame suitable or easily identified to build the look-up table.

- Even if some attempts are found in the literature [58, 85, 166], the inclusion of heat loss due to wall transfer or radiation requires strong additional modelling assumptions.

- Additional effort is required to model slow processes, such as post-flame NO_x and CO oxidation. Additional progress variable are often employed in that scope [122, 148, 213], but again additional modelling assumptions are generally needed to construct the look-up table and to make the bridge between laminar reference flames and turbulent cases.

4.4.3 Globally Reduced Chemistry

Globally reduced chemistries (GRCs) do not reproduce the details of the physics of the detailed mechanism. They are generally fitted to reproduce essential properties of the flame, such as flame speed and burnt gas temperature and generally contain up to ten species and reaction steps. Because of their simplicity, these mechanisms have a very limited cost and their implementation in LES computations is straightforward. They have been extensively used, from short carbon chain to longer carbon chain. For example for methane-air oxidation, the mechanism from *Jones and Lindstedt* [93], the 2-step 2S_CH4_BFER mechanism [60, 179] are available, and with a simplified description of NO_x formation [178]. Global reduced mechanisms are also available for aeronautical, such as the 2-step 2S_KERO_BFER mechanism derived from the Luche detailed mechanism [128].

GRC derivation

The derivation process might be based on general optimisation methods such as genetic algorithm [50]. More empirical methods are also suitable. For instance, the 2S_BFER methodology [64], applicable to potentially any fuel, presumes the form of the mechanism which is decomposed into two reaction steps as

$$\text{R1: } \mathrm{F} + \mathrm{xO_2} \longrightarrow \mathrm{yCO} + \mathrm{zH_2O}\,, \tag{4.42}$$

$$\text{R2: } \mathrm{CO} + 0.5\mathrm{O_2} \longrightarrow \mathrm{CO_2}\,, \tag{4.43}$$

where F is the fuel species. The rates of these reaction steps are written in an Arrhenius-like form but do not correspond to elementary reactions. For example the rate of reaction R1 reads

$$r_1 = f_1\left(\phi\right) k_1 [F]^{n_1} [\mathrm{O_2}]^{n_2} T^{\beta_1} \exp\left(\frac{-E_{a,1}}{RT}\right). \tag{4.44}$$

In this expression, k_1 and $E_{a,1}$ can be adjusted to match laminar flame speeds, whereas the concentration exponents n_1 and n_2 are adjusted to retrieve the correct pressure

dependency of the laminar flame speed [64]. In addition f_1 is a shape function of the equivalence ratio to correct the flame speed for rich mixtures. The essential role of reaction R2 is to yield correct prediction of the flame temperature by considering the CO/CO_2 equilibrium.

2S_CH4_BFER and 2S_KERO_BFER schemes are employed in this work respectively for methane-air computations and kerosene-air computations. The two schemes are detailed in Appendix. A.

Limitations of GRCs

However, this type of approach has several limitations:

- By construction, global reduced mechanisms are accurate on a given canonical problem (e.g. laminar premixed flame) with given conditions in terms of pressure, fresh gas temperature and equivalence ratio. But there is no guarantee that they yield accurate results outside of this range, since the derivation is not based on physical grounds.
- Information about the intermediate species is generally lost or inaccurate, therefore they are generally not suitable to predict pollutant prediction or complex effect such as the impact of stretch on the flame structure.

4.4.4 Skeletal mechanism

Skeletal mechanisms are obtained by reduction of detailed mechanism. Detailed mechanism are built to describe a large variety of phenomena, e.g. autoignition, extinction, low temperature chemistry for a wide range of validity in terms of pressure, temperature and equivalence ratio. However in practical combustion applications, the operating conditions are known *a priori* and flame propagation is the dominant mechanism. Therefore the chemical description does not need to include such a variety of phenomena. Species and reactions that are not relevant to the problem considered might simply be removed from the mechanism. This is known as *skeletal reduction*.

A wide variety of techniques are available to identify species and reactions that can be removed from a mechanism without altering its prediction capability. Graph methods, such as directed relation graph method (DRG) [125] and Directed Relation Graph method with Error Propagation (DRGEP) [150] are commonly used.

DRGEP approach

The fundamental idea behind the approach is to build-up a graph of interaction between

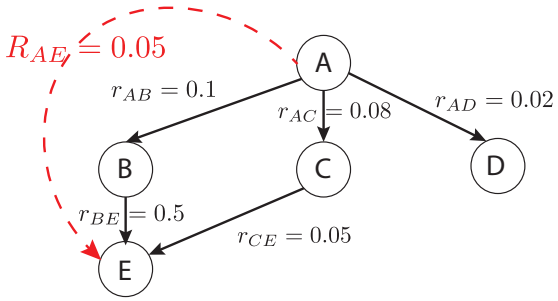

Figure 4.11: Part of a directed relation graph method involving four species. Adapted from [149].

the species of the chemical mechanism. A species is connected to another when they participate in at least one common reaction. The strength of the direct connection between a species A and a species B is the interaction coefficient r_{AB}, which quantifies the impact of B to the prediction of A. For example, in [149], it is defined as

$$r_{AB} = \frac{\left| \sum_{i=1}^{n_{reac}} \nu_{i,A} r_i \delta_B^i \right|}{\max\left(P_A, C_A\right)}, \tag{4.45}$$

where r_i is the rate of the i^{th} reaction, $\nu_{i,A}$ is the net stoichiometric coefficient of species A in the i^{th} reaction and δ_B^i is defined as

$$\delta_B^i = 1 \qquad \text{if the } i^{th}\text{reaction involves species B}\,, \tag{4.46}$$

$$\delta_B^i = 0 \qquad \text{, otherwise}\,. \tag{4.47}$$

P_A and C_A are normalisation coefficients that bound the interaction coefficient between 0 and 1. Their expressions reads

$$P_A = \sum_{i=1}^{n_{reac}} \max\left(0, \nu_{i,A} r_i\right), \tag{4.48}$$

$$C_A = \sum_{i=1}^{n_{reac}} \max\left(0, -\nu_{i,A} r_i\right). \tag{4.49}$$

Now we assume that A is the target species. The impact of a species B on A is obtained by considering the ensemble of paths $\mathcal{P}$ from A to B. For a given path $p = (A, S_2, S_3, ..., S_{n-1}, B) \quad \mathcal{P}$, the path interaction coefficient of A with B is given by the product of the interaction coefficients of the species that compose the path as

$$r_{AB,p} = \prod_{i=1}^{n} r_{S_i S_{i+1}}\,. \tag{4.50}$$

This geometric damping allows to take into account the error propagation, that is that a species that is involved through a long path in the prediction of A has typically a

smaller effect than a species that is more directly connected to A. The global interaction coefficient between A and B is finally taken to be the maximum over all paths

$$R_{AB} = \max_{p \ \mathcal{P}} r_{AB,p} \,. \tag{4.51}$$

The species with the weakest global interaction coefficients can be removed from the mechanism. An illustration is given in Fig. 4.11. In this example, A strongly interacts with B, and B strongly interacts with E. Because of the geometric damping, the global interaction coefficient between A and E, $R_{AE} = \max(r_{AB}r_{BE}, r_{AC}r_{CE}) = 0.05$ is weaker. Therefore in this case, removing E is expected to introduce an error which is lower than removing C but higher than removing D.

Compared to detailed mechanisms, skeletal mechanisms contain only the species and reactions that are relevant for the target application considered. This can significantly reduce the cost of the mechanism in terms of transported species, especially for long hydrocarbon fuels. However, highly reactive intermediates that take part in the fuel oxidation process are still required in the mechanism. The spatial and temporal stiffness of the mechanism might not be significantly reduced by the skeletal reduction. Several issues limit the use of skeletal mechanism in LES computations:

- The number of species in the mechanism and therefore the number of conservation equations to solve for the species remains high.
- Highly reacting intermediates are temporally and spatially stiff. Therefore the grid resolution needed to directly resolve the flame front is outside the scope of LES. In addition, stiff implicit integration of the chemical system requires the evaluation of the Jacobian, whose cost scales as n_{spec}^3 [127]. Explicit integration is much less costly and should be preferred, but can only be stable if the chemical time scales lower than the integration time-step are removed or treated in an alternative way, as detailed in the next subsection.

4.4.5 Analytically reduced chemistry

Two approaches widely found in the literature to remove short time-scales are the **Partial-Equilibrium Approximation** (PEA) and **Quasi-Steady State** (QSS) approximation.

Partial-Equilibrium Approximation (PEA)

This approach aims at reducing the stiffness that is associated with a fast reversible

reaction. The reaction rate of a reversible reaction i can be decomposed into a forward and a backward contribution

$$r_i = r_i^f - r_i^b \,. \tag{4.52}$$

If the reaction is much faster than other processes, the equilibrium of this reaction (partial equilibrium) is rapidly reached. The net rate of the reaction r_i vanishes

$$r_i \simeq 0 \,. \tag{4.53}$$

However, since it is the difference between the contribution of two stiff terms, it can lead to large numerical integration errors. To circumvent this stiffness, the PEA rather imposes directly the partial equilibrium

$$r_i = 0 \,, \tag{4.54}$$

This leads to the following constraint

$$\frac{r_i^b}{r_i^f} = 1 \; = \; \prod_{k=1}^{n_{spec}} c_k^{\nu_{ik}} = K_i^{eq} \tag{4.55}$$

on the species concentrations. This constraint can be satisfied in practice by introducing a small correction to the rate of the reaction so that Eq. 4.55 is satisfied at the end of the iteration. [127].

Quasi Steady State Approximation (QSSA)

A QSS species must remain in low concentration, with a net production rate that is low compared to its creation and destruction rates. The conservation equation for the k^{th} can be rewritten in terms of concentration c_k as

$$\frac{Dc_k}{Dt} = S_{diff,k} + \omega_{c_k}^+ - \omega_{c_k}^- \,, \tag{4.56}$$

where the net production rate ω_{c_k} is decomposed into a creation rate $\omega_{c_k}^+$ and a destruction rate $\omega_{c_k}^-$. $S_{diff,k}$ is the contribution of the diffusive flux. When considering elementary reactions, the destruction term is proportional to the concentration of the species, thus Eq. 4.56 can be rewritten as

$$\frac{Dc_k}{Dt} = S_{diff,k} + \omega_{c_k}^+ - \frac{c_k}{\tau_k} \,, \tag{4.57}$$

where τ_k is the chemical time-scale of the destruction rate. For QSS approximation to be suitable, the destruction process must be faster than other processes. Thus τ_k is an asymptotically small parameter

$$\tau_k = \epsilon \,, \text{ with } \epsilon \to 0 \,. \tag{4.58}$$

From an asymptotic analysis of Eq. 4.57, it can be shown that

$$c_k = O(\epsilon) = \epsilon\omega_{c_k}^{+} = \tau_k\omega_{c_k}^{+}\,, \tag{4.59}$$

which can also be written

$$\omega_{c_k} = \omega_{c_k}^{+} - \omega_{c_k}^{-} = 0\,. \tag{4.60}$$

Eq. 4.59 or equivalently Eq. 4.60 gives the expression of the QSS species concentration. This concentration is asymptotically small, and does not depend on transport phenomena. For simplicity, only linear coupling is allowed in the present work, so that the explicit expression can be automatically derived and integrated in the LES solver.

Several methods are available in the literature to select the appropriate QSS candidates [124, 126, 194]. The method retained in this work in the Level of Importance (LOI) technique [123, 124].

Level Of Importance (LOI) criterion

The steady state parameter of a species S is defined as

$$\Omega_S \quad [S]\tau_S\,, \tag{4.61}$$

where $[S]$ is the species concentration and τ_S is a measure of its chemical time scale. In the present case, it is expressed as

$$\tau_S = -\left[\frac{\partial\left(P_S - C_S\right)}{\partial[S]}\right]^{-1}\,, \tag{4.62}$$

where P_S and C_S are defined in Eq. 4.48 and Eq. 4.49f. Therefore in Eq. 4.61 a species is suitable for QSSA if it combines the property of remaining in a small concentration and to be highly reactive, as already highlighted by the asymptotic development.

Solving the system of QSS concentrations

Once QSS species are identified, a system must be resolved in terms of QSS species concentrations satisfying

$$\omega_k = 0\,, \tag{4.63}$$

for each QSS species k. This system can be resolved numerically, however this is too costly for LES computations. Rather, given that the chemical system contains elementary reactions, the QSS species source terms can be rewritten in the form of a linear system of the QSS species concentrations. In this purpose, it may require to remove reactions between QSS species causing higher order coupling terms: a reaction between two QSS species generally has a negligible rate because the concentrations of the QSS species involved in the reaction are both small. Once the linear system is obtained, it can be inverted analytically to end up with automatically generated expressions of the QSS concentrations.

4.5 Subgrid turbulence-chemistry interaction closure

The filtering operator introduced by the LES formalism leaves unclosed chemical source terms. These source terms occur at very small scales and are highly non-linear. Being quite sensitive to the unresolved scales of the turbulent motions, their closure is of critical importance in LES computations and is at the base of the development of numerous combustion models. The general approaches able to handle complex chemistry effects are categorised and described in the following.

4.5.1 PDF methods

In the PDF method, the fundamental idea is that the fluctuations lost by the filtering procedure can be described by introducing a probability density function $\mathcal{P}(\Phi)$ in the phase space, which describes the chemical state of the system: $\Phi = \left(Y_1, Y_2, ..., Y_{n_{spec}}, T\right)$ [163]. Given this PDF, the filtered source term can be reconstructed as

$$\widetilde{\omega} = \int \omega(\Phi)\mathcal{P}(\Phi)d\Phi\,. \tag{4.64}$$

This leaves the question of how the PDF is obtained.

4.5.1.1 Presumed PDF methods

The presumed PDF method is suitable when the chemistry is described by a few control variables, which is the case for tabulated chemistry. Typically, for premixed manifolds, the phase is reduced to $\Phi = (Z, c)$ and the source terms reads

$$\widetilde{\omega} = \int_c \int_Z \omega(\Phi)\mathcal{P}(Z', c')dZ'dc'. \tag{4.65}$$

A first common hypothesis is to assume a decorrelation between Z and c which leads to

$$\mathcal{P}(Z, c) = \mathcal{P}_1(Z)\mathcal{P}_2(c)\,. \tag{4.66}$$

Furthermore the shape of the PDF is **presumed**. From DNS analysis, β-PDF are generally found to be suitable. This type of PDF depends of only the first and second order statistics. For example, for the β-distribution of mixture fraction, it can be expressed based on the local statistical mean and variance as $\beta(\widetilde{Z}, Z^2)$. The statistical mean is obtained by the LES transport equation for $\widetilde{Z}$. The variance Z^2 can either be obtained by a direct closure using a gradient assumption [199] or by additional transport equations for the variances that includes subgrid production and dissipation [45, 114].

This type of approach has been extensively used combined with tabulated chemistry approach. It has several limitations:

- The actual statistical behaviours of scalars might strongly deviates from the presumed distribution, for example when Z is no longer a passive scalar such as in two-phase flow configurations [130].

- To take into account more effects (heat loss, radiation, slow chemistry, liquid fuels), additional control variables are included in the phase space [58, 61, 85], but their statistical behaviour and cross-correlations are generally not known and thus often neglected. .

- For Arrhenius-based chemistry the phase space is described by all the species mass fractions and the temperature, that are highly correlated, the shape of the statistical distribution is hard to assume and cannot be easily decomposed into canonical PDF functions. Thus presumed PDF approach are not applicable in this case.

4.5.1.2 Stochastic PDF methods

In the stochastic PDF approach, the PDF is no longer presumed. Instead, transport equations are solved for the coarse grain PDF arising from Boltzmann equation

$$\mathcal{P}(\Phi, \mathbf{x}, t) = \int \delta[\Phi - \Psi(x', t)] G(x' - x, \Delta) dx' \tag{4.67}$$

$$\frac{\partial \overline{\rho}\mathcal{P}}{\partial t} + \frac{\partial}{\partial x_j}\big[\overline{\rho}\mathcal{P}\widetilde{u}_j\big] = -\sum_{k=1}^{N_s} \frac{\partial}{\partial \Phi_k}\big[\frac{1}{\rho}\omega_k(\Phi)\overline{\rho}\mathcal{P}(\Phi)\big] - \frac{\partial}{\partial x_j}\big[\ u_j - \widetilde{u}_j \mid \Phi\ \overline{\rho}\mathcal{P}(\Phi)\big] + \sum_{k=1}^{n_{spec}} \frac{\partial}{\partial \Phi_k}\ \langle \frac{1}{\rho}\frac{\partial J_{ik}}{\partial x_i} \mid \Phi\ \overline{\rho}\mathcal{P}(\Phi) \tag{4.68}$$

Due to its high dimensionality, this PDF transport equation cannot be solved directly. Two approach are generally found in the literature to solves an approximation of this equation.

- In the Eulerian stochastic field method [94, 95, 195], the transport equation for the coarse grain PDF is approximated by transport equations for $N_{stoch} \simeq 10$ stochastic Eulerian fields. The filtered quantities are obtained by direct averaging of the stochastic fields. It has for example been applied to the LES of the Sandia Flame Series [94] and to a model gas turbine combustor [27] in combination with schemes comprising about 20 species.

- In the Lagrangian Monte Carlo approach [164], the phase space is described by fluid particles corresponding to a particular state Φ in the phase space. The fluid particles evolves in a Lagrangian framework. From the ensemble of particles, the

approximated PDF can be retrieved to compute the filtered source terms. Typically, 10 particles in each cells are needed to correctly reconstruct the associated PDF and evaluate the filtered source terms. This method was for example applied bye *Heye et al.* [80] for the simulation of ethanol spray flame.

Both methods yield excellent description of the subgrid scale interactions. They can handle multiple combustion regimes, autoignition phenomena [81] and two-phase flow combustion [80, 95]. Their main drawbacks are the complexity of their implementation and the associated cost: in the Eulerian method, the number of transport equations is $N_{sto} \times N_{phase}$ which can be tremendous for large chemistries; in the Lagrangian approach, the required number of particles is proportional to the grid resolution, which also drastically increases the computational cost.

4.5.1.3 Conditional Moment Closure

The CMC approach, [30, 99, 143] appears as an intermediate between the presumed PDF method and the full PDF method. Similarly to the PDF method, a coarse-grain PDF is introduced, only this time the phase space is represented by the mixture fraction η. It reads

$$\mathcal{P}(\eta, \mathbf{x}, t) = \int \delta[\eta - \zeta(\mathbf{x}', t)] G(x' - x, \Delta) dx' \,, \tag{4.69}$$

where ζ is the fine grain mixture fraction. Finally, the scalar describing the chemical system are conditioned on η as

$$Y_k(\eta, \mathbf{x}, t) = \frac{1}{\overline{\rho}\mathcal{P}(\eta)} \int \rho Y_k \delta[\eta - \zeta(\mathbf{x}', t)] G(\mathbf{x} - \mathbf{x}', \Delta) \mathbf{dx}' \,. \tag{4.70}$$

Conditional transport equations are solved for the conditioned scalars, and the unconditional scalars are recovered following

$$\widetilde{Y}_k(\mathbf{x}, t) = \int Y_k(\eta, \mathbf{x}, t) \mathcal{P}(\eta) d\eta \,. \tag{4.71}$$

For the conditional source terms $\omega_k(Y_k, T) \mid \eta \simeq \omega_k(\, Y_k \mid \eta \;,\; T \mid \eta \,)$, a first order closure is employed, assuming that the statistical fluctuations decorrelated from η are small. The probability distribution is obtained by a β-PDF reconstruction from mixture mean and sub-grid variance.

4.5.2 Artificially Thickened Flame model

4.5.2.1 The Thickened Flame model

The typical grid size Δx employed for LES are generally coarser than the premixed laminar flame thickness δ_l. The fundamental idea behind the Thickened Flame model

(TF) is to artificially broaden the flame front to allow it correct resolution on LES grids. Recalling the asymptotic analysis of Sec. 4.2.1 it can shown than the laminar flame speed and thickness scale as

$$S_l \quad \overline{\omega D}\,, \tag{4.72}$$

$$\delta_l \quad \overline{D/\omega}\,. \tag{4.73}$$

Therefore, if the following transformation is applied to the diffusivities and the source terms

$$D \rightarrow \mathcal{F} D\,, \tag{4.74}$$

$$\omega \rightarrow \frac{\omega}{\mathcal{F}}\,, \tag{4.75}$$

one obtains

$$S_l \rightarrow S_l\,, \tag{4.76}$$

$$\delta_l \rightarrow \mathcal{F}\delta_l\,, \tag{4.77}$$

The laminar flame speed is conserved and the flame front is thickened. This fundamental idea is at the basis of the thickened flame model. The thickening factor $\mathcal{F}$ is adjusted to obtain the needed grid resolution to correctly resolve the flame front. However, when the flame is thickened, it alters the interaction with turbulence. In particular, the flame wrinkling is reduced and the time scale ratio between turbulence and chemistry is modified. To compensate for these effects, an efficiency function $\mathcal{E}$ is also introduced

$$D \rightarrow \mathcal{E}\mathcal{F} D\,, \tag{4.78}$$

$$\omega \rightarrow \mathcal{E}\frac{\omega}{\mathcal{F}}\,, \tag{4.79}$$

which increases the flame speed without impacting the flame thickness:

$$S_l \rightarrow \mathcal{E} S_l \tag{4.80}$$

$$\delta_l \rightarrow \mathcal{F}\delta_l\,. \tag{4.81}$$

This function must compensate the reduction of the flame surface wrinkling. It is defined as the ratio between the unthickened flame of thickness δ_l and the thickened flame

$$\mathcal{E} = \frac{\Xi(\delta_l)}{\Xi(\mathcal{F}\delta_l)}\,. \tag{4.82}$$

The wrinkling factors involved in this expression is described by an efficiency function [34, 38]. In this work, two models are employed, the **Colin et al. efficiency function**

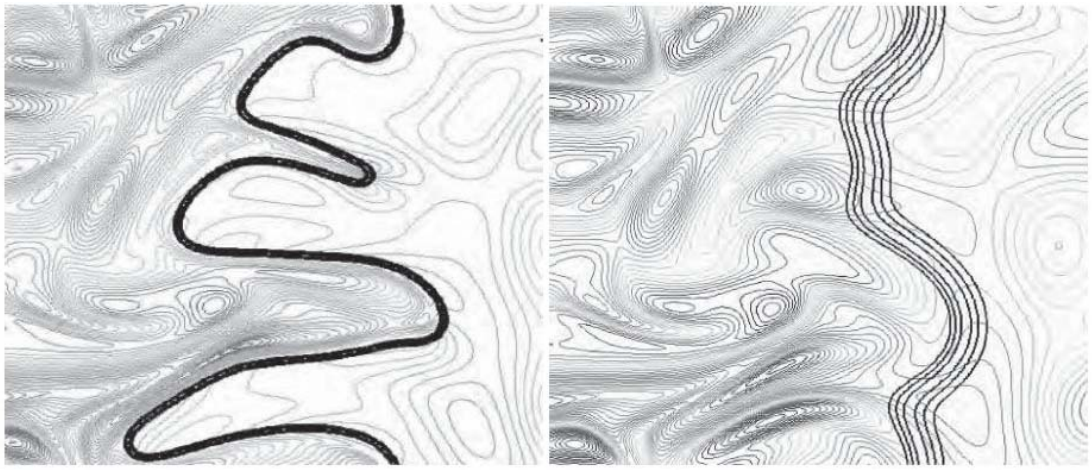

Figure 4.12: DNS of flame/vortex interactions. Left: non-thickened flame, right: thickened flame. [7, 38]

[38] and the **Charlette et al. efficiency function** [34]. They both rely on the assumption of equilibrium between turbulence and subgrid scale flame surface and the evaluation of velocity fluctuations at the filter scale u'_Δ estimated as [38].

$$u'_\Delta = c_2 \Delta_x^3 \left| \frac{\partial^2}{\partial x_j \partial x_j} \left(\epsilon_{lmn} \frac{\partial \widetilde{u}_n}{\partial x_m}, \right) \right| \tag{4.83}$$

This operator is based on the rotational of the velocity to remove the dilation contribution. The constant c_2 is estimated using homogeneous isotropic turbulence (HIT) simulations [7]. where $c_2 \simeq 2$ and ϵ_{lmn} is the permutation tensor.

- In **Colin et al. model** [38] the wrinkling factor is expressed as

$$\Xi(\delta_l) = 1 + \alpha(Re_t)\Gamma\left(\frac{\Delta_e}{\delta_l}, \frac{u'_\Delta}{S_l}\right)\frac{u'_\Delta}{S_l} \tag{4.84}$$

  where α is a function depending on the turbulent Reynolds number Re_t, Δ_e is the effective filter size and Γ is a function taking into account the subgrid strain rate depending on subgrid velocity fluctuations and the filter size.

- In **Charlette et al. model** [34], a power-law wrinkling model extends the formulation of Colin of Eq. 4.84. The expression of the wrinkling factor reads

$$\Xi(\delta_l) = \left(1 + \min\left[\frac{\Delta_e}{\delta_l}, \Gamma\left(\frac{\Delta_e}{\delta_l}, \frac{u'_\Delta}{S_l}, Re_{\Delta_e}\right)\frac{u'_\Delta}{S_l}\right]\right)^\beta \tag{4.85}$$

  where $\beta \simeq 0.5$ is the model parameter. Contrarily to the Colin model, no global quantity such as the integral length scale is needed because the Reynolds number Re_{Δ_e} employed is based on the filter scale Δ_e rather than on the integral scale.

4.5.2.2 The dynamic thickened flame model (DTFLES)

The TFLES model was initially developed for perfectly premixed flames. For partially premixed situations, applying a uniforming thickening would damp scalar fluctuations in non-reacting mixing regions because of the artificially increased diffusion. Therefore a dynamic procedure is employed [112] (DTFLES). A sensor is employed to trigger the TFLES correction only in the flame region. The local thickening applied is expressed as

$$\mathcal{F} = 1 + (\mathcal{F}_{max} - 1)\mathcal{S} \tag{4.86}$$

where $\mathcal{S}$ is the local sensor and $\mathcal{F}_{max}$ is the maximum thickening which is determined locally by comparing the grid resolution and the laminar flame thickness

$$\mathcal{F}_{max} = N_c \frac{\Delta_x}{\delta_l} \,. \tag{4.87}$$

The control parameter N_c is roughly the number of cells used to the resolve the flame front. For global reduced mechanism, $N_c \simeq 5$ in most situations and the sensor $\mathcal{S}$ is generally based on the fuel reaction, by introducing an Arrhenius-like expression

$$\Omega = Y_F^{n_F} Y_O^{n_O} \exp\left(-\Gamma \frac{E_a}{RT}\right) \,, \tag{4.88}$$

which is evaluated locally and compared to the value Ω_0 obtained from a 1D premixed flame calculation. The final expression for the sensor reads

$$\mathcal{S} = \tanh\left(\beta' \frac{\Omega}{\Omega_0}\right) \,. \tag{4.89}$$

with $\beta' \simeq 50$. The quantity Ω has the form of a reaction rate, and the parameter $\Gamma = 0.5$ allows to trigger the sensor at lower temperature than the actual reaction in the scheme. This is done to better capture the low temperature region of the flame.
An alternative approach to build the sensor $\mathcal{S}$ will be highlighted in Sec. 6.4, because the present one suffers some limitations, and is not directly applicable to ARC mechanisms.

4.5.3 Combustion modelling in the present work

The DTFLES model is retained for the present work because it can applied combined with several chemical descriptions (tabulated, global, and analytically reduced chemistry), and is capable of handling multiphase flow combustion [146], which is a critical point for the target aeronautical applications. Moreover its simplicity makes it applicable and robust for industrial configuration applications [14, 51, 136, 208].

Part II

Strategies for pollutant prediction with Large Eddy Simulation

5

A hybrid model for NO_x prediction: the NOMAGT model

Contents

5.1 Objectives

In this part, two approaches for pollutant prediction are constructed and validated. The ARC/TFLES, which is central in this thesis, is based on the derivation of ARC including pollutant chemistry, that are further combined with the thickened flame model. The approach will be introduced in Chapter 6 and validated in Chapter 7.

An alternative approach is detailed in the present chapter. It is based on the NOMANI model [148], which is a tabulated chemistry model for NO_x prediction initially developed by *Pecquery* [147] in the context of the PCM/FPI model. The novelty of this chapter is to extend this model to the TFLES formalism with Globally Reduced Chemistry (GRC), leading to the **NOMAGT** model (**NOMA**NI/**G**RC/**T**FLES). The main advantage of this approach is that the NO_x model can be rapidly applied a posteriori, starting from a solution of a stabilised LES computation with GRC, thus leading to a moderate overcost. Since GRC combined with TFLES is the current standard for industrial applications performed with AVBP, this approach has a strong industrial

interest: the NO_x model can be employed only at the end of the LES computation chain, thus leading to a rapid evaluation of NO_x levels with very moderate additional computational cost.

The chapter is organised as follows:

- Firstly, the necessity to adapt tabulated models to correctly handle the slow and fast processes of NO_x chemistry is illustrated (Sec. 5.2).
- Then the tabulated NOMANI model that is retained is introduced (Sec. 5.3). Its limitations are discussed and compared with other models from the literature. In particular, a comparison is performed with the NORA model [198], which is based on similar concepts for the burnt gas NO_x chemistry.
- Finally, the model is extended to the GRC/TFLES context leading to the NOMAGT model, and validated on laminar cases (Sec. 5.4).

5.2 Chemistry tabulation for pollutant prediction

In the classical FPI/FGM approaches (Sec. 4.4.2), the progress variable c is used to describe the phase space trajectory of the chemical system through the flame. However, the inclusion of NO_x chemistry introduces slower time scales, that are not correctly captured with a unique progress variable built to describe only the fast fuel oxidation reaction zone.

The disparity of scales between the fuel oxidation chemistry and the NO_x chemistry is illustrated in Fig 5.2 for a one-dimensional methane-air premixed flame. The peak of CH_4 consumption is located in the flame front and rapidly vanishes downstream (Fig. 5.1(a)). Because of the interaction with the fuel oxidation chemistry, there is also a NO formation peak inside the flame. However the production of NO continues in the burnt gases with smaller intensity, and only vanishes once the chemical equilibrium has been reached. Given that the NO formation is slow, this equilibrium is reached much further downstream, after more than 10 ms of residence time in burnt gases, compared to the $\simeq 0.1$ ms spent in the flame front. When looking at CH_4 and NO source terms in the progress variable space (Fig. 5.1(b)), it can be seen that the progress variable c cannot correctly describe the post-flame region where the NO source term continues to evolve whereas the progress variable is almost constant at $c \simeq 1$. To circumvent this issue, *Godel et al.* [71] and *van Oijen and de Goey* [196] proposed to include nitrogen containing species such as NO and NO_2 in the definition of the progress variable.

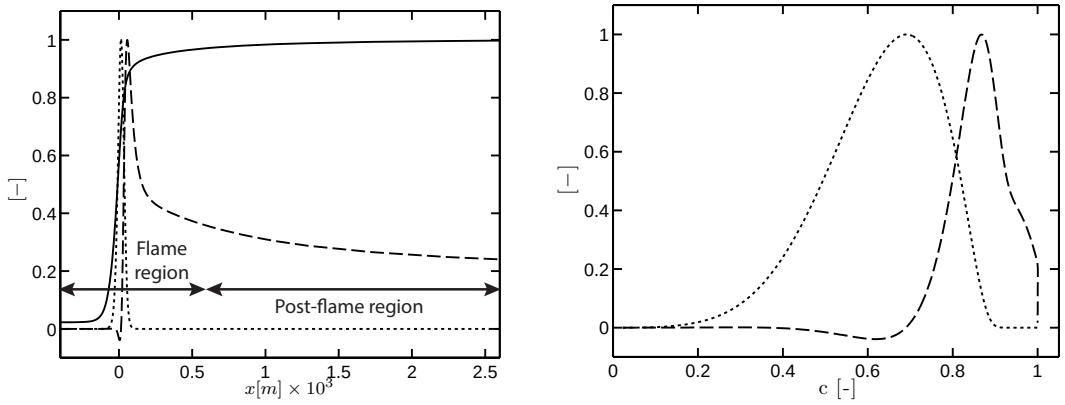

(a) Profiles vs the axial coordinate x.

(b) Profiles vs the progress variable c.

Figure 5.1: One-dimensional methane-air premixed flame at $\phi = 1.0$ ($T = 680\,\mathrm{K}$ and $P = 3\,\mathrm{bars}$ - SGT-100 conditions). Profiles of progress variable (—) (for a) only), NO source term ($--$) and CH_4 consumption term ($\cdots$) vs a) axial coordinate and b) progress variable. Quantities are normalised by their maximum value.

However the construction of the progress variable is not straightforward and is complexified by the strong disparity in terms of mass fractions between NO_x species and major species. In this work, we retain the alternative approach proposed by *Pecquery et al.* [147, 148], which consists in the introduction of an additional progress variable specifically defined to describe the NO_x chemistry. This definition relies on the existence of a low-dimensional manifold for the evolution of NO_x in burnt gas chemical phase space. This model, called NOMANI (Nitrogen Oxide emission model with one-dimensional MANIfold) is detailed in the next section and compared with other approaches available in the literature.

5.3 The NOMANI model

5.3.1 Model description

The NOMANI model was initially developed by *Pecquery et al.* [148] in the context of the PCM-FPI turbulent combustion model [45], to correctly account for NO_x formation in burnt gases. A conventional tabulated model is used to describe the fuel oxidation, as already described in Sec. 4.4.2. The chemical state of the system is described by a mixture fraction variable Z and a progress variable c which must be monotonic through the flame front. The choice retained in this work is based on a combination of species mass fractions,

$$Y_c = Y_{CO} + Y_{CO_2} + Y_{H_2O}\,. \tag{5.1}$$

Then, the normalised progress variable is defined as

$$c = Y_c / Y_c^{eq} , \tag{5.2}$$

where the subscript $_{eq}$ denotes the equilibrium state. Based on a series of laminar premixed flames at various equivalence ratios, the source term of the progress variable is tabulated as a function of these two control parameters

$$\omega_{Y_c} = \omega_{Y_c} (Z, c) \ . \tag{5.3}$$

This formulation corresponds to the original FPI model [70].

To compute NO_x production that is a slow process, two additional transport equations for the concentrations of NO and NO_2 are solved. Indeed, and as shown in Sec. 5.2, a direct extraction of the concentrations from the table would not be accurate [201] as NO and NO_2 concentrations do not depend solely on the local chemical state but also on history effects (e.g. residence time) occurring in the burnt gases via scalar transport. The originality of NOMANI is to construct the source terms for these two additional transport equations from the same series of laminar premixed flame, but with a post-flame progress variable. A study from *Nafe and Maas* [141] revealed that NO evolves along a low-dimensional manifold in the burnt gases. This study was extended by *Pecquery et al.*, who showed that under certain conditions, the NO_x chemical trajectories in burnt gases rapidly converge to evolve along a single trajectory that can be parametrised with the NO mass fraction Y_{NO}, used therefore as an additional progress variable. The evolution of the NO source term as a function of the flame progress variable c and the NO mass fraction Y_{NO} are shown in Fig. 5.2(a) and Fig. 5.2(b) respectively, for a stoichiometric methane-air flame. From these profiles, it can be deduced that i) the evolution of the NO source term is appropriately parametrised by the NO mass fraction Y_{NO} in the post-flame region (Fig. 5.2(b)) and ii) the NO source term in the flame region is best described by the flame progress variable c (Fig. 5.2(a)). This figure also clearly illustrates the separation of scales between the flame and the post-flame regions.

Therefore a combination of both progress variables (i.e. c and Y_{NO}) is needed to correctly describe the NO in the whole domain. The same findings hold for NO_2 [147]. It leads to a double tabulation of NO_x species source terms, which is the specificity of the NOMANI model:

- In the flame region, the NO_x source terms are described by the progress variable c, and are appropriately retrieved from the look-up table based on Z and c:

$$\omega_{NO} = \omega_{NO} (Z, c) \ , \tag{5.4}$$

$$\omega_{NO_2} = \omega_{NO_2} (Z, c) \ . \tag{5.5}$$

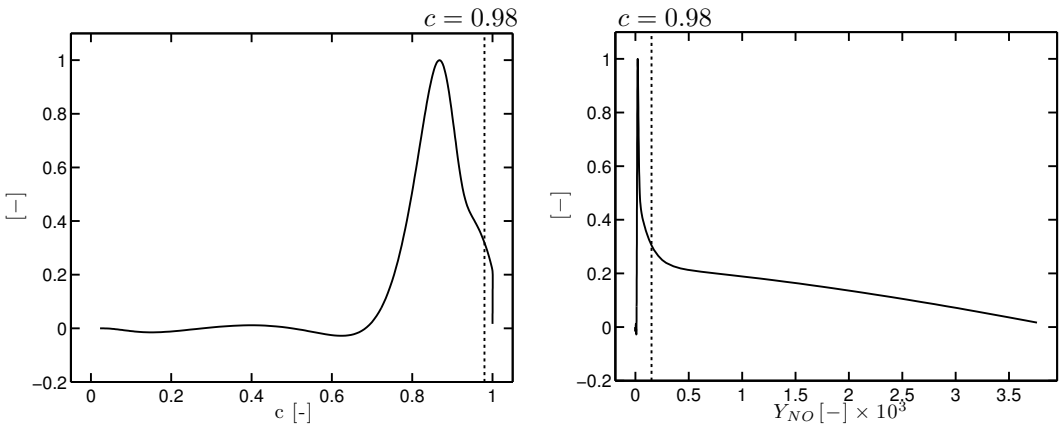

(a) NO source term vs c.

(b) NO source term vs Y_{NO}.

Figure 5.2: One-dimensional premixed methane-air flame at $\phi = 1.0$ ($T = 680\,\mathrm{K}$ and $P = 3\,\mathrm{bars}$ - SGT-100 conditions). NO source term vs a) progress variable c and b) NO mass fraction Y_{NO}. Quantities are normalised by their extrema. The vertical line corresponds to $c = 0.98$.

- In the post-flame region, Y_{NO} is used instead of c and the source terms are extracted from the look-up table based on Z and Y_{NO} as

$$\omega_{\mathrm{NO}} = \omega_{\mathrm{NO}}\left(Z, c_{\mathrm{NO}}\right) , \tag{5.6}$$

$$\omega_{\mathrm{NO_2}} = \omega_{\mathrm{NO_2}}\left(Z, c_{\mathrm{NO}}\right) , \tag{5.7}$$

  defining the normalised NO mass fraction $c_{\mathrm{NO}} = Y_{\mathrm{NO}}/Y_{\mathrm{NO}}^{eq}$ as a progress variable evolving from 0 to 1 when NO equilibrium concentration is reached.

- The switch from c to c_{NO} is based on a threshold value $c = c_{switch}$. This value must be carefully chosen to fall in the transition region between flame and post-flame $\mathrm{NO_x}$ chemical processes. A switch value too low would cause the NO source term to be poorly captured in the flame region. Conversely, a switch value too close to unity would lead to an incorrect description of the low-dimensional $\mathrm{NO_x}$ chemical processes in burnt gases. Following *Pecquery* [147], the value $c_{switch} = 0.98$ is retained in the present work. The pertinence of this choice is illustrated in Fig. 5.2: this value falls in a region where both progress variables are suitable, and thus allows a smooth transition between the two regimes. Eventually, the final expressions of NO and $\mathrm{NO_2}$ source terms read

$$\omega_{\mathrm{NO}} = \mathbf{1}_{c<0.98}\,\omega_{\mathrm{NO}}\left(Z, c\right) + \mathbf{1}_{c\ \ 0.98}\,\omega_{\mathrm{NO}}\left(Z, c_{\mathrm{NO}}\right) , \tag{5.8}$$

$$\omega_{\mathrm{NO_2}} = \mathbf{1}_{c<0.98}\,\omega_{\mathrm{NO_2}}\left(Z, c\right) + \mathbf{1}_{c\ \ 0.98}\,\omega_{\mathrm{NO_2}}\left(Z, c_{\mathrm{NO}}\right) . \tag{5.9}$$

where $\mathbf{1}_X$ is the indicator function. This source term modelling is retained in the present work and will be combined with TFLES and GRC, as will be detailed in Sec. 5.4.

5.3.2 Discussion of model validity and assumptions

Apart from classical modelling assumptions associated to tabulated chemistry, the NOMANI model might suffer some limitations due to underlying assumptions.

In the flame region, Eq. 5.4 assumes that the NO_x formation rate is independent of the NO_x concentrations, which is valid only if NO_x concentrations in the flame front remain close to the values obtained in the one-dimensional laminar cases. However, in three-dimensional cases, history effects due to transport can lead to NO_x concentrations significantly different from the one-dimensional cases in the flame region. This typically occurs when hot gases with high NO_x concentrations are recirculated towards the flame region. A dependency of the NO_x source terms to NO_x concentrations can be considered to take this effect into account. This approach is retained for example in [85, 98]. In the work of *Ihme and Pitsch* [85], a linear dependency to Y_{NO} is assumed, by decomposing the NO source term into a production and destruction term as

$$\omega_{NO}(Z, c, Y_{NO}) \simeq \omega^{+}_{NO}(Z, c) - \omega^{-}_{NO}(Z, c) \times Y_{NO}\,, \tag{5.10}$$

In the work of *Zoller et al.* [213], it is argued that the linearisation can lead to strong misprediction of NO formation. To better capture the dependency, a new methodology is introduced:

- Firstly, a flamelet library is computed, and a conventional look-up table is constructed for carbon chemistry.
- Secondly, each point of the library table is treated as a perfectly-stirred reactor (PSR), where nitrogen related species are set to zero (except N_2) and carbon chemistry is frozen. The NO source term is extracted from the temporal evolution of the PSR towards equilibrium. However the NO equilibrium value obtained with the PSR differs from the one obtained with the flamelets. Therefore it can only be used for low to moderate NO concentrations.

In the post-flame region, the description of NO_x trajectories by a single progress variable based on the NO mass fraction relies on some assumptions regarding the ratio of flow to chemical time scales. Following [148], the linearisation of the chemical system yields the following dynamic system

$$\frac{\partial \Psi}{\partial t} = J\Psi\,, \tag{5.11}$$

where J is the chemical Jacobian and Ψ is the perturbation of the chemical system. The eigenvalues λ_i of J yield the characteristic time scales sorted in decreasing order $\mathcal{T} = (\tau_1 = -1/\lambda_1 > \tau_2 = -1/\lambda_2 > ... > \tau_N = -1/\lambda_N)$. The analysis showed that NO_x

chemistry is the slower process in burnt gases, and is controlled by the first eigenvector and associated time scale τ_1. For the one-dimensional manifold assumption to be valid, this time scale must be much slower than the others, which imposes the condition $\tau_1 >> \tau_2$. In real three-dimensional cases, perturbations of the chemical system by external forcing, typically dilution by fresh gases or unmixedness introduce a new characteristic time scale τ_{pertub}. For the one dimensional manifold assumption to remain valid, all chemical processes other than NO_x chemistry must remain faster than this forcing, thus imposing the condition $\tau_2 < \tau_{perturb}$. It is however not clear whether this condition is always verified in complex and intense turbulent flows.

Non-adiabaticity

Heat losses and radiative transfers are not considered in the present model. However enthalpy losses can be taken into account in tabulated chemistries [58, 198]. Radiative heat losses have been included by *Ihme and Pitsch* [85] and *Zoller et al.* [213] for NO_x tabulated models. In the present case, it could be modelled by considering an enthalpy defect ΔH as an additional control variable for the calculation of the premixed flamelet series.

5.3.3 Similarities with the NORA model

The NORA model [198] was successfully applied to internal combustion engine configurations for a large range of pressures in combination with the 3-Zones Extended Coherent Flame Model [37]. An extension including NO_2 formation was also derived in [100].

In this model, NO_x formation is accounted for through a relaxation to equilibrium approach, using a collection of PSRs, which makes the construction of the table simpler. This approach accounts for NO formation in burnt gases, where it is mostly produced through the thermal pathway. It does not account for the rapid NO formation in the flame region, mainly controlled by the prompt NO pathway. This last contribution generally represents only 20% to 50% of the overall NO production, depending on the combustion regime and operating conditions. Therefore the NORA model is sufficient to give a first evaluation of NO emission levels. The methodology detailed in [198] is the following:

- In a first step, the reactor is set to equilibrium at a given mixture fraction Z.
- In a second step, the NO mass fraction is perturbed by an amount $\Delta Y_{\mathrm{NO}} = Y_{\mathrm{NO}} - Y_{\mathrm{NO}}^{eq}$, while keeping the atomic and enthalpy budgets constant.

- The PSR is then integrated in time. NO returns to equilibrium. It allows to extract a characteristic relaxation time τ and to finally express the NO source term in a quasi-linear form as follows

$$\omega_{Y_{\mathrm{NO}}} = \frac{Y_{\mathrm{NO}}^{eq}(Z) - Y_{\mathrm{NO}}}{\tau} \,. \tag{5.12}$$

The relaxation time $\tau = \tau\,(Z, \mid \Delta Y_{\mathrm{NO}} \mid)$ is parametrised by the mixture fraction Z and the amplitude of the initial perturbation $\mid \Delta Y_{\mathrm{NO}} \mid$. The dependency in ΔY_{NO} allows to correctly reproduce the deviation from non-linear behaviour when NO concentration is far from equilibrium. An enthalpy defect ΔH can also be easily introduced [198] to take non-adiabaticity into account.

The NORA model is very similar to the burnt gas part of the NOMANI model. The main difference is that the NO source term is extracted from a PSR instead of a premixed flame. As mentioned earlier, NO_x chemistry essentially evolves on a one-dimensional manifold in the burnt gases [141, 148], so the two methods are expected to yield similar source terms in this region. This is confirmed by a comparison of both methodologies, illustrated in Fig. 5.3. For given initial conditions ($\phi = 1.0$, $T = 680\,\mathrm{K}$ and $P = 3\,\mathrm{bars}$ - SGT-100/Case A), the NO and NO_2 source terms obtained from one-dimensional flame computations for the NOMANI model is compared to the NORA methodology based on PSRs. It can be seen that both NO (Fig. 5.3(a)) and NO_2 (Fig. 5.3(b)) source terms from the NOMANI methodology rapidly converge towards the chemical trajectory of the NORA case in Y_{NO} space, confirming the existence of the low-dimensional manifold in burnt gases. Note also the strong differences in the flame zone, as NORA does not model the fast NO_x chemistry in the flame front. The NORA approach has the advantage to cover a large range of NO_x concentrations, whereas NOMANI is limited to values below equilibrium as found in premixed flames. In addition, the formulation of Eq. 5.12 is less demanding in terms of memory, because the parameter τ only varies slightly with the mass fraction ΔY_{NO}. This allows to include additional control parameters, such as pressure P or enthalpy defect ΔH, both needed for internal combustion engines.

On the other side, the NOMANI model has the ability to capture the fast NO_x formation in flame region, which can contribute up to 75% of the total NO production for lean ultra-low NO_x combustors [18, 111]. This justifies the preferred use of NOMANI in this work.

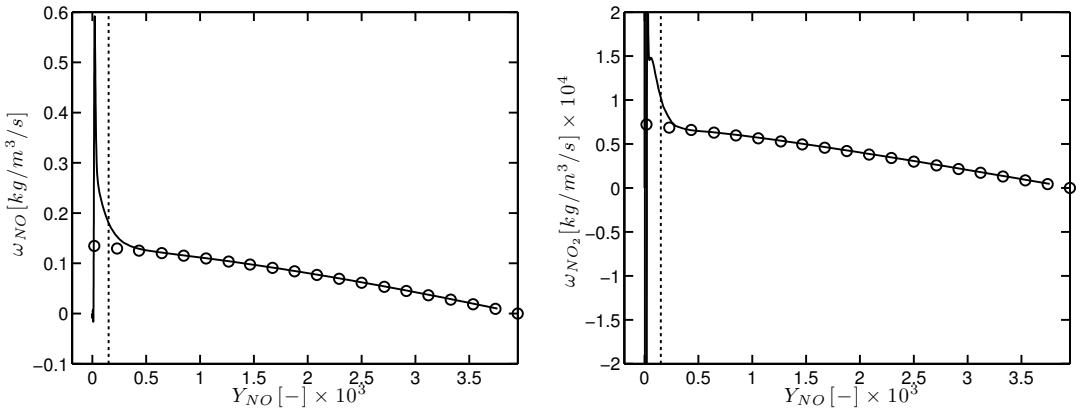

(a) NO source term.

(b) NO_2 source term.

Figure 5.3: a) NO **source term and b)** NO_2 **source term vs** NO **mass fraction. Comparison between the NOMANI methodology based on premixed flames (—) and the NORA methodology based on PSRs (○), for a methane-air mixture at** $\phi = 1.0$ **(**$T = 680\,\mathrm{K}$ **and** $P = 3\,\mathrm{bars}$ **- SGT-100 Case A conditions). The vertical line corresponds to** $c = 0.98$**.**

5.4 Extension of the NOMANI model to thickened flame model with globally reduced chemistry: the NOMAGT model

To describe flame-turbulence interaction, the current state of the art for LES of industrial configurations with AVBP is to employ global reduced mechanism with TFLES model. Thus, coupling NOMANI with this methodology allows an efficient and practical way to estimate NO_x *a posteriori*, from simulations performed with the standard methodology, which has proven to be efficient to capture flame structure and dynamics. The NOMANI model previously introduced was initially developed in the context of tabulated chemistry (FPI, Sec. 4.4.2) with a presumed-PDF approach (PCM, Sec. 4.5.1.1). This section therefore focuses on the adaptation of the NOMANI model to the GRC/DTFLES approach.

5.4.1 NOMANI with Globally Reduced Chemistry

Globally Reduced Chemistry does not include NO_x chemistry or usual variables of tabulated models. Thus, following *Lecocq* [109], a hybrid approach is used: the flame is directly calculated with the GRC, while the NO_x chemistry is obtained via the tabulated model previously introduced. This implies to define adequate mixture fraction Z and progress variable c, that are consistent with both the GRC and the look-up table. To do this, the methodology employed in the present work is based on the findings of

Lecocq [109] and is detailed in the following.

Mixture fraction

For the applications considered in this work, GRC is typically based on a 2-step chemistry [64], which includes the fuel, O_2 N_2, CO, CO_2 and H_2O species (see Appendix. A). For the sake of simplicity, methane is considered in the following, but other fuels can be handled in a similar manner. The mixture fraction can be easily reconstructed from these species, similarly to Eq. 4.27. Since there are generally no differential diffusion effects in GRCs, the mixture fraction calculation is simply based on the carbon atom conservation. The mixture fraction can be expressed as

$$Z = W_{\mathrm{CH_4}} \times \left(Y_{\mathrm{CH_4}}/W_{\mathrm{CH_4}} + Y_{\mathrm{CO}}/W_{\mathrm{CO}} + Y_{\mathrm{CO_2}}/W_{\mathrm{CO_2}} \right) , \tag{5.13}$$

so that it is equal to 0 in pure oxidiser and to 1 in pure methane.

NO progress variable c_{NO}

Once the mixture fraction Z is known, the NO progress variable can be directly estimated as $c_{\mathrm{NO}} = Y_{\mathrm{NO}}/Y^{eq}_{\mathrm{NO}}(Z)$, where Y_{NO} is obtained via the transport equation and $Y^{eq}_{\mathrm{NO}}(Z)$ is extracted from the look-up table.

Fuel oxidation progress variable c_{2s}

Consistently with the progress variable chosen to represent trajectories in the tabulated chemistry, a progress variable c_{2s} based on the species mass fractions from the GRC can be computed:

$$c_{2s} = \left(Y_{\mathrm{CO}} + Y_{\mathrm{CO_2}} + Y_{\mathrm{H_2O}} \right) / \left(Y^{eq}_{\mathrm{CO}}(Z) + Y^{eq}_{\mathrm{CO_2}}(Z) + Y^{eq}_{\mathrm{H_2O}}(Z) \right) . \tag{5.14}$$

In this expression, Y_{CO}, $Y_{\mathrm{CO_2}}$ and $Y_{\mathrm{H_2O}}$ are the mass fractions of the transported species from the GRC, whereas the equilibrium values (superscript ^{eq}) are extracted from the look-up table. However, as pointed out by *Lecocq* [109], the profile of c_{2s} strongly differs from the progress variable profile obtained with the tabulated chemistry, which is built on detailed kinetics. This is exemplified in Fig. 5.4. The profile from GRC is much steeper compared to the detailed GRI 2.11 mechanism. In particular, the post-flame zone is much shorter. Thus using c_{2s} to enter in the NO_x look-up table would lead to a strong misprediction of NO production. In particular the switch to the post-flame source term table at $c_{switch} = 0.98$ would occur too quickly. This issue has already been encountered by *Lecocq et al.* [109] for soot modelling. To circumvent it, and similarly to the FPI model, a progress variable c^* is introduced, solution of a transport equation

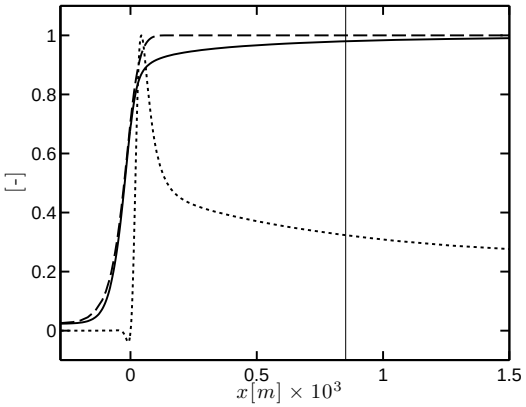

Figure 5.4: One-dimensional methane-air premixed flame at $\phi = 1.0$ ($T = 680\,\mathrm{K}$ and $P = 3\,\mathrm{bars}$ - SGT-100/Case A conditions). Profiles of progress variable from detailed chemistry (—), two-step GRC c_{2s} (−−) and normalised $\mathrm{NO_x}$ source term from detailed chemistry ($\cdots$). The vertical line corresponds corresponds to the switch value $c^* = 0.98$.

for $Y_{c^*} = c^* \times Y_{c^*}^{eq}$, controlled by the source term obtained from the tabulated detailed chemistry as

$$\omega_{Y_{c^*}} = \omega_{Y_c}(c*, Z)\,. \tag{5.15}$$

By construction, c^* is fully consistent with tabulated chemistry. To ensure that c^* is also consistent with the globally reduced chemistry in the flame zone, the source term in this zone is replaced by a relaxation towards c_{2s}

$$\omega_{Y_c^*} = \frac{Y_{c,2s} - Y_c^*}{\tau_{relax}} \text{ when } c_{2s} < c_{relax}\,, \tag{5.16}$$

where τ_{relax} is the relaxation time and c_{relax} is the threshold value to delimit the region where the relaxation is imposed. In practice the relaxation time is chosen of the order of ten time steps $\tau_{relax} \simeq 10\Delta t$ and a typical value for c_{relax} is $c_{relax} \simeq 0.5$. The impact of this parameter is discussed in Sec. 5.4.4. This strong relaxation allows to recover

$$c^* = c_{2s} \text{ when } c_{2s} < c_{relax}\,, \tag{5.17}$$

thus ensuring that the progress variable c^* describe the GRC flame zone and the tabulated post-flame zone.

5.4.2 NOMANI with the DTFLES formalism

The TFLES approach is applied to Y_c^*, NO and $\mathrm{NO_2}$ in the same way as for other species, as presented in Sec. 4.5.2.2. Diffusivities are multiplied by the local efficiency $\mathcal{E}$ and the thickening factor $\mathcal{F}$, while the source terms extracted from the table are corrected by $\dfrac{\mathcal{E}}{\mathcal{F}}$. The final model expressions read:

- **Mixture fraction** - direct reconstruction from species mass fractions:

$$Z = W_{\mathrm{CH_4}} \times \left(Y_{\mathrm{CH_4}}/W_{\mathrm{CH_4}} + Y_{\mathrm{CO}}/W_{\mathrm{CO}} + Y_{\mathrm{CO_2}}/W_{\mathrm{CO_2}} \right) , \tag{5.18}$$

- **Progress variable** - transport equation with tabulated source term:

$$\omega_{Y_{c^*}} = \frac{\mathcal{E}}{\mathcal{F}} \left[\mathbf{1}_{c_{2s}<c_{relax}} \frac{Y_{c,2s} - Y_{c^*}}{\tau_{relax}} + \mathbf{1}_{c_{2s}\geq c_{relax}} \omega_{Y_c}(c^*, Z) \right] \tag{5.19}$$

  where $c_{relax} = 0.5$ and $\tau_{relax} = 10\Delta t$.

- NO **and** NO_2 - transport equation with tabulated source terms:

$$\omega_{\mathrm{NO}} = \frac{\mathcal{E}}{\mathcal{F}} \left[\mathbf{1}_{c^*<0.98}\, \omega_{\mathrm{NO}}\left(Z, c^*\right) + \mathbf{1}_{c^*\geq 0.98}\, \omega_{\mathrm{NO}}\left(Z, c_{\mathrm{NO}}\right) \right] , \tag{5.20}$$

$$\omega_{\mathrm{NO_2}} = \frac{\mathcal{E}}{\mathcal{F}} \left[\mathbf{1}_{c^*<0.98}\, \omega_{\mathrm{NO_2}}\left(Z, c^*\right) + \mathbf{1}_{c^*\geq 0.98}\, \omega_{\mathrm{NO_2}}\left(Z, c_{\mathrm{NO}}\right) \right] . \tag{5.21}$$

It should also be noted that a simplified transport assumption is made for Y_{c^*}, NO and NO_2. Their Schmidt number is taken equal to the Schmidt number of the species from the reduced mechanism which are all equal ($Sc = 0.7$).

5.4.3 Validation of the model on one-dimensional premixed flames

The goal of this subsection is to validate the NOMAGT model. Laminar premixed flame computations using Cantera [74] with the detailed GRI 2.11 mechanism are used as a reference to compare with the NOMAGT model implemented in AVBP.

Numerical setup for NOMAGT in AVBP

Simulations are conducted on a one-dimensional domain, with a grid size $\Delta x = 0.55\,\mathrm{mm}$ which is representative of the grid resolution in the target application (SGT-100). The TTGC numerical scheme is employed. The TFLES model is employed in its dynamic formulation. The maximum thickening factor is determined according to Eq. 4.87. Note that the dynamic thickening is used, thus $\mathcal{F} = 1$ for the slow evolution of the post-flame region. The 2S_CH4_BFER GRC detailed in Appendix. A is employed to describe the methane-air oxidation.

To allow an easy comparison of the thickened flame in AVBP with the Cantera flame, a transformation is applied to the spatial coordinate $\mathbf{x}$ as follows:

$$\mathbf{x}^* = \int \frac{\mathbf{dx}}{\mathcal{F}(\mathbf{x})} . \tag{5.22}$$

Whereas the thickened flame in AVBP is thicker than the Cantera flame in $\mathbf{x}$-space, they are expected to have the same structure in $\mathbf{x}^*$-space.

The comparison is performed for three representative equivalence ratios $\phi = 0.6, 1.0$ and 1.4 in the SGT-100/Case A conditions ($T = 680\,K$, $P = 3\,\text{bars}$). A difficulty remains in the optimal choice of c_{relax}:

- A too low value may lead to a mismatch with the GRC flame zone.
- A too high value would increase the deviation from detailed chemistry due to the steeper behaviour of c_{2s} in the post-flame zone.

A switch value $c_{relax} = 0.5$ is retained here. The influence of this parameter is discussed later in Sec. 5.4.4.

Stoichiometric case

The comparison at stoichiometric conditions $\phi = 1.0$ is shown in Fig. 5.5 and Fig. 5.6. Note that source terms, mass fractions and thickening factor are normalised by their maximum value obtained with NOMAGT. The location of the symbols corresponds to the position of the grid points. As shown in Fig. 5.5, the shape of the progress variable c^* in AVBP, using $c_{relax} = 0.5$ is fully consistent with the detailed chemistry. In particular, the slower evolution at the end of the flame and in the post-flame region ($c^* > 0.9$) is well-captured. Contrastingly, it can be seen that the progress variable from the GRC c_{2s} is much steeper in that region. The comparison of the NO mass

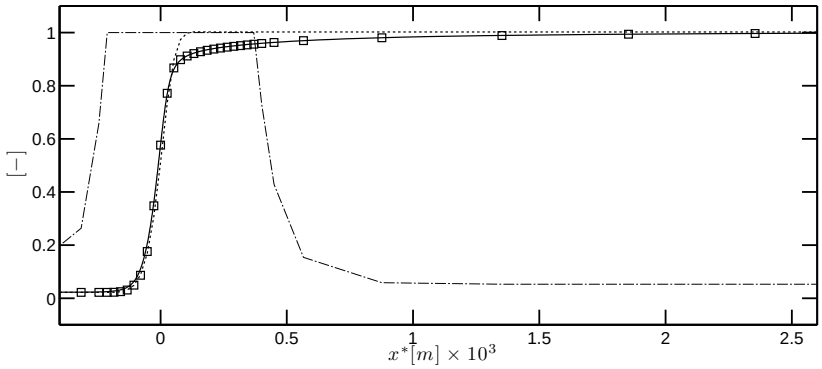

Figure 5.5: Comparison of the NOMAGT model with detailed chemistry on a one-dimensional methane-air premixed flame at $\phi = 1.0$: normalised profiles of thickening factor ($-\cdot-$), progress variable c_{2s} ($\cdots$), progress variable c^* ($\square$) and progress variable obtained with Cantera (—).

fraction and source terms in Fig. 5.6 shows that the NO formation in the flame region is correctly reproduced. In the post-flame region, the smooth evolutions of NO mass fraction and source term are correctly reproduced as well. Note the smooth transition at $c^* = 0.98$ with no spurious behaviour observed when the switch from c^* to c_{NO} to extract the NO_x source terms occurs.

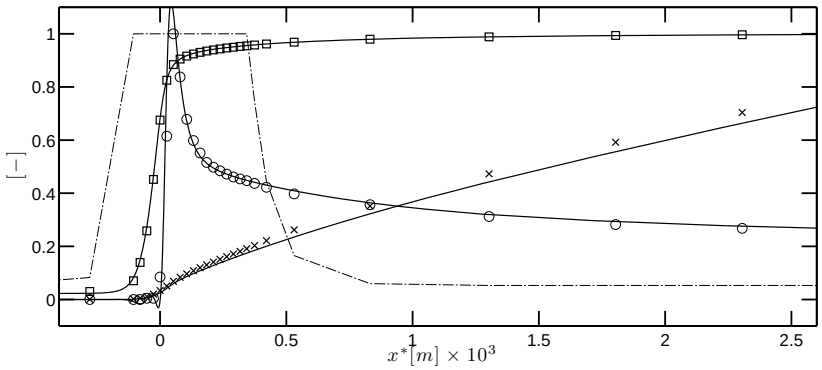

Figure 5.6: Comparison of the NOMAGT model with detailed chemistry on a one-dimensional methane-air premixed flame at $\phi = 1.0$: normalised profiles of thickening factor ($- \cdot -$), progress variable c^* ($\square$), NO mass fraction from NOMAGT ($\times$) and NO source term from NOMAGT ($\circ$). The continuous lines corresponds to the results obtained for the detailed mechanism with Cantera.

Lean case

On the lean case (Fig. 5.7), a similar agreement is obtained. It should be noted that the relative contribution of the flame region to the overall NO formation is much higher in this case.

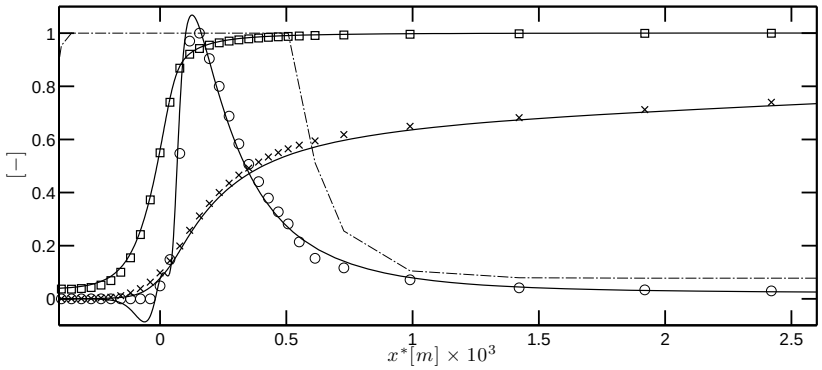

Figure 5.7: Comparison of the NOMAGT model with detailed chemistry on a one-dimensional methane-air premixed flame at $\phi = 0.6$: normalised profiles of thickening factor ($- \cdot -$), progress variable c^* ($\square$), NO mass fraction from NOMAGT ($\times$) and NO source term from NOMAGT ($\circ$). The continuous lines corresponds to the results obtained for the detailed mechanism with Cantera.

Rich case

In the rich case (Fig. 5.8), the NO production in the flame region is again largely dominant compared to post-flame processes. Some discrepancies appear in the flame region. The main error comes from the disparity between the flame speed of the detailed mechanism and the GRC for rich conditions. In particular, the flame speed is lower by 13% compared to the detailed chemistry value, which typically increases the residence

time in the flame and in turns the NO production. The same case with GRC re-adjusted for rich flames is presented in Sec. 5.4.4, showing again an excellent agreement when the flame speeds match exactly.

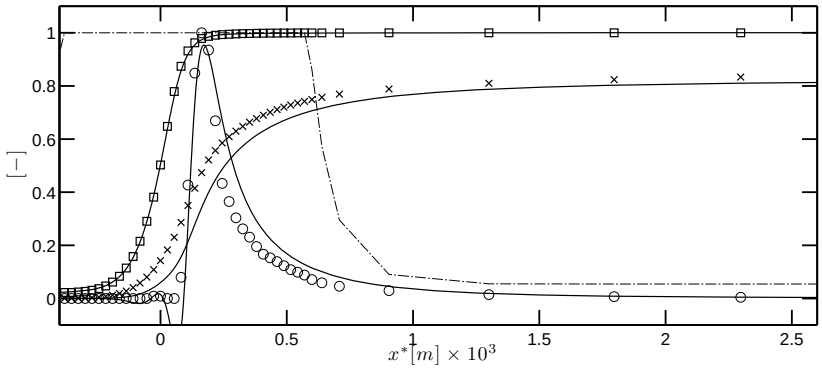

Figure 5.8: Comparison of the NOMAGT model with detailed chemistry on a one-dimensional methane-air premixed flame at $\phi = 1.4$: normalised profiles of thickening factor ($- \cdot -$), progress variable c^* ($\square$), NO mass fraction from NOMAGT ($\times$) and NO source term from NOMAGT ($\circ$). The continuous lines corresponds to the results obtained for the detailed mechanism with Cantera.

5.4.4 Influence of the switch value c_{relax}

The influence of c_{relax} is evaluated by comparing the progress variable profiles for two values $c_{relax} = 0.5$ and 0.2 on the laminar flame cases of the previous section. In the first two cases ($\phi = 0.6$ and 1.4) (Fig. 5.9(a) and Fig. 5.9(b)), the predicted progress variable is rather insensitive to the choice of c_{relax}. This can be explained by the good consistency between the reduced and the detailed chemistries: flame speeds are almost equal (6 and 1% departure respectively), and the spatial profiles of their respective progress variable is similar up to $c = 0.8$. Therefore the switch value has a negligible impact and the NO levels are completely similar in both cases.

For the rich case ($\phi = 1.4$) (Fig. 5.10(a)), the progress variable c^* deviates more strongly from the detailed profile when $c_{relax} = 0.2$. This discrepancy is again attributed to the flame speed error of the GRC. It is 13% lower for the GRC, which impacts the spatial profile of the progress variable. This is confirmed by performing the same simulation with an adjusted GRC (Fig. 5.10(b)). In this case the correct spatial profile of c^* is retrieved for both switch values and the prediction of NO spatial profile is improved (Fig. 5.11). With this flame speed adjustment, the slight NO overprediction previously observed for this case is reduced.

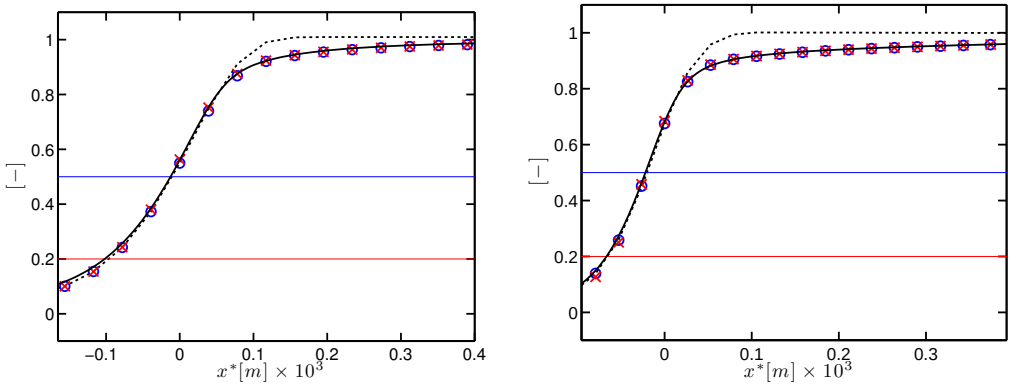

(a) $\phi = 0.6$. (b) $\phi = 1.0$.

Figure 5.9: Comparison of the NOMAGT model with detailed chemistry on a one-dimensional methane-air premixed flame. Impact of c_{relax} on the progress variable c^*: $c_{relax} = 0.5$ (○), and $c_{relax} = 0.2$ (×). The progress variable of the reduced chemistry c_{2s} (···) and from the detailed chemistry (—) are also shown for comparison. The switch thresholds are indicated by the horizontal lines.

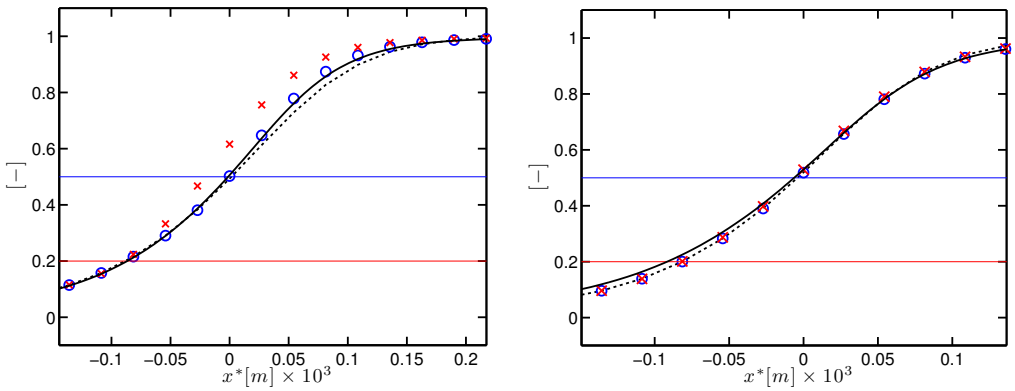

(a) $\phi = 1.4$. (b) $\phi = 1.4$ with adjusted flame speed.

Figure 5.10: Comparison of the NOMAGT model with detailed chemistry on a one-dimensional methane-air premixed flame. Impact of c_{relax} on the progress variable c^*: $c_{relax} = 0.5$ (○), and $c_{relax} = 0.2$ (×). The progress variable of the reduced chemistry c_{2s} (···) and the detailed chemistry (—) are shown for comparison. The switch thresholds are indicated by the horizontal lines.

Conclusion on the choice of the switch value c_{relax}

The choice of the switch value $c_{relax} = 0.5$ is based on the following grounds:

- The progress variable c_{2s} from the reduced chemistry is largely consistent with detailed chemistry computations for low progress variable values, the steeper behaviour of the GRC only occurs after $c \simeq 0.8$ in all cases. Therefore the retained value $c_{relax} = 0.5$ leaves a safe margin from this region.

- The comparison between $c_{relax} = 0.5$ and $c_{relax} = 0.2$ reveals that the sensitivity

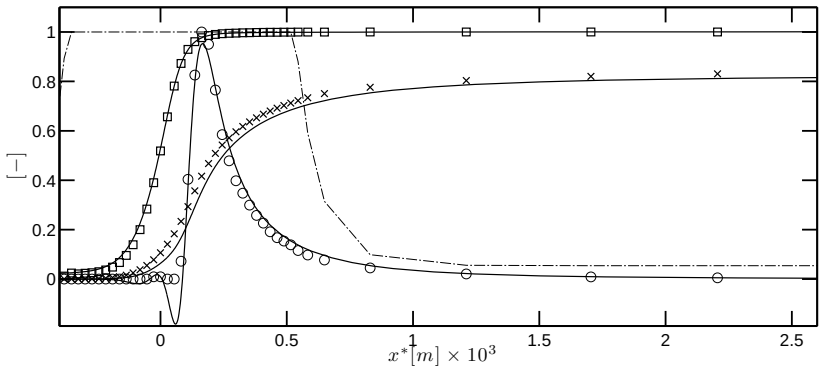

Figure 5.11: Comparison of the NOMAGT model with detailed chemistry on a one-dimensional premixed methane-air flame at $\phi = 1.4$ with adjusted flame speed: thickening factor ($-\cdot-$), progress variable c^* ($\square$), NO mass fraction from NOMAGT ($\times$) and NO source term from NOMAGT ($\circ$). The continuous lines corresponds to the results obtained for the detailed mechanism with Cantera.

of the prediction to departures between the detailed and the reduced chemistries is increased with lower c_{relax} values. This can be overcome by re-adjusting the GRC. This is constraining in practice, and only marginally improves the accuracy of NO prediction.

The method presented in this chapter will be employed on the SGT-100 configuration and its prediction capability compared with the ARC/DTFLES approach which is developed in Chapter 6.

6

Analytically Reduced Chemistry with accurate pollutant prediction in the LES context

Contents

6.1 Objectives

The objective of this chapter is to introduce the ARC methodology for accurate flame structure and pollutant prediction and its application in the LES context. First, the derivation of an ARC with accurate NO_x and CO prediction for methane-air mixture is detailed, and validate on laminar canonical cases. Then, various issues arising from the implementation of ARCs in the LES solver are addressed: transport modelling, combination with TFLES model and temporal integration of the chemical system. A thorough validation of the ARC and the numerical implementation will be performed in Chapter 7 in conditions representative of the target applications of this thesis.

6.2 Derivation and validation of an ARC for methane-air flames with accurate CO and NO_x chemistry

6.2.1 The YARC tool

The YARC reduction tool was developed by *Pepiot-Desjardins* [149]. It is employed throughout this thesis to derive ARCs from detailed mechanisms. The tool incorporates the DRGEP and LOI reduction techniques introduced in Sec. 4.4.5. The flame solutions needed as sampled applications for the reduction techniques are computed using the software FlameMaster [156]. Interfacing between FlameMaster and the reduction algorithms is automatically handled by YARC. The canonical cases that can be considered for the reduction process are: auto-ignition; one-dimensional premixed flames and diffusion flames. These cases can be combined. The ranges of pressure, temperature and equivalence ratio are also defined by the user. However, to keep the computational cost of the reduction process moderate, the sampled applications consist in practice of a limited number of pertinent cases that are sufficient to involve all the relevant chemical pathways to be preserved in the reduced mechanism.

6.2.2 Derivation of the reduced mechanisms

Objective of the reduction process

In the present section, the objective is to derive ARCs suitable for methane-air combustion application in the conditions of the Sandia flame D configuration. The reduction process is oriented towards preserving essential properties of interest: flame temperature, consumption speed, as well as correct prediction of NO and CO formation. The same methodology will later be applied in Chapter 10 to kerosene-air combustion.

Reference detailed mechanism

The reference detailed mechanism retained for methane-air oxidation is the GRI mechanism, available in two versions: GRI 2.11 [23] and GRI 3.0 [22]. The differences between the two mechanisms were highlighted by *Cao and Pope* [32] and *Barlow et al.* [11]. The prediction of CH radical is different between the two versions and leads to significantly higher prompt NO prediction by GRI 3.0. To allow a fair assessment of this impact, both versions of the GRI are considered here for the reduction process.

Existing reduced mechanisms in the literature

Existing reduced mechanisms with accurate NO chemistry [126, 191] were based only on the GRI 3.0. In the work of *Lu and Law* [126], the reduced mechanism was derived using DRG [125] and QSSA. The input data set are autoignition and perfectly-stirred reactor test cases for equivalence ratios in the range $\phi = 0.5 - 1.5$, pressure in the range $P = 1 - 30$ bars and initial temperature in the range $T = 1000 - 1600$ K. The final reduced mechanism comprises 21 transported species and was also validated on laminar premixed flames and non-premixed opposed-jet flames, where it shows good prediction of major and intermediate species, as well as NO concentrations. In the work of *Sung et al.* [191] a 21 transported species reduced mechanism is derived based on PSRs computations, and was validated on laminar methane-air premixed flames and diffusion flames.

Choice of the target canonical application

A set of five laminar freely-propagating premixed flames, with an equivalence ratio in the range $\phi = 0.6 - 1.4$, at atmospheric pressure and temperature is chosen as input data set for the reduction process. This choice guarantees that the reduced mechanism behaves correctly for premixed combustion regime for a wide range of equivalence ratios. The prediction capability of the resulting reduced mechanisms in the non-premixed combustion regime will be assessed *a posteriori*. All the steps of the reduction process are performed with the YARC reduction tool [149] and are detailed in the following for the GRI 2.11 based reduction.

6.2.2.1 First step: Skeletal reduction

The first step is to identify and to remove the species and reactions that are of minor importance. To do so, the DRGEP [150] (Sec. 4.4.5) is used to discriminate unimportant species. In the case of the GRI 2.11, eight species, HCCOH, C_2H, CH_2CO, CH_2OH, CN, NH_3, H_2CN and HCNN are removed, as well as reactions involving these species. In addition, 114 unimportant reactions (note that forward and backward reactions are counted separately) are further removed to reduce the stiffness and the complexity of

the mechanism. The resulting skeletal mechanism contains 40 species and 320 reactions. The maximum relative error introduced by this first reduction step is 3% for the laminar flame speed, 9% for CO and 6% for NO mass fractions for the set of 5 flames chosen.

6.2.2.2 Second step: QSSA

To further reduce the skeletal mechanism, the QSSA is employed. The appropriate QSS species are identified using the LOI criterion [123, 124]. Most intermediate species related to NO_x chemistry (N, NH, NNH, HNO, NH_2, NCO, HCNO, HNCO, HOCN) are found to be good candidates for QSS approximation. HCN and N_2O species which are related respectively to the prompt NO and N_2O chemical pathways, as well as the final products of the NO_x chemistry (NO and NO_2) are kept as transported species. For the methane oxidation part, 9 species, namely C, CH, CH_2, CH_2(S), HCO, CH_3O, C_2H_3, C_2H_5 and HCCO are retained for QSS approximation. Direct analytical expressions are derived for the concentrations of QSS species from the algebraic QSS system. Finally, 22 non-QSS species remain in the resulting Analytically Reduced Chemistry (ARC) named ARC_22_GRI211 in the following. Compared to the GRI 2.11, the maximum relative error of ARC_22_GRI211 is 5% for the laminar flame speed, 8% for CO and 2% for NO mass fractions on the 5 selected flames.

The final mechanism obtained in the FlameMaster/YARC format is converted into a Fortran subroutine to be employed in Cantera and AVBP solvers.

6.2.2.3 Alternative ARC derivation based on GRI 3.0

The exact same methodology is applied to the GRI 3.0 mechanism, resulting in a second reduced scheme named ARC_22_GRI30. Compared to ARC_22_GRI211 it contains the same 22 transported species. It also contains the QSS species of ARC_22_GRI211, but in addition, 3 species, namely CN, H_2CN and CH_2OH are also retained for QSS approximation whereas they were excluded from the mechanism in the derivation of the ARC_22_GRI211. Compared to GRI 3.0, the maximum relative error of ARC_22_GRI30 is 7% for laminar flame speed, 10% for CO and 9% for NO species for the selected application cases.

6.2.2.4 Comparison with existing mechanisms of the literature

Compared to the reduced mechanisms for methane-air oxidation derived in previous studies [126, 191], the ARC_22_GRI30 is similar to the mechanism obtained by *Lu and*

Law [126] although very different sampled applications were used for the reduction process: autoignition and perfectly-stirred reactor in [126] and laminar premixed flames in the present study. The fuel oxidation part of the two mechanisms are identical in terms of retained and QSS species, except for CH_2CO and CH_2CHO which are discarded in the present reduction. Concerning NO_x chemistry, the N_2O pathway and NO_2 formation are accounted for in the ARC_22s while they were discarded in [126]. Finally, more intermediates related to prompt NO formation are retained in the present study, such as NCO, HCNO, HNCO and HOCN. O atom was retained as a QSS species in the work of *Sung et al.* [191], whereas it was found to be only a marginally acceptable QSS species in [126]. In the present study, including O as additional QSS species was found to lead to deviations up to 20% for the quantities of interest.

6.2.3 Validation of the ARCs on laminar unstretched premixed flame

The objective of this subsection is to assess the ARC_22_GRI211 and ARC_22_GRI30 on laminar cases corresponding to the canonical problem employed to derive the schemes. A good agreement is therefore expected between reduced and detailed mechanisms. This enables to validate the derivation performed and to illustrate the differences between GRI 2.11 and GRI 3.0 regarding NO_x formation. About 20 flames were computed, covering the full range of equivalence ratios.

6.2.4 Comparison of spatial profiles

Two examples have been selected, corresponding to a lean case with $\phi = 0.8$ (Fig. 6.1) and a rich case at $\phi = 1.2$ (Fig. 6.2), to illustrate the behaviour of the reduced schemes.

In the **lean case** ($\phi = 0.8$), the two detailed and reduced mechanisms exhibit the same temperature and CO evolution (Fig. 6.1). In particular, the peak of CO is well captured by the two reduced mechanisms. In this example, the NO mass fraction increases through the flame at a rate that is of the same order of magnitude in the flame and in the post-flame regions, and the disparities between the two detailed mechanisms are small. The ARC_22_GRI211 matches perfectly the GRI 2.11 for all quantities while the ARC_22_GRI30 slightly overpredicts the NO levels compared to GRI 3.0.

In the **rich case** ($\phi = 1.2$) shown in Fig. 6.2, the flame structure is again well reproduced by the two reduced mechanisms compared to their respective detailed chemistry references. In contrast with the lean case, the NO profile exhibits a change of slope. This indicates a switch from rapid prompt NO formation in the flame region to slower NO formation in the burnt gases. NO levels in the burnt gases are twice as high for

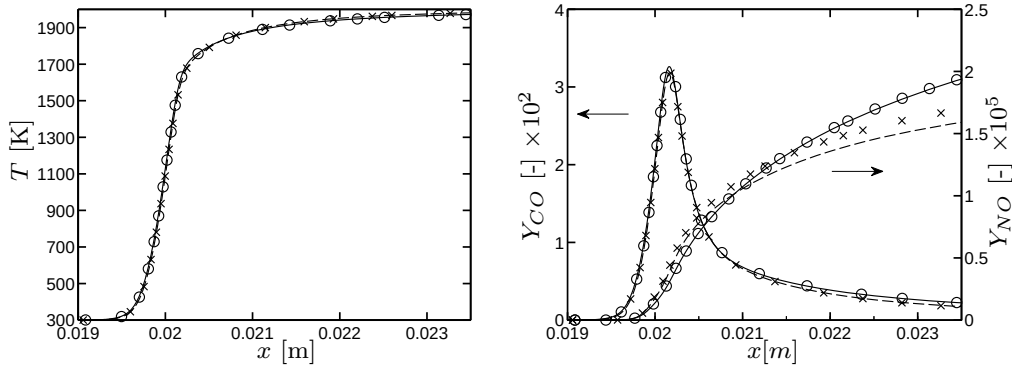

(a) Temperature profile. (b) Species mass fraction profiles.

Figure 6.1: One-dimensional premixed unstrained methane-air laminar flame in atmospheric conditions at an equivalence ratio $\phi = 0.8$. Comparison between GRI 2.11 (—), ARC_22_GRI211 ($\circ$), GRI 3.0 ($--$), ARC_22_GRI30 ($\times$).

GRI 3.0 compared to GRI 2.11. This is attributed to the increased production of prompt NO in GRI 3.0. The agreement is here again very good between the two reduced mechanisms and the detailed mechanisms.

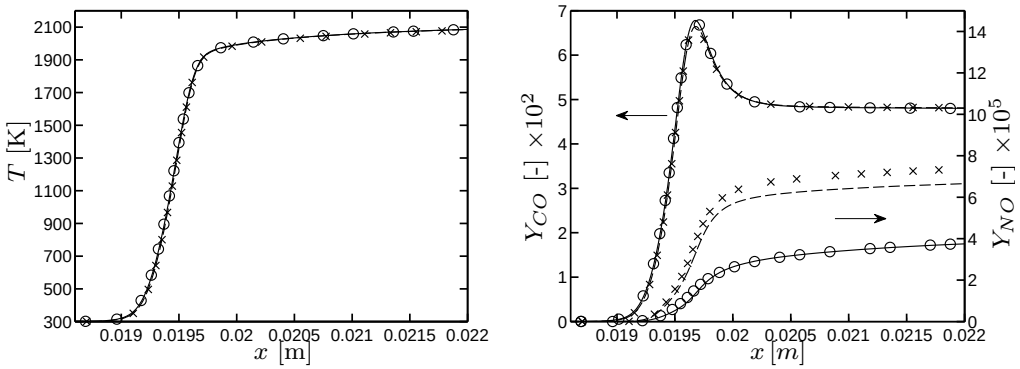

(a) Temperature profile. (b) CO and NO mass fraction profiles.

Figure 6.2: One-dimensional premixed unstrained methane-air laminar flame in atmospheric conditions at an equivalence ratio $\phi = 1.2$. Comparison between GRI 2.11 (—), ARC_22_GRI211 ($\circ$), GRI 3.0 ($--$), ARC_22_GRI30 ($\times$).

6.2.5 Comparison of global flame quantities

To assess the global performance of the reduced mechanisms, the main properties of interest, namely laminar flame speed, NO and CO formation rate integrated through the flame (i.e. total production rate in the flame) are shown as functions of the equivalence ratio ($\phi = 0.6-1.6$) in Fig. 6.3. To focus on the flame zone, NO and CO total production rates are integrated up to $c = 0.98$, where $c = \left(Y_{\mathrm{CO}} + Y_{\mathrm{CO_2}} + Y_{\mathrm{H_2O}}\right) / \left(Y^{eq}_{\mathrm{CO}} + Y^{eq}_{\mathrm{CO_2}} + Y^{eq}_{\mathrm{H_2O}}\right)$

is the progress variable, with the superscript ^{eq} denoting equilibrium values

$$\omega^{tot}_{\mathrm{NO,CO}} = \int_{c<0.98} \omega_{\mathrm{NO,CO}}\, dx\,. \tag{6.1}$$

The value $c = 0.98$ is sufficiently high to capture CO and NO formation in the flame front and sufficiently low to exclude slow post-flame chemical processes. It also corresponds to the switch between prompt and thermal NO in the NOMAGT model. Note that integrating over the whole range of c would lead to comparing CO and NO equilibrium values only. The ARCs recover very well the laminar flame speed, NO and CO flame production rates for the whole range of equivalence ratios considered, with only a slight over-prediction of NO production rate by ARC_22_GRI30, by about 10% in the range $\phi = 1 - 1.2$.

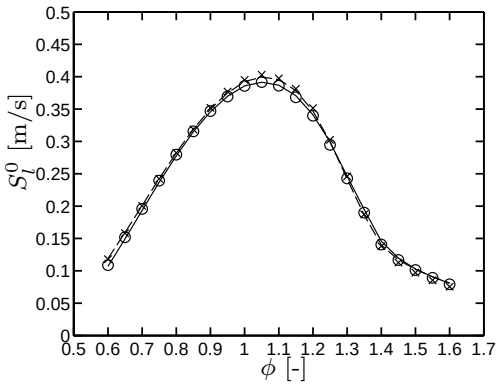

(a) Laminar flame speed.

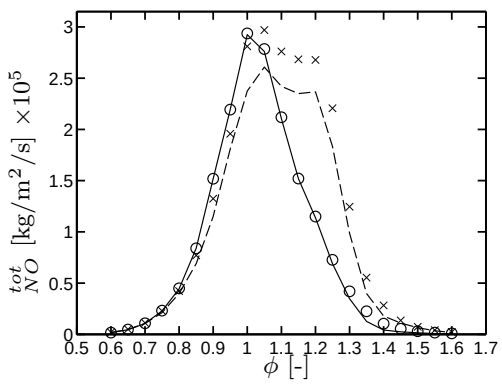

(b) Flame NO production.

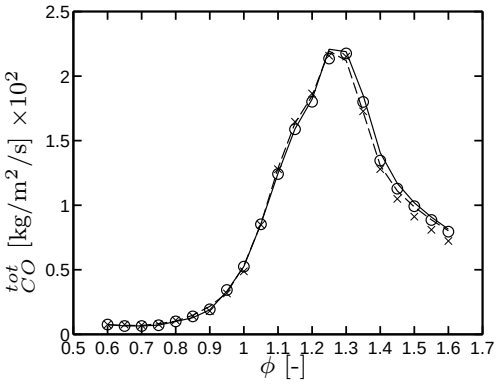

(c) Flame CO production.

Figure 6.3: One-dimensional premixed unstrained methane-air laminar flames in atmospheric conditions. Comparison between GRI 2.11 (—), ARC_22_GRI211 (∘), GRI 3.0 (−−), ARC_22_GRI30 (×) in terms of laminar flame speed, CO and NO flame production.

6.2.6 Preliminary conclusions about ARCs for methane-air combustion

The laminar validation cases illustrate the capability of ARCs to accurately describe the flame structure and pollutant formation. However, it should be noted that all these results were obtained using Cantera, which includes detailed transport models and is restricted to laminar cases. To use ARCs in the LES context, further development are needed to combine them with simplified transport description and turbulent combustion model. Theses steps are detailed in the next sections.

6.3 Transport modelling for ARCs in the LES context

In Cantera, several transport models are available. The reference transport model employed in this work for Cantera computations is the "Mix" model, based on the evaluation of species diffusion coefficient in the mixture (Eq. 2.18) based on binary diffusion coefficients, as described in Sec. 2.2.5. It serves as the reference transport model and is named Trans_Mix in the following. Simplified transport model can also be used in Cantera to evaluate the impact on the prediction of the flame structure. As detailed in Sec. 2.2.5, a simplified transport model is employed in AVBP to avoid a costly computation of binary diffusion coefficients. Instead, a constant Schmidt number for each species and a constant Prandtl number assumption is used to compute thermal and species diffusivities. These coefficients must be carefully chosen.

6.3.1 Transport modelling for GRCs

For **GRC**, the species Schmidt numbers are generally taken constant and equal, with a unity Lewis number assumption (although non unity Lewis numbers are possible). This is for example the case for the 2S_CH4_BFER scheme detailed in Appendix A. This assumption is made *a priori*, therefore it is taken into account when optimising the GRC to reproduce the global flame quantities of detailed chemistry computations.

6.3.2 Transport modelling for ARCs

For **ARC**, the reduction process preserves the physics of the detailed mechanism. The reaction parameters (pre-exponential constants, activation energy, etc.) are the ones of the detailed chemistry and no *a priori* assumption is made on the transport properties. Thus, to recover the correct flame properties (flame speed, response to strain and curvature) in LES, realistic transport properties must be employed for the species of the reduced chemistry. The choice retained in the present work is to employ the Schmidt

and Prandtl numbers found in the burnt gases at stoichiometric conditions from Cantera computations with detailed transport. This choice is based on the observations that i) the reaction zone where diffusive processes are significant is generally located at high temperatures ($> 1500\,K$) and ii) is located around stoichiometric conditions for non-premixed cases. This transport model is named **Trans_ARC** in the following. The impact of this modelling assumption will be further assessed in Chapter 7.

6.4 Artificially thickened flame model for ARCs

The dynamically thickened flame conventionally employed in AVBP was introduced in Sec. 4.5.2.2. The theoretical framework at the basis of the TFLES model is still valid in the context of ARCs. However, from a more practical point of view, identifying the flame region where the TFLES model must be applied is not so straightforward with ARC, as the chemical structure is more complex with hundreds of elementary reaction steps. Therefore, the construction of the sensor for dynamic thickening is completely redefined in this section to obtain a versatile and parametrisable methodology applicable to both GRCs and ARCs. First, the unsatisfactory behaviour of the standard methodology is illustrated and then the new methodology is presented.

6.4.1 Standard methodology

The standard methodology was introduced in Sec. 4.5.2.2. Incorrect behaviours were already highlighted in the thesis of *Franzelli* [60], as illustrated on a one-dimensional stoichiometric premixed methane-air flame in Fig. 6.4. With the standard method, the thickening sensor is very steep and fails to capture the gradient variations at the flame foot. This causes a bump in the temperature and density profiles at the flame base and can lead to inaccurate flame speed prediction. In addition it generates pressure oscillations potentially leading to numerical instabilities. The strategy proposed by *Franzelli* is to smooth and widen the sensor profile, to cover the whole region with significant gradients. This was done by so-called "Gather/Scatter" operations that acts as a filter. With the "Gather/Scatter" method, as also shown in Fig. 6.4, the sensor profile is broadened and correctly captures the flame front: the resulting temperature profile is correctly recovered and no numerical spurious oscillation is observed.

In the present work, the "Gather/Scatter" methodology is not retained because i) it is not easily parametrisable (the only control parameter is the number of iterations of the Gather/Scatter loop) and ii) the computational cost of successive Gather/Scatter operations increases dramatically for highly partitioned meshes on massively parallel

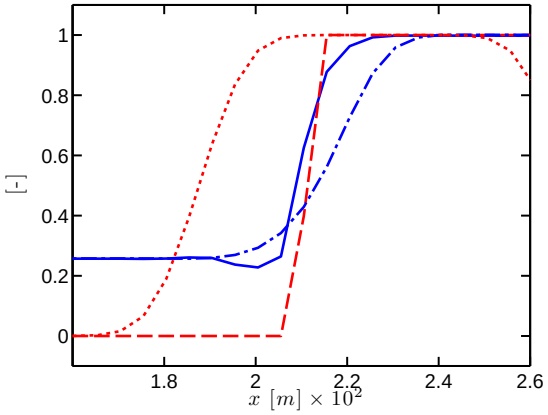

Figure 6.4: One-dimensional unstrained premixed laminar flame in SGT-100 Case A conditions at $\phi = 1.0$ with 2S_CH4_BFER mechanism. Comparison of normalised spatial profiles of temperature (Standard method: —, Gather/Scatter method: $-\cdot-\cdot$) and thickening sensor (Standard method: −−, Gather/Scatter method: $\cdots$).

architectures. In the next subsections, a new sensor is defined, using a new filtering approach detailed in Sec. 6.4.3. All validations and illustrations are then performed with the ARC_22_GRI211.

6.4.2 Flame front detection: unfiltered sensor

The first step is to develop a criterion to identify the flame front. In the work of *Franzelli* [60], the sensor is based on species source terms. Its expression reads

$$\mathcal{S}_k = \min\left(\frac{\mid \omega_k \mid}{\mid \omega_k \mid_{1D}^{max}}, 1\right) , \tag{6.2}$$

where $\mid \omega_k \mid_{1D}^{max}$ is the maximum value of the source term extracted from a one-dimensional premixed flame computation in representative conditions. It depends on the choice of the species k. In the work of *Franzelli et al.* [62], the sensor is based on the net production rate of CO and CO_2 species for application to the PRECCINSTA burner.

In the present work, a similar approach is retained. To illustrate the global distribution of chemical source terms, a sensor envelope is defined by the maximum of individual species sensors, considering all species except NO_x-related species

$$\mathcal{T} = \max_k \mathcal{S}_k \, . \tag{6.3}$$

The allure of this envelope is shown for a one-dimensional premixed flame in Fig. 6.5. It is compared with normalised CH_4 source term and heat release rate. Both are more

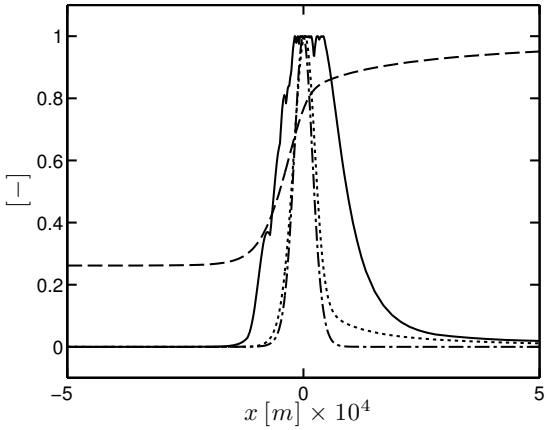

Figure 6.5: One-dimensional unstrained premixed laminar flame in SGT-100 Case A conditions at $\phi = 1.0$ with ARC_22_GRI211. Sensor envelope $\mathcal{T}$ (—), CH_4 source term (−·−·), heat release rate (···) and temperature (−−) normalised profiles.

spatially localised that the overall envelope, even if the heat release rate remains non-zero in a wider region in the post-flame zone, because of slow CO oxidation in CO_2. Based on this observation, the approach retained is to construct a sensor which is localised around the highly reacting inner flame region. It will be further spatially-filtered to enlarge its width. The final sensor must have the following properties:

1. It must correctly encompass the source terms of the reaction zone
2. It must correctly encompass the density/temperature gradients on the cold side to avoid the numerical issues illustrated in Sec. 6.4.1
3. In the post-flame region, it should rapidly vanish to avoid thickening of slow post-flame processes with smooth gradients.

Two physical quantities, heat release rate and fuel source term are compared to build the sensor. The envelope $\mathcal{T}$ could also be a relevant choice, however it extends too much in the post-flame region and is thus discarded. Similarly to Eq. 6.2, the sensor is expressed as

$$\mathcal{S} = \max\left[\min\left(2\Omega - 1, 1\right), 0\right] , \tag{6.4}$$

to normalise the sensor between 0 and 1. Ω is either based on the fuel source term (CH_4 in the present case)

$$\Omega = \frac{\mid \omega_{CH_4} \mid}{\sigma \mid \omega_{CH_4} \mid_{1D}^{max}} , \tag{6.5}$$

or alternatively the heat release rate

$$\Omega = \frac{\mid HRR \mid}{\sigma \mid HRR \mid_{1D}^{max}} . \tag{6.6}$$

In these expressions, σ is a threshold value defined as

$$\sigma = \frac{1}{\mathcal{F}_{max}}, \tag{6.7}$$

where $\mathcal{F}_{max}$ is the thickening factor with fully triggered sensor. This choice for σ guarantees that unthickened source terms remain lower than the maximum value in the thickened region. The two sensors based on fuel source term and heat release rate are compared on a one-dimensional premixed flame in Fig. 6.6.

- The sensor based on CH_4 **source term** (Fig. 6.6(a)) is localised in the strong temperature gradient. It does not cover the temperature gradient variations in the flame front nor in the post-flame region. The sensitivity to σ is assessed by performing the same case with σ divided by 2: the shape of the sensor remains almost identical between the two cases.

- The sensor based on **the heat release rate** (Fig. 6.6(b)) has a similar spatial extension in the fresh gas side but is more extended on the burnt gas side. It exhibits strong sensitivity to σ, with a much larger width when σ is divided by 2.

The sensor based on the fuel source term is preferred, as its width can be better controlled, being almost insensitive to σ. It is narrower than the reaction zone and the region of significant gradients but this will be compensated by the filtering procedure detailed in Sec. 6.4.3. The final sensor reads then

$$\mathcal{S} = \max\left[\min\left(2\frac{\mathcal{F}_{max} \mid \omega_{\mathrm{CH_4}} \mid}{\mid \omega_{\mathrm{CH_4}} \mid_{1D}^{max}} - 1, 1\right), 0\right]. \tag{6.8}$$

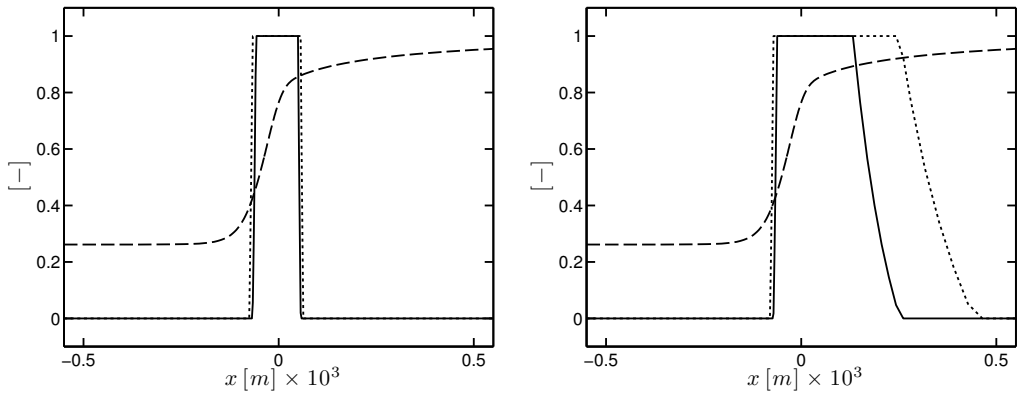

(a) Sensor based on CH_4 source term.

(b) Sensor based on heat release rate.

Figure 6.6: One-dimensional unstrained premixed methane-air laminar flame in SGT-100 Case A conditions at $\phi = 1.0$. Normalised spatial profiles of temperature (−−), thickening sensor (—) and thickening sensor with $\sigma \to \sigma/2$ ($\cdots$) based a) on fuel source term and b) on heat release rate.

6.4.3 Filtering the sensor

We now have an unfiltered sensor $\mathcal{S}$ that is able to detect the flame front. As already emphasised, this sensor is spatially too narrow. With the same objective as the "Gather/Scatter"method, an efficient filtering operation is performed to obtain a wider sensor $\widehat{\mathcal{S}}$, as illustrated in Fig. 6.7.

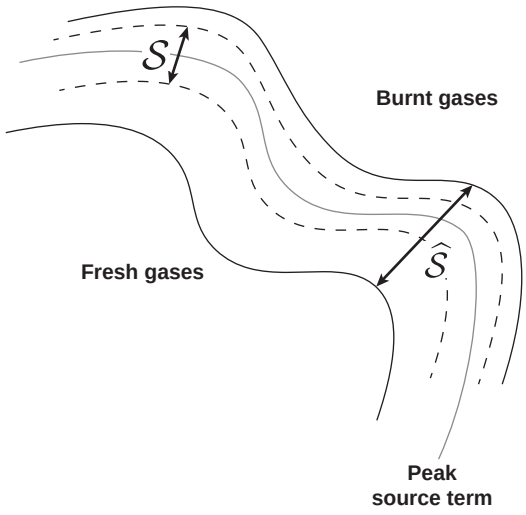

Figure 6.7: Illustration of the sensor filtering procedure.

The general form of a filter, applied to a scalar field $(\underline{x})$, can be expressed as

$$\widehat{}(\underline{x}) = \int_{-\infty}^{\infty} (\underline{x}')G(\underline{x} - \underline{x}')d\underline{x}' \,, \tag{6.9}$$

where $G(\underline{x})$ is the filter kernel, for example the Gaussian kernel. In many practical applications, this expression can be simplified by considering only the first moments of the filter. For example, a Gaussian filter may be rewritten in an approximated form [137] as

$$\widehat{}(\underline{x}) = (\underline{x}) + \frac{\Delta^2}{24}\nabla^2 \quad , \tag{6.10}$$

where Δ is the filter width. This expression is similar to a diffusion equation. It can be solved implicitly or in an iterative way. In this last case, it may be rewritten in the form of a diffusion equation

$$\frac{\partial}{\partial \tau} = D_\psi \nabla^2 \quad , \tag{6.11}$$

where τ is a dual (non-physical) time-step for the filtering procedure and D_ψ is the diffusivity. These iterations need to be performed at each physical time step and would be too costly in practice. Rather, the approach retained here is to apply a time-evolving diffusion process using the time-step of the LES simulation

$$\frac{\partial}{\partial t} = D_\psi \nabla^2 \quad . \tag{6.12}$$

This is done in practice in the LES solver by solving a transport equation for the scalar , which is of the form

$$\frac{\partial}{\partial t}(\rho\ \ ) + \frac{\partial}{\partial x}(\rho u\ \ ) = \nabla\cdot(\rho D_\psi \nabla\ \ ) + \rho\omega_\psi\,. \tag{6.13}$$

In this equation, the source term take the following form:

$$\omega_\psi(\underline{x}) = \frac{_0 - \ \ (\underline{x})}{\tau_0}\,, \qquad \text{if } \mathcal{S}(\underline{x}) > 0.8\,, \tag{6.14}$$

$$\omega_\psi(\underline{x}) = \frac{0 - \ \ (\underline{x})}{\tau_1}\,, \qquad \text{if } \mathcal{S}(\underline{x}) < 0.05\,, \tag{6.15}$$

with $\tau_0 << \tau_1$ and $_0 > 1$. The source term ω_ψ acts as a relaxation towards the unfiltered sensor and allows to follow it: when the unfiltered sensor detects a flame front ($\mathcal{S}(\underline{x}) \simeq 1$), is rapidly relaxed towards $_0$ via the source term given in Eq. 6.14; conversely, when the unfiltered sensor is close to zero, is slowly relaxed towards 0 to counteract the diffusion process which tends to broaden the peak of . The final filtered sensor is obtained as

$$\widehat{\mathcal{S}}(\underline{x}) = \max\left[\min\left(\ \ (\underline{x}), 1\right), \mathcal{S}(\underline{x})\right]\,. \tag{6.16}$$

The method is summarised in Fig. 6.8. is initialised with $\mathcal{S}$, then the transport equation of Eq. 6.13 leads to a typical function shown in Fig. 6.8. Then the filtered sensor is obtained from using Eq. 6.16. This is done at each iteration with the same time-step as the LES simulation.

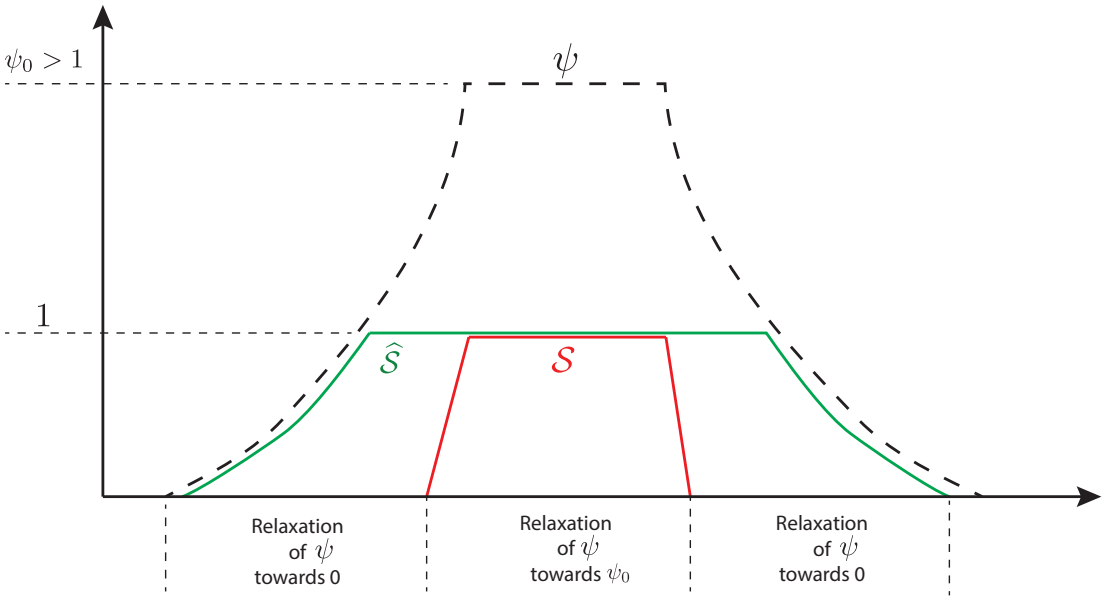

Figure 6.8: Spatial shapes of the quantities used for the sensor filtering procedure.

Choice of the parameters

τ_0 should be as low as possible to ensure that

$$\simeq \quad _0 \qquad\qquad \text{when } \mathcal{S}(\underline{x}) \simeq 1\,. \tag{6.17}$$

In practice, τ_0 is chosen of the order of $10\Delta t$ to preserve numerical stability. It should be noted that this parameter has no influence on the filter width. Indeed, the filter length results from the balance between the source term and the diffusion process of the scalar . From a one-dimensional analysis it can be shown that the filter length Δ_{filt} is linked to the main control parameters by the following relation

$$\Delta_{filt} \qquad \overline{D_\psi \tau_1} \log \quad _0 \qquad \overline{D_\psi \tau_1}\,. \tag{6.18}$$

This asymptotic analysis reveals that the filter width is also weakly dependent on $_0$ (logarithmic dependency). Thus this value is fixed to an arbitrary value $_0 = 20$ which preserves numerical stability. From Eq. 6.18, D_ψ and τ_1 appear as the two control parameters of the filter width. They are related to premixed flame characteristics by introducing two non-dimensional numbers

$$\tau_1 = \alpha \tau_{chem} = \alpha \frac{\delta_T}{S_l}\,, \tag{6.19}$$

$$D_\psi = \beta D_T\,, \tag{6.20}$$

or equivalently

$$Sc_\psi = Pr/\beta\,. \tag{6.21}$$

When substituted in Eq. 6.18, the following expression is obtained

$$\frac{\Delta_{filt}}{\delta_T} \qquad \overline{\alpha\beta}\,. \tag{6.22}$$

using the relation $\delta_T \qquad \overline{D_T \tau_{chem}}$. It shows that the filter width can be controlled by α and β and that this rewriting in terms of flame characteristics allows to obtain a filter length Δ_{filt} which scales with the flame thickness δ_T. However, the actual flame is thickened and Δ_{filt} should scale with the thickened flame thickness $\delta_T^* = \mathcal{F}\delta_T$. To do so, the same artificial correction of the TFLES model is applied to

$$D_\psi \rightarrow \mathcal{E}\mathcal{F} D_\psi\,, \tag{6.23}$$

$$\omega_\psi \rightarrow \frac{\mathcal{E}}{\mathcal{F}} \omega_\psi\,, \tag{6.24}$$

and one finally obtains

$$\Delta_{filt} \qquad \overline{\alpha\beta}\, \mathcal{F}\delta_T\,. \tag{6.25}$$

This enables the filter size to be consistent with the flame thickness regardless of the thickness factor employed, and thus no further adjustment of α and β is required is the

thickening factor/grid resolution is modified, as it will be illustrated in Sec. 6.4.5.

Note that, in order to have an optimum control of the filter length in both the fresh and burnt gas sides that behave differently, two values of the relaxation time are employed: $\tau_{1,cold}$ in the fresh gas side, and $\tau_{1,hot}$ in the hot gases. The temperature switch value between the cold and the hot side is $T_{switch} = 1600\,\mathrm{K}$.

6.4.4 Determination of the thickening factor

The methodology of Sec. 4.5.2.2 is employed to determine the thickening factor. The maximum thickening factor results from the ratio of the mesh characteristic size Δ_x to the flame thickness δ_T (evaluated on one-dimensional representative premixed flame)

$$\mathcal{F}_{max} = \frac{n_{\mathcal{F}} \Delta_x}{\delta_T}\,, \tag{6.26}$$

where the parameter $n_{\mathcal{F}}$ is the desired number of points in the flame thickness. A typical value $n_{\mathcal{F}} = 5$ is employed for GRCs. For ARCs, the value of $n_{\mathcal{F}}$ is based on one-dimensional premixed flame computations: as will be illustrated in Sec. 7.2, the value $n_{\mathcal{F}} = 5$ also yields a satisfactory accuracy for the ARC_22_GRI211.

The final thickening factor is obtained via a blending function of the filtered sensor $\widehat{\mathbb{S}}$

$$\mathcal{F}(\underline{x}) = \left(1 - \widehat{\mathbb{S}}(\underline{x})\right) \times 1 + \widehat{\mathbb{S}}(\underline{x}) \times \mathcal{F}_{max}(\underline{x})\,, \tag{6.27}$$

to obtain $\mathcal{F} = 1$ outside the flame region and $\mathcal{F} = \mathcal{F}_{max}$ inside the flame region.

6.4.5 Illustration on a reference case

In this subsection, the thickening methodology introduced above is illustrated on a representative test case: a one-dimensional unstrained premixed flame at $\phi = 1.0$ with the ARC_22_GRI211 in SGT-100/Case A conditions (680K, 3bars). In these conditions, the chemical time of the premixed flame is $\tau_{chem} = 1.3 \times 10^{-4}\,\mathrm{s}$ and the Prandtl number $Pr = 0.7$. The baseline parameters employed are summarised in Tab. 6.1. The Schmidt number Sc_ψ is taken equal to the lowest species Schmidt number of the ARC_22_GRI211, which is $Sc_H = 0.13$. Indeed, lower values would increase the filter width, but could exceed the stability limit of the diffusion operator employed. With this Sc_ψ, α_{cold} and α_{hot} were calibrated to correctly encompass the flame reaction zone and the gradient region. As shown in Fig. 6.9(a), the whole region of significant temperature gradient is well inside the zone defined by the filtered sensor with parameters of Tab. 6.1. Note the gap of an order of magnitude between α_{cold} and α_{hot}.

α_{cold}	α_{hot}	Sc_ψ
1/3	1/30	$0.13 = 0.19\,Pr$

Table 6.1: Baseline parameters for the application case.

Influence of control parameters

The sensitivity to the parameters is now studied.

First, the influence of the **relaxation characteristic times** is assessed by dividing α_{cold} by 4 (Fig. 6.9(a)) and α_{hot} by 4 (Fig. 6.9(b)). According to the asymptotic behaviour (Eq. 6.18), the width of the filter should be reduced by a factor 2 on the cold and hot side respectively: this is exactly the case for the hot side. For the cold side, the width reduction is slightly lower: it may be due to convective effects that are neglected in the asymptotic analysis.

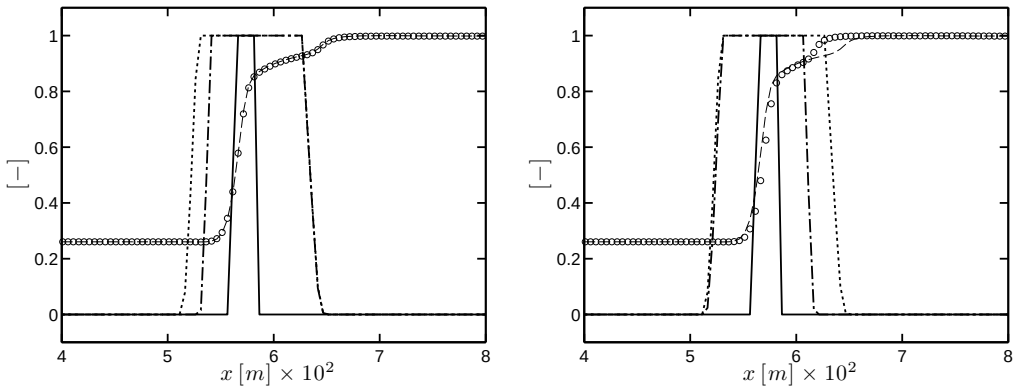

(a) Influence of α_{cold}.

(b) Influence of α_{hot}.

Figure 6.9: One-dimensional unstrained premixed laminar flame in SGT-100 Case A conditions at $\phi = 1.0$. Unfiltered thickening sensor (—), normalised spatial profiles of temperature with baseline parameters (−−) and modified parameters (∘), filtered thickening sensor with baseline parameters (· · ·) and modified parameters (− · −·).

Then, the influence of the **diffusion coefficient** is assessed by multiplying by 4 the Schmidt number of . As shown in Fig. 6.10, the width of the thickened region is approximately divided by 2, consistently with the asymptotic analysis of Eq. 6.18. This illustrates the easy control of the thickened region width via these two parameters.

Consistency with TFLES

To illustrate the consistency of the filtering procedure with TFLES formalism, a comparison between the baseline case for which $n_{\mathcal{F}} = 5$ with a case for which $n_{\mathcal{F}} = 10$ is

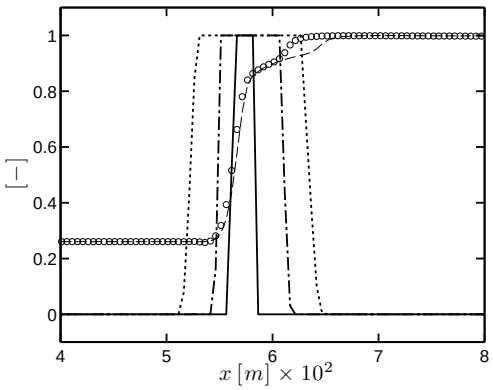

Figure 6.10: One-dimensional unstrained premixed laminar flame in SGT-100 Case A conditions at $\phi = 1.0$. Unfiltered thickening sensor (—), normalised spatial profiles of temperature with baseline parameters (−−) and modified Sc (∘), filtered thickening sensor with baseline parameters (···) and modified Sc (− · −·).

performed: the baseline case yields a thickening factor $\mathcal{F}_{max} = 19$, and $\mathcal{F}_{max} = 38$ for the $n_{\mathcal{F}} = 10$ case. The comparison of the two resulting sensors is shown in Fig. 6.11. In the spatial domain, the flame is two times larger because of the increased thickening factor with $n_{\mathcal{F}} = 10$, and so should be the thickened region. This is actually the case. It is confirmed by the comparison in x^*-space (spatial coordinate corrected by thickening factor, see Eq. 5.22) of Fig. 6.11(b), which reveals that both sensors are identical in x^*-space and that the exact flame structure is obtained. The methodology is therefore fully consistent with the TFLES formalism which makes its parametrization independent of the grid resolution, contrarily to the "Gather/Scatter" approach.

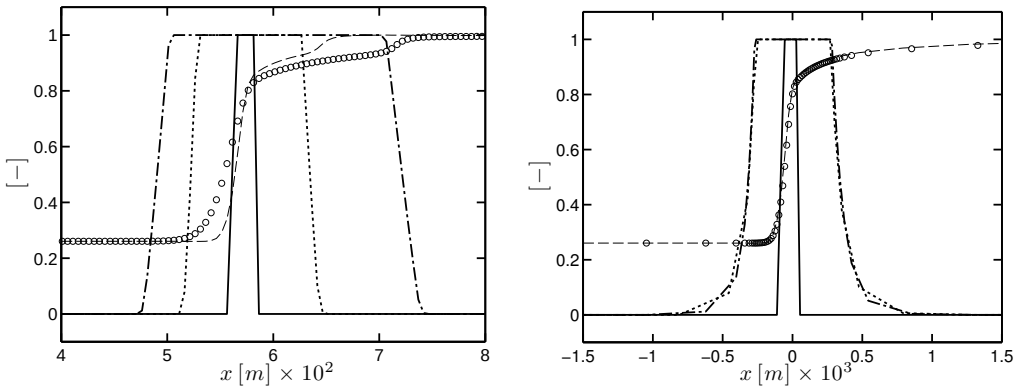

(a) In x space.

(b) In x^* space.

Figure 6.11: One-dimensional unstrained premixed laminar flame in SGT-100 Case A conditions at $\phi = 1.0$. Unfiltered thickening sensor (—), normalised spatial profiles of temperature with baseline parameters (−−) and $n_{\mathcal{F}} = 10$ (∘), filtered thickening sensor with baseline parameters (···) and filtered thickening sensor with $n_{\mathcal{F}} = 10$ (− · −·).

6.4.6 Conclusions about the methodology

The above example shows that the methodology offers several advantages compared to the former "Gather/Scatter" methodology previously employed:

- The width of the thickened region is easily adjusted using the control parameters.
- The filtering procedure is consistent with the asymptotic behaviour of the flame: few adjustments of the parameter values are expected from one case to another.
- The filtering procedure is consistent with TFLES: once suitable parameters are found, they are independent of the grid resolution.

The question of the robustness of the method in three-dimensional cases is still posed and will be addressed when applied to realistic configurations in Chapter 9 and Chapter 10.

6.5 Temporal integration of the chemical system

Compared to GRCs, ARCs contain highly reactive intermediate species. Even if QSSA reduces the overall stiffness of the mechanism, some species might still exhibit time scales lower than the unsteady time-step Δt, raising stability issues. Several strategies are proposed in this section to handle such situation.

6.5.1 Evaluation of the chemical time scales

A crude estimate of the chemical time scale of each species can be obtained from the species source term and mass fraction as

$$\tau_k = \frac{Y_k^{max}}{\omega_{Y_k}^{max}}\,, \tag{6.28}$$

where the superscript ^{max} denotes the maximum value over the domain. This estimation can be refined by decomposing the net formation rate of a species into production and destruction contributions [88]

$$\omega_{Y_k} = \omega_{Y_k}^{+} - \omega_{Y_k}^{-}\,, \tag{6.29}$$

where the superscripts $^{+}$ and $^{-}$ denote production and destruction respectively. Two time scales, respectively associated to production and destruction are then deduced

$$\tau_k^{+} = \frac{Y_k^{max}}{\omega_{Y_k}^{+,max}}\,, \tag{6.30}$$

$$\tau_k^{-} = \frac{Y_k^{max}}{\omega_{Y_k}^{-,max}}\,. \tag{6.31}$$

This definition is of interest for species exhibiting a strong disparity in time scale between production and destruction, which is typical for CO: the production occurring in the flame region is generally much faster than the oxidation into CO_2 in the flame and post-flame regions. To obtain a more accurate and local estimate of the chemical time scales, the Jacobian matrix of the chemical system, defined as

$$J_{ij} = \frac{\partial \omega_{Y_i}}{\partial Y_j}\,, \tag{6.32}$$

can be employed. This matrix is involved in the temporal evolution of the linearised chemical system

$$\frac{\partial \mathbf{Y}}{\partial t} = \mathbf{J}\mathbf{Y}\,, \tag{6.33}$$

and thus the chemical time scale of the k^{th} species can be estimated by considering diagonal terms of $\mathbf{J}$ as

$$\tau_k = \frac{1}{\mid J_{kk} \mid}\,. \tag{6.34}$$

This expression gives a good estimate of the species time scales, even if non-diagonal cross coupling terms can also have a significant impact on the chemical system dynamics.

Once species time scales are known, stiff species can be tracked by comparison of their time scale with the unsteady time step of the simulation. If a species is suspected to generate numerical instabilities, two solutions can be applied:

- Going back to the reduction process: stiff species are likely to be good QSS candidates. However this might deteriorate the prediction capability of the ARC if the species is only a marginal QSS candidate.
- Using numerical strategies to improve the stability of the temporal integration, as detailed in the next two subsections.

6.5.2 Sub-iterations for the time integration of the chemical system

One way to improve the stability of the explicit time integration is to perform n_{sub} explicit sub-iterations for the chemical system with a time-step

$$\Delta t^* = \Delta t / n_{sub}\,, \tag{6.35}$$

The integration of the system can be done with a simple Euler explicit scheme and n_{sub} can be adjusted so that Δt^* yields a satisfactory numerical stability margin. To obtain the source terms to be used in the transport equations of the LES solver, the

n_{sub} sub-iterations are performed starting from the state at the instant n (start of the iteration in the LES solver),

$$\mathbf{Y}^{*,0} = \mathbf{Y}^{n}\,, \tag{6.36}$$

$$\mathbf{Y}^{*,j+1} = \mathbf{Y}^{*,j} + \boldsymbol{\omega_Y}\left(\mathbf{Y}^{*,j}, T^n, P^n\right)\Delta t^* \;\text{ for } j = 0..n_{sub}-1\,. \tag{6.37}$$

Finally, the source terms applied in the LES transport equations are then expressed as

$$\boldsymbol{\omega_Y} = \frac{1}{\Delta t}\sum_{j=0}^{n_{sub}-1}\boldsymbol{\omega_Y}\left(\mathbf{Y}^{*,j}, T^n, P^n\right)\Delta t^* = \frac{\left(\mathbf{Y}^{*,n_{sub}} - \mathbf{Y}^{n}\right)}{\Delta t}\,. \tag{6.38}$$

Note that in Eq. 6.37, pressure and temperature values are taken at the beginning of the iteration (instant n) and are considered frozen because they evolve on slower scales than the integration time-step Δt.

This approach is computationally interesting if the required number of sub-iterations to perform is moderate. Otherwise, the increased number of evaluations of the chemical source terms proportionally increases the computational cost, and alternative methods should be used, like implicit integration, as presented below.

6.5.3 Partially-implicit method for the integration of the chemical system

An interesting alternative to sub-iterations is based on the observation that only a very limited number of species might be numerically stiff. Thus an intermediate approach between explicit and fully implicit methods is to use partially implicit integration: only the species exhibiting stiff time-scales are treated implicitly. For this approach to be computationally efficient, analytical expressions are derived for the inversion of the implicit system, as detailed below.

We start from the direct explicit integration of the chemical system

$$\mathbf{Y}^{n+1} = \mathbf{Y}^{n} + \boldsymbol{\omega_Y}\left(\mathbf{Y}^{n}, T^n, P^n\right)\Delta t\,, \tag{6.39}$$

where the superscript ^{n} denotes the state at the current iteration and Δt is the integration time-step. Since ARCs contain elementary reactions, the source term of the j^{th} species to be treated implicitly can be rewritten in a quasi-linear form as a function of the j^{th} species mass fraction Y_j as

$$\omega_{Y_j}\left(\mathbf{Y}^{n}, T^n, P^n\right) = \omega^{+}_{Y_j}\left(\mathbf{Y}^{n}, T^n, P^n\right) - \omega^{-}_{Y_j}\left(\mathbf{Y}^{n}, T^n, P^n\right)Y_j^n\,, \tag{6.40}$$

where $\omega^+_{Y_j}, \omega^-_{Y_j} > 0$. Based on this decomposition, the system can be partially implicited by substituting Y_j^{n+1} for Y_j^n on the right-hand side

$$Y_j^{n+1} = Y_j^n + \left[\omega^+_{Y_j}\left(\mathbf{Y}^n, T^n, P^n\right) - \omega^-_{Y_j}\left(\mathbf{Y}^n, T^n, P^n\right) Y_j^{n+1}\right] \Delta t\,. \tag{6.41}$$

From this expression, the species mass fraction Y_j^{n+1} can be obtained analytically, and using Eq. 6.40, it can be rewritten in a form consistent with Eq. 6.39

$$Y_j^{n+1} = Y_j^n + \frac{\omega_{Y_j}\left(\mathbf{Y}^n, T^n, P^n\right)}{1 + \omega^-_{Y_j}\left(\mathbf{Y}^n, T^n, P^n\right)\Delta t}\Delta t\,. \tag{6.42}$$

Subsequently the expression of the species source term to be used in the transport equation of species j is deduced

$$\omega_{Y_j} = \frac{\omega_{Y_j}\left(\mathbf{Y}^n, T^n, P^n\right)}{1 + \omega^-_{Y_j}\left(\mathbf{Y}^n, T^n, P^n\right)\Delta t}\,. \tag{6.43}$$

The remaining source terms are computed directly, taking into account the updated value of Y_j^{n+1}

$$\omega_{Y_k} = \omega_{Y_k}(\mathbf{Y}^n, Y_j^{n+1}, T^n, P^n)\,. \tag{6.44}$$

This method is computationally interesting because it requires only one evaluation of the chemical source terms. In addition, the partial implicitation of species j strongly improves the stability of the temporal integration: negative predicted species concentration

$$0 > {Y_j}^{n+1} = {Y_j}^n + \omega_{Y_j}\Delta t \tag{6.45}$$

typically occurs because of reactions with high forward and backward rates at equilibrium in burnt gases or too fast intermediate species destruction in the flame region and may lead to numerical oscillations. The partial implicitation ensures positivity and negative values cannot appear anymore. Numerical validation of the methodology will be performed in Sec. 7.2, in which an implicit treatment is applied to H_2O_2 species for the ARC_22_GRI211.

7

Validation of ARC in the LES solver

Contents

7.1 Objectives

The objective of this chapter is to validate ARCs and their implementation in the LES solver. For canonical cases representative of the target applications of the thesis, a systematic validation is performed:

- First the ARC is validated against detailed chemistry using Cantera computations.

- Further, the impact of simplified transport modelling is assessed.
- Finally, the computations are performed within the AVBP solver with realistic numerical parameters and grid resolution, and compared with Cantera results.

This allows notably to assess the impact of grid resolution, as well as the importance of QSSA, and to validated the temporal integration strategy.

7.2 One-dimensional premixed flames in SGT-100 conditions

The ARC derivation presented in the previous chapter was performed in ambient conditions, however industrial configurations are generally operated at high pressure. For the application to the SGT-100 configuration, only the ARC_22_GRI211 is retained. It must further be validated on laminar cases representative of the higher pressure and temperature conditions of the two operating points considered: SGT-100 Case A and Case B. As it will be further discussed in Chapter 9, this combustor is operated in a stratified premixed regime, thus laminar unstrained premixed flames are a relevant choice to validate the ARC in these conditions.

7.2.0.1 ARC validation

The ARC_22_GRI211 is validated in these conditions by performing a series of one-dimensional unstrained premixed flame computations for equivalence ratios in the range $\phi = 0.4 - 1.6$ with Cantera, using Trans_Mix transport introduced in Sec. 6.3.

Figure. 7.1 shows the comparison between the GRI 2.11 and the ARC_22_GRI211 in SGT-100 conditions for both Case A (3 bars, 680K) and Case B (3 bars, 680K). The overall agreement is excellent for laminar flame speed (Fig. 7.1(a)), flame CO production (Fig. 7.1(b)) and flame NO production (Fig. 7.1(c)). In particular, the impact of the increased pressure in Case B is well captured for the three quantities.

7.2.1 Transport modelling validation

In the LES solver, a simplified transport is used named Trans_ARC, as detailed in Sec. 6.3. The transport coefficients retained for Trans_ARC computations are given in Appendix. B. To validate this modelling assumption, computations are performed with Cantera with the detailed transport model (Trans_Mix) and the transport model employed in the LES solver (Trans_ARC). A comparison is also performed with an additional transport model named Trans_GRC hereafter, for which a unity Lewis number

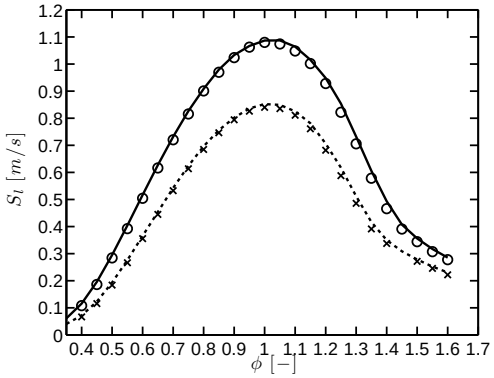

(a) Laminar flame speed.

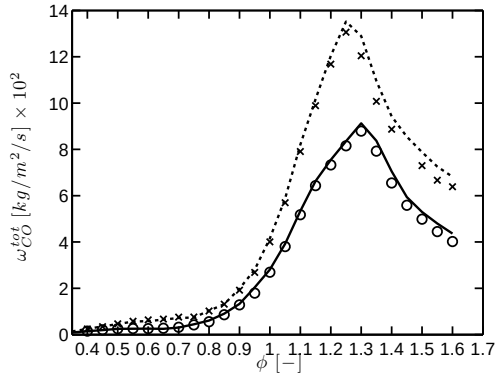

(b) Flame CO production.

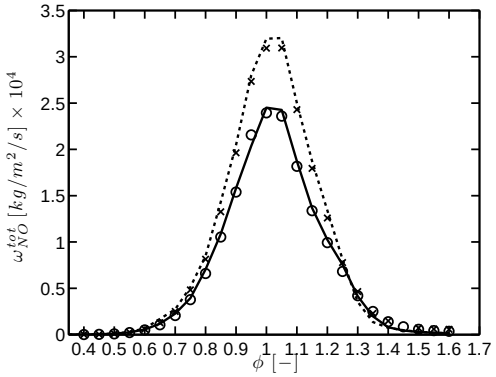

(c) Flame NO production.

Figure 7.1: One-dimensional unstrained premixed methane-air laminar flames in the SGT-100 conditions. Comparison between the GRI 2.11 detailed mechanism (Case A: —, Case B: ⋯) and the ARC_22_GRI211 (Case A: ∘, Case B: ×) in terms of global flame quantities.

assumption is used.

The validation is performed for the same series of flames introduced above in SGT-100/Case A conditions. Figure. 7.2 shows the excellent agreement between Trans_Mix and Trans_ARC for flame speed, flame NO and CO production. A slight underestimation is observed on the rich side $\phi > 1.2$ for laminar flame speed (Fig. 7.2(a)) and flame CO production (Fig. 7.2(b)). On the overall, the accuracy of the Trans_ARC is satisfactory. Contrastingly, the unity Lewis number assumption of the Trans_GRC leads to important deviations for all quantities, illustrating the importance of an accurate transport model.

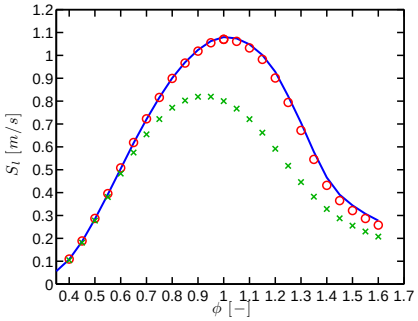

(a) Laminar flame speed.

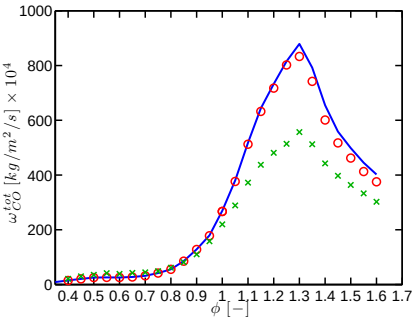

(b) CO production.

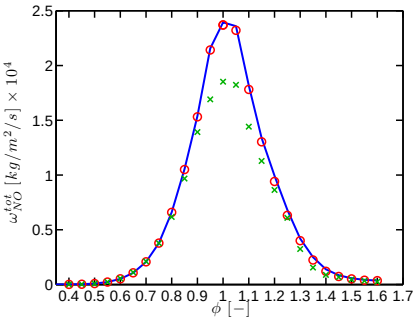

(c) NO production.

Figure 7.2: Impact of the transport model on one-dimensional unstrained premixed flames in SGT-100/Case A conditions with the ARC_22_GRI211 (Cantera). Comparison between Trans_Mix —, Trans_ARC ∘ and Trans_GRC ×.

7.2.2 Numerical setup for AVBP computations

At this stage, the ARC_22_GRI211 and associated transport modelling were validated with Cantera computations. To assess the robustness and accuracy of the implementation in the LES solver, three flame computations are performed with AVBP in SGT-100/Case A conditions at $\phi = 0.6$, 1.0 and 1.4 and compared with Cantera solutions. Note that AVBP computations are performed with the simplified Trans_ARC transport model whereas Trans_Mix is used for reference Cantera computations.

For AVBP computations, H_2O_2 species of the ARC_22_GRI211 scheme is treated implicitly following the method of Sec. 6.5.3. The grid is uniform with a characteristic size $\Delta x = 0.5\,\text{mm}$, and the unsteady time-step is $\Delta t = 75\,\text{ns}$. The convective scheme is the TTGC scheme (see Sec. 2.4.2). The Colin artificial viscosity sensor (Sec. 2.4.3) is employed with $\mathcal{S}_{\mu_2} = 0.05$ and $\mathcal{S}_{\mu_4} = 0.005$. These parameters correspond to the typical values in the LES computations of the SGT-100.

The ARC/TFLES approach is employed to dynamically thicken the flame. The parameters employed correspond to the parameters given in Sec. 6.4.5.

7.2.3 Comparison with Cantera

The comparison between AVBP results and Cantera are shown in Fig. 7.3, Fig. 7.4 and Fig. 7.5, for $\phi = 1.0$, $\phi = 0.6$ and $\phi = 1.4$ respectively. The spatial coordinate is corrected by the thickening factor (Eq. 5.22) to allow for direct comparison between the unthickened flame from Cantera and the thickened flame from AVBP. For the stoichiometric case (Fig. 7.3), a very good agreement is obtained for major species, intermediate species and pollutants. A slight misprediction of the H_2O_2 peak is observed (Fig. 7.3(d)), as well as a slight undershoot below 0 of intermediate carbon species (Fig. 7.3(e)), with a maximum error of 20% relatively to the peak values. However these discrepancies do not affect other species profiles. For the lean case (Fig. 7.4), the findings are similar, the overall agreement is again largely satisfactory. In the rich case (Fig. 7.5), there is no undershoot below 0 of carbon intermediate profiles, but NO is slightly underpredicted (Fig. 7.5(a)).

A quantitative comparison of relevant global quantities, namely flame speed, flame consumption speed, CO and NO is performed to assess the overall accuracy of the method for three selected equivalence ratios ($\phi = 0.6$, 1.0, and 1.4). The velocity u_f imposed on the fresh gas side corresponds to the laminar flame speed obtained with Cantera. As the flame speed obtained with AVBP might slightly differ, the flame can move, thus the laminar flame speed is obtained as follows [159]

$$S_l = u_f + \frac{\rho_b u_b - \rho_f u_f}{\rho_b - \rho_f}\,, \tag{7.1}$$

where the subscripts $_f$ and $_b$ denote respectively the unburnt and burnt gas sides. In unstretched one-dimensional premixed flames, the laminar flame speed is equal to flame consumption S_c, obtained using Eq. 4.13. Given that the flame is unstretched, the two quantities should be equal. Flame CO and NO production rates are defined as the integral through the flame of their respective source term up to a given progress variable value, following Eq. 4.7.

Table. 7.1 shows that there is a good consistency between the laminar flame speed and the consumption speed, and that AVBP yields satisfactory prediction of the flame speed, even if the error is more significant for the rich case ($\phi = 1.4$). Higher errors are observed for CO and NO production rates. However NO and CO productions are conditioned on progress variable values $c < 0.98$. The truncation at $c = 0.98$ is numerically difficult, as this region is discretised with few grid points. It increases the uncertainty related to the extraction of these quantities, especially for CO.

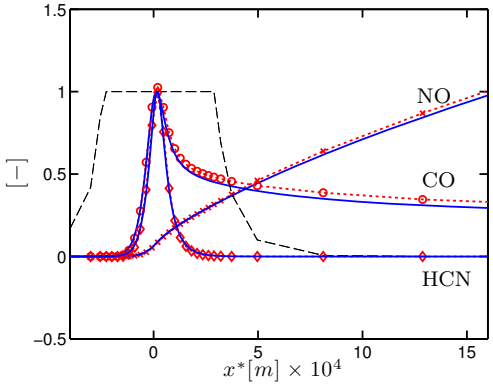

(a) NO, CO and HCN spatial profiles.

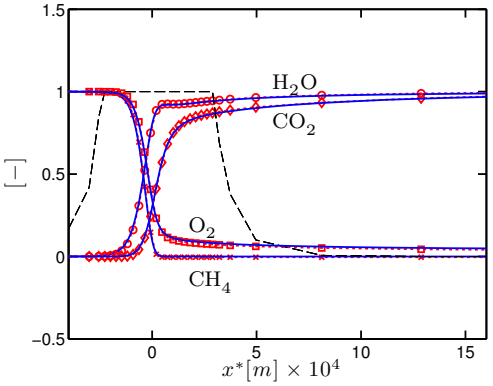

(b) CH_4, O_2, CO_2 and H_2O spatial profiles.

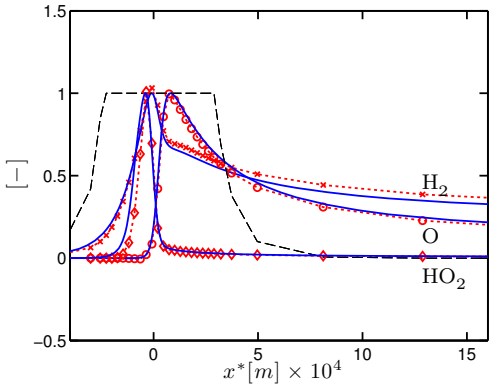

(c) HO_2, O and H_2 spatial profiles.

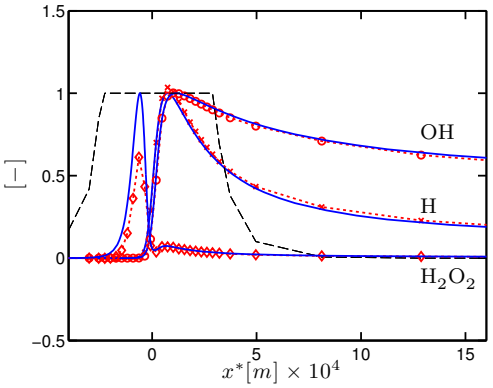

(d) H_2O_2, H and OH spatial profiles.

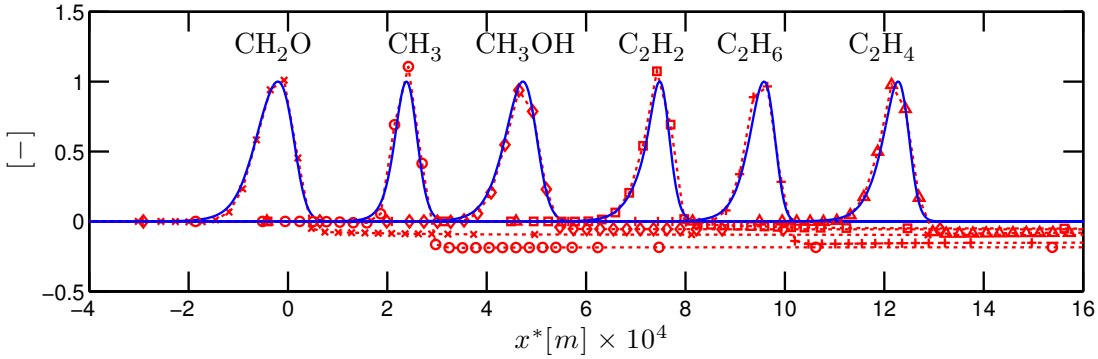

(e) CH_2O spatial profile and spatially-shifted profiles of CH_3, CH_3OH, C_2H_2, C_2H_6 and C_2H_4.

Figure 7.3: One-dimensional premixed flame in SGT-100/Case A conditions at $\phi = 1.0$. Comparison of mass fraction profiles from Cantera (—) and AVBP (dotted line with symbols). The thickening sensor θ_F (−−) profile is also shown. The markers correspond to the grid nodes of the AVBP computation. All the species mass fractions are normalised by their maximum value obtained in Cantera.

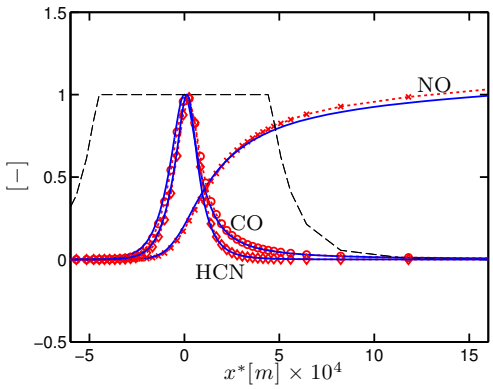

(a) NO, CO and HCN spatial profiles.

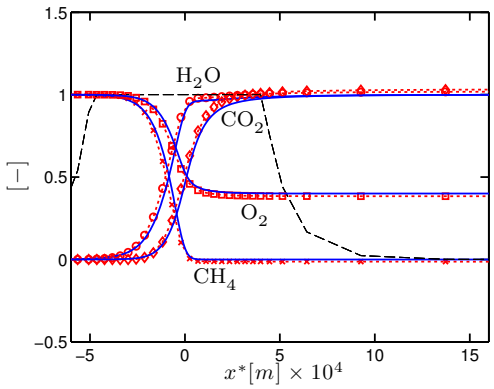

(b) CH_4, O_2, CO_2 and H_2O spatial profiles.

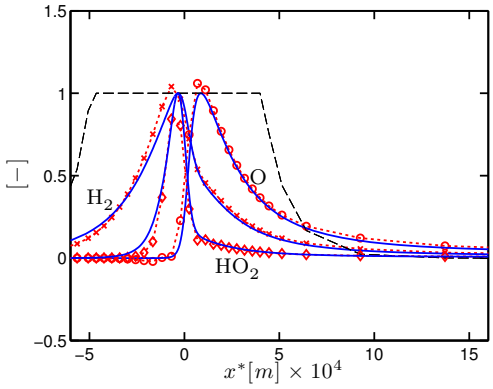

(c) HO_2, O and H_2 spatial profiles.

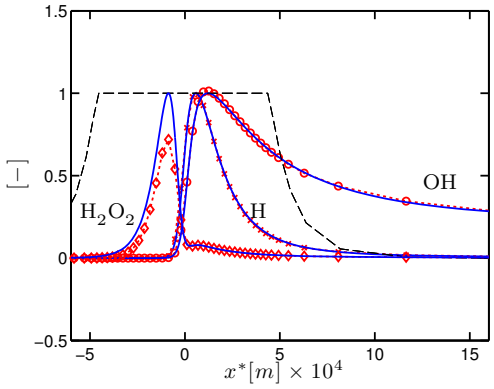

(d) H_2O_2, H and OH spatial profiles.

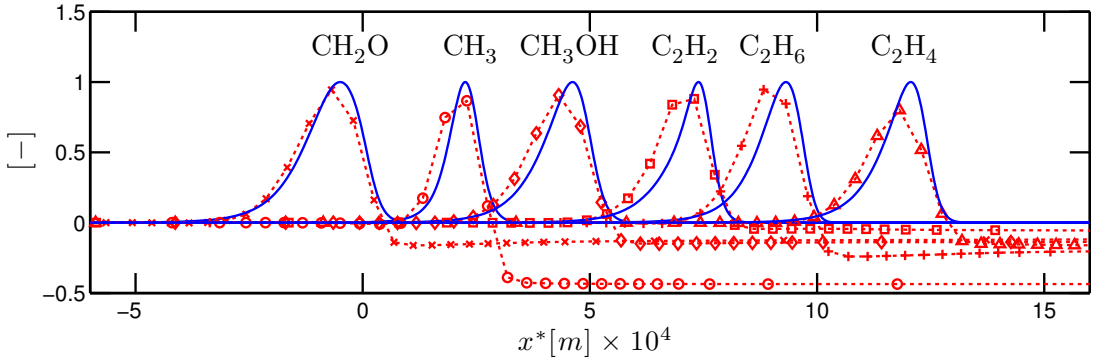

(e) CH_2O spatial profile and spatially-shifted profiles of CH_3, CH_3OH, C_2H_2, C_2H_6 and C_2H_4.

Figure 7.4: One-dimensional premixed flame in SGT-100/Case A conditions at $\phi = 0.6$. Comparison of mass fraction profiles from Cantera (—) and AVBP (dotted line with symbols). The thickening sensor θ_F (−−) profile is also shown. The markers correspond to the grid nodes of the AVBP computation. All the species mass fractions are normalised by their maximum value obtained in Cantera.

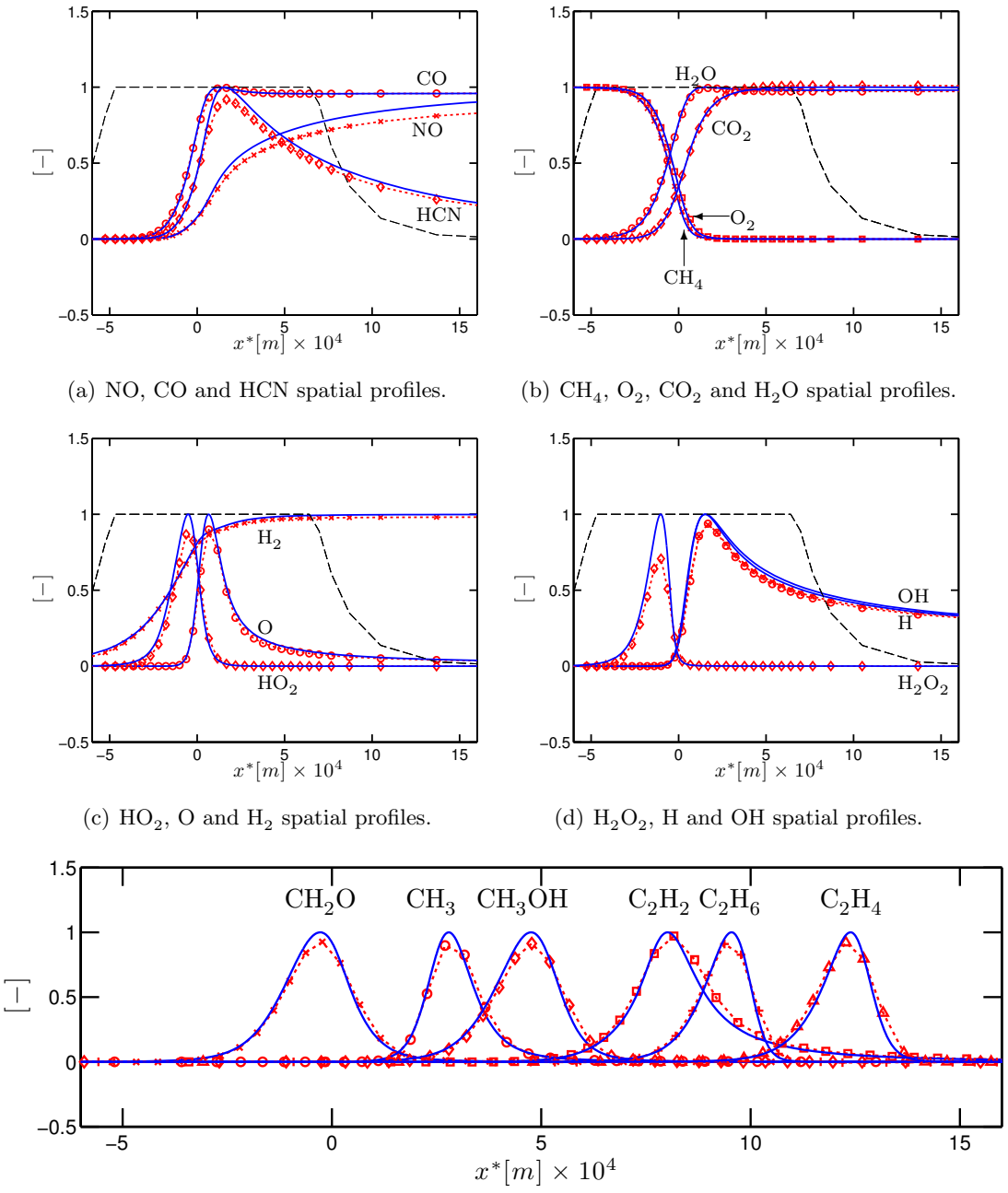

(a) NO, CO and HCN spatial profiles.

(b) CH_4, O_2, CO_2 and H_2O spatial profiles.

(c) HO_2, O and H_2 spatial profiles.

(d) H_2O_2, H and OH spatial profiles.

(e) CH_2O spatial profile and spatially-shifted profiles of CH_3, CH_3OH, C_2H_2, C_2H_6 and C_2H_4.

Figure 7.5: One-dimensional premixed flame in SGT-100/Case A conditions at $\phi = 1.4$. Comparison of mass fraction profiles from Cantera (—) and AVBP (dotted line with symbols). The thickening sensor θ_F (−−) profile is also shown. The markers correspond to the grid nodes of the AVBP computation. All the species mass fractions are normalised by their maximum value obtained in Cantera.

ϕ	1.0	0.6	1.4
S_l [m/s] (Cantera)	1.08	0.504	0.466
Relative error (AVBP)	-1.1%	1.4%	-7.4%
S_c [m/s] (Cantera)	1.07	0.496	0.462
Relative error (AVBP)	0.4%	2.6%	-6.5%
$\omega^{tot}_{\mathrm{CO}}$ [kg/m^2/s] (Cantera)	2.8×10^{-2}	2.8×10^{-3}	6.6×10^{-2}
Relative error (AVBP)	9.1%	11.6%	-6.7%
$\omega^{tot}_{\mathrm{NO}}$ [kg/m^2/s] (Cantera)	2.3×10^{-4}	5.0×10^{-6}	1.3×10^{-5}
Relative error (AVBP)	10.6%	2.1%	-9.6%

Table 7.1: Comparison of flame speed S_l, flame consumption speed S_c, flame CO production $\omega^{tot}_{\mathrm{CO}}$ and flame NO production $\omega^{tot}_{\mathrm{NO}}$, extracted from Cantera and AVBP one-dimensional flame computations for three equivalence ratios.

Impact of transport modelling

The case $\phi = 1.4$ exhibits the largest discrepancies: the flame speed is under-predicted as well as NO formation (Fig. 7.5(a)). It was shown in Sec. 7.2.1 that the Trans_ARC assumption has a more significant impact for rich cases. This is confirmed by performing a Cantera computation at $\phi = 1.4$ with Trans_ARC transport model. The resulting flame speed $S_l = 0.43\,\mathrm{m/s}$ becomes then fully consistent with the AVBP value (0.1% gap) and the agreement of spatial NO profile is significantly improved.

7.2.4 Temporal integration and link with QSS approximation

Temporal stiffness reduction by QSS approximation

To evaluate the temporal stiffness of the chemical system, the chemical time $\tau_{chem,k}$ of each species is evaluated from Cantera computations, using the Jacobian matrix (Eq. 6.34) and taking the minimum value over all grid points. The actual chemical times in the AVBP computations might actually be higher, because of flame thickening of the TFLES model which increases the chemical times by a factor $\mathcal{F}$. Results are shown in Fig. 7.6(a) for all transported species, showing that all species chemical times remain higher than the integration time step Δt, at the exception of H_2O_2 species. In the AVBP simulations, H_2O_2 was found to lead to significant numerical oscillations of pressure, which justified its implicit numerical treatment. QSS species chemical times are shown in Fig. 7.6(b): several exhibit time-scales much lower than Δt, and thus would lead to numerical instabilities if kept as transported species.

Validation of the implicitation method

To validate the implicit treatment of H_2O_2 species, the solution obtained is compared with a computation where 100 sub-iterations are applied to the chemical system without

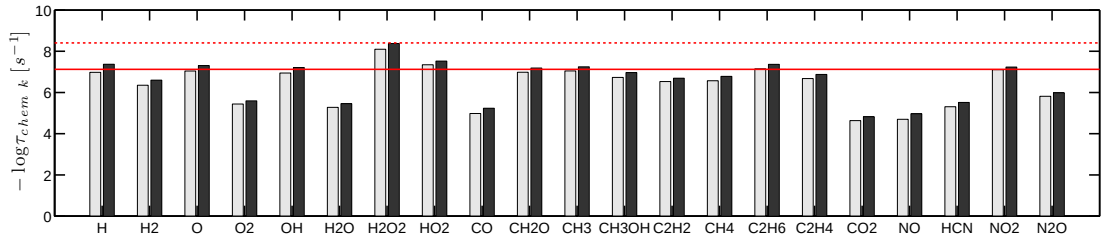

(a) Transported species.

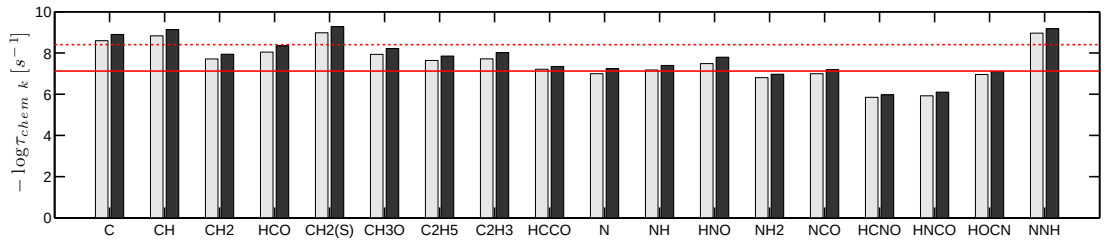

(b) QSS species.

Figure 7.6: Species chemical times extracted from a one-dimensional premixed flame at $\phi = 1.0$ in SGT-100 conditions (White: Case A - 3 bars, Black: Case B - 6 bars). The continuous line corresponds to the time-step of the computations ($\Delta t = 7.5 \times 10^{-8}$ s) and the dotted line to $\Delta t/\mathcal{F}$.

implicit integration of H_2O_2, for the case $\phi = 0.6$. The comparison of spatial profiles (Fig. 7.7) reveals that both integrations give identical results.

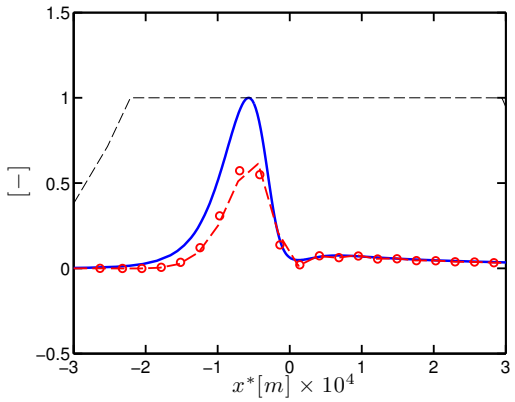

Figure 7.7: Effect of temporal integration on one-dimensional premixed flame in SGT-100/Case A conditions at $\phi = 1.0$. Comparison of H_2O_2 mass fraction profiles from Cantera (—) and AVBP with implicit integration of H_2O_2 (−−) and explicit integration with $n_{sub} = 100$ sub-iterations (○). All the species mass fractions are normalised by their maximum value obtained with Cantera.

7.2.5 Influence of the grid resolution

The impact of the grid resolution is assessed by modifying the thickening factor $\mathcal{F}$ via the control parameter $n_{\mathcal{F}}$ set at $n_{\mathcal{F}} = 7.5$ and $n_{\mathcal{F}} = 10$ compared to the original value

$n_{\mathcal{F}} = 5$. As illustrated by the CH_3 profile of Fig. 7.8(a), increasing the grid resolution effectively reduces the carbon intermediate undershoots below 0 at the end of the flame region. The H_2O_2 peak (Fig. 7.8(b)) is also better captured. However, the standard choice $n_{\mathcal{F}} = 5$ is retained for three-dimensional computations, because it yields sufficient accuracy with moderate levels of flame thickening. The good numerical behaviour with $n_{\mathcal{F}} = 5$ will be further illustrated for three-dimensional cases in the following section (Sec. 7.3).

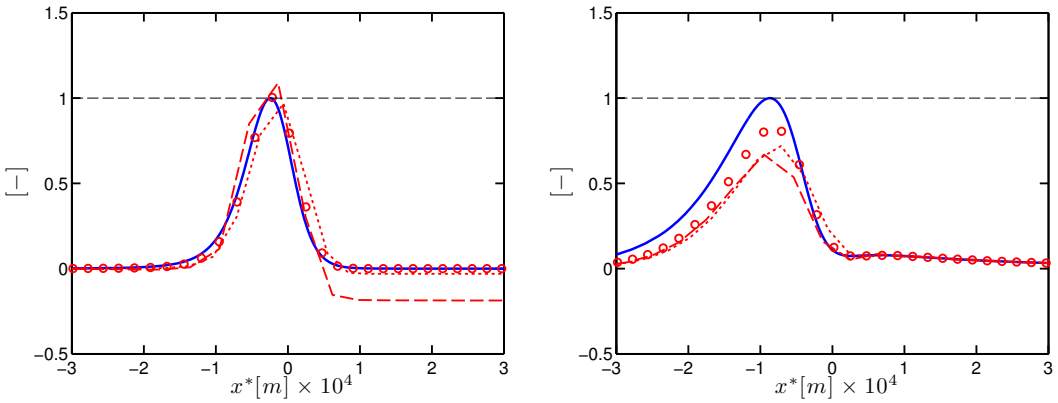

(a) CH_3 mass fraction.

(b) H_2O_2 mass fraction.

Figure 7.8: Effect of grid resolution on one-dimensional premixed flame in SGT-100/Case A conditions at $\phi = 0.6$. Comparison of mass fraction profiles from Cantera (—) and AVBP with $n_{\mathcal{F}} = 5$ (−−), $n_{\mathcal{F}} = 7.5$ (··) and $n_{\mathcal{F}} = 10$ (○). The species mass fractions are normalised by their maximum value obtained with Cantera.

7.3 Three-dimensional premixed planar flames in SGT-100 conditions

The one-dimensional cases presented above are a first validation step of the ARC/TFLES implementation in the LES solver. However, regular grids are used, which are not representative of the tetrahedral grids employed for LES computations. To evaluate the numerical method in conditions closer to three-dimensional computations, planar flame computations in a three-dimensional, tetrahedral domain are performed and validated against Cantera one-dimensional reference simulations. In particular, the impact of the location of source term calculation (@ nodes or @ cells, as introduced in Sec. 2.4.4) is highlighted.

7.3.1 Numerical setup

The numerical setup only differs from the one-dimensional cases of Sec. 7.2 by the grid. A rectangular box of size $50 \times 10 \times 10\,\text{mm}$ comprising 170,000 tetrahedral elements of characteristic size identical to one-dimensional cases $\Delta x = 0.5\,\text{mm}$ is employed. An illustration of the computational domain is shown in Fig. 7.9. A periodic boundary condition is imposed on the side walls. The simulations are initialised with one-dimensional solutions.

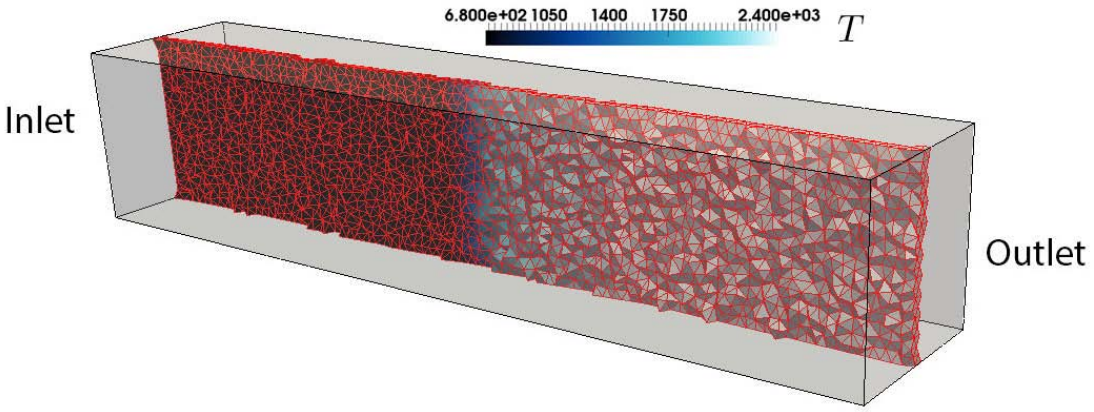

Figure 7.9: Computational domain for three-dimensional planar flame computation, and grid in the mid-plane cut.

7.3.2 Comparison with Cantera and impact of source term calculation method

The comparison of the CH_4, CO and NO mass fraction profiles of Fig. 7.10(a) shows the excellent agreement between Cantera and AVBP for both cell and nodal calculations of the chemical source terms. This is confirmed by the comparison of the source terms for the same species, that are satisfactorily recovered (Fig. 7.10(b), despite a slight damping of the peaks in the flame region, more pronounced for the nodal source term calculation.

Similarly to one-dimensional cases, a quantitative comparison of global quantities is given in Table. 7.2. Flame consumption speeds and flame speeds are well consistent, and a very good agreement with Cantera is obtained. Similarly to one-dimensional cases, a satisfactory agreement is obtained for NO production. For the same reason as one-dimensional cases, larger discrepancies of about 16% appear for CO. However the agreement appears excellent from the spatial profiles shown in Fig. 7.10(a). On the overall, the agreement is satisfactory and the cell and nodal approaches yield similar results. Thus the nodal approach is retained for LES computations, because of its lower computational cost, as will be highlighted in Sec. 9.8.

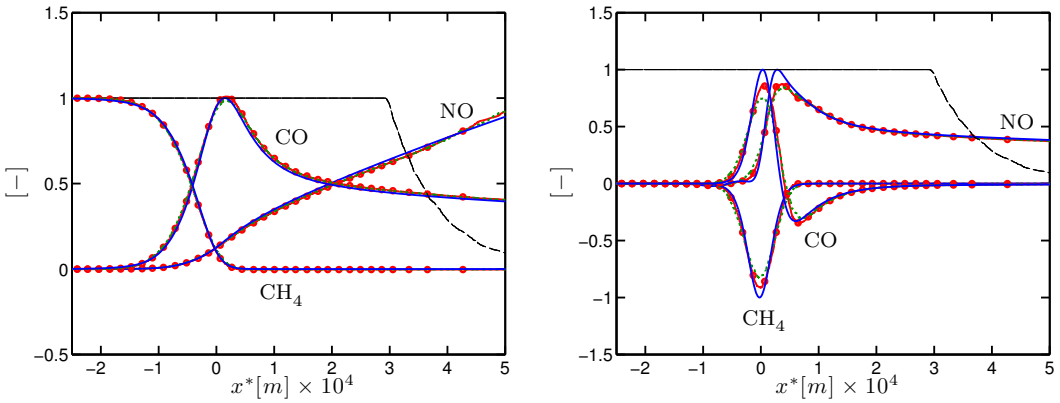

(a) CH_4, CO and NO mass fractions.

(b) CH_4, CO and NO source terms.

Figure 7.10: Three-dimensional premixed plane flame in SGT-100/Case A conditions at $\phi = 1.0$. Comparison of mass fraction profiles from Cantera (—), AVBP with source terms @ cells (− • −) and AVBP with source terms @ nodes (· · ·). The thickening sensor θ_F (−−) profile is also shown. Quantities are normalised by their maximum value obtained with Cantera.

ϕ [−]	1.0	0.6	1.4
S_l [m/s] (Cantera)	1.08	0.504	0.466
Relative error (AVBP @ cells)	-1.9%	0.1%	-6.6%
Relative error (AVBP @ nodes)	-1.8%	0.4%	-7.2%
S_c [m/s] (Cantera)	1.07	0.496	0.462
Relative error (AVBP @ cells)	-0.4%	2.2%	-5.7%
Relative error (AVBP @ nodes)	-0.2%	2.4%	-6.3%
ω^{tot}_{CO} [kg/m^2/s] (Cantera)	2.8×10^{-2}	2.8×10^{-3}	6.6×10^{-2}
Relative error (AVBP @ cells)	16%	16.1%	-5.9%
Relative error (AVBP @ nodes)	15%	17.2%	-6.9%
ω^{tot}_{NO} [kg/m^2/s] (Cantera)	2.3×10^{-4}	5.0×10^{-6}	1.3×10^{-5}
Relative error (AVBP @ cells)	1.7%	6.8%	−5.9%
Relative error (AVBP @ nodes)	3.7%	6.5%	−5.4%

Table 7.2: Comparison of flame speed S_l, flame consumption speed S_c, flame CO production ω^{tot}_{CO} and flame NO production ω^{tot}_{NO}, extracted from Cantera and AVBP three-dimensional planar flame computations for three equivalence ratios.

7.4 Strained counterflow diffusion flames in Sandia flame D conditions

7.4.1 ARC validation

In many applications, partial premixing leads to non-premixed combustion. As it will be highlighted in Sec. 8.6, the Sandia flame D is dominated by a non-premixed combustion. Therefore, it is important to validate the reduced mechanisms for such combustion regimes. To do so, the reduced mechanisms are applied to a series of counterflow flames, as introduced in Sec. 4.3. To be representative of the operating conditions of the Sandia flame D, the conditions are chosen accordingly: the oxidiser inlet is composed of fresh air at ambient conditions while the fuel inlet is a methane-air mixture at ambient conditions with an equivalence ratio $\phi = 3.17$. It was shown that depending on the fuel side equivalence ratio, the flame structure switches from a double flame structure to a single diffusion flame [57]. In the present case, the fuel side equivalence ratio is far off the rich flammability limit, which is around $\phi_{\text{lim}} = 1.85$. A simple diffusion flame structure is therefore expected. The response to strain is assessed by varying the global strain rate

$$a = \frac{u_{ox} + u_{fuel}}{L}\,, \tag{7.2}$$

where L is the distance between the two inlets and u_{ox}, u_{fuel} are respectively the oxidiser and fuel inlet velocities. A large range of strains is considered here $a = 20 - 300\,\text{s}^{-1}$, given that the extinction strain rate is $a \simeq 400\,\text{s}^{-1}$. The response of the different mechanisms to the global strain rate is shown in Fig. 7.11. The maximum temperature decreases from the adiabatic temperature at low strains to significantly lower values close to the extinction. The evolution is similar for all the schemes. The fuel consumption rate and CO formation of the detailed mechanisms exhibit a monotonic response to strain which is identical for both version of the GRI, and that is excellently reproduced by the two ARCs.

The response of NO production to strain is more complex. For low strain values, the NO production rapidly increases with strain. Then the slope decreases, and becomes negative for higher strain values. The peak of NO production does not correspond to the hottest flame, which tends to indicate that it is not only linked to the thermal NO mechanism. The findings of the premixed case in terms of differences between the mechanisms still hold for diffusion flames. The NO production levels of the ARC_22_GRI30 are overestimated by 10 to 15% compared to GRI 3.0. A very good agreement is obtained between ARC_22_GRI211 and GRI 2.11, which again yields NO formation rates significantly lower than the GRI 3.0. On the overall, the accuracy of

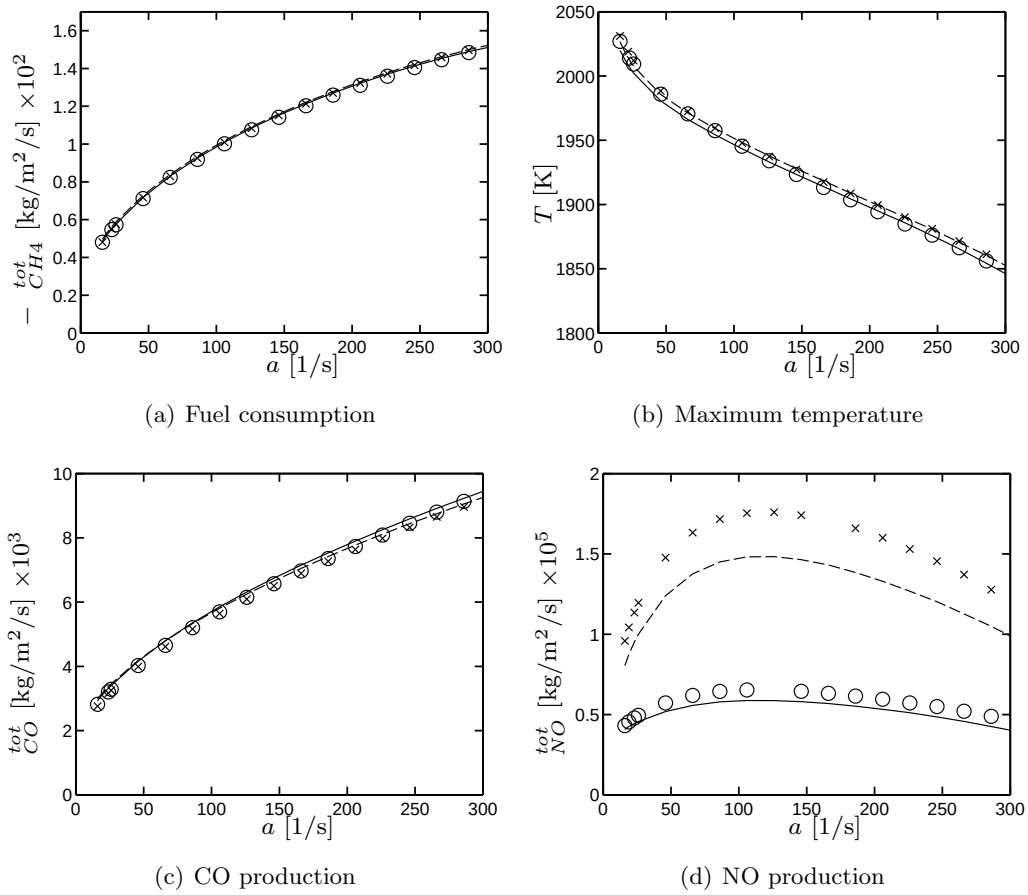

(a) Fuel consumption

(b) Maximum temperature

(c) CO production

(d) NO production

Figure 7.11: Laminar counterflow diffusion flames in Sandia Flame D conditions. Comparison of the response to global strain rate between GRI 2.11 (—), ARC_22_GRI211 (○), GRI 3.0 (−−), ARC_22_GRI30 (×). in terms of a) total fuel consumption, b) maximum temperature, c) total CO production and d) total NO production.

the two ARCs is largely satisfactory to be applicable for the LES of the Sandia flame D.

Comparison with experimental data

Experimental data for this type of flame configuration is available from *Barlow et al.* [11]. In the experiments, the flame is stabilised on a porous cylindrical burner (Tsuji burner) in a low-velocity flow of air. The estimated global strain rate for the experiments is $a = 2U_\infty/r = 25\,\mathrm{s}^{-1}$ based on the air approach velocity U_∞ and the radius r of the cylinder. Calculations were also performed with GRI 3.0 and GRI 2.11 using a dedicated code that treats the Tsuji flame geometry as a two-point boundary value problem.

To compare the experimental results with the present set of counterflow computations, spatial profiles of mixture at various strain rates are compared with the experimental profiles. Figure 7.12 shows that the best agreement is obtained with $a = 10^{-1}$, even if

the profile of Z is not exactly recovered.

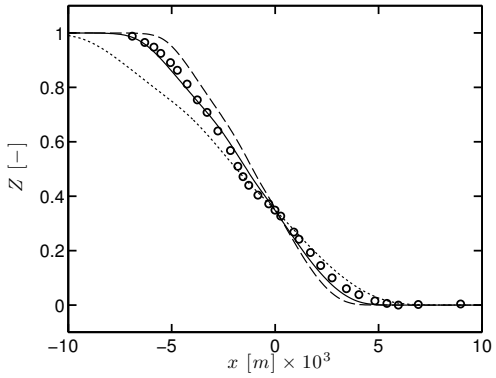

Figure 7.12: Measured profiles of mixture fraction (○) from *Barlow et al.* [11]. Comparison with counterflow flames at global strain rate $a = 5\mathrm{s}^{-1}$ (· · ·), $10\,\mathrm{s}^{-1}$ (—) and $15\mathrm{s}^{-1}$ (– –).

Based on this choice for the global strain rate value, H_2, CO and NO profiles in Z-space are compared with the measurements in Fig. 7.13. Note that estimated experimental uncertainties are 10% for H_2, 10% for CO and 15% for NO. On the overall, a good consistency is obtained between the detailed and reduced mechanisms. A fair agreement is obtained for H_2 and CO between calculations and measurements, even if the discrepancies are larger on the rich side, which might be partially related to the different mixing structure between the one-dimensional counterflow flame and the actual burner geometry. For NO, the concentrations are significantly higher with the GRI 3.0 version (Fig. 7.13(c)) compared to the GRI 2.11 version which is also above the experimental levels. This overprediction was also observed in the adiabatic computations of *Barlow et al.* [11]. Satisfactory levels were obtained when considering radiative heat losses with GRI 2.11, whereas they remain too high with GRI 3.0. This clearly tends to indicate that GRI 3.0 tends to overpredict NO formation on this type of configuration.

7.4.2 Transport modelling validation

Similarly to the validation performed from premixed cases, the Trans_Mix and Trans_ARC models are compared on the counterflow flame series. The comparison is shown in Fig 7.14. Excellent agreement is obtained for fuel consumption (Fig. 7.14(a) and flame CO production (Fig. 7.14(c)). An acceptable deviation of about 5 % occurs for flame NO production (Fig. 7.14(d)) over the whole strain range which might be related to the slight overall overestimation of the maximum temperature (Fig. 7.14(b)). This shows again that the flame properties are satisfactorily reproduced with the Trans_ARC.

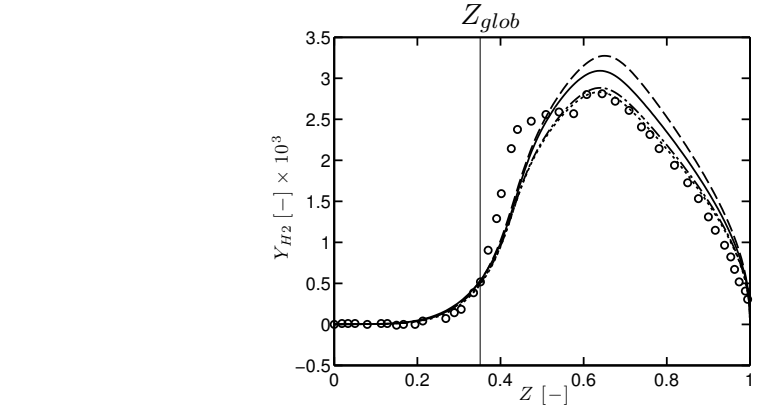

(a) H_2 mass fraction.

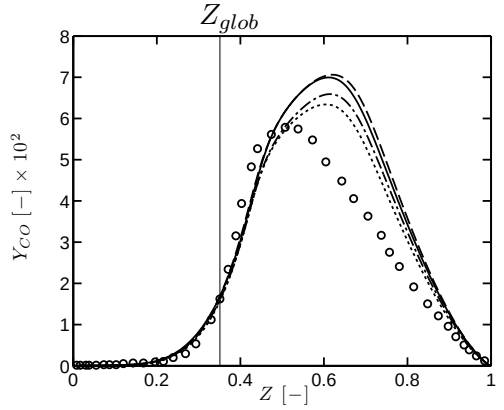

(b) CO mass fraction.

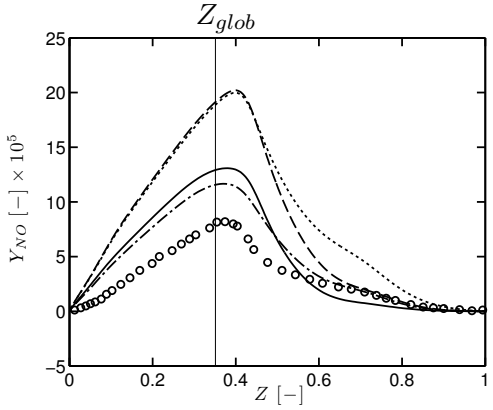

(c) NO mass fraction.

Figure 7.13: Profiles in Z-space of a) H_2 mass fraction, b) CO mass fraction and c) NO mass fraction. Comparison between measured profiles from *Barlow et al.* [11] (∘) and computations at global strain rate $a = 10\,\mathrm{s}^{-1}$ with GRI 2.11 (—), ARC_22_GRI211 ($\cdot - \cdot -$), GRI 3.0 ($- -$) and ARC_22_GRI30 ($\cdots$). The vertical line corresponds to the stoichiometric mixture fraction.

7.4.3 Numerical setup for two-dimensional non-premixed flames in AVBP

Now that the ARC and associated transport modelling are validated on the counterflow flame series with Cantera, the capability of the LES solver combined with ARC and simplified transport to correctly reproduce the features of the non-premixed flame series is assessed. Similarly to the premixed cases of the previous sections, the numerical setup is first introduced, and the results obtained with AVBP are further compared to reference solutions from Cantera. Again, note that AVBP computations are performed with the simplified Trans_ARC transport model whereas Trans_Mix is used for Cantera computations.

An overview of the numerical domain used for AVBP computations is shown in Fig. 7.15. It corresponds to a counterflow configuration, with two inlets for the fuel and oxidiser

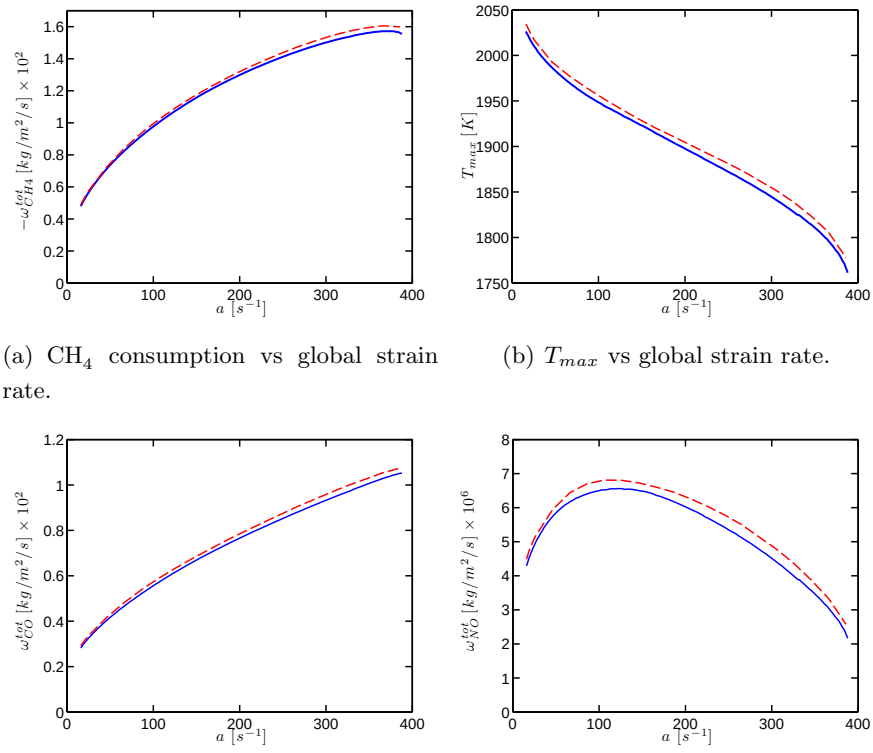

(a) CH_4 consumption vs global strain rate.

(b) T_{max} vs global strain rate.

(c) CO production vs global strain rate.

(d) NO production vs global strain.

Figure 7.14: Impact of the transport model on one-dimensional diffusion flames. Comparison between Trans_Mix — and Trans_ARC −−.

injections. The domain is two-dimensional. A symmetry condition is imposed at the axis of the counterflow configuration, whereas a large volume is used at the outlet to smoothly evacuate the flow and the perturbations. The TTGC scheme (see Sec. 2.4.2) is employed and the Colin artificial viscosity sensor is employed with $\mathcal{S}_{\mu_2} = 0.05$ and $\mathcal{S}_{\mu_4} = 0.005$. This choice of parameters corresponds to the values employed in the target application (Sandia flame D). The grid of triangular elements has a uniform characteristic size $\Delta x = 0.15\,\text{mm}$, which is a typical characteristic grid size employed in the LES. Given the grid resolution, the unsteady time-step imposed by the CFL condition is $\Delta t = 45\,\text{ns}$.

7.4.4 Comparison with Cantera

The flame structure obtained in AVBP is compared to Cantera solutions for four global strain rates, $a = 40$, 80, 160, and $320\,s^{-1}$. The latter value is close to the extinction strain rate which is approximately $a_{quench} = 400\,\text{s}^{-1}$. From the AVBP solutions, profiles along the symmetry axis are extracted and compared to reference counterflow computations performed with Cantera in the same conditions. The mixture fraction is based on

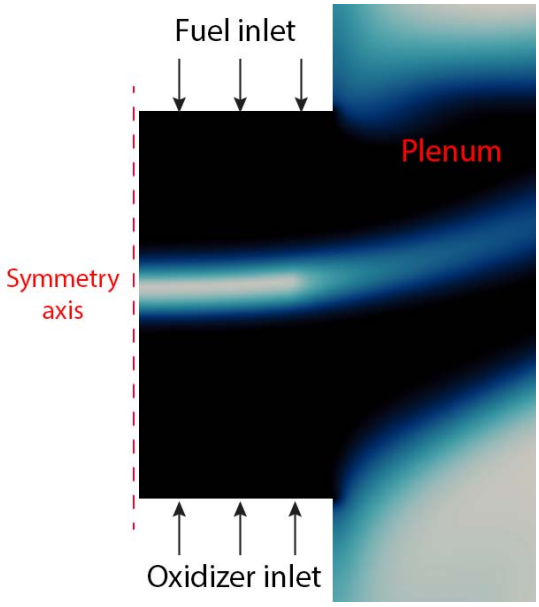

Figure 7.15: Computational domain for two-dimensional counterflow flame.

the carbon atom following Eq. 4.27. The stoichiometric mixture fraction is $Z_{st} = 0.351$.

Mixture fraction and scalar dissipation rate

The mixture fraction profiles are compared for the four different strain rates in Fig. 7.16(a). Note that the zero x-coordinate corresponds to the stoichiometric mixture fraction. Mixture fraction profiles are very close. The scalar dissipation rate profiles (Fig. 7.16) show that a similar mixing structure is obtained in Z-space. However the peak value around $Z = 0.4$ is about 10% lower for the AVBP cases, the full resolution of the Navier-Stokes equations in the LES solver and the simplified counterflow flame equations resolved in Cantera do no yield the same spatial structure. This difference is also illustrated by the axial velocity profile shown in Fig. 7.17 for the $a = 320\,\mathrm{s}^{-1}$ case, which is slightly different between Cantera and AVBP. Since mixture fraction and scalar dissipation are the two variables that control the diffusion flame structure, the difference obtained for scalar dissipation rate profiles should be kept in mind when comparing the flame structure obtained with AVBP and Cantera, especially for species highly sensitive to strain rate.

Qualitative comparison: species and source terms profiles in Z-space

Figure. 7.18 shows species mass fraction profiles in Z-space. The impact of strain rate is well captured for intermediate species, such as HO_2 (Fig. 7.18(a)) and O (Fig. 7.18(b)), even if some discrepancies appear for the higher strain case ($a = 320\,\mathrm{s}^{-1}$). Similarly, CO mass fraction is correctly predicted. Discrepancies are larger for NO, despite the good agreement of NO source term in Z-space (Fig. 7.19(c) and Fig. 7.19(d)), whose

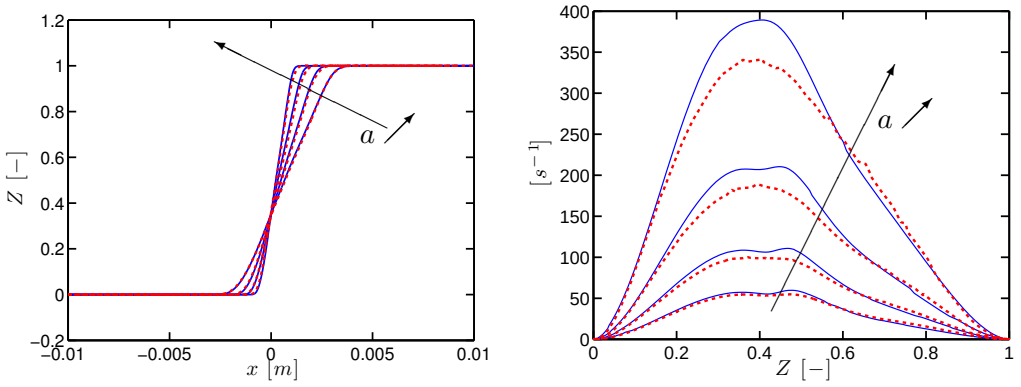

(a) Mixture fraction profiles.

(b) Scalar dissipation rate profiles in Z-space.

Figure 7.16: Counterflow computations in Sandia flame D conditions at global strain rates a = 40, 80, 160, and 320 s^{-1}. Comparison of mixture fraction and scalar dissipation rate profiles from Cantera (—) and AVBP ($\cdots$).

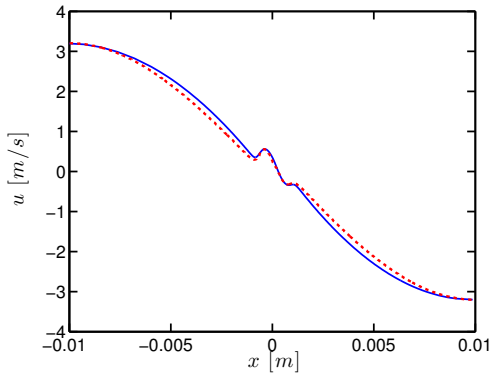

Figure 7.17: Counterflow computations in Sandia flame D conditions at global strain rate $a = 320\,s^{-1}$. Comparison of axial velocity profile from Cantera (—) and AVBP ($\cdots$).

non-monotonic behaviour is well captured. Being a slow-chemistry species, NO concentration might be more sensitive to the local scalar dissipation rate, which is not exactly similar between AVBP and Cantera computations,. The impact of strain rate, which tends to increase CH_4 (Fig. 7.19(a) and CO (Fig. 7.19(b)) source terms is also correctly captured, even if again discrepancies are larger for higher strain rate.

Quantitative comparison: global flame quantities

To assess quantitatively the ability of AVBP to correctly reproduce the global properties of the diffusion flame, the integrated production rate of CH_4, CO and NO are compared to Cantera in Tab. 7.3. As already observed, the error increases with the strain rate: excellent agreement is obtained for both fuel and pollutant species is obtained at low to moderate strain rates, but larger discrepancies appear for higher strain rates. This can be related to insufficient resolution of the reaction layer thickness, as

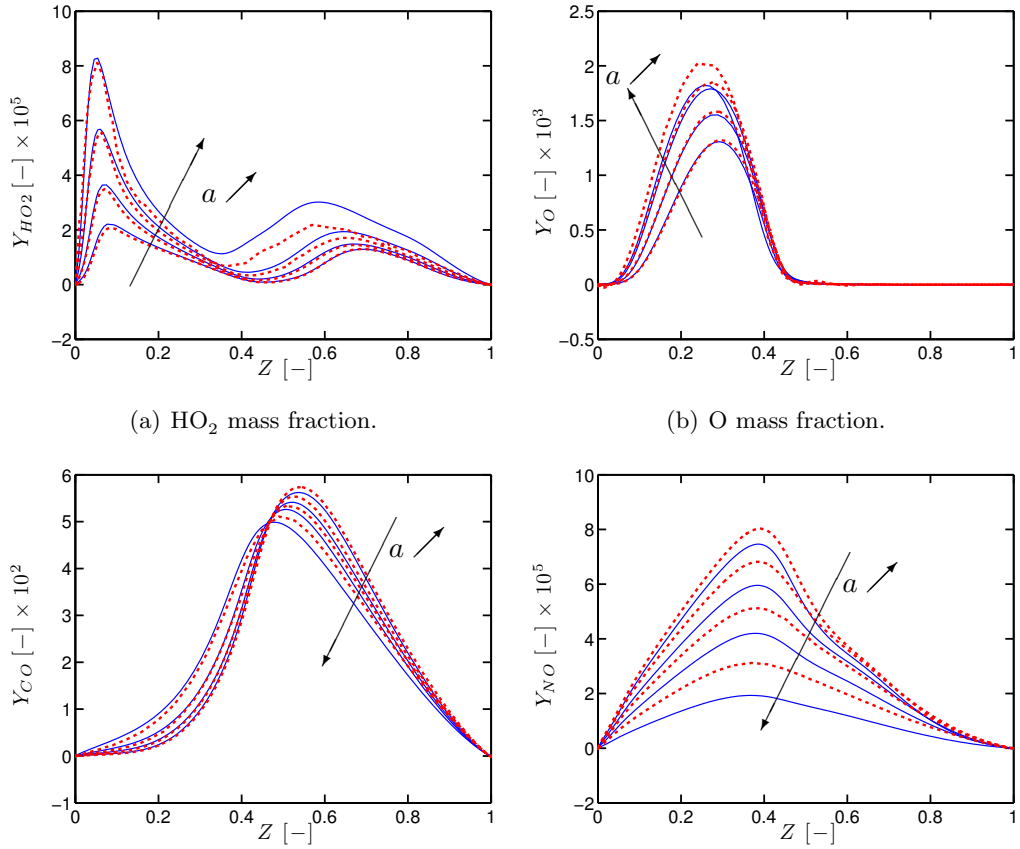

(a) HO_2 mass fraction.

(b) O mass fraction.

(c) CO mass fraction.

(d) NO mass fraction.

Figure 7.18: Counterflow computations in Sandia flame D conditions at global strain rates $a = 40,\ 80,\ 160,\ 320\,s^{-1}$. Comparison of species mass fractions from Cantera (—) and AVBP (···) in Z-space.

will be shown later in Sec. 7.4.5.

$a\,[\mathrm{s}^{-1}]$	40	80	160	320
$-\omega^{tot}_{\mathrm{CH_4}}$ [kg/m^2/s] (Cantera)	6.3×10^{-3}	8.5×10^{-3}	11.5×10^{-3}	15.1×10^{-3}
Relative error (AVBP)	-1.6%	-1.2%	-4.4%	-4.6%
$\omega^{tot}_{\mathrm{CO}}$ [kg/m^2/s] (Cantera)	3.6×10^{-3}	4.8×10^{-3}	6.7×10^{-3}	9.4×10^{-3}
Relative error (AVBP)	+5.5%	+2%	-6%	-7.5%
$\omega^{tot}_{\mathrm{NO}}$ [kg/m^2/s] (Cantera)	5.3×10^{-6}	6.2×10^{-6}	6.5×10^{-6}	4.4×10^{-6}
Relative error (AVBP)	+5%	+6%	+16%	+40%

Table 7.3: Counterflow flames in Sandia flame D conditions. Integrated source terms of CH_4, CO and NO: comparison between Cantera and AVBP.

Temporal stiffness and integration

Similarly to the premixed validations cases, species chemical time scales are extracted from the Cantera solutions for two global strain rates $a = 40$ and $320\,\mathrm{s}^{-1}$. Both trans-

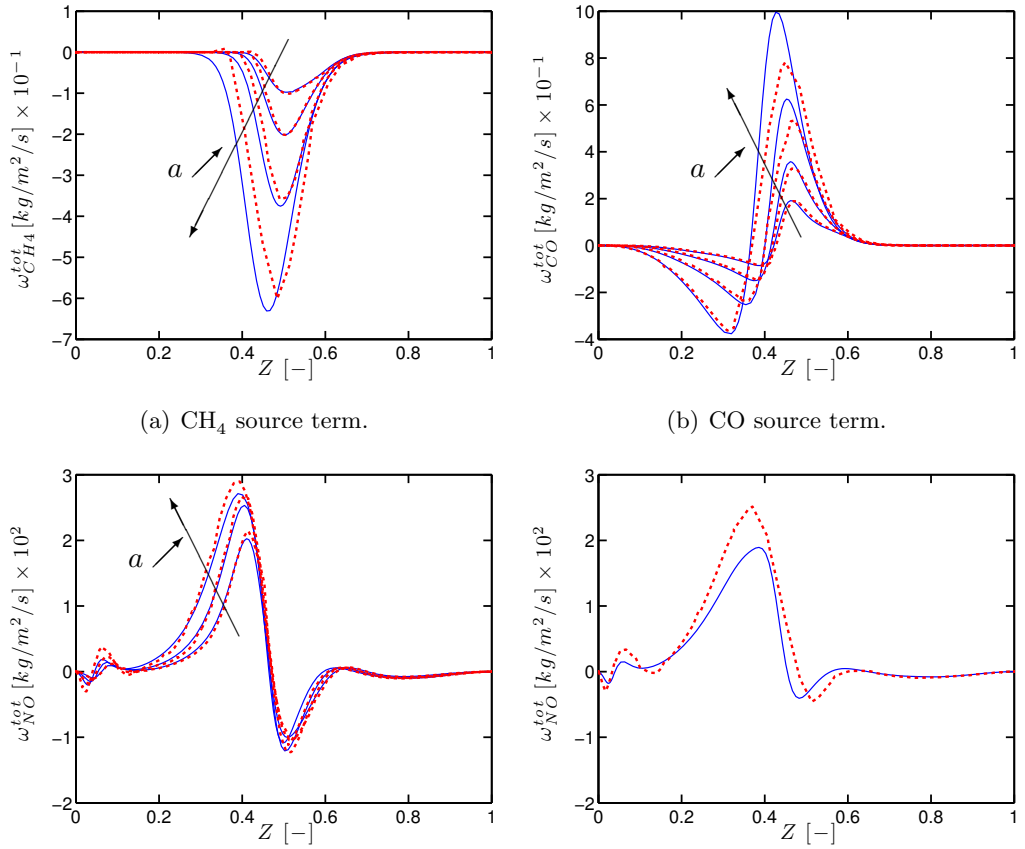

(a) CH_4 source term.

(b) CO source term.

(c) NO source term ($a = 40\ \ 80\ \ 160\,s^{-1}$).

(d) NO source term ($a = 320\,s^{-1}$).

Figure 7.19: Counterflow computations in Sandia flame D conditions at global strain rates a = 40, 80, 160, 320 s^{-1}. Comparison of source terms from Cantera (—) and AVBP (· · ·) in Z-space.

ported species (Fig. 7.20(a)) and QSS species (Fig. 7.20(b)) chemical times are rather insensitive to strain rate. All transported species exhibit time scales significantly lower than the unsteady time-step Δt, thus justifying full explicit integration of the chemical system in this case. It should be also noted that 6 QSS species exhibit time-scales lower than Δt: this shows again the importance of QSSA to reduce the overall stiffness of the chemical system.

Impact of transport modelling

Cantera computations were conducted with Trans_Mix transport, whereas Trans_ARC detailed is employed in the AVBP computations. It was checked that the flame structure obtained with Cantera computations with Trans_ARC performed in Sec. 7.4.2 are identical. Similarly, global flame quantities are impacted by less than 1% by simplified transport modelling.

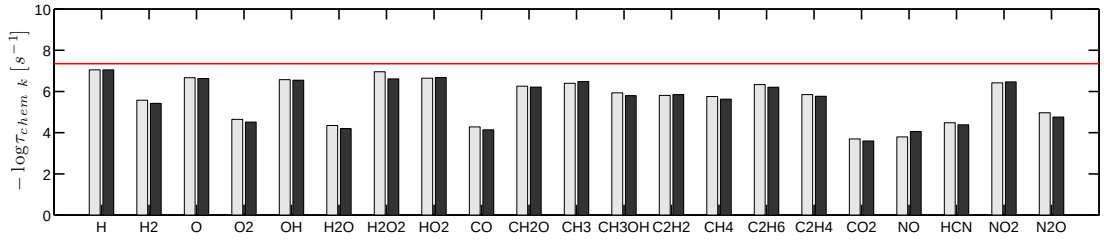

(a) Transported species.

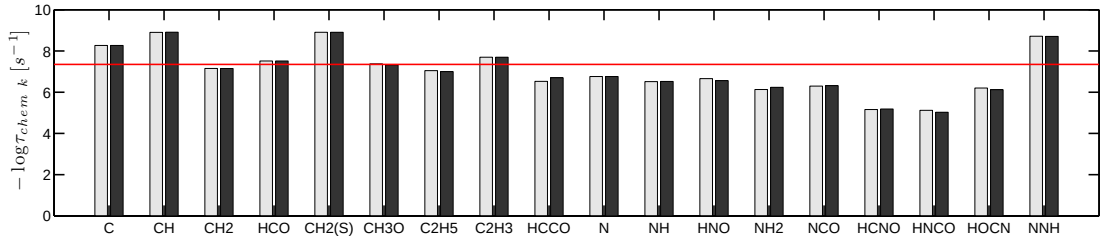

(b) QSS species.

Figure 7.20: Species chemical times extracted from counterflow flame computations in Sandia flame D conditions at global strain $a = 40\,\mathrm{s}^{-1}$ (white) and $a = 320\,\mathrm{s}^{-1}$ (black). The continuous line corresponds to the time-step of the computations ($\Delta t = 4.5 \times 10^{-8}\,\mathrm{s}$)

7.4.5 Impact of grid resolution and flow prediction

The discrepancies observed for the higher strain rate case ($a = 320\,\mathrm{s}^{-1}$) may arise from insufficient grid resolution. Indeed, for counterflow diffusion flames, as detailed in Sec. 4.3, the flame scales are related to the flow scales, thus they decrease for increasing strain rate. The mixing thickness is related to the scalar dissipation rate, as

$$l_Z \quad 1/\mid \nabla Z \mid . \tag{7.3}$$

In the present case $l_Z = 2.5\,\mathrm{mm}$ for $a = 320\,\mathrm{s}^{-1}$, therefore the mixture fraction gradient is discretised with 16 grid points, which appears to be sufficient to correctly capture the mixing process. Following Eq. 4.32, the reaction layer thickness l_{reac} is expected to be lower and proportional to l_Z. l_{reac} can be estimated by considering the region where the CH_4 source term is above 5% of the peak value [49]. In the present case, this gives $l_{reac} = 0.45\,\mathrm{mm}$, so that the reaction zone is discretised with 3 grid points only. For lower strain rate values at least 5 grid points were located in the reaction zone.

The sufficient resolution of the mixing layer is confirmed by performing the case $a = 320\,\mathrm{s}^{-1}$ with a refined grid with a characteristic size $\Delta x = 0.075\,\mathrm{mm}$, i.e. 2 times smaller than the reference case. The comparison of scalar dissipation profiles in Z-space of Fig. 7.21 shows no difference between the 2 grids. The obtained peak value is still lower for the AVBP case, and appears to be closest to the Cantera flame at

$a = 280\,\mathrm{s}^{-1}$ rather than the imposed value of $a = 320\,\mathrm{s}^{-1}$. This strong difference in terms of mixing structure can significantly affect species concentrations and source terms, therefore both Cantera flames at $a = 320\,\mathrm{s}^{-1}$ and $a = 280\,\mathrm{s}^{-1}$ are retained for further comparisons.

The species profiles comparison in Z-space (Fig. 7.22) shows that the AVBP flame is much closer to the Cantera flame with $a = 280\,\mathrm{s}^{-1}$. In particular, overall NO concentrations are significantly increased from $a = 320\,\mathrm{s}^{-1}$ to $a = 280\,\mathrm{s}^{-1}$. The impact of the grid resolution is significant for HO_2 and NO, which are significantly closer to the Cantera flame at $a = 280\,\mathrm{s}^{-1}$ for the refined case. Similarly, Figure 7.23 reveals a slight improvement of the prediction of CH_4, CO and NO source term peaks with finer grid resolution.

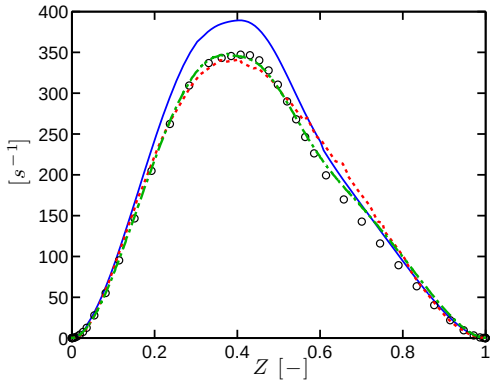

Figure 7.21: Counterflow computations in Sandia flame D conditions at global strain rate $a = 320\,s^{-1}$. Comparison of scalar dissipation rate profiles from Cantera (—), AVBP with baseline grid resolution ($\Delta x = 0.15\,\mathrm{mm}$) ($\cdots$) in Z-space and AVBP with refined grid ($\Delta x = 0.075\,\mathrm{mm}$) ($- \cdot -$) . Cantera flame at global strain rate $a = 280\,\mathrm{s}^{-1}$ ($\circ$) is also shown.

Global quantities are further compared for the two grids in Table. 7.4 between AVBP and Cantera flames at $a = 320\,\mathrm{s}^{-1}$. The departure from Cantera is slightly reduced in the refined case, even if a gap of 23% is still observed for NO formation. This gap is essentially due to the different mixing structure, to which NO is highly sensitive. When comparing the two AVBP cases with the Cantera flame at $a = 280\,\mathrm{s}^{-1}$, which is the closest in terms of mixing structure, the discrepancy observed for NO production is reduced to 6% for the refined grid case (Tab. 7.5). The departure remains higher with the coarse grid (30%), which is attributed to the insufficient resolution of the NO source term peaks observed in Fig. 7.23(c).

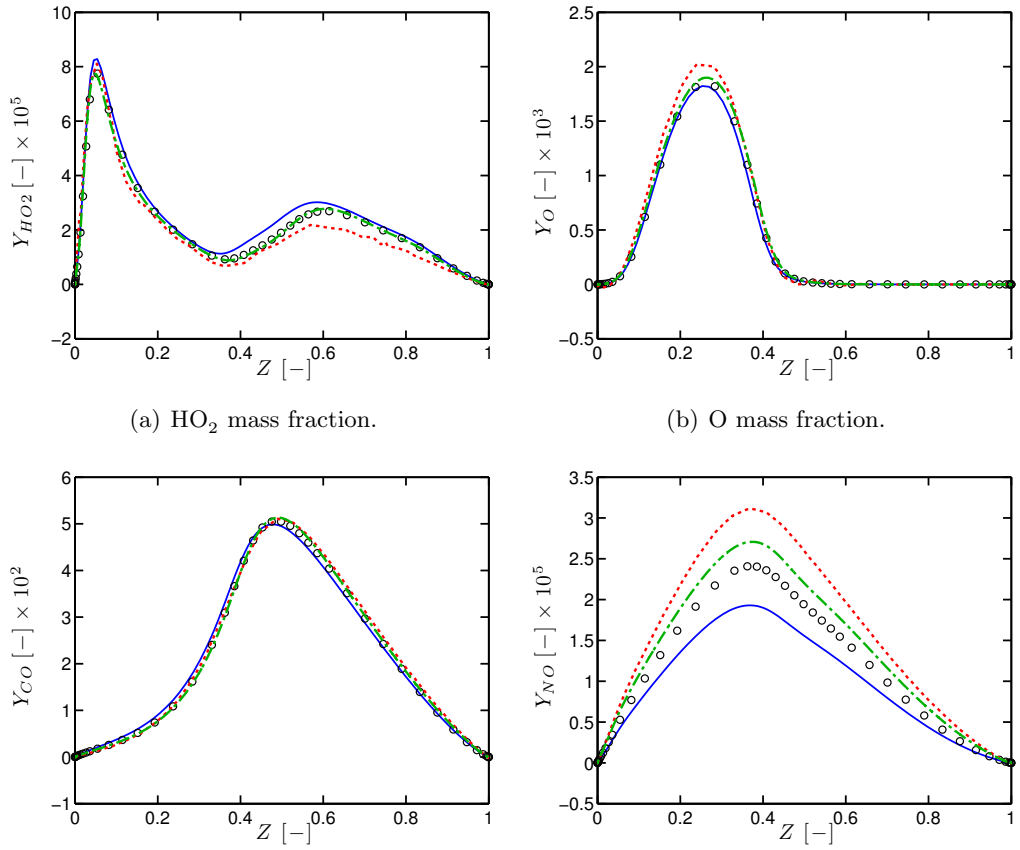

(a) HO_2 mass fraction.

(b) O mass fraction.

(c) CO mass fraction.

(d) NO mass fraction.

Figure 7.22: Counterflow computations in Sandia flame D conditions at global strain rate $a = 320\,s^{-1}$. Comparison of species mass fractions from Cantera (—), AVBP with baseline grid resolution ($\Delta x = 0.15\,\mathrm{mm}$) ($\cdots$) in Z-space and AVBP with refined grid ($\Delta x = 0.075\,\mathrm{mm}$) ($\cdot - \cdot -$) . Cantera flame at global strain rate $a = 280\,\mathrm{s}^{-1}$ ($\circ$) is also shown.

	Cantera	AVBP: $\Delta x = 0.15\,\mathrm{mm}$	AVBP: $\Delta x = 0.075\,\mathrm{mm}$
$-\omega^{tot}_{\mathrm{CH_4}}$ [kg/m^2/s]	15.1×10^{-3}	-4.6%	-2.6%
$\omega^{tot}_{\mathrm{CO}}$ [kg/m^2/s]	9.4×10^{-3}	-7.5%	-3.2%
$\omega^{tot}_{\mathrm{NO}}$ [kg/m^2/s]	4.4×10^{-6}	+40%	+23%

Table 7.4: Counterflow flames in Sandia flame D conditions. Integrated source terms of CH_4, CO and NO. Comparison of Cantera flame and AVBP flame at global strain rate $a = 320\,\mathrm{s}^{-1}$ for two grid resolutions.

7.5 Conclusions

The validation cases performed in this chapter illustrate the large range of validity of ARCs, which in the present case extends largely beyond the initial derivation range in terms of operating points and combustion regimes. This is essentially due to the fact that the derivation process preserves an accurate physical description of the inner flame

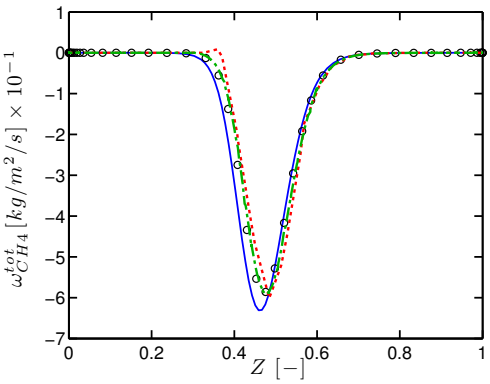

(a) CH_4 source term.

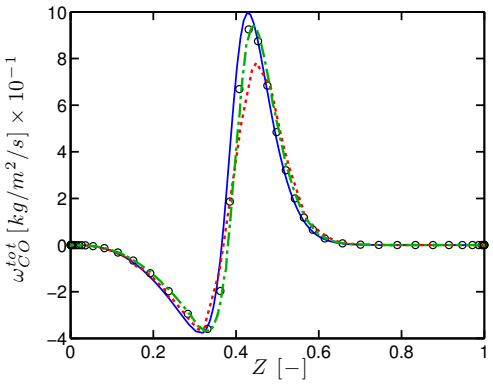

(b) CO source term.

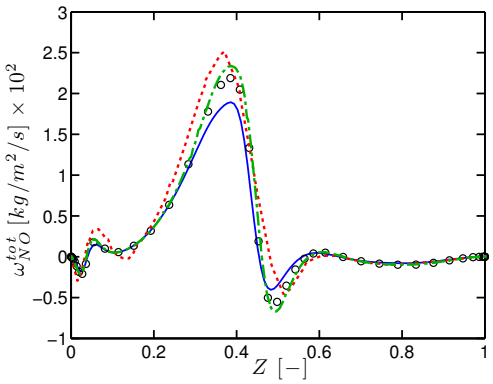

(c) NO source term ($a = 40\ \ 80\ \ 160\,s^{-1}$).

Figure 7.23: Counterflow computations in Sandia flame D conditions at global strain rate $a = 320\,s^{-1}$. Comparison of source terms from Cantera (—), AVBP with baseline grid resolution ($\Delta x = 0.15\,\text{mm}$) ($\cdots$) in Z-space and AVBP with refined grid ($\Delta x = 0.075\,\text{mm}$) ($\cdot - \cdot -$) .

	Cantera	AVBP: $\Delta x = 0.15\,\text{mm}$	AVBP: $\Delta x = 0.075\,\text{mm}$
$-\omega^{tot}_{\text{CH}_4}$ [kg/m^2/s]	14.4×10^{-3}	0%	+2%
ω^{tot}_{CO} [kg/m^2/s]	8.8×10^{-3}	-1%	+3%
ω^{tot}_{NO} [kg/m^2/s]	5.1×10^{-6}	+29%	+6%

Table 7.5: Counterflow flames in Sandia flame D conditions. Integrated source terms of CH_4, CO and NO. Comparison of Cantera flame at global strain rate $a = 280\,\text{s}^{-1}$ and AVBP flame at global strain rate $a = 320\,\text{s}^{-1}$ for two grid resolutions.

structure.

The ARC_22_GRI211 and ARC_22_GRI30 exhibit a very satisfactory agreement with their respective reference detailed mechanisms for non-premixed cases at atmospheric conditions: both are retained for the numerical study of the Sandia flame D in Chapter 8, in order to quantify the sensitivity of the results to the chosen mechanism. The

ARC_22_GRI211 will be further applied for the study of the SGT-100 configuration in Chapter 9.

The validation cases performed indicate that the Trans_ARC approximation is satisfactory in terms of accuracy. Similarly, when ARCs are employed with relatively loose grid discretisation typically encountered for three-dimensional configuration, the uncertainty introduced by the numerical errors is of the same order as the error introduced by the reduction process. The numerical accuracy of the methodology is thus largely satisfactory.

Part III

Applications

8

LES of the turbulent Sandia flame D

Contents

8.1 Objectives

The objective of this chapter is to demonstrate the capability of ARCs to accurately predict pollutant emissions in turbulent configurations, by performing a highly-resolved LES of the Sandia flame D configuration. This turbulent non-premixed flame was studied experimentally by *Barlow and Frank* [10]. It is of particular interest as a large amount of data is available for temperature, major species and pollutant concentrations in the flame and post-flame region, compared to more realistic gas turbine configuration, for which pollutant data are often limited to exhaust gas composition measurements. Thus, this configuration was extensively used as a validation case for pollutant formation modelling, as it contains essential features of turbulence/chemistry interaction. To

the best of our knowledge, this is the first attempt to perform LES of the Sandia flame D with a realistic chemistry including NO_x formation, which gives access to a wide variety of information about the flame structure and the chemical response to the turbulent flow. The sensitivity of the results to the retained chemical description is also addressed.

Two ARCs, namely the ARC_22_GRI211 and ARC_22_GRI30 derived in Sec. 6.2 were evaluated on canonical cases representative of the Sandia flame D in Sec. 7.4.1. Both are used in the LES computations to evaluate the differences between the two mechanisms, notably on pollutant prediction in the turbulent flame. The prediction capability of LES is evaluated by comparison with available measurements in terms of mixing, temperature and pollutant concentrations. The chemical response to unsteady flow features in terms of flame structure and pollutant formation is further analysed and compared with the canonical flamelet solutions, enabling a better understanding of pollutant formation in this turbulent flame.

8.2 Experimental configuration

The burner consists of three coaxial jets shown in Fig. 8.1. The main central jet is injected through a pipe of diameter $D = 7.2\,\text{mm}$ with a bulk velocity of $49.6\,\text{m/s}$. It is composed of a rich methane-air mixture, with an equivalence ratio $\phi = 3.17$, at ambient conditions. The flame is stabilised via a pilot flow around the main jet, having a bulk velocity of $11.4\,\text{m/s}$. It consists of burnt gases at an equivalence ratio $\phi = 0.77$. Finally, an external coflow of air at ambient conditions is injected at $0.9\,\text{m/s}$ and surrounds the pilot jet. This configuration is particularly well-documented and is a reference case for NO model validation. The retained values for the three inlet compositions and temperatures in the LES computations are summarised in Tab. 8.1.

	T [K]	Y_{CH_4}	Y_{O_2}	Y_{CO_2}	Y_{H_2O}	Y_{CO}	Y_{NO}	ϕ
Main (Central)	294	0.156	0.197	0	0	0	0	3.17
Pilot	1880	0	0.054	0.111	0.0942	4×10^{-3}	2×10^{-5}	0.77
Coflow	291	0	0.230	0	0	0	0	0.0

Table 8.1: Composition (mass fractions) and temperature of the three inlets of the Sandia flame D retained for laminar and turbulent computations.

Measurements

Raman-Rayleigh measurements of species and temperature were performed by *Barlow and Frank* [10] at several axial locations located at 1, 2, 3, 7.5, 15, 30, 45, 60 and $75D$ from the main jet exit. The estimated uncertainties are 3% for temperature,

5% for major species and 15% for NO concentration. Two-component Laser Doppler Velocimetry (LDV) measurements are also available for the same measurement planes.

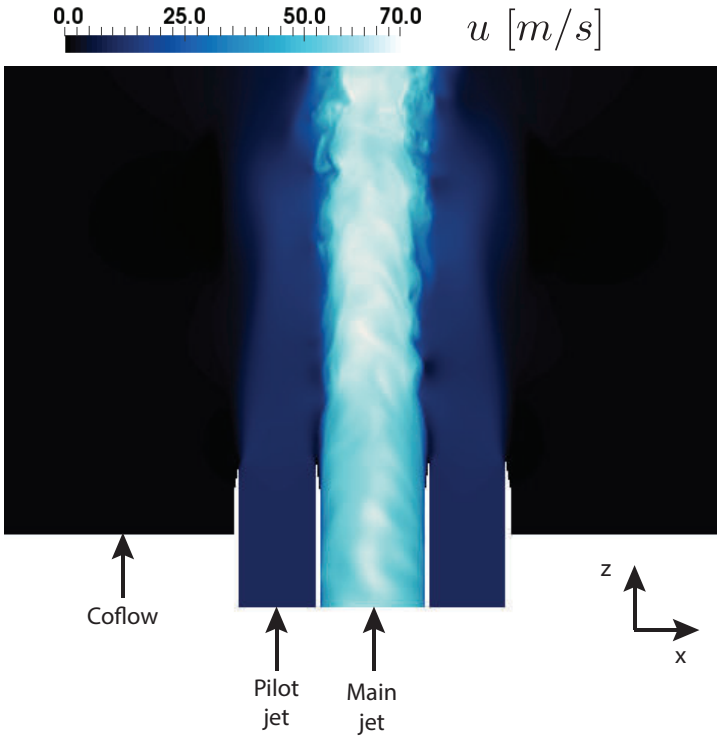

Figure 8.1: View of the three coaxial jets of the Sandia flame D configuration with instantaneous LES axial velocity field.

8.3 Previous studies of the Sandia flame D

In the last decade, the Sandia flame D has been the subject of various numerical studies, mainly using LES, but RANS studies [77] and PDF model calculations [32, 168, 210] were also performed and yield satisfactory prediction of temperature and major species. LES studies including NO prediction were mostly conducted with tabulated chemistry. Both premixed manifolds [148, 201] and non-premixed flamelet manifolds [85, 122, 201, 213] were employed. The turbulence-chemistry closure was generally based on a statistical approach using either presumed PDF [85, 86, 87, 122, 148, 201] or transported PDF closure [180, 213].

In these various studies, a satisfactory prediction of NO was generally obtained, with a typical accuracy that falls in the experimental uncertainty range. In addition, the NO prediction was found to be sensitive to the modelling assumptions employed. *Ihme and Pitsch* [85] and *Zoller et al.* [213] showed that a typical reduction of 20% of the peak NO concentration occurred under the effect of thermal radiation. Differences in

the description of NO_x chemistry between kinetics schemes was also shown to have a significant impact on the prediction, as shown by *Pecquery et al.* [148] and *Cao and Pope* [32]. However, the simultaneous prediction of NO and CO was more rarely addressed, and larger discrepancies were generally observed for CO, as pointed out in the work of *Vreman et al.* [201].

The use of reduced chemistry was also considered for Sandia flame D simulations. *Mustata et al.* [140] employed a four-step GRC combined with an Eulerian Monte Carlo field method, and *Raman and Pitsch* [169] employed a 16-species ARC combined with a Lagrangian particle scheme for subgrid closure. More recently, *Jones and Prasad* [94] employed a 15-step ARC [191] on the Sandia Flame Series (D, E and F) combined the Eulerian stochastic method for subgrid closure. A very good agreement with measurements was obtained for temperature and major species. CO concentrations were satisfactorily predicted as well. However NO_x chemistry was not included in any of these studies.

8.4 Numerical setup

LES is performed using AVBP with the TTGC scheme [39]. The three inlets and the outlet are described by Navier-Stokes Characteristic Boundary Conditions (NSCBC) [160] to ensure proper treatment of acoustics. The computational grid is fully unstructured and comprises 375 million tetrahedral elements. The characteristic element size is $\Delta x = 90\,\mu m$ in the injection tubes and in the flame region, down to the axial position $z = 3D$. Downstream of this axial position, the grid is linearly stretched to reach a characteristic size $\Delta x = 150\,\mu m$ at $z = 7.5D$ which is kept until $z = 30D$. The grid is further coarsened downstream. The time step imposed by the acoustic CFL condition is $\Delta t = 16\,ns$. This low value enables direct explicit integration of the chemical source terms of the two ARCs.

8.4.1 Flame-turbulence interaction

The Kolmogorov length scale estimated *a priori* as $\eta_\kappa \sim l_t\, Re_t^{-3\ 4}$ [165], where Re_t is the turbulent Reynolds number and l_t is the integral length scale, is found here about $\eta_\kappa \simeq 15 - 45\,\mu m$, with l_t based on the main jet diameter and u' based on measured rms velocity at the main jet exit. In the flame region the ratio of the grid size Δx to the Kolmogorov length scale η_κ falls in the range $\dfrac{\Delta x}{\eta_\kappa} \sim 2 - 6$. Thus the unresolved scales are expected to represent a very small part of the total fluctuating energy. This is supported by the very small values obtained for the subgrid turbulent viscosity calculated with the SIGMA eddy viscosity model [144], except in the central

core of the main jet where the subgrid turbulent viscosity is of the order of the laminar viscosity. In addition, numerical studies of chemical response of laminar methane-air diffusion flames to unsteady strain rate by *Im et al.* [88] indicates that the response of flame structure is rapidly suppressed for high frequencies fluctuations (typically beyond 1000 Hz). In the present study, the typical lifetime of subgrid turbulent structures can be estimated as

$$\tau_{\Delta x} = k_{\Delta x}/\epsilon = u_{\Delta x}^2/\epsilon \tag{8.1}$$

where $k_{\Delta x}$ is the kinetic energy at the filter scale Δx. ϵ is the rate of energy dissipation, which scales under the turbulent energy cascade assumption as [165]

$$\epsilon \quad \frac{u_{\Delta x}^3}{\Delta x} \simeq \frac{u'^3}{l_t}\,. \tag{8.2}$$

From these two equations, the typical lifetime is estimated to be $\tau_{\Delta x} = 0.1$ ms which corresponds to a characteristic frequency $f_{\Delta x} = 10\,000$ Hz, which is thus expected to be too high to impact the flame structure. Based on these observations, sub-grid flame-turbulence interaction is neglected in the present work.

8.4.2 Turbulent flow injection

The theoretical velocity profile corresponding to a turbulent pipe flow at the corresponding Reynolds number $Re = 22\,400$ is imposed at the inlet of the main injection tube, along with velocity fluctuations superimposed with a turbulent intensity matching the experimental data ($u' = 2$ m/s). This allows to recover the experimental velocity profiles at the first measurement axial location $z/D = 1$. The turbulent boundary layer is not resolved on the grid ($\Delta x \sim 0.09$ mm) and a slip velocity condition is applied on the injection tube walls.

8.4.3 Radiative heat losses

An *a posteriori* evaluation of the heat losses due to thermal radiation using the optically-thin-limit model described in [178] shows that they represent only 3% of the total heat release rate between the jet exits and the axial location $z = 30D$. Previous numerical studies [85, 213] of the Sandia flame D suggested that radiative effects have a very limited impact on the temperature and major species in this flame. The impact on NO formation remained limited as well, with no significant impact before $z = 40D$ and a reduction of about 10 to 20% afterwards. Based on these observations, radiative heat losses are not considered in the present work.

8.4.4 Averaging procedure

The flow-through time of the configuration based on the bulk velocity of the main jet and the distance between the end of the injection tube and the axial location $z = 30D$ is about 4.3 ms. Statistics are collected over 15 ms for the ARC_22_GRI211 case and over 8 ms for the ARC_22_GRI30 case. In addition, azimuthal averaging is applied when considering radial distributions of mean and root-mean-square (rms) quantities.

8.5 Results

The ARC_22_GRI211 and ARC_22_GRI30 mechanisms were found to yield almost identical LES results. Thus they are presented as "ARC_22" without distinction, except for quantities related to NO for which differences between the two mechanisms are observed, similarly to the laminar cases.

Instantaneous snapshots of mixture fraction, temperature and NO mass fraction fields in the mid-plane at the same physical instant are shown in Fig. 8.2. The mixing layers between the 3 jets develop, generating turbulent structures that grow and lead to jet opening. The shear layer between the pilot jet and main jet destabilises faster than the shear layer between the coflow and the pilot jet, as indicated by the larger amount of fine-scale structures. Note already the isolated pockets of high NO concentration between $z = 15D$ and $z = 30D$, located in regions of high temperature.

The ratio of subgrid turbulent to laminar viscosity is commonly used to estimate *a posteriori* the ratio of resolved to unresolved scales. Figure 8.3 shows a scatter plot of this ratio at axial locations $z = 7.5D$ and $z = 15D$. The mixture fraction Z follows the same definition as in Sec. 7.4.1. The subgrid turbulent viscosity is at maximum of the order of the laminar viscosity in the central region of the jet, where Z is close to 1, and is of the order of 0.02 around stoichiometry, with maximum values close to 0.1. Based on this ratio, a rough estimate of the ratio of the grid size to the Kolmogorov scale can be obtained as $\Delta x/\eta_\kappa = (\nu_t/\nu_{lam})^{1\ 2}/C_s$ [97], where $C_s^2 = 0.032$. With this expression, $\Delta x/\eta_\kappa \sim 5.6$ is found in the central core which is close to the *a priori* estimation given in Sec. 8.4.1. In the range $Z = 0.2 - 0.6$ where the reaction layer is located, the turbulent viscosity is found to be negligible, thus validating the assumption of neglecting the subgrid-scale turbulence-chemistry interactions.

8.5.1 Velocity profiles

A good agreement is obtained between LES results and experiments for the radial profiles of mean axial velocity at the different axial locations (Fig. 8.4). The mean

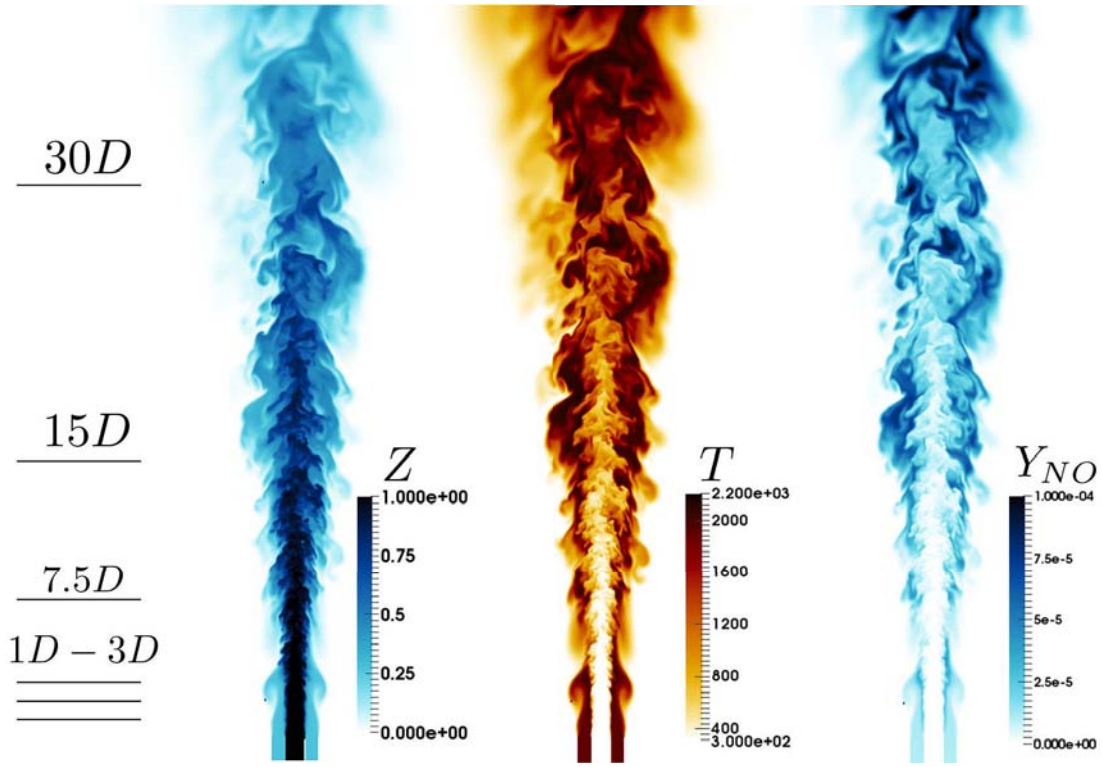

Figure 8.2: Sandia flame D: Instantaneous fields in the mid-plane of mixture fraction (left), temperature (middle) and NO mass fraction (right) for ARC_22_GRI211. The measurement axial locations are indicated on the left side.

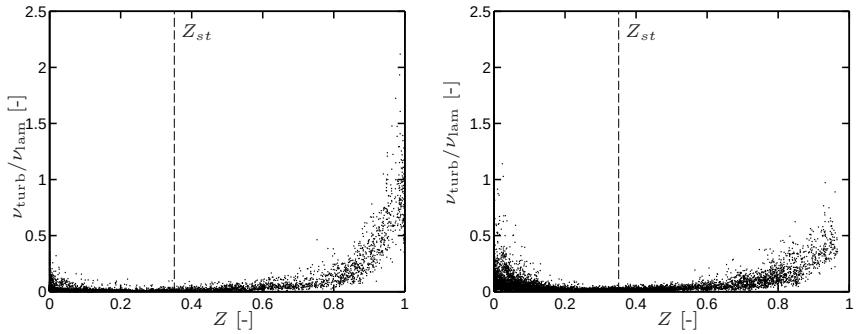

(a) Axial position $z = 7.5D$. (b) Axial position $z = 15D$.

Figure 8.3: Sandia flame D: Scatter plot of the ratio of sub-grid turbulent to laminar viscosity vs mixture fraction at axial locations $z = 7.5D$ and $z = 15D$.

velocity gradient in the shear layer between the main and the pilot jet is well captured even if it is slightly shifted towards the central axis. The overall axial velocity error of about 4% is within the experimental uncertainty margin. It is slightly more pronounced close to the centerline for axial positions in the range $z = 3D - 15D$.

Rms (root mean square) axial velocity levels shown in Fig. 8.5 are also in good agree-

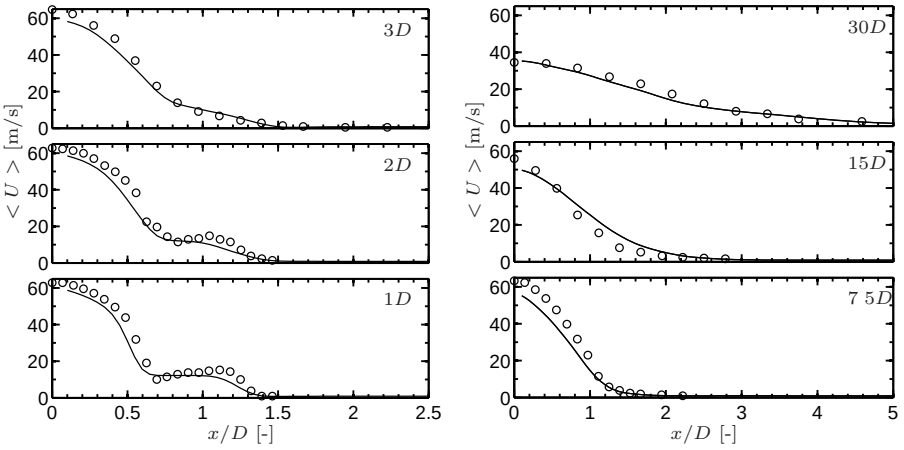

Figure 8.4: Sandia flame D: Radial profiles of mean axial velocity at several axial positions. – ARC_22, ∘ Experimental data.

ment with the experimental data. Some discrepancies appear in the first measurement plane, where the rms values are under-estimated in the exit region of the central main jet, i.e at $x/D = 0 - 0.6$. This may be a consequence of the flow injection with slipping velocity at walls. However, the axial velocity rms levels are well recovered in the measurement planes located downstream. As it follows the radial position of the shear layer, the peak of the fluctuations slightly shifts radially towards the centre.

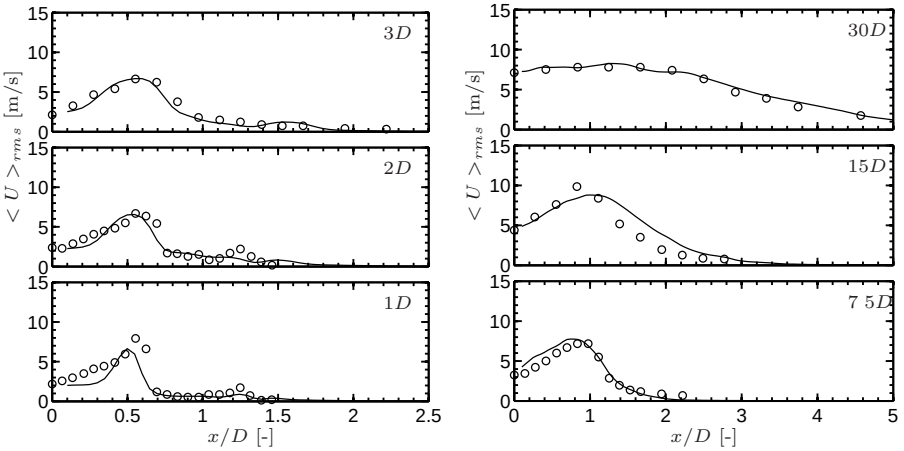

Figure 8.5: Sandia flame D: Radial profiles of rms axial velocity at several axial positions. – ARC_22, ∘ Experimental data.

8.5.2 Mixture fraction and temperature profiles

The axial mean mixture fraction profile is shown in Fig. 8.6(a). The evolution of the mixture fraction is well captured on the overall, despite a slight over-prediction of the mixing rate downstream the axial position $z = 10D$. Likewise, the axial mean

temperature profile shown in Fig. 8.6(b) is slightly over-predicted downstream the axial position $z = 10D$, which is consistent with the mixture fraction profile. The levels of mixture fraction and temperature fluctuations shown in Fig. 8.7 are in good agreement with the experiments, except at the first location downstream the injection tubes, where fluctuations of the mixture fraction is still close to 0 in the LES whereas they are already significant in the experiments. This non-zero measured rms value of the mixture fraction is however contradictory with the almost zero temperature fluctuation measured at the same location. Radial profiles of the mean mixture fraction and the mean temperature at the different locations, shown in Fig. 8.8 and in Fig. 8.9 respectively, are also in good agreement with the experimental data except at location $z = 30D$ where the profiles flatten too much, which might be due to the relatively coarser grid at this location.

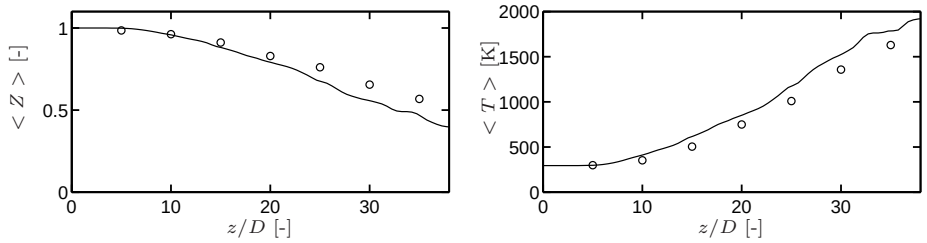

(a) Mixture fraction (b) Temperature

Figure 8.6: Sandia flame D: Axial profiles of mean mixture fraction and temperature. – ARC_22, ∘ Experimental data. .

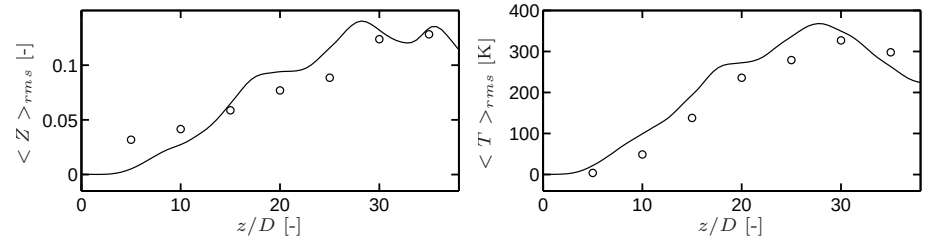

(a) Rms mixture fraction. (b) Rms temperature.

Figure 8.7: Sandia flame D: Axial profiles of a) rms mixture fraction and b) rms temperature fluctuations. – ARC_22, ∘ Experimental data.

8.5.3 NO and CO profiles

Figure 8.10(a) shows the mean CO mass fraction along the centerline, well captured by ARC_22. The slight overestimation is related to the similar overestimation of the mixing rate along the centerline seen in Fig. 8.6(a). The mean CO mass fraction radial profiles of Fig. 8.11 reveal also a very good agreement with the experiments and in

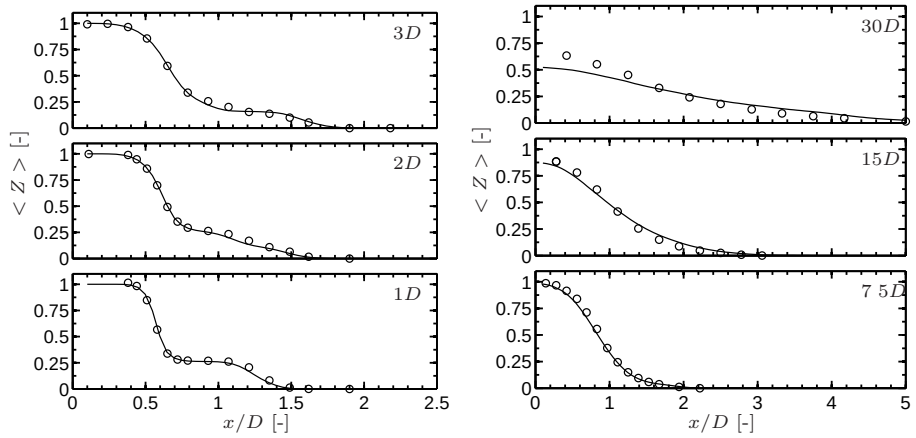

Figure 8.8: Sandia flame D: Radial profiles of mean mixture fraction at several axial positions. – ARC_22, ∘ Experimental data.

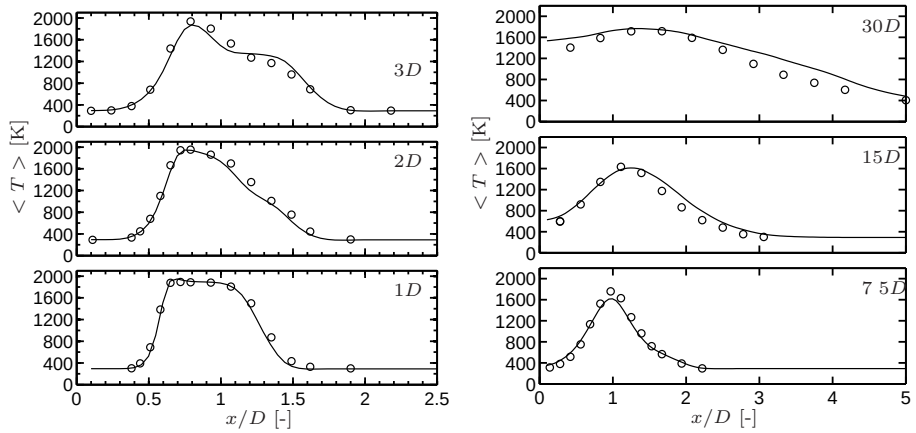

Figure 8.9: Sandia flame D: Radial profiles of mean temperature at several axial positions. – ARC_22, ∘ Experimental data.

particular a good prediction of the peak in the reactive zone.

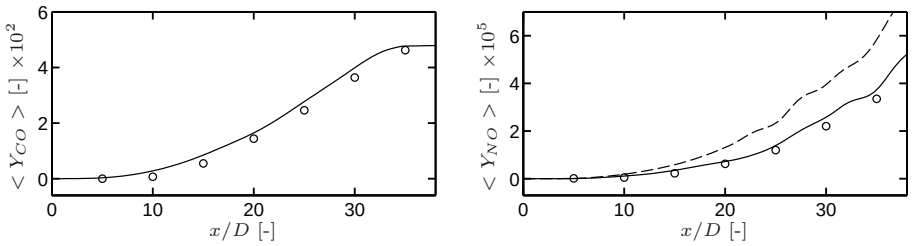

(a) CO mass fraction (b) NO mass fraction

Figure 8.10: Sandia flame D: Axial profiles along the centerline of a) mean CO mass fraction for ARC_22s (—) and b) NO mass fraction for ARC_22_GRI211 (–) and ARC_22_GRI30 (––). Experimental data ∘ .

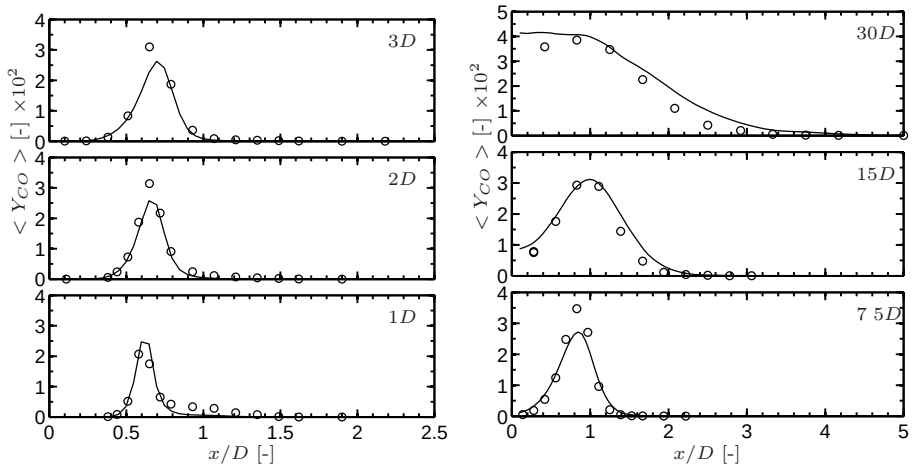

Figure 8.11: Sandia flame D: Radial profiles of mean CO mass fraction at several axial positions. – ARC_22, ∘ Experimental data.

The situation is different for NO, for which the two versions of the reduced mechanisms are now distinguished. As shown in Fig. 8.10, the axial evolution of the mean NO mass fraction is well reproduced by ARC_22_GRI211, while ARC_22_GRI30 leads to significantly higher values downstream $z = 15D$. The NO radial profiles at axial positions between $z = 1D$ and $z = 7.5D$ shown in Fig. 8.12 indicate that the NO peak value in the reaction zone is slightly overestimated with GRI 3.0, whereas ARC_22_GRI211 tends to underpredict the NO peak value. Further downstream, there is a significant overestimation of NO levels at axial position $z = 30D$ with ARC_22_GRI30. This over-estimation, almost by a factor 2 close to the central region at $z = 30D$ is consistent with previous observations [32] and with the laminar cases.

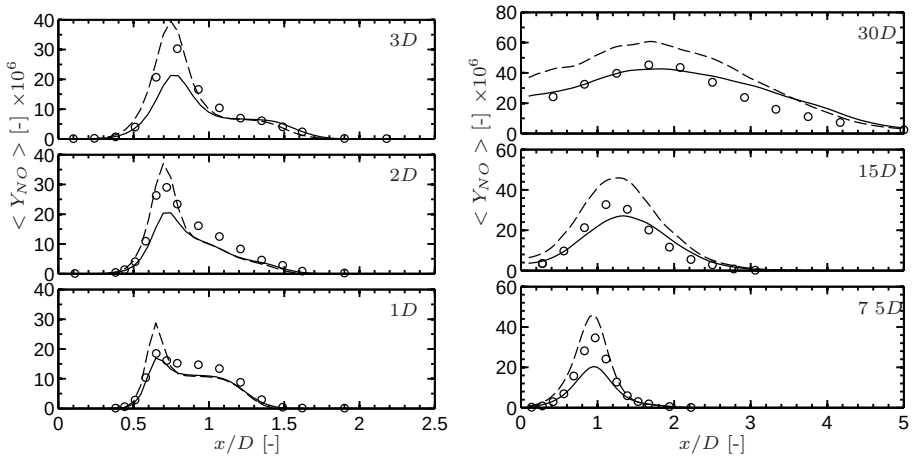

Figure 8.12: Sandia flame D: Radial profiles of mean NO mass fraction at several axial positions. ARC_22_GRI211 (–), ARC_22_GRI30 (––), and experimental data (∘).

8.6 Analysis of the flame structure

8.6.1 Representative laminar cases

In the turbulent flame, the fresh air of the coflow can mix with the hot air of the pilot prior to combustion of the fuel from the central jet, which then burns with a mix of fresh air and burnt gases. The presence of the pilot can significantly affect the flame structure. Two series of representative counterflow strained flamelets can be defined, corresponding to the two extreme situations where no mixing occurs between pilot and coflow prior to combustion.

- In the first series, the fuel burns with the coflow jet, with no impact of the pilot: the conditions of the coflow jet are imposed on one side and the conditions of the main central jet on the other side. It is named **coflow flamelet series** hereafter. Note that this flamelet collection has been employed in several LES studies employing tabulated chemistry [85, 201, 213], and has been validated numerically in the AVBP solver in Sec. 7.4.1.
- In the second series, named **pilot flamelet series** in the following, the pilot jet conditions replace the coflow ones, allowing to evaluate the influence of the pilot jet on the flame structure.

In this subsection, the results obtained for the coflow flamelet series are recalled and extended to the pilot flame series, to provide laminar references for the comparison with the turbulent case. Again, the response to strain is assessed by varying the inlet velocities. To facilitate the comparison with the turbulent cases, rather than using the global strain, the strain rate is evaluated via the scalar dissipation rate

$$\chi = 2D_T \mid \nabla Z \mid^2, \tag{8.3}$$

where D_T is the thermal diffusivity. From this definition, the strain rate of the flame is taken equal by definition to

$$a = \chi_{\,Z=0.4}. \tag{8.4}$$

The choice $Z = 0.4$ is based on the observation that chemical source terms and scalar dissipation rate peaks close to this mixture fraction, as will be further highlighted by the flame structures of Sec. 8.6.

The response of the different mechanisms to strain rate is shown in Fig. 8.13 for the two flamelet series. Note that a satisfactory agreement is obtained between the two ARCs and detailed mechanisms, with maximum deviation of 15% for NO production for ARC_22_GRI30. The maximum temperature (Fig. 8.13(a)) decreases less rapidly

with strain for the pilot flamelet series. The rapid decrease of maximum temperature for the coflow flamelet series for high strain values indicates that the extinction limit is reached around $a = 450\,\mathrm{s}^{-1}$. For the pilot series, a plateau value is reached corresponding to the pilot inlet temperature, around $a = 650\,\mathrm{s}^{-1}$ for GRI 2.11 and $a = 750\,\mathrm{s}^{-1}$ for GRI 3.0. When this plateau is reached, the total fuel consumption shown in Fig. 8.13(b) rapidly decreases to fall to values close to zero even if the flame is not, strictly speaking, extinct. The comparison with the total fuel consumption from the coflow series shows that the feeding with hot products from the pilot promotes combustion at high strain rates and delays the extinction.

CO production shown in Fig. 8.13(c) is also significantly impacted by the presence of the pilot. Notably, for low to moderate strain values, CO production is much higher for the pilot flamelet series. For NO, again, a typical factor 2 is obtained for GRI 3.0 compared to GRI 2.11 for both flamelet series. The response of NO production is monotonic, and is not significantly impacted by the choice of the flamelet series, despite their very different maximum temperature.

In Fig. 8.14, the flame structure in mixture fraction space for the two flamelet series is compared. Figure 8.14(a) shows that the temperature levels are typically higher for the pilot flames for mixture fraction close to the pilot inlet value ($Z_{pilot} = 0.27$). The CH_4 source term (Fig. 8.14(b)) is similar for the two cases, but is shifted towards leaner mixture fraction for the pilot series. The same observation can be made for CO, for which, in addition, the destruction occurring around lean and stoichiometric conditions is significantly reduced for the pilot series, resulting in higher total CO production for this flame type. The NO source term is also shifted towards leaner mixture fraction, with lower absolute intensity for the pilot case, even it the response to strain indicated that it does not have a significant impact on the total NO production.

8.6.2 Comparison of turbulent flame structure with laminar cases

To further analyse the flame structure, scatter plots of several quantities as functions of the mixture fraction are extracted at axial locations $z = 7.5D$ and $z = 30D$. The ARC_22_GRI211 scheme is retained for the analysis, since it yields on the overall the most satisfactory results. The scatter plots from LES are compared with the experimental data and with counterflow laminar flames, at a strain rate value corresponding to the mean value of the LES. At location $z = 7.5D$, the temperature distribution is typical of a turbulent non-premixed flame (Fig. 8.15(a)), with turbulent fluctuations around a mean temperature profile, due to strain rate fluctuations. Few points have a temperature significantly below any laminar strained counterflow flame, which indicates

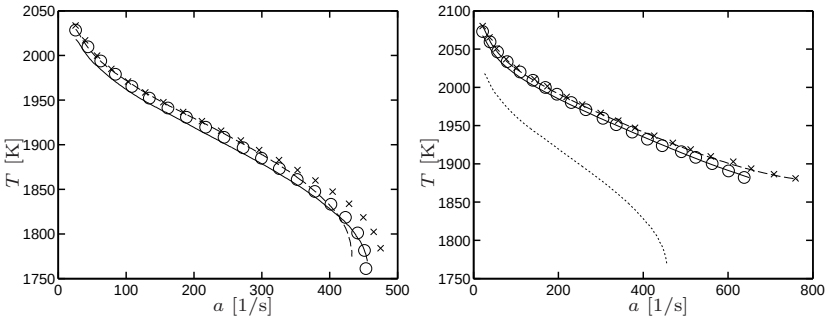

(a) Maximum temperature: coflow (left) and pilot (right) flamelet series.

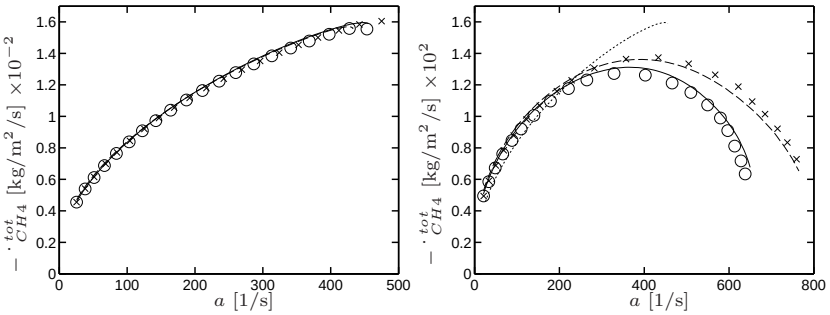

(b) Fuel consumption: coflow (left) and pilot (right) flamelet series.

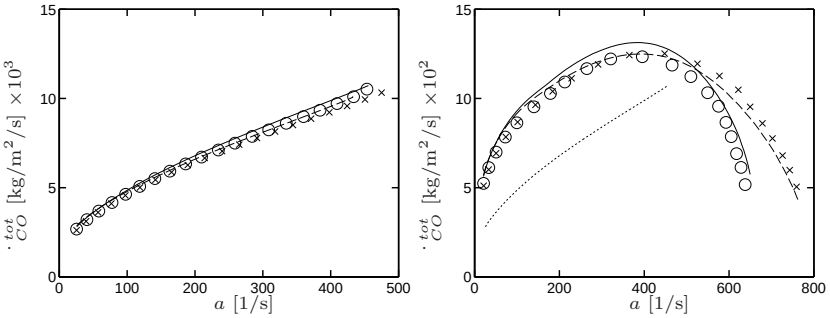

(c) CO production: coflow (left) and pilot (right) flamelet series.

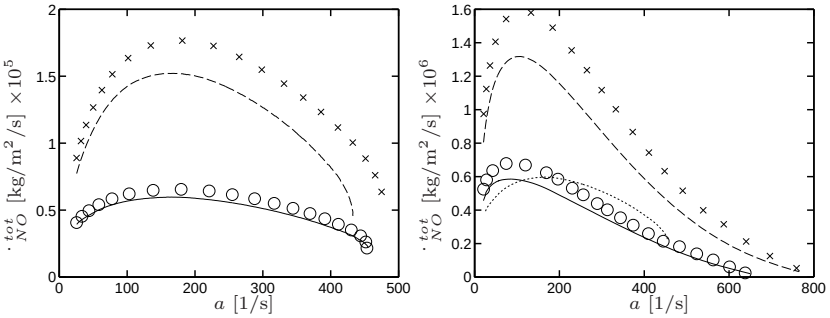

(d) NO production: coflow (left) and pilot (right) flamelet series.

Figure 8.13: Laminar counterflow flames. Comparison of the response to the strain rate a between GRI 2.11 (—), ARC_22_GRI211 (○), GRI 3.0 (−−), ARC_22_GRI30 (×) in terms of a) CH_4 total consumption rate, b) maximum temperature, c) CO total production rate and d) NO total production rate. The left side corresponds to the coflow flamelet series and the right side to the pilot flamelet series. The response of the coflow flamelet series with GRI 2.11 (···) is also recalled for the pilot flamelet series on the right side to ease up the comparison.

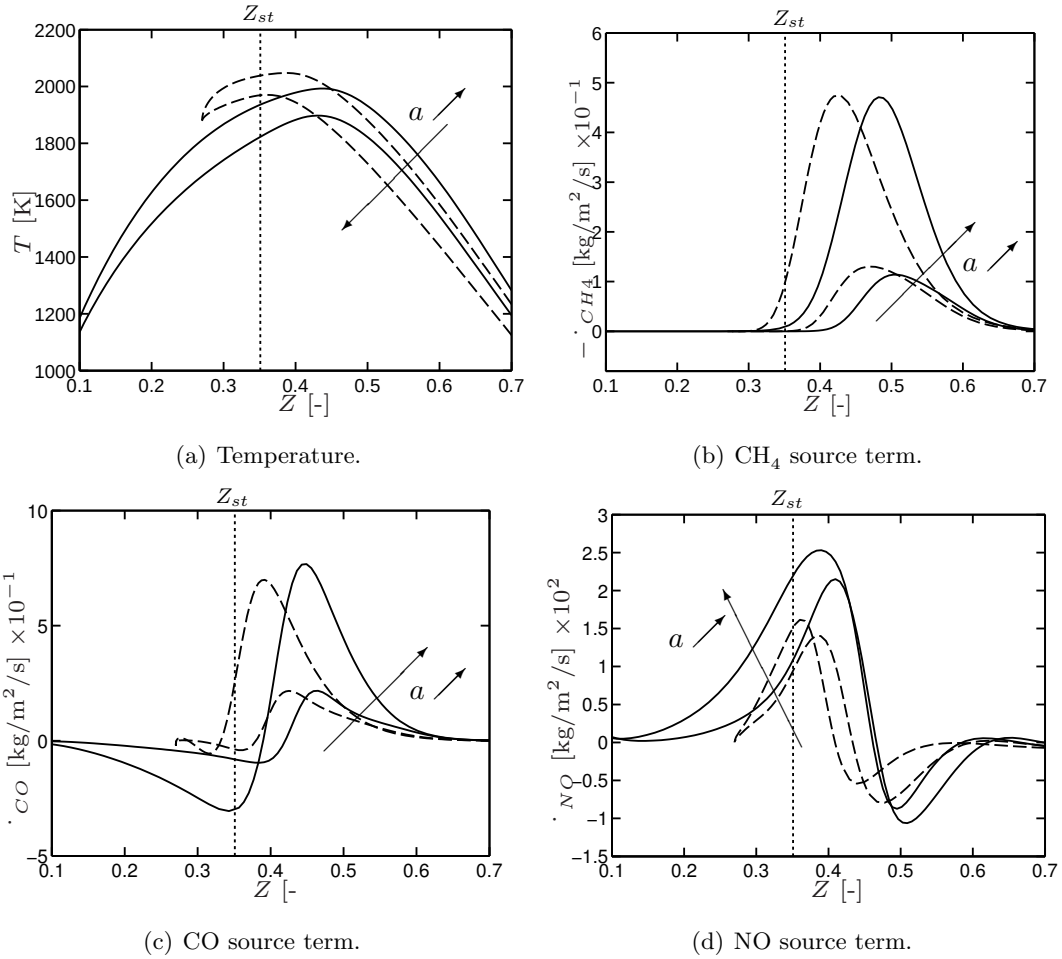

(a) Temperature.

(b) CH_4 source term.

(c) CO source term.

(d) NO source term.

Figure 8.14: Laminar counterflow flames with ARC_22_GRI211. a) Temperature, b) CH_4 source term, c) CO source term and d) NO source term vs mixture fraction. Comparison of coflow (—) and pilot (−−) counterflow flames at strain rates $a = 60\,\mathrm{s}^{-1}$ and $270\,\mathrm{s}^{-1}$.

a very low level of partial premixing and confirms the non-premixed flame structure at this location. The scatter plot from LES matches quite well with the experimental results, although the temperature dispersion in the rich core ($Z > 0.6$) is not fully captured.

Figure 8.15(b) shows that the global distribution of OH mass fraction, the peak in the reaction zone and the fluctuations are well reproduced. The CO and NO mass fraction distributions in mixture fraction space are shown in Fig. 8.15(c) and Fig. 8.15(d) respectively, and are again in good agreement with the experiments, although NO mass fraction is slightly underpredicted, consistently with the NO radial profiles of Fig. 8.12. Both CO and NO peak at rich conditions around $Z \simeq 0.4$. On the lean side, CO is rapidly oxidised in CO_2, leading to a sharp decrease of CO mass fraction. Both coflow and pilot laminar flame structures are consistent with the scatter plots of CO and NO.

To further analyse the flame structure, scatter plots of CH_4, CO and NO source terms are compared with reference flamelets at low and high strain values in Fig. 8.16. Despite the strong dispersion observed for the three source terms, most points fall in the envelope delimited by the weakly and highly strained cases.

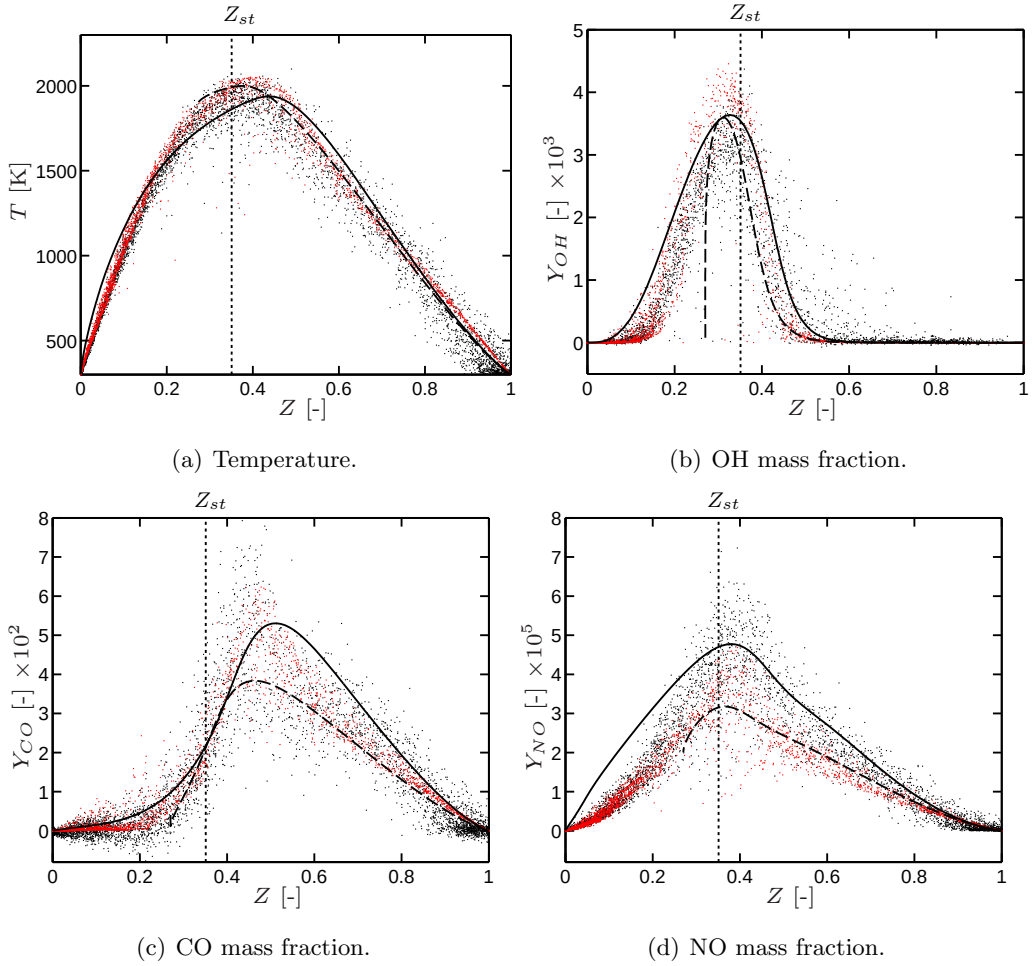

(a) Temperature.

(b) OH mass fraction.

(c) CO mass fraction.

(d) NO mass fraction.

Figure 8.15: Sandia flame D: Temperature, OH, CO and NO mass fractions vs mixture fraction at axial location $z = 7.5D$. Black dot: experiments, Red dot: LES. Coflow counterflow flame (—) and pilot counterflow flame (−−) at strain rate $a = 170\,\mathrm{s}^{-1}$.

Very similar results are obtained downstream at axial position $z = 30D$, as shown in Fig. 8.17 for temperature, OH, CO and NO mass fractions. Again LES data is in good qualitative agreement with the experiments, the global shape and dispersion being rather well captured. Note that the mean strain rate in the LES is significantly lower in this case ($a = 60\,\mathrm{s}^{-1}$ compared to $170\,\mathrm{s}^{-1}$ at $z = 7.5D$). Similarly to the previous axial location, only a small number of points are located at low temperature below any strained counterflow flamelet, indicating again a very low level of premixing. The turbulent flame structure is still consistent with the reference flamelets, except NO

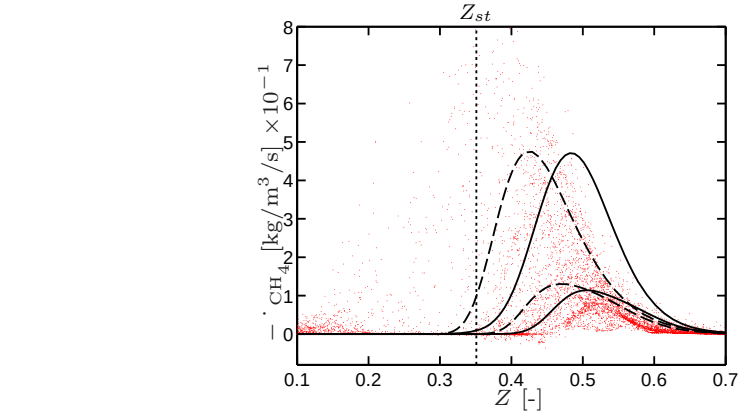

(a) CH4 source term.

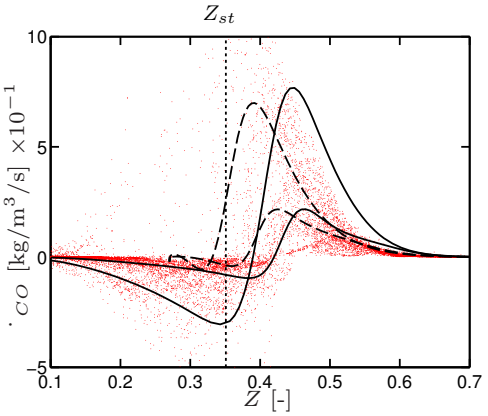

(b) CO source term.

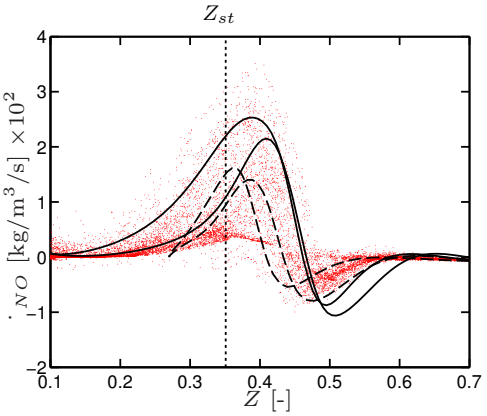

(c) NO source term.

Figure 8.16: Sandia flame D: Scatter plot of CH_4, CO and NO source terms vs mixture fraction at axial location $z = 7.5D$. Comparison of coflow (—) and pilot (−−) counterflow flames at strain rates $a = 60\,\mathrm{s}^{-1}$ and $270\,\mathrm{s}^{-1}$.

mass fraction which departs from the pilot flamelets. For pilot flamelet calculations, the imposed value for NO on the pilot side is $Y_{\mathrm{NO}} = 2 \times 10^{-5}$, which corresponds to the composition imposed at the pilot jet inlet in the LES computations. This value yields a good agreement between the pilot flamelets and the turbulent flame at axial location $z = 7.5D$. However, NO concentrations increase with axial position as NO is produced in the flame. Thus the levels observed in the turbulent flame are higher ($Y_{\mathrm{NO}} \simeq 5 \times 10^{-5}$) at $z = 30D$ than the boundary value used for flamelet calculations, which explains the discrepancy observed for NO mass fraction.

CH_4, CO and NO source terms shown in Fig. 8.18 again reveal a large dispersion. Because of the lower strain rates at this location, all source terms are significantly lower compared to the axial position $z = 7.5D$.

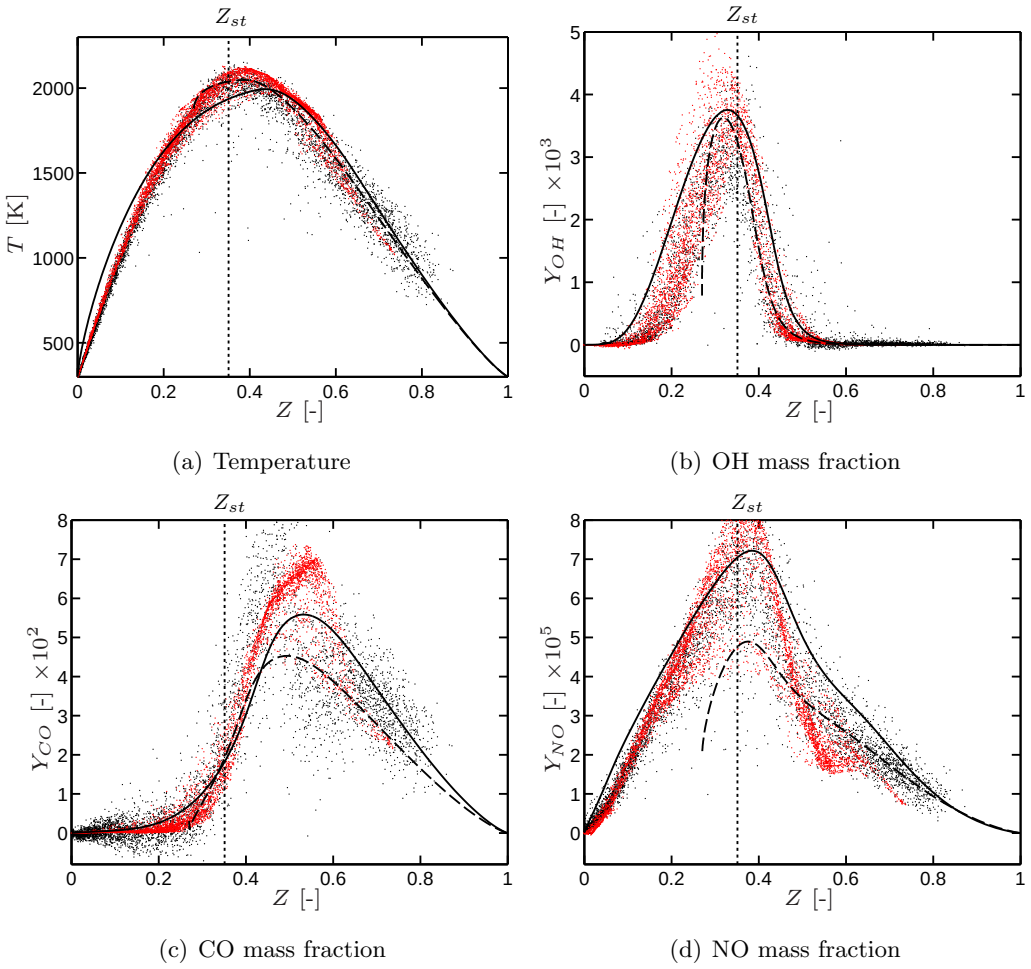

(a) Temperature

(b) OH mass fraction

(c) CO mass fraction

(d) NO mass fraction

Figure 8.17: Sandia flame D: Temperature, OH, CO and NO mass fractions vs mixture fraction at axial location $z = 30D$. Black dot: experiments, Red dot: LES. Coflow counterflow flame (—) and pilot counterflow flame (−−) at strain rate $a = 60\,\mathrm{s}^{-1}$.

8.6.3 Response to strain rate

The flame structure observed at the two axial positions in the previous section is consistent locally with non-premixed, strained laminar flames with a large range of strain rates because of turbulent strain fluctuations. Laminar cases (Sec. 8.6.1) showed a high sensitivity of the pollutant formation to the strain rate and to the flame type (coflow or pilot). Thus, in the turbulent case, the presence of the hot pilot jet is expected to significantly impact the flame structure and pollutant formation, especially close to the injection exits. To evaluate this effect, CH_4, CO and NO source terms are extracted along a $Z = 0.4$ isosurface from an instantaneous LES field, at two locations: the first in the vicinity of $z = 7.5D$ plane (between $7.5D$ and $10D$) and the second one close to $z = 30D$ plane (between $30D$ and $33D$). The distribution of CH_4 source term is first compared for the two axial locations in Fig. 8.19. Statistics con-

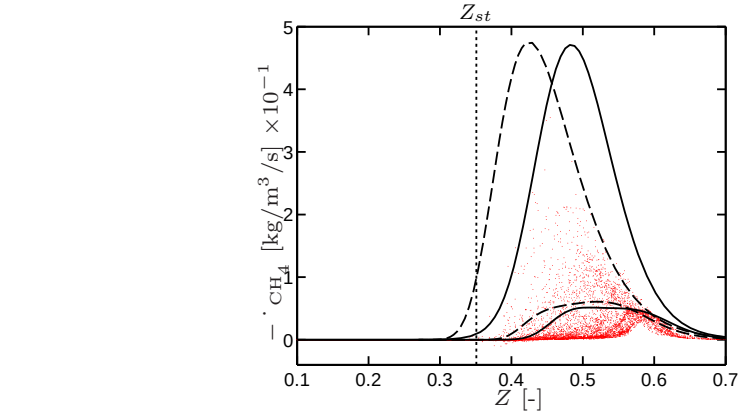

(a) CH4 destruction rate.

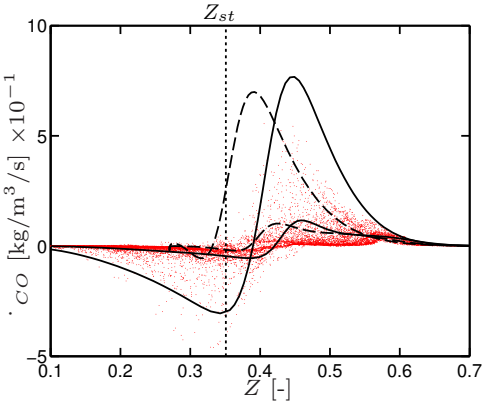

(b) CO production rate.

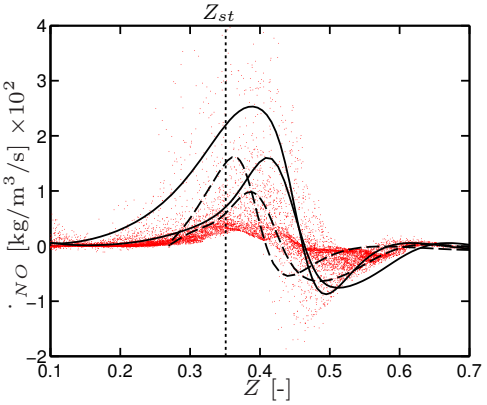

(c) NO production rate.

Figure 8.18: Sandia flame D: Scatter plot of CH_4, CO and NO source terms vs mixture fraction at axial location $z = 30D$. Comparison of coflow (—) and pilot (−−) counterflow flames at strain rates $a = 35\,\mathrm{s}^{-1}$ and $270\,\mathrm{s}^{-1}$.

ditioned on the local strain rate are also shown and provide an estimate of the local mean and dispersion. At low strain rate values, it appears that the fuel consumption has a bi-modal behaviour: data points are distributed either around the pilot or the coflow flamelet curve. This is more clearly visible at $z = 30D$ in Fig. 8.19(b). At higher strain rate values ($a > 200\,\mathrm{s}^{-1}$), the dispersion becomes very large. Note the non-quenched flame points at strain rates significantly beyond the extinction limits at location $z = 7.5D$. This can be attributed to the unsteady flame response to strain rate fluctuations [46, 88]. Despite the large dispersion, the behaviour of the conditional mean is found to be well consistent with the pilot flamelets at $z = 7.5D$ and with the coflow flamelets at $z = 30D$. This supports the strong influence of the pilot at locations close to the jet exits.

The same analysis is conducted for the CO source term in Fig. 8.20. For low to moderate strain rates ($0 < a < 200\,\mathrm{s}^{-1}$), CO production corresponds to pilot-type flamelet

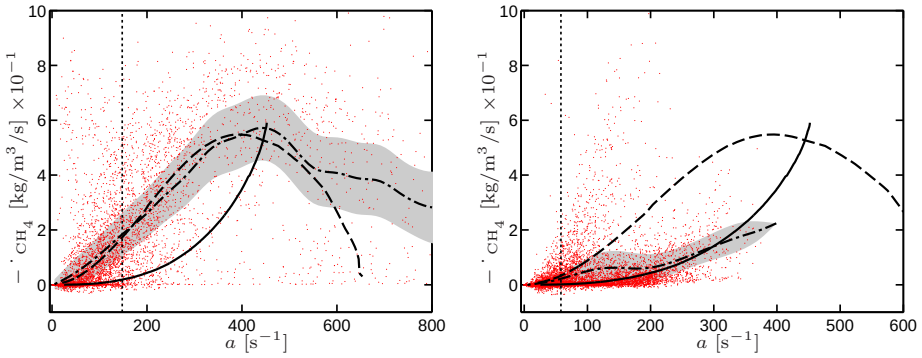

(a) $z = 7.5D$. (b) $z = 30D$.

Figure 8.19: Sandia flame D: Scatter plot of CH_4 consumption rate versus strain rate along the $Z = 0.4$ isosurface at axial locations a) $z = 7.5D$ and b) $z = 30D$. The grey shaded area corresponds to the conditional standard deviation around the conditional mean ($\cdot - \cdot -$). The vertical line corresponds to the mean strain rate. LES results are compared to the coflow counterflow flamelets (—) and the pilot counterflow flamelets ($--$).

burning while CO destruction is characteristic of coflow flamelets. Similarly to CH_4, the conditional mean is consistent with the pilot flamelets at $z = 7.5D$ and with the coflow flamelets at $z = 30D$.

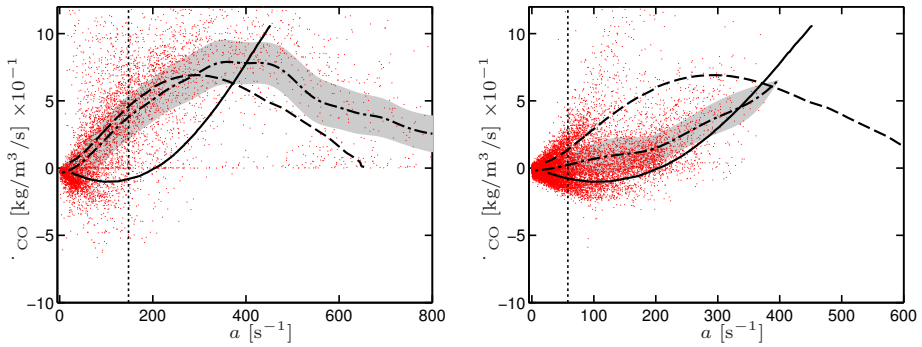

(a) $z = 7.5D$. (b) $z = 30D$.

Figure 8.20: Sandia flame D: Scatter plot of CO production rate versus strain rate along the $Z = 0.4$ isosurface at axial locations a) $z = 7.5D$ and b) $z = 30D$. The grey shaded area corresponds to the conditional standard deviation around the conditional mean ($\cdot - \cdot -$). The vertical line corresponds to the mean strain rate. LES results are compared to the coflow counterflow flamelets (—) and the pilot counterflow flamelets ($--$).

Finally the comparison of NO source term extracted from LES with flamelets is shown in Fig. 8.21. Again, a strong dispersion of the LES data is observed. However the NO source term is either positive or negative, whereas always positive in the reference

flamelets. Despite this difference, a good correlation is visible between LES and reference flamelets, particularly at $z = 30D$ (Fig. 8.21(b)) where the NO source term clearly matches the coflow flamelets manifold response for low to moderate strain rates. Once again, the conditional mean source term behaviour is consistent with the pilot flamelets at $z = 7.5D$ and with the coflow flamelets at $z = 30D$.

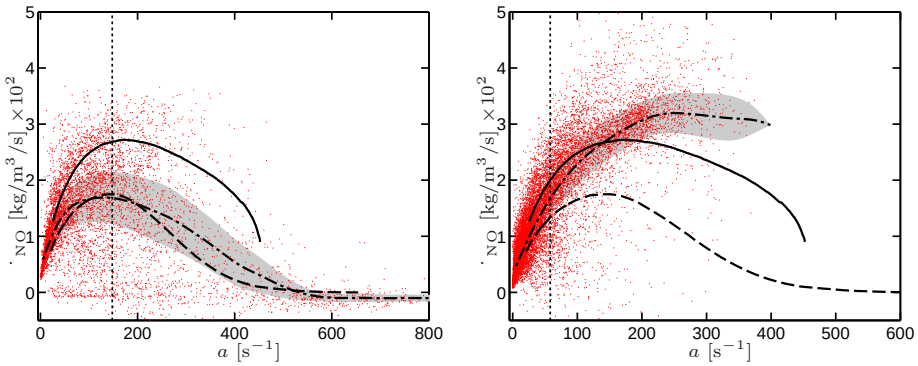

(a) $z = 7.5D$. (b) $z = 30D$.

Figure 8.21: Sandia flame D: Scatter plot of NO production rate versus strain rate along the $Z = 0.4$ isosurface at axial locations a) $z = 7.5D$ and b) $z = 30D$. The grey shaded area corresponds to the conditional standard deviation around the conditional mean ($\cdot - \cdot -$). The vertical line corresponds to the mean strain rate. LES results are compared to the coflow counterflow flamelets (—) and the pilot counterflow flamelets ($--$).

From the analysis of CH_4, CO and NO source term response to strain, and in light of the laminar cases, it can be concluded that the turbulent flame does not exhibit a single canonical structure, but rather follows a laminar structure that depends on the local mixing. The coflow and pilot counterflow flamelet series correspond to the two extreme states of burning, with either pure air or lean burnt gases, when no mixing between the pilot and the coflow gas occur. Close to the injection, at $z = 7.5D$, the good correlation of the three conditional mean source terms with the pilot flamelets tends to indicate that the flame structure is controlled by the pilot in this zone. Conversely, for downstream locations, the effect of the pilot, which represents only a 1/5 of the main central injection mass flow rate is expected to be weaker. This is supported by the chemical response observed at $z = 30D$, which correlates best with coflow flamelets, for which the pilot is not taken into account.

From the laminar cases (Fig. 8.13), it can be inferred that the strong influence of the pilot increases the total CO production rate, whereas NO production is less sensitive to the type of flamelet. This analysis has important consequences for tabulated chemistry

models [85, 201, 213], that require presumed reference flamelets to construct the look-up table. In most studies, the coflow flamelets were retained, missing the impact of the pilot flow. This might explain the unsatisfactory prediction of CO generally observed in tabulated chemistry models on this configuration [201]. To improve the local description of the flame structure, an additional parameter describing the mixing state between the coflow and the pilot can be introduced, as done in [122]. However, the evaluation of this parameter may be difficult in the turbulent flame.

8.7 Conclusions

In this chapter, a highly resolved LES of the Sandia flame D has been performed. Two ARCs based on GRI 3.0 and GRI 2.11 detailed mechanisms have been employed in the simulations. The mixture fraction, temperature and CO mass fraction profiles were shown to be in very good agreement with the experimental data. The slight discrepancies observed were essentially due to a slight over-prediction of the global mixing rate. Consistently with previous studies, strong disparities are observed between reduced mechanism based on GRI 3.0 and GRI 2.11 for NO prediction. While a very satisfactory agreement of NO is obtained with GRI 2.11, the reduced mechanism based on GRI 3.0 leads to a significant overprediction of NO produced by the flame.

A detailed analysis of the flame structure showed that the burning mode is essentially non-premixed. The turbulent flame structure and response to strain rate is similar to counterflow diffusion flamelets, despite a very large dispersion of the chemical source terms attributed to turbulent effects. A detailed analysis of the chemical source terms highlight the fact that the flame structure is significantly affected by the presence of the pilot, which was found to have a strong influence at the flame basis. This behaviour significantly impacts the flame structure and pollutant formation, with a strong increase of CO formation. This implies that the turbulent flame cannot be described accurately by a single flamelet table. The hybrid structure resulting from the mixing between main, coflow and pilot jets make it difficult to find a suitable reference flame for tabulated chemistry models.

This study demonstrates the strength of the ARC approach that allows for the direct integration of the chemistry and does not rely on the *a priori* identification of a reference laminar flame. ARC allows a faithful representation of the flame structure and response to local flow and mixing conditions in the turbulent flame. It is therefore a promising chemical modelling strategy for application to more complex industrial configurations, in which strong dilution, heat losses and two-phase flow combustion may occur.

9

LES of an industrial gas turbine combustor

Contents

9.1 Objectives

The objective of this chapter is to assess the capability of the methodologies developed in Chapter 5 and Chapter 6 to accurately reproduce the flame structure along with pollutants such as NO_x and CO in a realistic industrial configuration, the Siemens SGT-100 burner studied experimentally at DLR Stuttgart. LES of this configuration has already been performed by *Bulat et al.* [27], using the Eulerian stochastic field method [94] combined with an ARC including NO_x and CO chemistry [191]. In the present study, ARC combined with TFLES is applied in the LES of two operating points of the configuration.

After a description of the configuration and the experimental and numerical setups (Sec. 9.2), the LES results are compared with the experiments (Sec. 9.3). The response of the chemical system to local flow conditions and its impact on pollutant formation is further discussed and analysed in the light of reference laminar cases. Further, the comparison of the LES results on two operating points illustrates the impact of pressure and equivalence ratio on the flame structure and pollutant emissions (Sec. 9.6). The sensitivity of the results to numerical and physical modelling are finally discussed (Sec. 9.7). In particular, the impact of wall heat transfer on NO_x and CO prediction is assessed in this configuration.

9.2 Experimental and numerical setup

9.2.1 Description of the configuration

The SGT-100 configuration is studied experimentally in the high pressure facility at the German Aerospace Centre (DLR) Stuttgart, Germany. Figure 9.1 shows a schematic of the experimental configuration. It comprises a radial swirler, a mixing cylinder duct of diameter $D = 86\,\text{mm}$ with a sudden radial expansion into a square cross-section chamber. The main air flows through the radial swirler. Additional air leakages are referred to as panel leakage, window, and exhaust air leakage in Fig. 9.1 and Fig. 9.2. The combustor is operated with natural gas injected through multiple holes located on the swirler vanes, that are not detailed here for confidentiality purposes. The experimental combustor has the essential features of modern industrial burners: the swirl-stabilised flame is highly turbulent and burns in lean conditions at relatively high pressure and temperature. The mixture is rather well mixed prior to combustion, but a degree of partial premixing remains in the combustor.

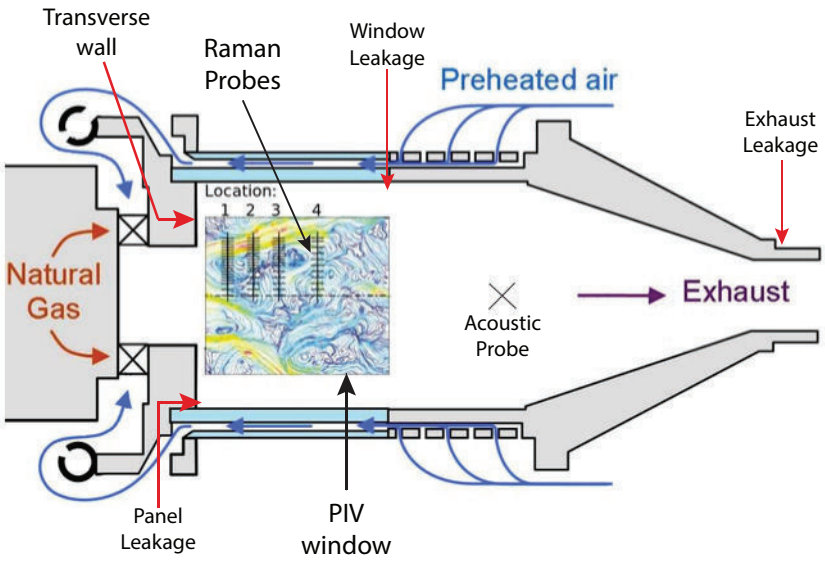

Figure 9.1: Schematic of the experimental SGT-100 configuration. The four 1D Raman measurement planes, the PIV window and the acoustic probe location are indicated. From [190].

9.2.2 Measurements

The experimental data are available from *Stopper et al.* [190] and were obtained in the framework of the TURCHEMI (TURbulence and CHEMistry interaction) project. The measurement techniques are also detailed in *Stopper* [188, 189], and were performed during three experimental campaigns from 2006 to 2008. Two-components Particle Image Velocimetry (PIV) was performed in the window shown in Fig. 9.1. OH^* chemiluminescence and OH Planar Laser-Induced Fluorescence (PLIF) were applied in the mid-plane of the combustor to assess the global flame structure and dynamics. Species concentrations (CO_2, O_2, N_2, H_2O and fuel) and temperature were obtained via one-dimensional Raman scattering at 60 measurement locations depicted in Fig. 9.1. Estimated experimental uncertainties for CO_2, O_2, N_2, H_2O and fuel concentrations are respectively 20%, 21%, 6%, 14% and 4% whereas the uncertainty for temperature is 13%. Exhaust measurements of CO and NO emissions were obtained by probe techniques. The acoustic activity of the combustor was measured via a dynamic pressure probe, located on the central axis as indicated by the cross in Fig. 9.1. Note that the uncontrolled mass flows of panel and window air leakages (Fig. 9.1) were estimated experimentally from exhaust O_2 concentrations. Measurements were performed on three operating points: two reacting cases (Case A and Case B) that are considered for the present study and introduced in the next subsection, and a non-reacting case.

9.2.3 Operating points for the LES study

The two operating points retained for the present LES study correspond respectively to Case A and Case B described in *Stopper et al.* [190]. Preliminary LES computations without adjusted boundary conditions for these cases lead to a significant overprediction of mixture fraction levels in the burnt gases, indicating that the actual global equivalence ratio of the combustor is actually lower than expected from the given inlet conditions. This discrepancy between global equivalence ratio of the operating points and measured mixture fraction levels is also pointed out in [190]. Therefore, the air mass flows had to be adjusted so as to recover the correct global equivalence ratio of the burner. It corresponds to an increase of the swirler air mass flow rate by 15% for Case A and 5% for Case B. Using this modified inlet conditions limits the possibility of comparison with the LES study of *Bulat et al.* [27], which was performed with the operating point of *Stopper et al.* [190], i.e. at a higher global equivalence ratio. The exact operating conditions employed for the LES are given in Tab. 9.1 in terms of pressure P, air temperature T_{air} and fuel temperature T_{fuel}. The fuel, swirler air and panel air mass flow rates (m) are used for the definition of the global equivalence ratio ϕ_{glob} of the flame. The window air mass flow rate m_{window} is not included in this definition as this leakage is located much further downstream in the combustor. The fuel

Case	P	T_{air}	T_{fuel}
A	3 bars	682 K	305 K
B	6 bars	683 K	304 K

Case	m_{fuel}	$m_{swirler}$	m_{panel}	m_{window}	ϕ_{glob}
A	6.24 g/s	183 g/s	16.2 g/s	17.3 g/s	0.52
B	12.8 g/s	338 g/s	30.9 g/s	33 g/s	0.59

Table 9.1: SGT-100: retained operating conditions for LES study of Case A and Case B.

employed in the experiments is German natural gas with the following composition in mass: $CH_4 = 96.97\%$, $C_2H_6 = 1.553\%$, $C_3H_8 = 0.35\%$, $C_4H_{10} = 0.05\%$, $CO_2 = 0.27\%$, $N_2 = 0.753\%$. It is simplified as pure methane in the present study.

9.2.4 Numerical setup

LES is performed using the AVBP solver (Sec. 2.4.1). The TTGC scheme is used (Sec. 2.4.2). A global view of the numerical domain is shown in Fig. 9.2. The panel and window air leakages are included in the computational domain. The latter may not significantly impact the flame structure but it can alter CO and NO evolutions in

burnt gases.

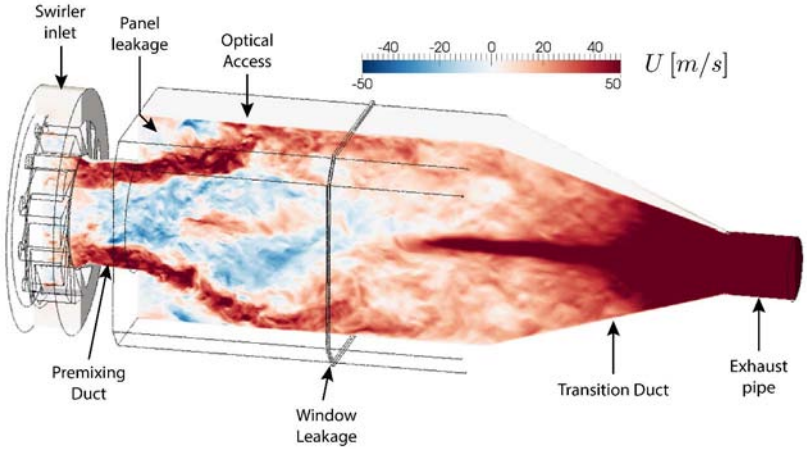

Figure 9.2: SGT-100: global view of the computational domain, with an instantaneous axial velocity field in the mid-plane.

The unstructured mesh comprises 120 million tetrahedral elements. The characteristic grid sizes are 0.8 mm in the swirler vanes, to ensure sufficient resolution of the turbulent scales, and 0.55 mm in both the premixing duct and the flame region, to keep reasonable levels of artificial thickening of the TFLES model. Typical flame thicknesses are $\delta_T = 0.25\,\text{mm}$ for Case A and 0.17 mm for Case B, resulting in thickening factors of respectively $\mathcal{F} \simeq 11$ and $\mathcal{F} \simeq 16$, by imposing $n_\mathcal{F} = 5$. Figure 9.3 shows a mid-plane cut of the characteristic grid size distribution, with refinements in the flame region and in the vicinity of the inlets. The small fuel injection holes in the swirler vanes are discretised with at least 6 elements in their diameter. These smaller elements impose the time step based on the acoustic CFL condition $\Delta t = 75\,\text{ns}$. This value allows direct explicit integration of the chemical source terms of the ARC, except for H_2O_2 which is treated implicitely, as discussed in Chapter 7.

The inlets and the outlet are described by Navier-Stokes characteristic boundary conditions (NSCBC) [160]. Mean turbulent velocity profiles are imposed for swirler and window leakage inlets. Constant velocity profiles are used for panel leakage and fuel injections. The combustor mean pressure is imposed at the outlet. The walls are considered non-slipping and adiabatic. Given the relatively low flame temperature ($T < 2000\,\text{K}$), radiative heat transfer is not considered. Turbulent subgrid stresses are modelled with the SIGMA eddy viscosity model [144].

The ARC_22_GRI211 mechanism detailed in Sec. 6.2 is employed in conjunction with the TFLES model, following the methodology detailed in Sec. 6.4. The parameters

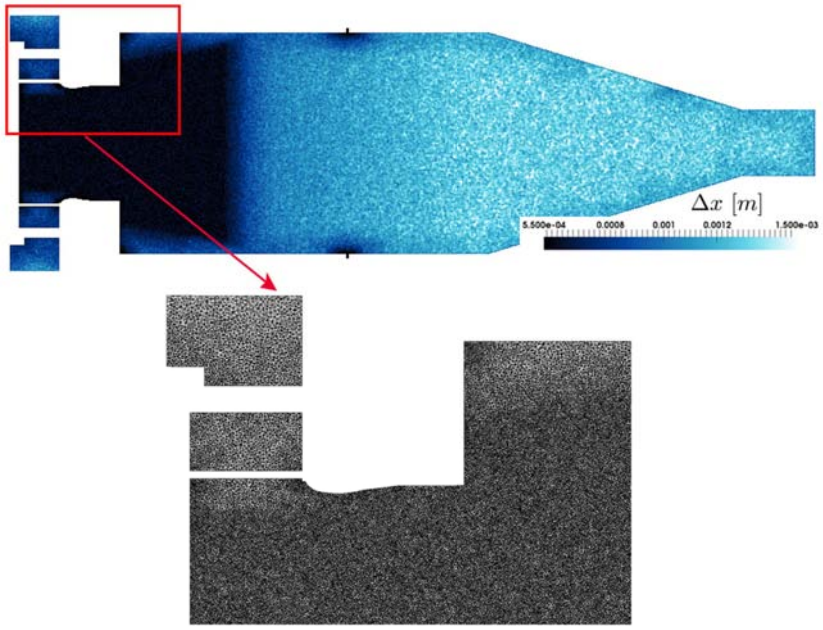

Figure 9.3: SGT-100: characteristic element size distribution in the mid-plane of the combustor.

retained for the dynamic sensor filtering are given in Tab. 9.2. Compared to laminar cases, the relaxation times parametrised by α_{cold} and α_{hot} (see Sec. 6.4.3) were divided by 20, essentially because of the choice of a narrower sensor width compared to laminar cases, but still large enough to encompass the strong gradient regions in the flame. Also, the sensor tends to spread more in the turbulent case because of three-dimensional effects (e.g. flame wrinkling).

	α_{cold}	α_{hot}	Sc_ψ
Laminar cases	1/3	1/30	0.13
SGT computations	1/60	1/600	0.13

Table 9.2: SGT-100: comparison of sensor filtering parameters between laminar cases (Sec. 6.4.5) and the present turbulent case.

In addition, the Charlette efficiency function [34] detailed in Sec. 4.5.2.1 is employed to account for subgrid turbulence-chemistry interaction.

This numerical setup constitutes a baseline reference for both Case A and Case B. In addition, the impact of several numerical and physical parameters will be assessed (for Case A only) in Sec. 9.7:

- **Impact of subgrid scale model**: comparison between SIGMA, WALE and Smagorinsky subgrid models (Sec. 9.7.1).

- **Impact of the chemical description**: comparison between ARC and NO-MAGT (Sec. 9.5) for NO_x prediction.
- **Impact of grid resolution/artificial thickening**: comparison between different levels of flame resolution (Sec. 9.7.2).
- **Impact of wall heat transfer**: comparison between adiabatic and non-adiabatic walls (Sec. 9.7.3).

9.3 Results: Case A

In the following, LES results for the baseline case are presented and validated against experimental data on Case A.

9.3.1 Flow dynamics

The instantaneous field of axial velocity in the mid-plane cut shown in Fig. 9.4 exhibits the typical features of a highly swirling flow, which is expected, given the high geometrical swirl number $S_g = 1.3$, based on the definition of [76],

$$S_g = \frac{2}{3}\frac{1-(D_{in}-D_{out})^3}{1-(D_{in}-D_{out})^2}\tan\theta\,, \tag{9.1}$$

where D_{in} and D_{out} are respectively the inner and outer diameters of the swirler and θ is the swirler vane angle. Because of the strong swirling motion, the high-velocity jet expands rapidly after the duct, leading to the formation of a large inner recirculation zone (IRZ) in the central part of the combustor. Outer recirculation zones (ORZ) also form in the combustion chamber corners under the effect of the outer shear layer of the swirling jet. The acceleration of the swirling flow at the exit of the combustor generates a strong exit vortex core (EVC), with significant velocity fluctuations on the centerline (Fig. 9.4d).

Comparison with the experimental data

Measurements were performed in the mid-plane of the combustor at four transverse locations shown in Fig. 9.4. The transverse position $y = 0$ corresponds to the centerline of the combustor. LES statistics were collected for 7 flow-through times ($\simeq 35\,\text{ms}$). Figure 9.5 shows the very good agreement between LES and measured mean and root mean square (rms) axial velocities. The jet opening and the intensity of the IRZ are correctly predicted. The peaks of fluctuations in the shear layers between the swirling jet and the recirculation zones are correctly captured, as well as the fluctuations close to the centerline associated to the EVC activity.

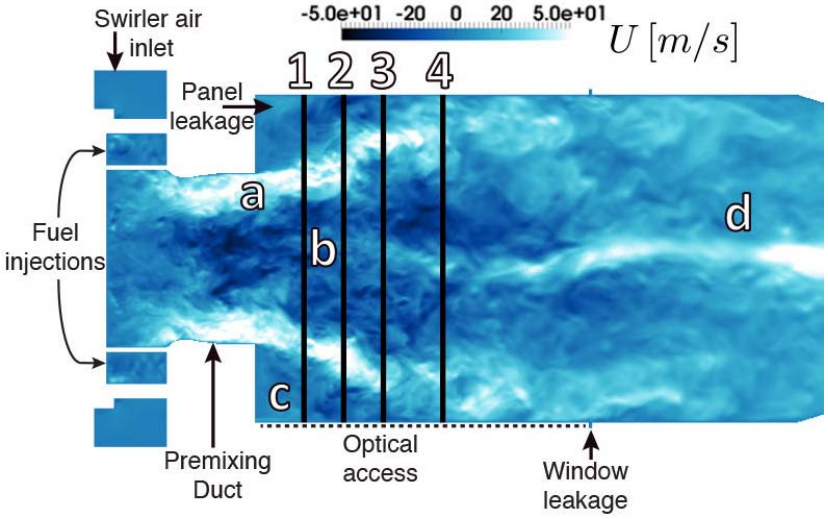

Figure 9.4: SGT-100/Case A: Instantaneous axial velocity from LES in the mid-plane of the combustor, truncated at the beginning of the transition duct. a) Swirling jet, b) IRZ, c) ORZ) and d) EVC. The vertical black lines denote the four axial locations of measurements.

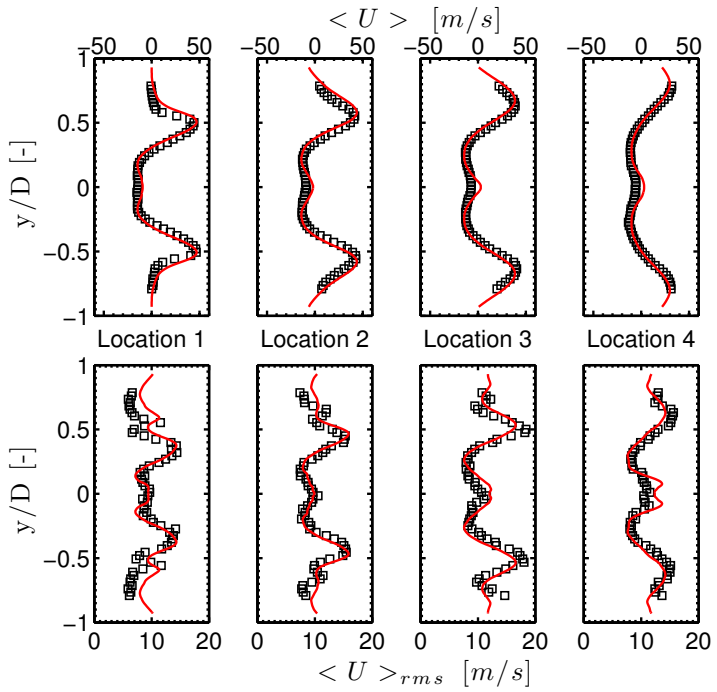

Figure 9.5: SGT-100/Case A: Transverse profiles of mean (top) and rms (bottom) axial velocity at the four measurement locations. Comparison between LES (–) and experiments (□).

9.3.2 Flame properties

An instantaneous snapshot of mixture fraction is displayed in Fig. 9.7a. The mixture fraction Z is based on the carbon atom and is normalised to vary from zero in the swirler air to 1 in the fuel injections. Note that, in the experiments, only major species

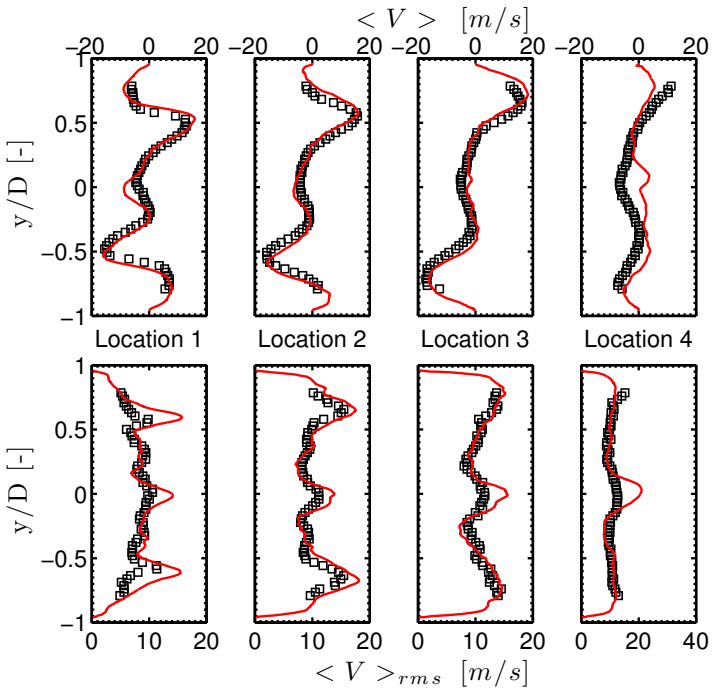

Figure 9.6: SGT-100/Case A: Transverse profiles of mean (top) and rms (bottom) transverse velocity at the four measurement locations. Comparison between LES (–) and experiments (□).

were used for mixture fraction evaluation. It was checked that it does not have an impact on the comparison between LES and experimental data. The stoichiometric value is $Z_{st} = 0.0565$ and the global mixture fraction is $Z_{glob} = 0.0303$. Figure 9.7a shows the rapid mixing of the fuel with the swirler air in the premixing duct. The mixture fraction rapidly falls below $Z = 0.04$ in the mixing tube, and is quite homogeneous and close to Z_{glob} further downstream. Some pockets of higher mixture fraction remain, highlighted by the isocontour at $Z = 0.032$, leading to a partially-premixed combustion regime. These richer pockets have a higher temperature (above $1850\,K$), as shown in Fig. 9.7b. An instantaneous heat release rate field in Fig. 9.7c highlights the M-shape flame. Compared to the branch in the shear layer between the jet and the IRZ, the outer branch located in the shear layer between the ORZ and the swirling jet has lower burning rates and only stabilises intermittently at the corner between the premixing duct and the transverse wall.

The NO source term shown in Fig. 9.7d peaks in the flame region because of the interaction with the fuel oxidation chemistry. The higher NO source term levels found in pockets with higher mixture fraction in the flame region confirm the strong dependency of NO formation on equivalence ratio. In burnt gases, slower chemical processes occur mainly via thermal NO [212], as will be further highlighted in Sec. 9.6.4. As the

threshold temperature for thermal NO ($\simeq 1850\,K$) is rarely crossed, NO production in burnt gases stays very moderate.

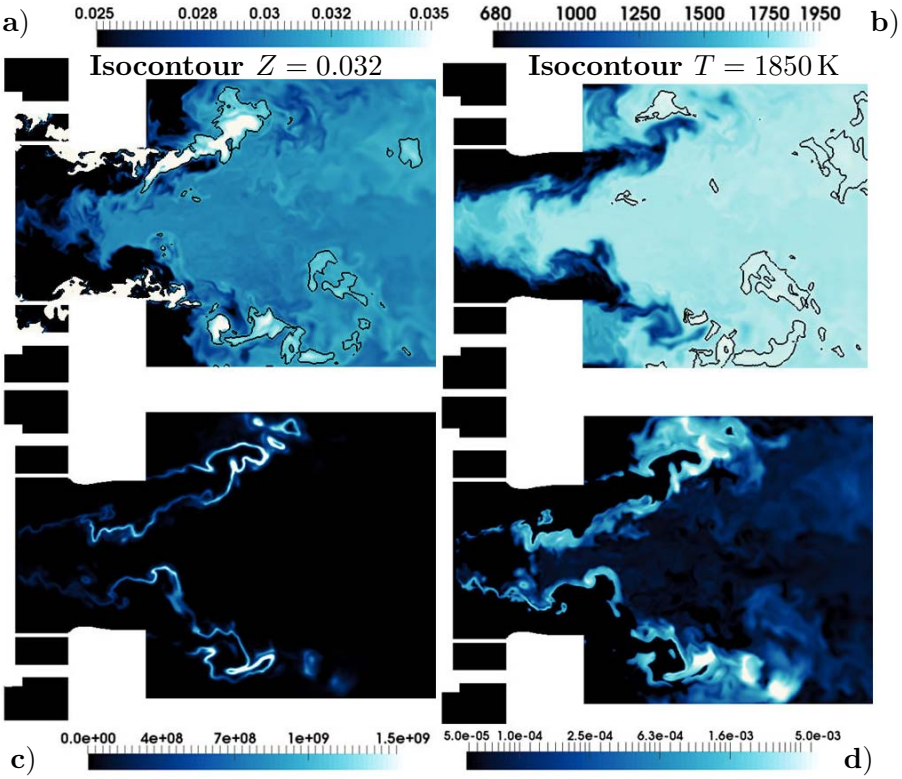

Figure 9.7: SGT-100/Case A: Instantaneous fields from LES in the mid-plane of the combustor, focused on the first half of the combustor. a) Mixture fraction, b) Temperature (K), c) Heat release rate ($\mathrm{W/m^3/s}$) **and d) NO source term** ($\mathrm{kg/m^3/s}$)**.**

Comparison with experimental data

The comparison of temperature and mixture fraction in Fig. 9.8 reveals a very good agreement for mean quantities, indicating that the flame shape is correctly predicted. The mixture fraction peak in the swirler jet decreases slightly more rapidly in the LES, which tends to indicate that the overall mixing rate tends to be overpredicted in the LES. A slight overprediction of temperature occurs in the central region of burnt gases, which can not be explained by mixture fraction differences. It is more likely due to heat losses, which are not taken into account in the baseline case. The shape of the fluctuations is well-captured (Fig. 9.9), but their intensity is under-estimated, particularly on the centerline of the combustor. However, similar discrepancy between LES and measurements was previously observed in [27]. *Stopper et al.* [190] also pointed out that the rms values in this region are about 6% of the mean values, and are therefore below the detection limit. This may at least partially explain the discrepancy.

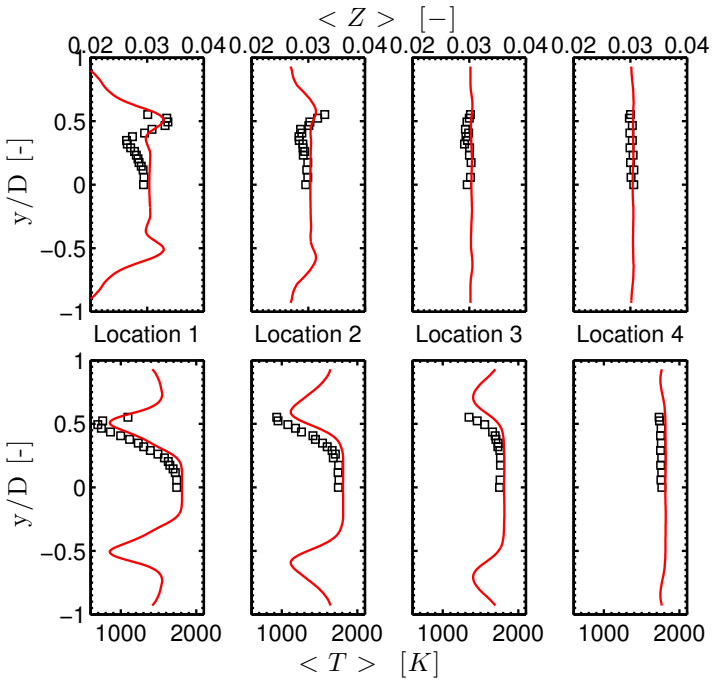

Figure 9.8: SGT-100/Case A: Transverse profiles of mean mixture fraction (top) and temperature (bottom). Comparison between LES (–) and experiments (□).

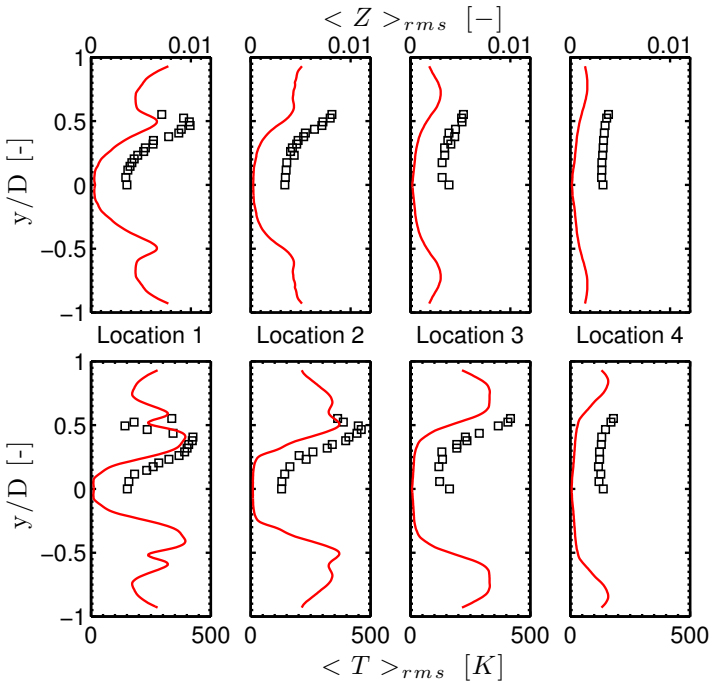

Figure 9.9: SGT-100/Case A: Transverse profiles of rms mixture fraction (top) and rms temperature (bottom). Comparison between LES (–) and experiments (□).

9.3.3 Point data statistics

To further compare the flame structure, scatter plots from LES and experiments are compared. Note that the experimental data were collected over several hours, whereas the collection time for LES is a sequence of 35 ms only, and sampled every 4 µs. The locations of the 6 probes (P100, P113, P116, P119, P314, P519) are shown in Fig. 9.10.

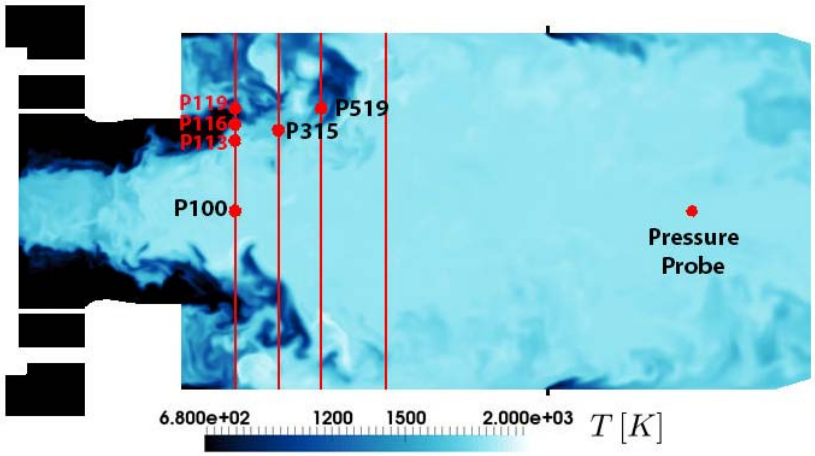

Figure 9.10: SGT-100: location of probes for point data comparison.

Scatter plots of temperature vs mixture fraction are shown at the 6 locations in Fig. 9.11, along with temperature and mixture fraction PDFs.

- **P100** is located in the centerline of the combustor, where the combustion process is complete. Consistently with mixture fraction and temperature rms values which are close to zero at this location (Fig. 9.9), the temperature and mixture fraction distributions in the LES are close to a Dirac distribution. The spreading is much larger in the experimental data. A significant number of experimental points are located above the equilibrium line, which is not physical, and might be attributed to experimental detection limit, as previously pointed out.

- **P119** is located in the outer shear layer. A very satisfactory agreement of numerical and experimental PDFs and global distributions is obtained. The large spreading of the temperature distribution can be attributed to the intermittent burning due to high strain at this location, as will be described in Sec. 9.4.2.

- **P113** and **P315** are located in the inner shear layer. They exhibit a bimodal PDF of temperature with a peak close to equilibrium and another peak close the mixing line, in both LES and experiments. It indicates that the mixture is either partially burnt or unburnt at this location. From the distribution of the mixture

fraction, it can be deduced that mixing is higher at P315 than P113 in the LES case.

- **P116** is located in the flame front. Again a bimodal PDF of temperature is obtained due to intermittency, with a more pronounced peak in the fresh gases.

- **P519** is located close to the flame tip. Both LES and experimental data are close to equilibrium, indicating almost complete combustion, with few remaining unburnt pockets. The peak of mixture fraction at the global value in the LES case indicates that mixing is almost complete, whereas significant dispersion remains in the experiments.

Overall trends are well captured at the different locations by the LES. Differences in the distributions mainly arise from the mixture fraction dispersion which is significantly higher in the experiments. This can partially be attributed to i) the collection time which is lower by several orders of magnitude in the LES case and ii) measurement noise which might lead to an overestimation of the dispersion, especially in the burnt gases where the fluctuations are relatively weak compared to mean quantities.

9.3.4 Pollutant emissions

CO and NO levels at the combustor outlet are compared to the available measurements. Note that the emission levels measured in the LES are corrected to 15% O_2 to be compared with measurements. A concentration of 3.8 ppmv at 15% O_2 is obtained for NO levels in the LES, to be compared to the experimental level of 5 ppmv. The slight underprediction of NO at the combustor exit could be attributed to the overall underestimation of temperature and mixture fraction fluctuations which tend to increase NO production [18], as will be further be highlighted in Sec. 9.4. As for CO, a concentration of 6 ppmv at 15% O_2 is consistent with the value of 4 ppmv measured in the experiments. Note that exhaust measurements were known only after conducting the LES: no model parameter adjustment was performed, highlighting the predictive capability of the methodology. However, there is a lack of estimation of numerical and experimental uncertainties to fully conclude on the accuracy of the prediction. The sensitivity of the results to physical and numerical parameters will be assessed in Sec. 9.7. In addition, a more thorough analysis of CO and NO_x formation will be performed when comparing Case A and Case B in Sec. 9.6.

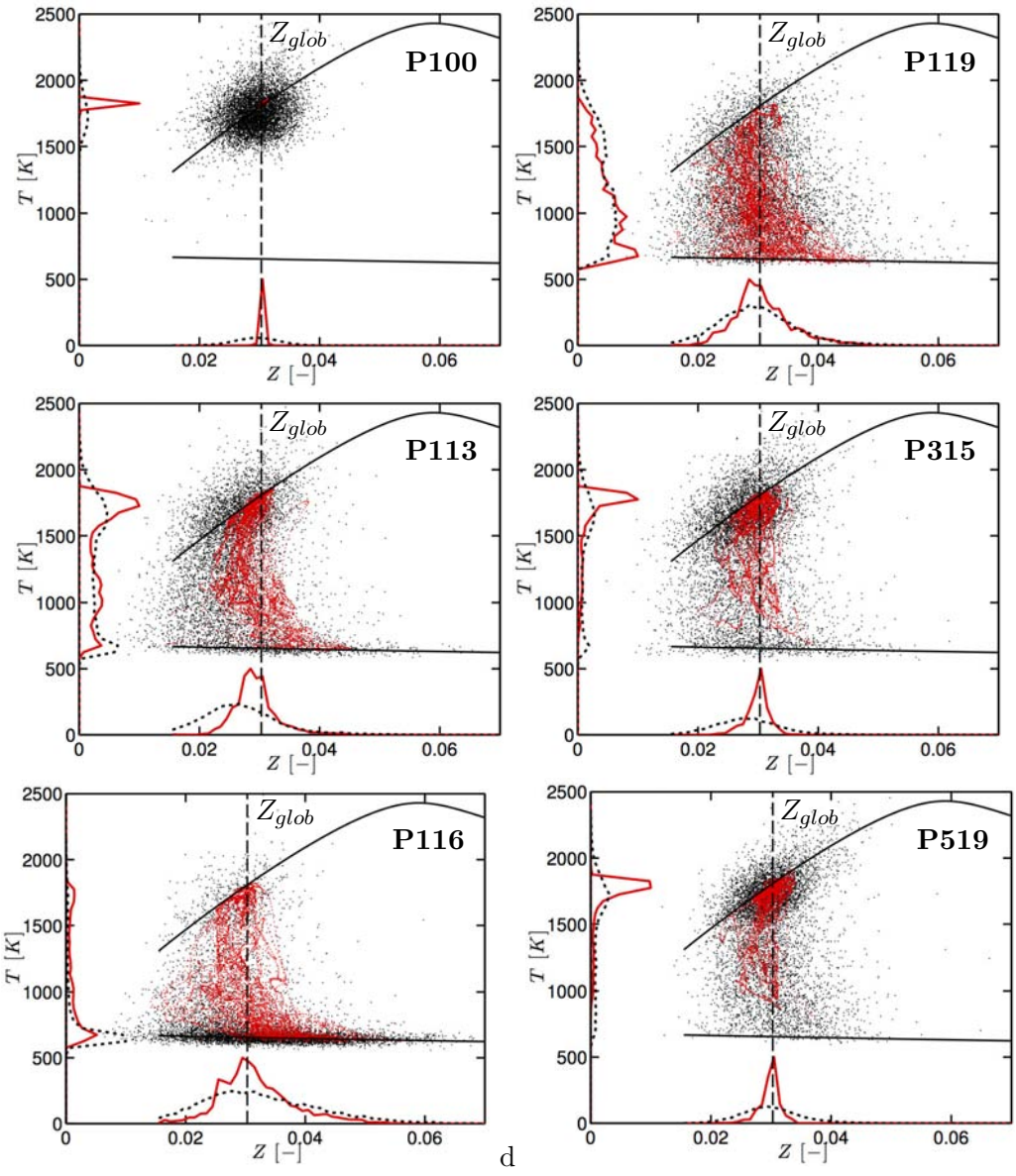

Figure 9.11: SGT-100/Case A: scatter plots of temperature vs mixture fraction at the 6 probes: experiments (·) and LES (·). PDFs of temperature and mixture fraction are also shown for experiments (· · ·) and LES (—). The continuous lines corresponds to equilibrium and mixing lines.

9.4 Flame structure analysis

9.4.1 Impact of mixture fraction inhomogeneity

The local flame structure may strongly deviate from the mean behaviour because of local flow conditions and mixing, with an important impact on NO and CO. The range of mixture fraction in which the fuel mostly burns is evaluated by integrating over the whole domain the fuel consumption rate conditioned on the mixture fraction. The resulting distribution (Fig. 9.12) highlights a partially-premixed combustion regime

where the fuel is essentially consumed in the range $Z = 0.02 - 0.04$ ($\phi = 0.43 - 0.61$), with a peak at the global mixture fraction $Z_{glob} = 0.030$.

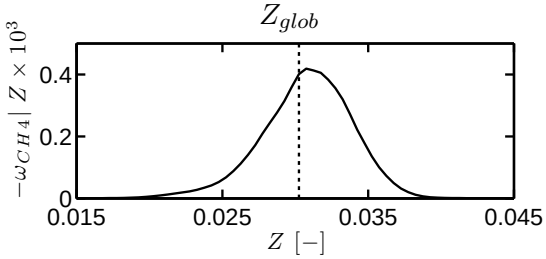

Figure 9.12: SGT-100/Case A: integrated fuel consumption ($\mathrm{kg/m^3/s}$) **(—) conditioned on the mixture fraction vs mixture fraction. The vertical line corresponds to the global mixture fraction.**

To assess the response of the chemical system in the partially-premixed combustion regime, the flame structure is first compared to unstrained one-dimensional premixed flames at three representative mixture fraction values ($Z = 0.025$; Z_{glob}; 0.035) in terms of fuel, CO and NO_x source terms. In Fig. 9.13, LES data are extracted from instantaneous snapshots and conditionally averaged on the progress variable (defined in Eq. 4.7) and the mixture fraction (for three mixture fraction values). At these lean conditions, both the laminar and turbulent flames are very sensitive to mixture fraction. The turbulent flame response is consistent with the laminar flames.

For pollutant species, the flame emission indices are defined as the ratio of total production in the flame to total fuel consumption,

$$\mathrm{EINO} = \frac{\omega^{tot}_{\mathrm{NO}}}{-\omega^{tot}_{\mathrm{CH_4}}}\,, \tag{9.2}$$

$$\mathrm{EICO} = \frac{\omega^{tot}_{\mathrm{CO}}}{-\omega^{tot}_{\mathrm{CH_4}}}\,, \tag{9.3}$$

where $\omega^{tot}_{\mathrm{NO}}$ and $\omega^{tot}_{\mathrm{CO}}$ are the flame total production rates defined in Eq. 6.1. Note that the emission indices are given in g/kg. The overall flame emission indices of CO and NO are sensitive to the local mixture fraction, as shown in Fig. 9.14 for laminar unstrained premixed flames: flame EINO is multiplied by 2.5 between $Z = Z_{glob}$ and $Z = 0.035$, while flame EICO is divided by 2. Therefore, even moderate variations of mixture fraction (by 15%) significantly alter CO and NO flame emission indices (by 100%).

Note that the conditionally averaged chemical source terms from LES tend to be lower than for laminar cases for all mixture fraction values. Also, a large dispersion around

the conditional mean is observed. This can be explained by the effect of strain, as further discussed (Sec. 9.4.2).

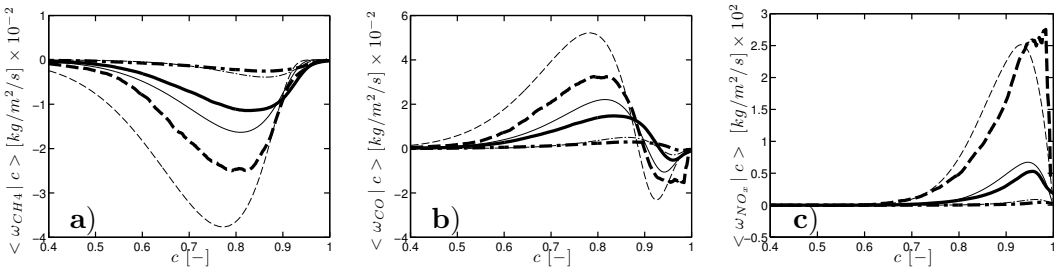

Figure 9.13: SGT-100/Case A: a) CH_4, b) CO and c) NO_x source terms conditionally averaged on progress variable and on mixture fractions $Z = 0.025$ (▬ ▪), $Z = Z_{glob}$ (▬) and $Z = 0.035$ (▬ ▬) (bold lines) vs progress variable. Thin lines correspond to the unstrained premixed laminar flame at the same mixture fraction values.

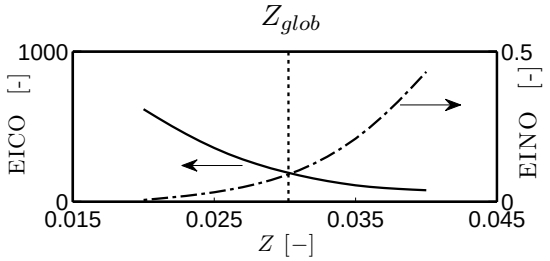

Figure 9.14: SGT-100/Case A: CO (—) **and** NO ($\cdot - \cdot -$) **flame emission indices of unstrained premixed laminar flames vs mixture fraction. The vertical line corresponds to the global mixture fraction.**

9.4.2 Impact of strain on the flame structure

In Chapter 8, strain rate was found to have a significant impact on the structure of non-premixed flames, on laminar and turbulent cases. Premixed flames are generally less sensitive to strain. However, for highly turbulent configurations, it can have a significant impact on the global flame properties. For example, *Knudsen et al.* [101] showed on a premixed jet flame that the flame structure was strongly impacted by turbulent strain, by comparing DNS and LES performed with strained and unstrained premixed flamelet models. In particular the flame height was reduced when the strain effect was not taken into account.

Similar effects can be expected in the present case. Indeed, in highly swirled configurations, the flame generally stabilises in shear layers where mean and instantaneous strain levels are high, leading to strong interaction between the flow and the chemistry. In particular, NO and CO are driven by slow chemical processes and thus are expected

to be more sensitive to strain, as it modifies the residence time in the flame. Therefore the impact of strain is studied in this section, first by an assessment on laminar cases which are further compared with the turbulent case.

9.4.2.1 Validation of ARC on laminar strained flames

The ARC_22_GRI211 scheme is assessed on laminar strained premixed flame using Cantera, in the counterflow configuration described in Sec. 4.2.2: for premixed case, fresh gases are injected against burnt gases at equilibrium. However, this is not the best choice, as taking equilibrium compositions for NO_x species lead to unrealistic NO concentrations in the flame front, not observed in LES where NO concentrations remain far from equilibrium. It leads to NO destruction rather than production in the flame front, as illustrated in Appendix. D. The best representative configuration uses adjusted NO_x concentration in the burnt gases, to obtain concentrations in the flame front corresponding to the values observed in LES. This would however lead to a double parametrization of the strained flame references, and was therefore not retained. Instead, NO_x related species are simply excluded from the burnt gas side composition. This assumption has no impact on the structure of the NO source term as long as NO concentrations in burnt gases remain very small compared to equilibrium values.

The response to strain of global flame quantities are shown in Fig. 9.15. Increasing strain rate tends to reduce the total fuel consumption (Fig. 9.15(a)). The flame NO emission index exhibits a monotonic decrease (Fig. 9.15(c)), indicating that flame NO production decreases more rapidly than total fuel consumption and thus has a higher sensitivity to strain, which can be attributed to the slower time-scales of NO_x formation. Conversely, the flame CO emission index exhibits a non-monotonic behaviour (Fig. 9.15(b)). The slow recombination of CO at the end of the flame region is more sensitive to strain than the production in the flame front. This results in a strong initial increase of CO flame index with strain. At higher strain values, CO formation in the flame front is also impacted, leading to a slow decrease of the emission index for $a > 6000\,\mathrm{s}^{-1}$. On the overall, an excellent agreement is obtained between the detailed mechanism and the ARC_22_GRI211, showing again its excellent prediction capability outside its derivation range. The same validation case was performed for SGT-100/Case B conditions and summarised in Appendix. C.

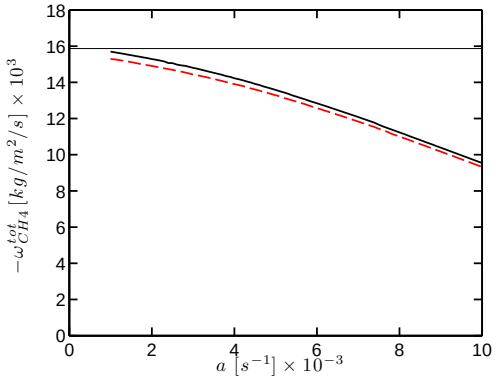

(a) CH_4 consumption.

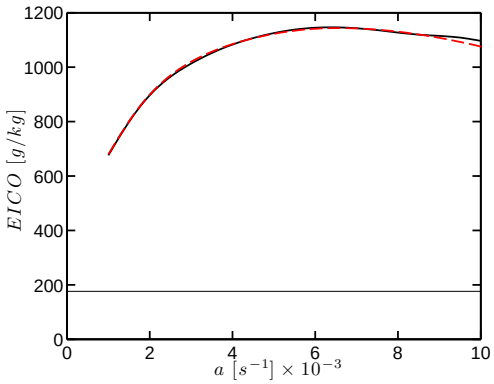

(b) Flame EICO.

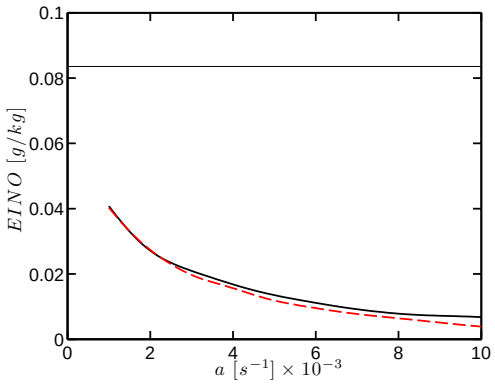

(c) Flame EINO.

Figure 9.15: One-dimensional strained premixed flames in SGT-100/Case A conditions at $\phi = \phi_{glob}$. Comparison of the response to strain of global quantities between GRI 2.11 (—), ARC_22_GRI211 (−−). The horizontal lines correspond to the unstrained values for GRI 2.11.

9.4.2.2 Impact of flame thickening

The interaction between aerodynamic strain and chemistry is controlled by the Damkohler number, whose expression is recalled from Eq. 4.23 as

$$Da(a) = \frac{\tau_{flow}}{\tau_c} \simeq \frac{1}{a}\frac{S_l}{\delta_T}\,. \tag{9.4}$$

When the TFLES model is applied, the flame quantities become

$$\delta_T \rightarrow \mathcal{F}\delta_T = \delta_T^*\,, \tag{9.5}$$

$$S_l \rightarrow \mathcal{E}S_l = S_l^*\,. \tag{9.6}$$

When substituted in Eq. 9.4, one obtains the Damkohler number of the thickened flame Da^*

$$Da^*(a) = \frac{\mathcal{E}}{\mathcal{F}a}\frac{S_l}{\delta_T} = \frac{\mathcal{E}}{\mathcal{F}}\,Da(a) = Da\left(\frac{\mathcal{F}a}{\mathcal{E}}\right)\,. \tag{9.7}$$

As the Damkohler number controls the interaction between the flow strain rate and the chemistry, it can be inferred from this equation that the response of the thickened

flame at a given strain rate a corresponds to the response of the unthickened flame at an effective strain rate $a^* = \dfrac{\mathcal{F}a}{\mathcal{E}}$. The transposition to global flame quantities is the following:

$$\omega^{tot,*}_{\mathrm{CH_4}}(a) = \mathcal{E}\,\omega^{tot}_{\mathrm{CH_4}}(a^*)\,, \tag{9.8}$$

$$\mathrm{EICO}^*(a) = -\frac{\mathcal{E}\omega^{tot}_{\mathrm{CO}}(a^*)}{\mathcal{E}\omega^{tot}_{\mathrm{CH_4}}(a^*)} = \mathrm{EICO}(a^*)\,, \tag{9.9}$$

$$\mathrm{EINO}^*(a) = -\frac{\mathcal{E}\omega^{tot}_{\mathrm{NO}}(a^*)}{\mathcal{E}\omega^{tot}_{\mathrm{CH_4}}(a^*)} = \mathrm{EINO}(a^*)\,. \tag{9.10}$$

The TFLES model is designed to recover the turbulent flame speed via the efficiency function that appears in Eq. 9.8. Its impact on pollutant emissions might be non-negligible because of the modified response to strain. To confirm this impact, laminar thickened flame computations are performed with $\mathcal{F} = 5$ and $\mathcal{E} = \mathcal{F}^{0.5}$ (the 0.5 exponent corresponds to the asymptotic behaviour of the Charlette efficiency function). Figure 9.16 shows the comparison of the response to strain of the unthickened and thickened flames. As theoretically predicted, the response to strain of the thickened flame is significantly impacted, with an increased sensitivity to strain rate compared to the unthickened flame. When quantities of the thickened flame are plotted vs the effective strain rate a^*, they collapse with the response of the unthickened flame, consistently with Eq. 9.8 to Eq. 9.10.

From this one-dimensional analysis, it can be concluded that the effective strain a^* should be considered when comparing the turbulent flame structure with reference laminar cases.

9.4.2.3 Impact of strain rate on the turbulent flame

Local strain fluctuations

The PDF of the tangential strain rate a_t (Eq. 4.18) is extracted from an instantaneous LES field and conditioned on the global mixture fraction Z_{glob} and the progress variable value $c = 0.8$, which corresponds roughly to the location of CH_4 and NO source terms peaks in progress variable space. The resulting distribution is shown in Fig. 9.17. The strain rate PDF is relatively large, covering the range $a_t = [-20000; 20000]\,\mathrm{s}^{-1}$ around the mean value $a_t^{mean} = 2500\,\mathrm{s}^{-1}$. This large range results from turbulent fluctuations, as shown by the spatial distributions of tangential strain rate (Eq. 4.18) (Fig. 9.18a. This can also be seen from the maximum strain rate (Fig. 9.18b), defined as the difference between the maximum and minimum eigenvalues of the strain rate tensor. Compared to instantaneous maximum strain rate, mean-velocity maximum strain rate

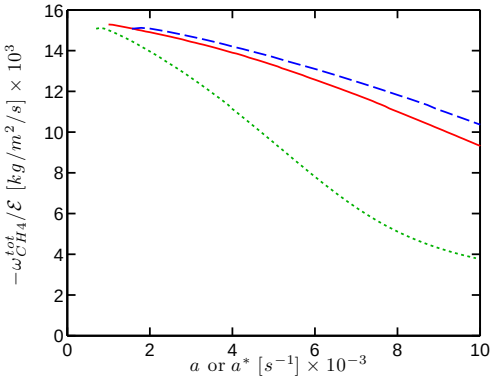

(a) Total fuel consumption rate over efficiency.

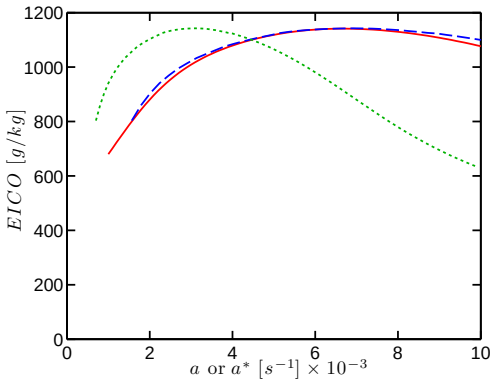

(b) Flame EICO.

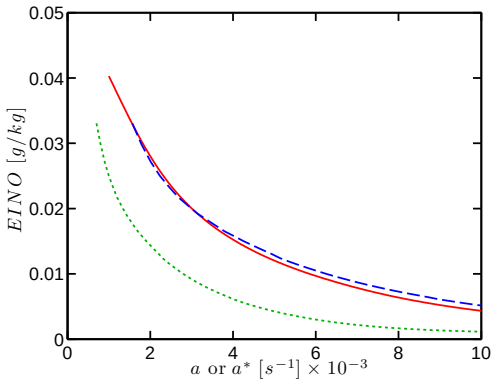

(c) Flame EINO.

Figure 9.16: One-dimensional strained premixed flames in SGT-100/Case A conditions at $\phi = \phi_{glob}$. Comparison of global flame quantities for unthickened flame response ($\mathcal{F} = 1$, $\mathcal{E} = 1$) (—), thickened flame response ($\mathcal{F} = 5$, $\mathcal{E} = \mathcal{F}^{0.5}$) ($\cdots$) to strain rate a and thickened flame response to effective strain rate $a^* = \dfrac{\mathcal{F}a}{\mathcal{E}} = \quad \bar{5}a$ (−−).

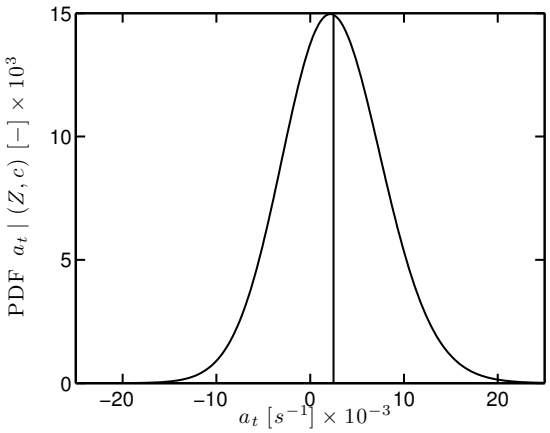

Figure 9.17: SGT-100/Case A: PDF of instantaneous tangential strain rate a_t (—) conditioned on $Z = Z_{glob}$ and $c = 0.8$. The vertical line correspond to the spatial mean value $a_t^{mean} = 2500\,\mathrm{s}^{-1}$.

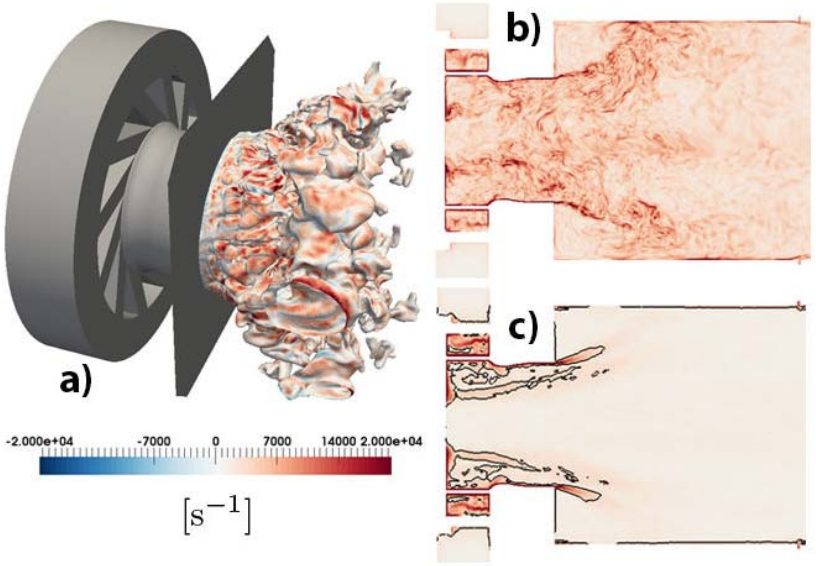

Figure 9.18: SGT-100/Case A: a) Instantaneous field of tangential strain rate on $c = 0.8$ isosurface. b) maximum strain rate of instantaneous velocity field and c) maximum strain rate of mean-velocity field in the mid-plane of the combustor.

shown in Fig. 9.18c is significant only in localised regions in the shear layers.

Global impact of strain

To evaluate the turbulent flame response to strain, scatter plots and conditional means of the chemical source terms at global mixture fraction Z_{glob} are compared to unstrained and strained laminar premixed flames at the same mixture fraction Z_{glob} (Sec. 9.4.2.1) for three representative strain rate values ($a = 1000, 6000, 11000\ \mathrm{s}^{-1}$). Figure 9.19 shows that both fuel and pollutant source terms are sensitive to strain on laminar cases, as already highlighted in Sec. 9.4.2.1. Due to the high strain fluctuations, the turbulent flame data of Fig. 9.19 shows a very large dispersion around the conditional mean. Still, the mean turbulent flame structure appears to be closest to the moderately strained ($a \simeq 6000\,\mathrm{s}^{-1}$) laminar flame, which is consistent with the mean effective strain rate ($a^{*,mean} = \mathcal{F}/\mathcal{E} \times a^{mean} \simeq 9000\,\mathrm{s}^{-1}$). Based on the laminar strained flames of Sec. 9.4.2.1, this corresponds roughly to a decrease by 20% of the flame consumption speed compared to the unstrained flame, with an increase of flame CO production and decrease of flame NO production by one order of magnitude. Based on the trends of laminar cases, it can therefore be inferred that the high strain intensity has a significant impact on pollutant formation.

Source term correlations with strain rate

Considerable scatter was obtained when correlating local instantaneous strain rate with

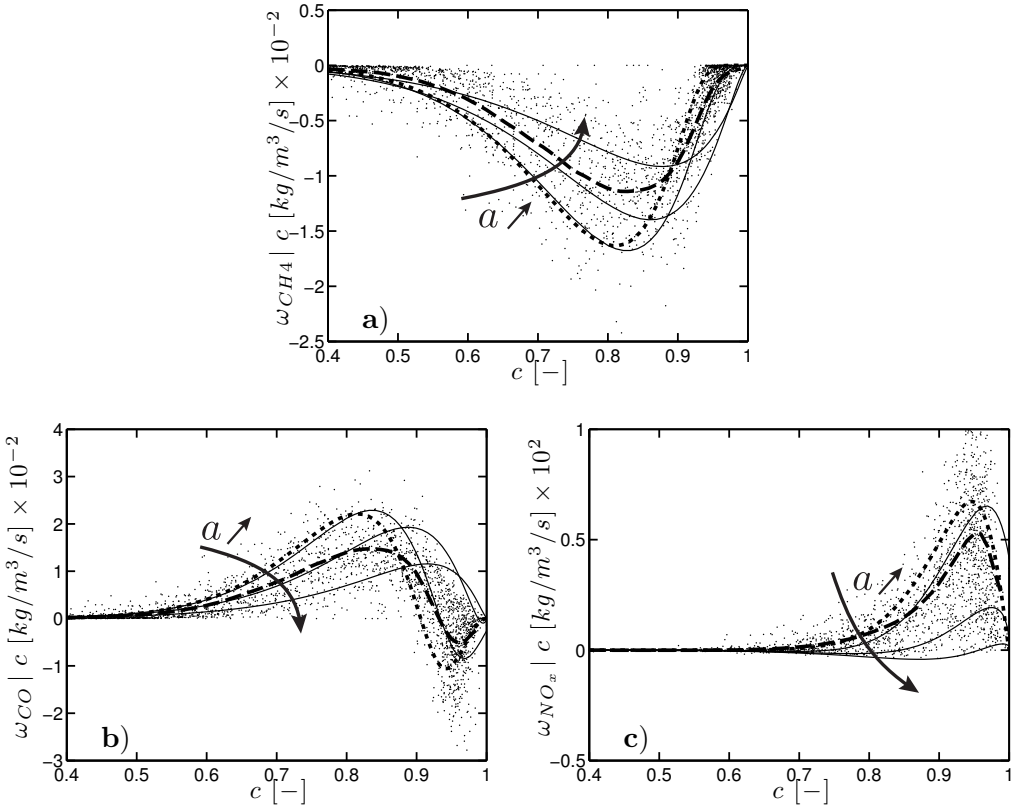

Figure 9.19: SGT-100/Case A: Scatter plot (·) and conditional mean (▬▬) of a) CH_4, b) CO and c) NO_x instantaneous source terms conditionally averaged on progress variable and mixture fraction Z_{glob}. The unstrained laminar premixed flame response (▪ ▪) and strained laminar premixed flame cases (—) at strain rate $a = 1000, 6000, 11000\ s^{-1}$ are also shown for comparison.

chemical sources terms, which may be attributed to the unsteady response of the flame structure to high-frequency strain rate fluctuations [49]. A more significant correlation was obtained between chemical source terms and effective mean-velocity strain rate, as shown in Fig. 9.20. Despite the very large dispersion of chemical source terms attributed to the combined effect of strain fluctuations and unsteady flame response, a good correlation is obtained between the conditionally averaged source terms and effective mean-velocity strain rate, and is similar to the laminar flame response. This supports the significant impact of strain rate on the structure of the turbulent flame.

Local impact in highly strained regions

The comparison of Fig. 9.18b) and Fig. 9.18c) shows that even if the turbulent strain exhibits large values in the whole flame region, the mean-velocity strain rate remains significantly high in localised regions, typically in the shear layers between the swirling jet and the recirculation zones. This locally strong mean strain rate is likely to significantly modify the flame structure. To illustrate this impact, an indicator θ is defined

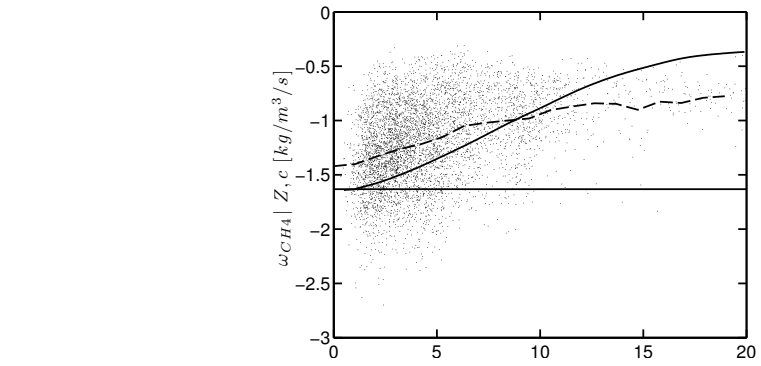

(a) CH_4 source term.

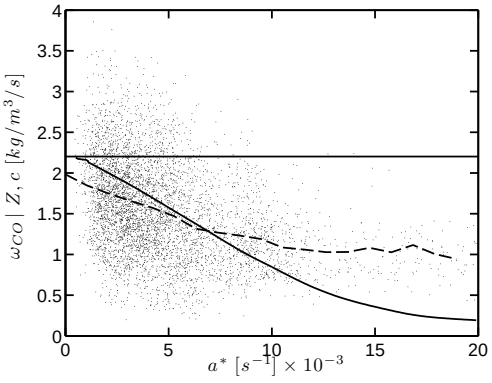

(b) CO source term.

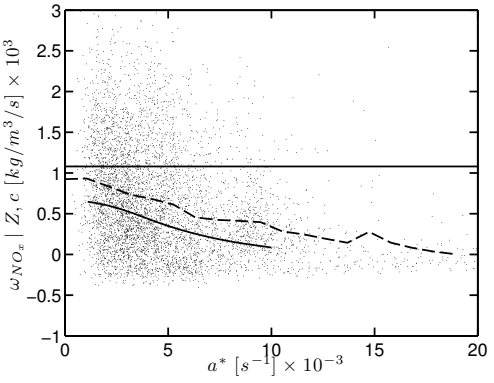

(c) NO_x source term.

Figure 9.20: SGT-100/Case A: Scatter plot at mixture fraction value Z_{glob} and progress variable value $c = 0.8$ of a) CH_4, b) CO and c) NO_x instantaneous source terms vs effective mean-velocity strain rate a^*. LES data are conditionally averaged ($--$) on the effective mean-velocity strain rate. The strained laminar premixed flame response (—) and unstrained response (horizontal line) are also shown for comparison.

as

$$\theta = \frac{\mid \omega^{LES}_{\mathrm{CH_4}} \mid}{\mid \omega^{1D}_{\mathrm{CH_4}}(Z^{LES}, c^{LES}) \mid}, \tag{9.11}$$

where $\omega^{LES}_{\mathrm{CH_4}}$ is the CH_4 source term from the LES and $\omega^{1D}_{\mathrm{CH_4}}(Z^{LES}, c^{LES})$ is the chemical source term of the unstrained laminar flame at the local mixture fraction and progress variable extracted from LES. The indicator is evaluated on the $c = 0.8$ isosurface in Fig 9.21a. θ is close to zero in the shear layer between the jet and the ORZ, confirming that the flame is highly strained or even quenched in that region. This behaviour is well correlated with the mean-velocity strain rate field shown in Fig. 9.21b on the same isosurface, which exhibits highest levels in that high shear region. This effect directly impacts the flame stabilisation, which anchors intermittently at the corner between the end of the premixing duct and the transverse wall.

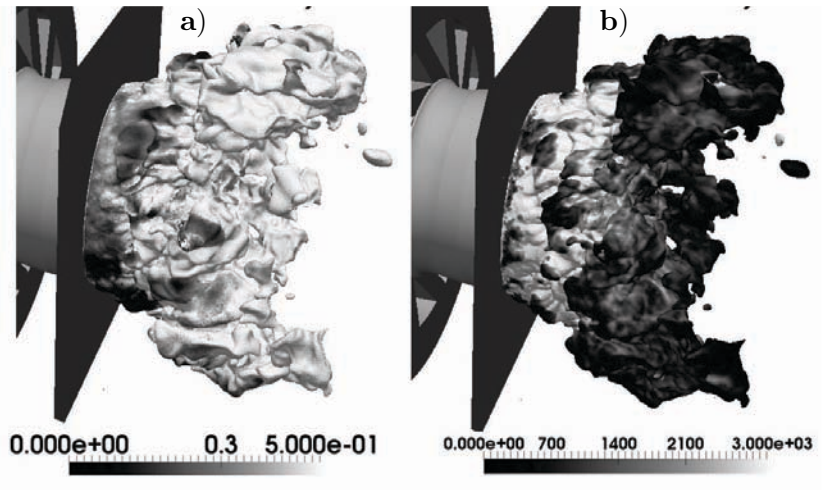

Figure 9.21: SGT-100/Case A: Instantaneous snapshot of $c = 0.8$ isosurface coloured by a) the local value of θ and b) the mean-velocity strain rate.

Summary of the effect of strain

The interaction between strain and the flame chemical response has been shown to be subject to high fluctuation intensity, resulting in a strong dispersion of instantaneous strain and turbulent flame structure compared to the laminar cases. Localised regions in the shear layer between the swirling jet and the CRZ have a high mean-velocity strain close to the extinction limit and intermittently lead to quenching. The turbulent flame has a statistical behaviour similar to laminar strained flames, for fuel as well as pollutant species, for which high strain levels significantly modify the species source terms. The response to strain is however altered by the flame thickening of the TFLES model, which modifies the effective strain seen by the flame. This impact will be discussed in more details in Sec. 9.7.2.

9.4.3 Impact of flame curvature

The local flame curvature, which also significantly impacts the local chemical response of the flame [49] is briefly analysed in this subsection. The instantaneous curvature $\mathcal{K}$ (Eq. 4.19) along $c = 0.8$ isosurface is shown in Fig. 9.22(a). Contrarily to strain rate, there are no particular region of high curvature, but a continuous alternation of positive and negative curvature zones. The resulting PDF (also conditioned on $Z = Z_{glob}$) shown in Fig. 9.22(b) is centred around zero.

To analyse the effect of curvature, LES data is extracted from one instantaneous solution and conditioned on $Z = Z_{glob}$ and $c = 0.8$. The resulting scatter plots of source terms vs curvature shown in Fig. 9.23 indicate a partial correlation with a trend to decrease source terms with increasing curvature. Note that there is no laminar reference

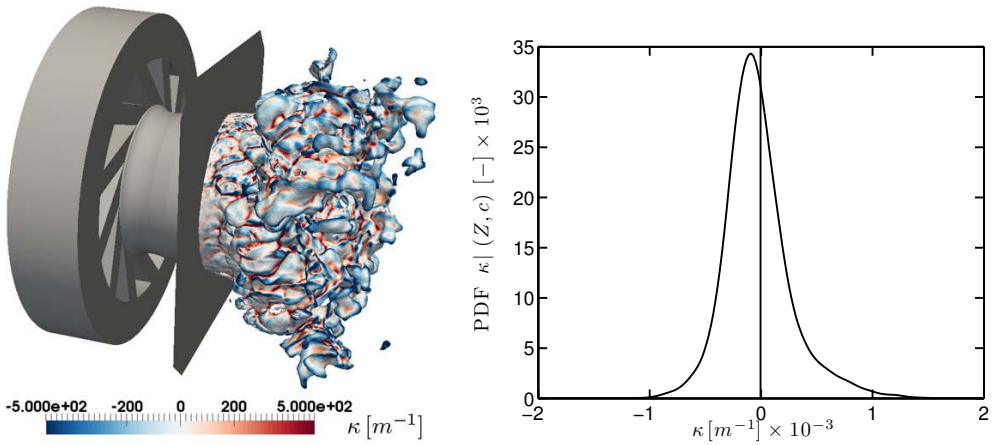

(a) (b)

Figure 9.22: SGT-100/Case A: a) Instantaneous field of curvature on $c = 0.8$ isosurface and b) PDF of curvature at $Z = Z_{glob}$ and $c = 0.8$.

for comparison in this case, which would require flame-vortex interaction computations.

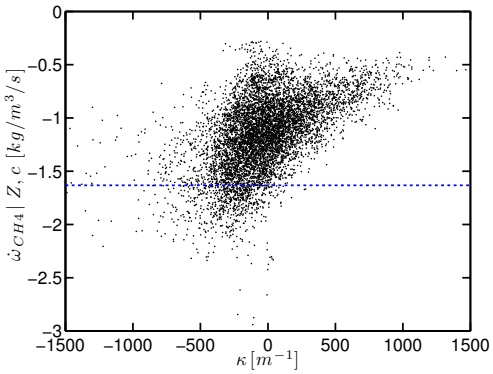

(a) CH_4 source term.

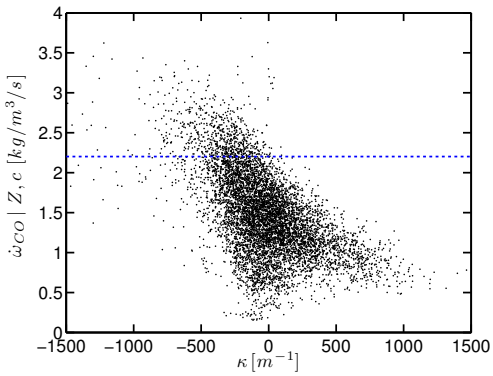

(b) CO source term.

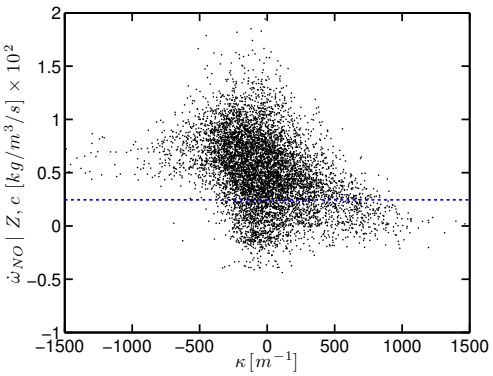

(c) NO source term.

Figure 9.23: SGT-100/Case A: scatter plot (·) of a) CH_4, b) CO and c) NO instantaneous source terms at $Z = Z_{glob}$ and $c = 0.8$ vs curvature. The unstrained laminar premixed flame response (· · ·) is also shown.

In average, negative and positive curvature effects tend to cancel out and thus have no significant impact on the flame structure.

9.5 Impact of chemical description: comparison with the NOMAGT approach

In this section, the NOMAGT (NOMANI/GRC/TFLES) model described in Chapter 5 is applied for comparison purposes. Compared to the ARC approach, the differences are the following:

- The methane-air chemistry is described by the 2S_CH4_BFER mechanism detailed in Appendix. A, where a validation on laminar cases corresponding to the SGT-100 operating point is also provided.
- The NOMAGT model is employed to describe NO_x formation. The numerical parameters retained for the method are given in Tab. 9.3, and are identical to the parameters used for the validation of the model on laminar cases in Chapter 5. The look-up table comprises 300 points in the Z-direction and 200 points in c^* and c_{NO} direction.

c_{relax}	c^*_{switch}
0.5	0.98

Table 9.3: SGT-100/Case A - NOMAGT: Parameters of the NOMAGT model.

The exact same methodology as for ARC is employed to dynamically thicken the flame front.

9.5.1 Comparison of mean profiles

A comparison of mean profiles between the two cases is first performed. The mean and rms velocity profiles for the NOMAGT case are identical to the baseline case, the flame chemical description having only a very weak impact on flow aerodynamics. Similarly, the mixture fraction profiles are identical (Fig. 9.24 top). A more significant impact is found for temperature profiles (Fig. 9.24 bottom): whereas ARC and GRC yield similar temperature levels in burnt gases in the centerline of the combustor, the temperature levels are globally higher in the jet region in the GRC case, which tends to indicate that the flame is slightly shorter in this case.

This is supported by the comparison of CH_4 and CO_2 mole fraction profiles of Fig. 9.25 which reveals that the remaining fuel at Location 3 and Location 4 is lower in the NOMAGT case, confirming that the combustion process occurs more rapidly in this case. This is also supported by the comparison of instantaneous flame structures, as shown in the next subsection.

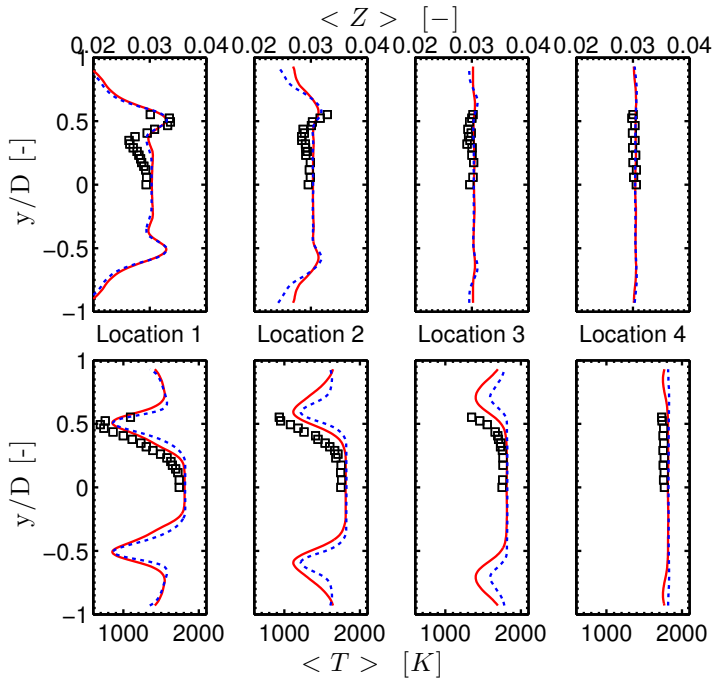

Figure 9.24: SGT-100/Case A - NOMAGT: Transverse profiles of mean mixture fraction (top) and temperature (bottom). Comparison between LES with ARC (—), LES with GRC (−−) and experiments (□).

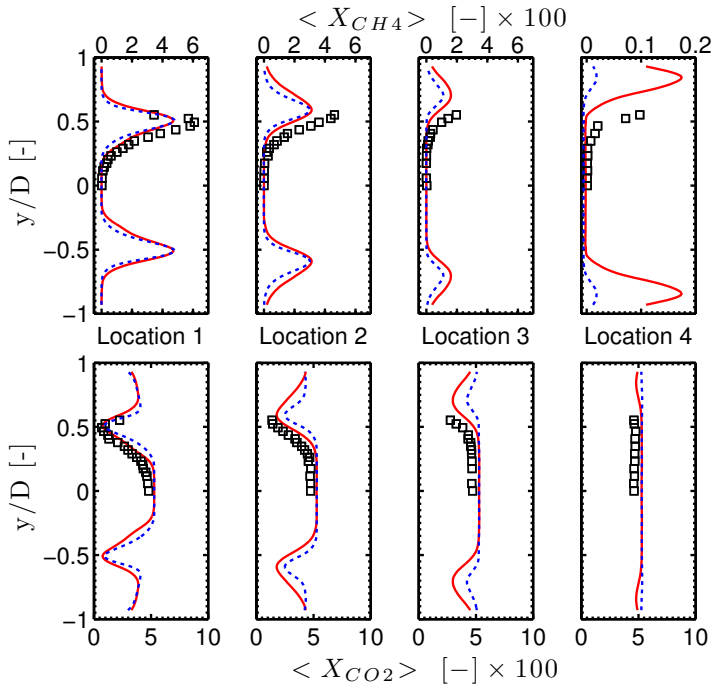

Figure 9.25: SGT-100/Case A - NOMAGT: Transverse profiles of CH_4 mole fraction (top) and CO_2 mole fraction (bottom). Comparison between LES with ARC (—), LES with GRC (···) and experiments (□).

9.5.2 Instantaneous flame structure

Two instantaneous LES fields are extracted at random instants from the ARC and NOMAGT cases and compared in Fig. 9.26. The intensity of the heat release rate is globally higher for the GRC case. Significant burning occurs in the outer shear layer for the GRC case, whereas only weak and strongly intermittent burning occurs in this zone for the ARC case. Similarly, the burning intensity is much higher for the GRC case in the inner shear layer. This is attributed to the insensitive response to strain of the 2-step mechanism, which is shown in Fig. 9.27 for laminar strained premixed flames.

This leads to a flame more compact and attached to the end corner of the premixing duct. This is also evidenced by the instantaneous temperature fields (Fig. 9.26(b)), showing higher temperature levels in the outer shear layer of the jet and very few unburnt pockets at downstream locations for the GRC case. This is also consistent with the findings of *Bulat et al.* [27] on the same configuration: with a 4-step global mechanism [93], also weakly sensitive to strain, the resulting flame was more compact and strongly anchored to the combustor walls compared to simulations with more refined chemistry.

9.5.3 NOMAGT model

Fictive progress variable

From Chapter 5, we recall that a key point of the methodology is to introduce a progress variable c^* based on tabulated source term, that matches the 2-step chemistry progress variable c_{2s}, at the beginning of the flame region and correctly reproduces the end of the flame and the post-flame region of the detailed chemistry. From the comparison of instantaneous fields shown in Fig. 9.28, indeed the progress variable c^* appears to correctly follow c_{2s}. In addition, the comparison of the isocontour of $c^* = 0.98$ and $c_{2s} = 0.98$ in Fig. 9.28(b) reveals that c^* describes a more extended post-flame region. This shows that c^* has the expected behaviour.

The good behaviour of c^* is quantitatively supported by the distribution of c^* vs c_{2s} on an instantaneous field shown in Fig. 9.29: for $c^* < c_{relax}$, almost all data points fall on the line $c^* = c_{2s}$, indicating that c^* correctly follows c_{2s}, thanks to the relaxation source term (Eq. 5.19). For $c^* > c_{relax}$, the correlation drops because of the steeper behaviour of c_{2s} in the end of the flame and the post-flame region.

NO_x formation

Despite the flame structure differences, a good qualitative agreement of the NO source

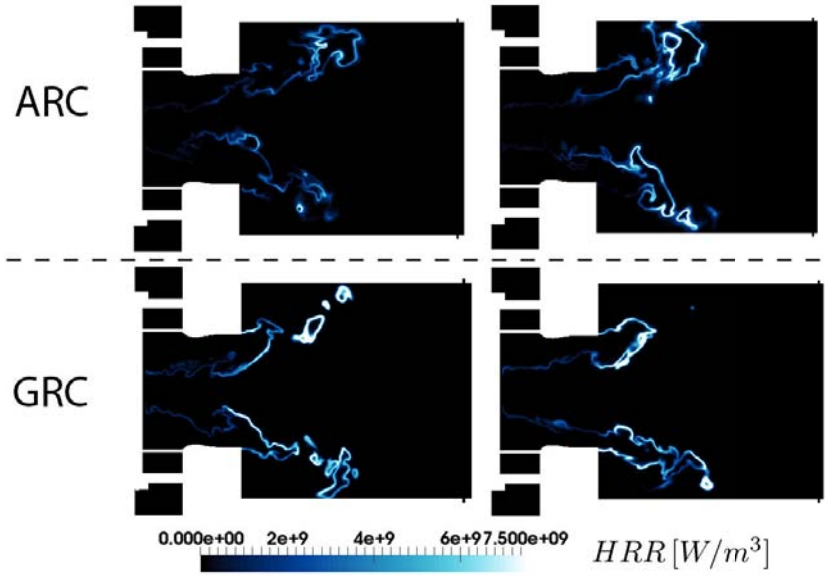

(a) Heat release rate.

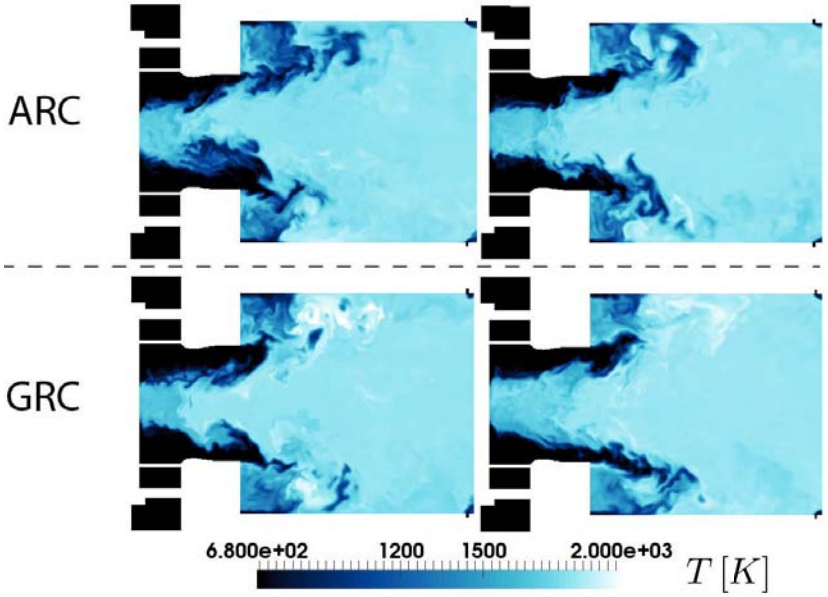

(b) Temperature.

Figure 9.26: SGT-100/Case A: comparison of two instantaneous fields of a) heat release rate and b) temperature for ARC (baseline case) and GRC (NOMAGT) case in the mid-plane of the combustor.

term is obtained between NOMAGT and ARC, as shown in Fig. 9.30: the high source term in the flame region and lower source term in the post-flame region look similar for both cases. The comparison of the isocontour at $c = 0.98$ for ARC and $c^* = 0.98$ for NOMAGT shows that the choice of $c^*_{switch} = 0.98$ is appropriate to distinguish between the rapid NO formation in the flame region and slower NO production in the burnt gases. The overall quantitative agreement is also fair, and reported in Tab. 9.4.

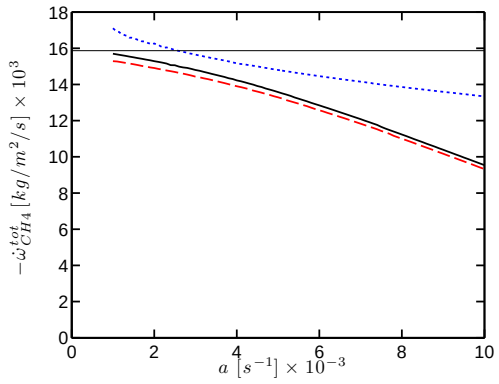

Figure 9.27: One-dimensional strained premixed flames in SGT-100/Case A conditions at $\phi = \phi_{glob}$. Comparison of the response to strain of CH_4 consumption between GRI 2.11 (—), ARC_22_GRI211 (−−), and 2S_CH4_BFER ($\cdots$). The horizontal line corresponds to the unstrained value for GRI 2.11.

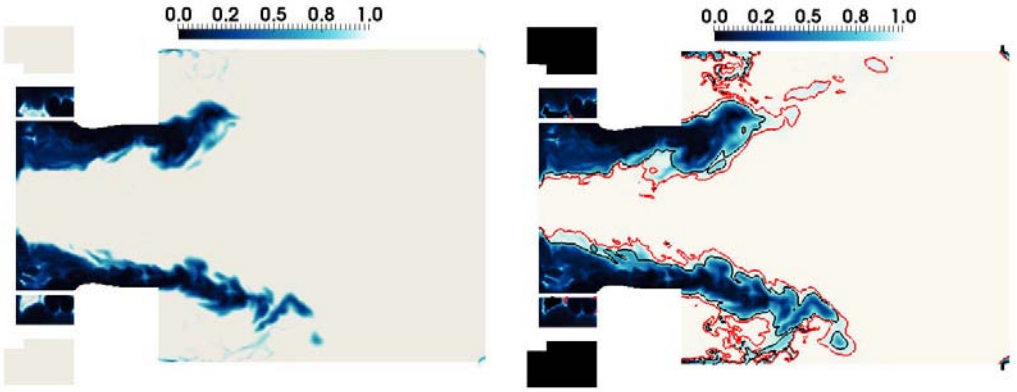

(a) GRC progress variable c_{2s}.

(b) Progress variable c^*.

Figure 9.28: SGT-100/Case A - NOMAGT: Instantaneous fields of a) progress variable from 2-step chemistry c_{2s} and b) progress variable c^* with $c_{2s} = 0.98$ isocontour (black) and $c^* = 0.98$ isocontour (red).

Compared to the baseline case, the NOMAGT model leads to an increase by only 8% of NO concentration at the combustor exit. Based on the thickening sensor of the TFLES model, the flame region can be delimited, and its contribution to the overall NO production evaluated. This is relevant since the same thickening sensor methodology is used for the two cases. The flame contribution to total NO production is very close in both cases and corresponds to almost a half of the total NO production.

9.6 Effect of the operating conditions: comparison with Case B

To assess the ability of the LES methodology to reproduce the experimental trends and to capture the impact of operating conditions, the experimental Case B (Tab. 9.1) is also

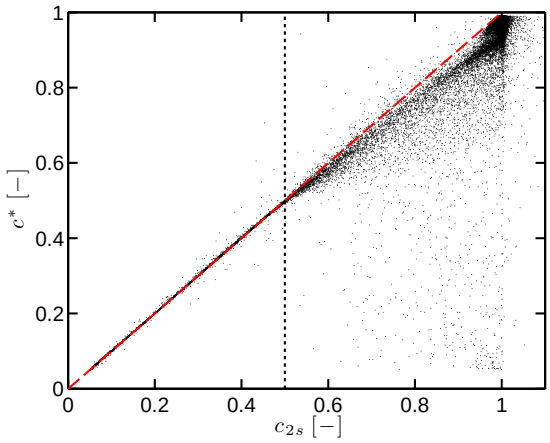

Figure 9.29: SGT-100/Case A - NOMAGT: scatter plot of c^* vs c_{2s}. The vertical line corresponds to the switch value $c_{relax} = 0.5$. The first bisector ($c^* = c_{2s}$) (−−) is also shown.

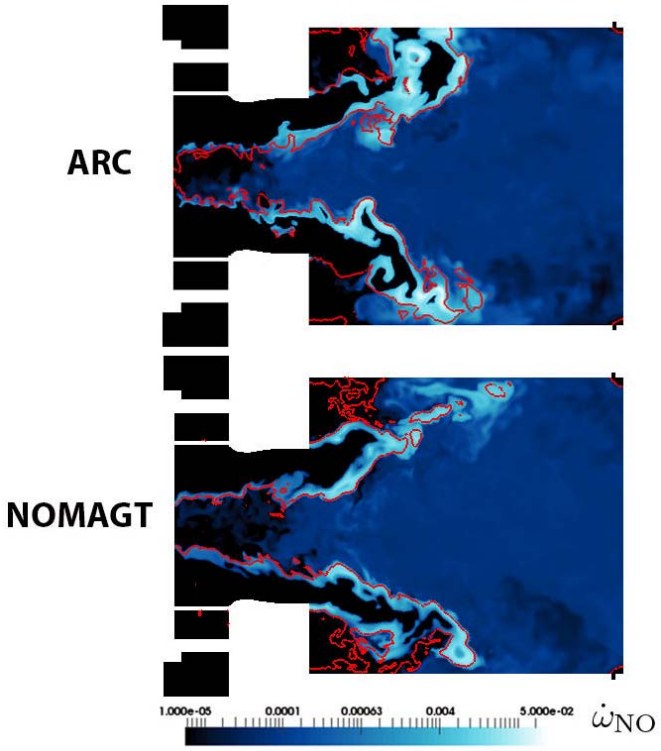

Figure 9.30: SGT-100/Case A - NOMAGT: comparison of instantaneous fields of NO source term ($kg/m^3/s$) between ARC (baseline case) and NOMAGT case in the mid-plane of the combustor. Isocontour of progress variable $c = 0.98$ for the ARC case, and $c^* = 0.98$ for the NOMAGT case.

calculated. To the best of our knowledge, this is the first LES study of this operating point. The significant difference with Case A is the combustor pressure, which is 6 bars compared to 3 bars for Case A, while inlet temperatures are kept unchanged. The global equivalence ratio is also slightly increased ($\phi = 0.59$ instead of $\phi = 0.52$). The

	NO (ppmv)	Flame Contribution to total NO production (%)
Experiments	5.0	-
ARC (baseline case)	3.8	40%
NOMAGT	4.1	41%

Table 9.4: SGT-100/Case A - NOMAGT: Comparison of NO emissions at the combustor exit between ARC and NOMAGT cases.

increased pressure has several impacts:

- Because of higher gas density, the Reynolds number based on the swirling jet velocity and the jet width is multiplied by a factor 2 from $Re \simeq 40 \times 10^3$ for Case A to $Re \simeq 80 \times 10^3$ for Case B.
- Increased pressure also significantly impacts the chemical structure of the flame. Because of lower diffusivities at higher pressure, the flame thickness is reduced. In addition, chemical times are shorter, which modifies the turbulence/chemistry interaction, with a general trend of increased turbulent flame speed [121]. Auto-ignition delays are reduced as well [185]. Concerning pollutants, increased pressure tends to promote the recombination of CO in CO_2 and also impacts the NO_x chemical processes [18], notably the thermal NO pathway.

The same numerical setup as for Case A described in Sec. 9.2.4 is employed. The only difference concerns the flame thickening factor: because of reduced laminar flame thickness from $\delta_T = 0.25\,\text{mm}$ to $0.17\,\text{mm}$, the thickening factor is increased from $\mathcal{F} = 11$ to 16, i.e. multiplied by 1.5. This should have a moderate impact on the resolved flame wrinkling, as analysed in Sec. 9.7.2.

9.6.1 Comparison of Case B with experiments

A very good agreement between LES and measurements is obtained for the mean axial velocity (Fig. 9.31 top), and the agreement is also fair for rms axial velocity (Fig. 9.31 bottom), even if a slight underestimation appears in the central region. It may indicate an underprediction of the intensity of the EVC or an underprediction of velocity fluctuations due to the acoustic activity. Measurements indicate that the acoustic activity is higher for Case B [190]: pressure fluctuations with an amplitude representing 1.9% of the mean pressure are observed compared to 0.6% for Case A. This trend is not observed in the LES. It may be due to the presence of a choked nozzle after the combustor exhaust in the experimental setup, which is not included in the computational domain.

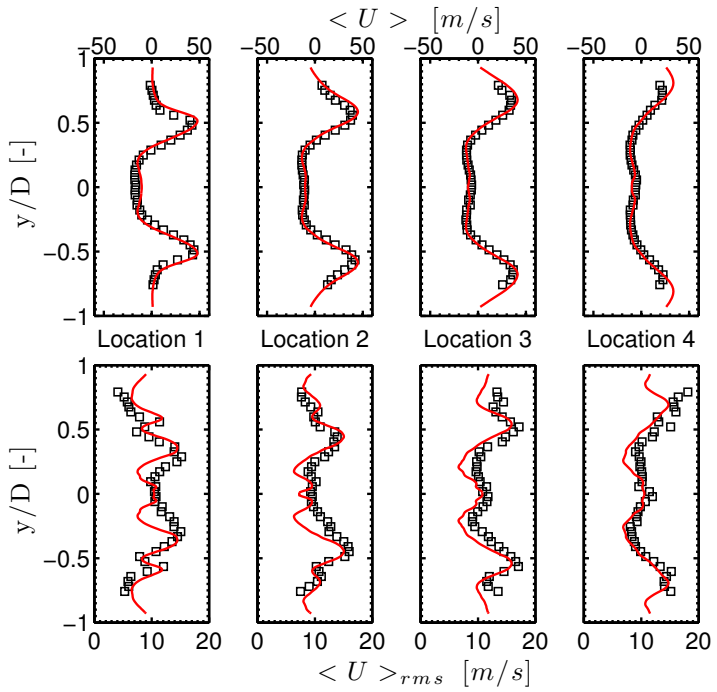

Figure 9.31: SGT-100/Case B: Transverse profiles of mean (top) and rms (bottom) axial velocity at the four measurement locations. Comparison between LES (–) and experiments (□).

The shape of the mean mixture fraction profiles (Fig. 9.32 top) is also well reproduced. The mixture fraction peaks in the swirling jet region. A slight overall overprediction of mixture fraction levels occur at Locations 3 and 4, leading to a slight overprediction of the mean temperature levels (Fig. 9.32 bottom) in the burnt gases close to the centerline. A very good prediction of the mean temperature evolution is otherwise obtained in the flame region at Locations 1 and 2. Temperature and mixture fraction fluctuation profiles are also well-captured in shape (Fig. 9.33), but levels are underpredicted as for Case A.

On the overall, the same trends already observed in Case A are found in Case B, with similar fluctuation levels for both LES and experimental results.

9.6.2 Comparison between Case A and Case B in canonical cases

Laminar unstrained premixed flames

The ARC_22_GRI211 scheme validation performed in SGT-100/Case B conditions on laminar unstrained premixed flames in Sec. 7.2 is shown in Fig. 9.34. Because of reduced thermal and species diffusivities, the laminar flame speed is smaller in Case B conditions (Fig. 9.34(a)). The flame CO emission index is slightly increased in the range of equivalence ratios of interest ($\phi = 0.4 - 0.6$), whereas a slight reduction of the

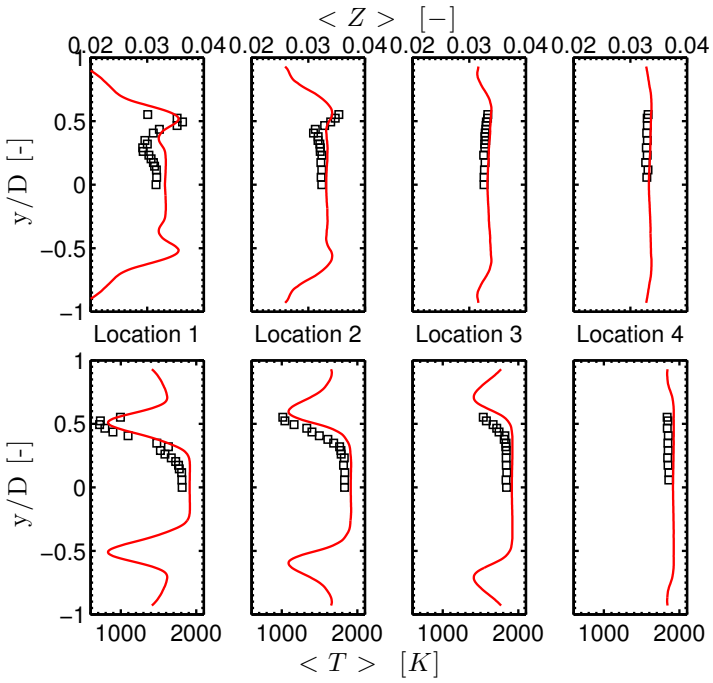

Figure 9.32: SGT-100/Case B: Transverse profiles of mean mixture fraction (top) and temperature (bottom). Comparison between LES (–) and experiments (□).

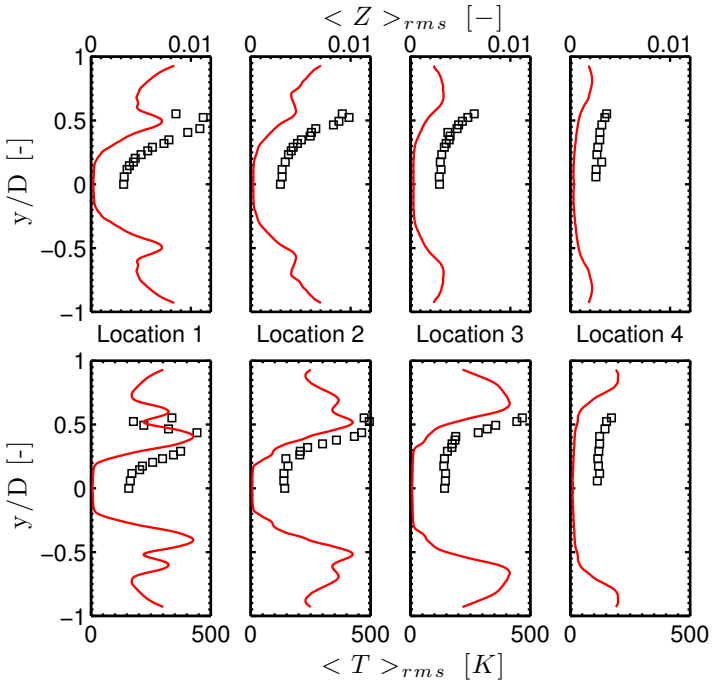

Figure 9.33: SGT-100/Case B: Transverse profiles of rms mixture fraction (top) and rms temperature (bottom). Comparison between LES (–) and experiments (□).

flame NO emission index is observed (Fig. 9.34(c)).

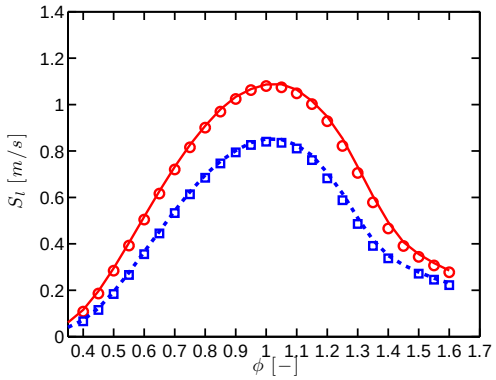

(a) Laminar flame speed.

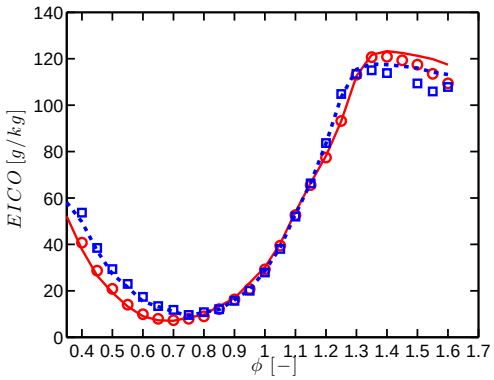

(b) EICO.

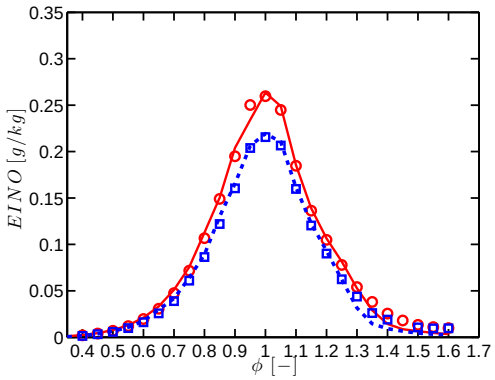

(c) EINO.

Figure 9.34: One-dimensional unstrained premixed laminar flames in SGT-100 conditions. Comparison between Case A: GRI 2.11 (—), ARC_22_GRI211 (○) and Case B: GRI 2.11 (−−), ARC_22_GRI211 (□) of a) laminar flame speed, b) EICO and c) EINO.

Pollutant chemistry in burnt gases

To study the impact of pressure on chemical processes in the burnt gases, PSRs computations are performed where an initial perturbation of the pollutant mass fraction is added to the equilibrium composition at $\phi = 0.52$ (following the NORA methodology introduced in Sec. 5.3.2). The resulting evolution of NO and CO source terms in phase space of Fig. 9.35 reveals that the higher pressure tends to promote both CO destruction and NO formation in burnt gases.

The impact of equivalence ratio is also assessed by comparing similar PSRs computations at $\phi = 0.52$ and $\phi = 0.59$ at 6 bars in Fig. 9.36. The CO destruction is rather insensitive to the increased equivalence ratio (Fig. 9.36(a)), whereas NO production is increased by one order of magnitude. Thus, the effect of equivalence ratio is expected to be dominant compared to the effect of pressure on NO formation in burnt gases.

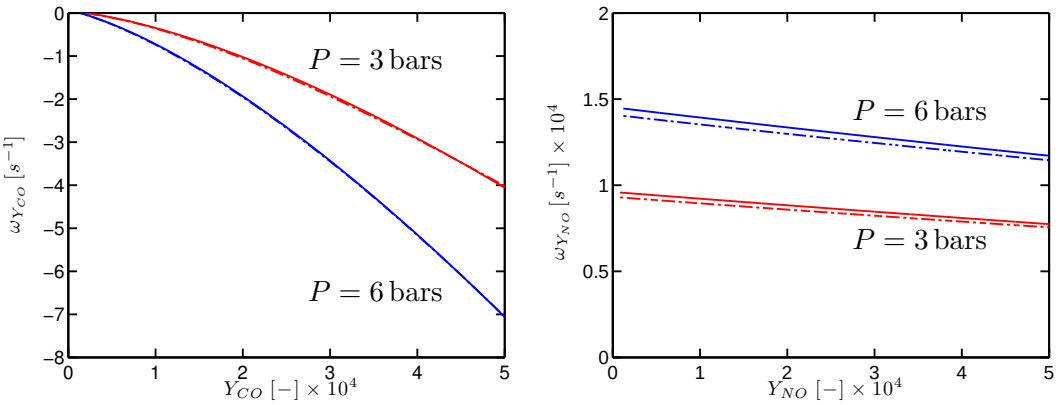

(a) CO source term in phase space.

(b) NO source term in phase space.

Figure 9.35: Evolution of PSRs in phase space after an initial perturbation of equilibrium composition at $\phi = 0.52$ for Case A (3 bars) and Case B (6 bars). Comparison between ARC_22_GRI211 ($\cdot - \cdot -$) and GRI 2.11 (—).

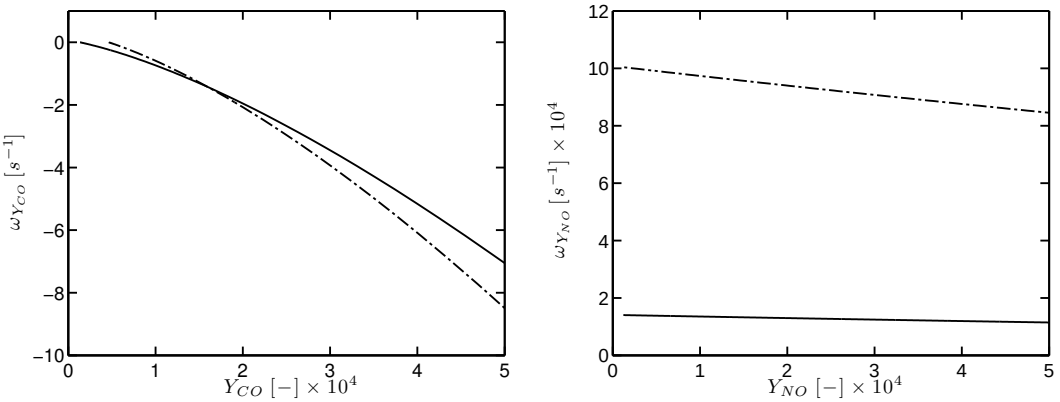

(a) CO source term in phase space.

(b) NO source term in phase space.

Figure 9.36: Evolution of PSRs in phase space after an initial perturbation of equilibrium composition for Case B, with an equivalence ratio $\phi = 0.52$ (—) and $\phi = 0.59$ ($\cdot - \cdot -$) using ARC_22_GRI211 .

9.6.3 Comparison of flame structure between Case A and Case B

Qualitative comparison

Instantaneous snapshots of OH concentration picked at random physical times are compared to instantaneous OH PLIF data in Fig. 9.37 for Case A and Case B. In both cases, no significant OH concentration is found in the outer shear layer, indicating that the flame is close to extinction in this region. The main difference between the cases appears in the inner shear layer between the swirling jet and the recirculation zone: whereas OH concentration predicted by LES is weak in that region compared to the flame tip for Case A, it is significantly higher for Case B, indicating that the mechanism promoting the flame stabilisation by the recirculation of hot gases is stronger in

this region. This behaviour is supported by the OH PLIF pictures, which also exhibit significantly higher intensity in the inner shear layer. A similar behaviour is observed

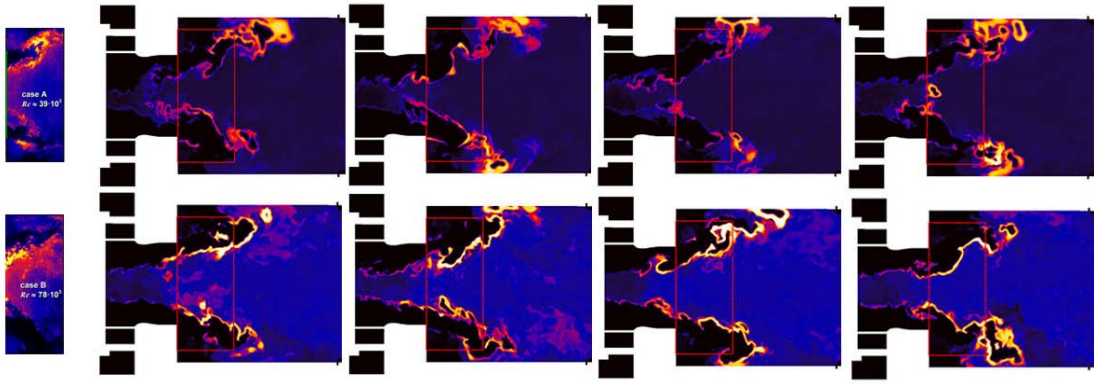

Figure 9.37: Comparison between Case A (top) and Case B (bottom) of one mapping of OH PLIF intensity and four instantaneous OH concentration fields from LES.

for CH_4 destruction rate LES snapshots in Fig. 9.38, which shows that the fuel consumption rate is higher and less intermittent for Case B in the inner shear layer than for Case A.

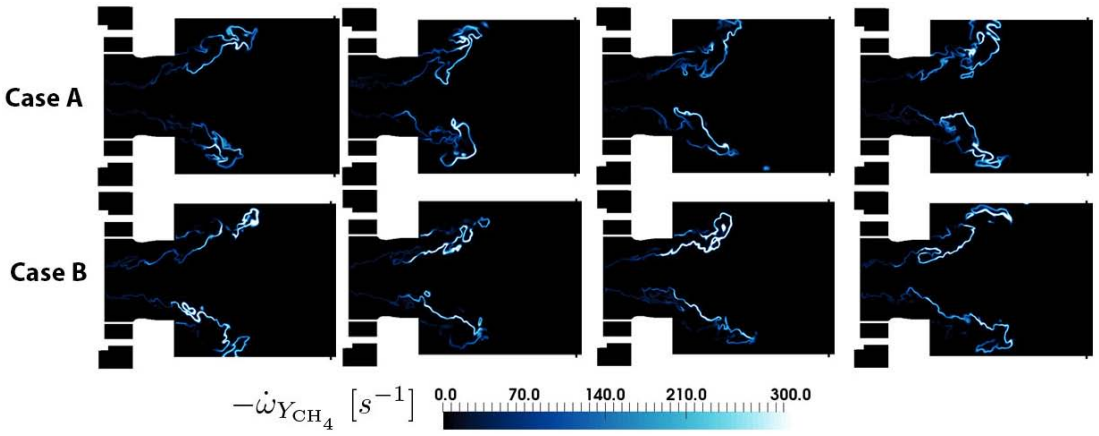

Figure 9.38: SGT-100: Comparison between Case A and Case B: four instantaneous snapshots of CH_4 destruction rate from LES.

From these observations, it can be concluded that the LES is able to qualitatively reproduce the impact of operating conditions on the flame structure.

Quantitative comparison

A quantitative comparison between the two cases of the total fuel consumption conditioned on the mixture fraction is given in Fig. 9.39. The distribution for Case B is slightly shifted towards higher Z values because of the higher global mixture fraction

(Z_{glob} = 0.0335 instead of 0.030). The levels of mixture fraction fluctuations in the flame region, characterised by the spreading of the distribution is similar for the two cases.

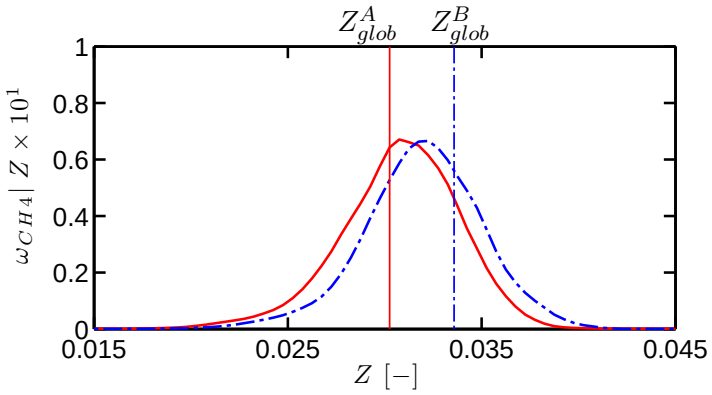

Figure 9.39: SGT-100: Normalised integrated fuel consumption conditioned on the mixture fraction vs mixture fraction. Comparison between Case A (—) and Case B (· – ·–). The vertical lines correspond to the respective global mixture fraction of both cases.

9.6.4 Impact on CO and NO_x formation

Given the distribution of emission indices shown in Fig. 9.40, under the combined effect of pressure and equivalence ratio, flame EINO and EICO increase by 50% and 10% respectively on laminar cases.

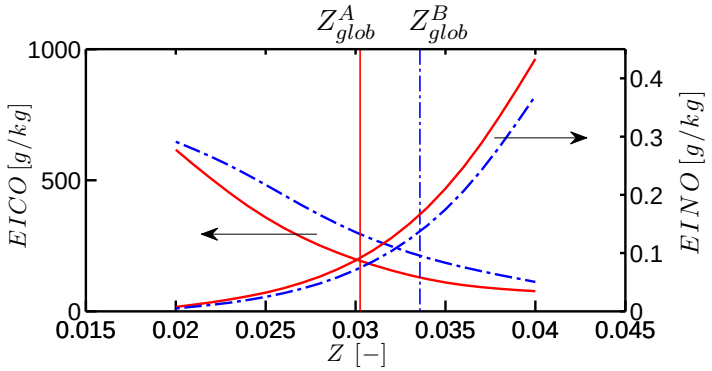

Figure 9.40: CO **and** NO **flame emission indices from unstrained premixed laminar flames vs mixture fraction. Comparison between Case A (—) and Case B (· – ·–). The vertical lines correspond to the respective global mixture fraction of both cases.**

For the turbulent flame, the actual exhaust emission values are given in Tab. 9.5. Compared to Case A, NO exhaust concentration is multiplied by 3 in the LES of Case B, and CO exhaust concentration is multiplied by 2. The impact is significantly higher than in the laminar cases, and is attributed to the post-flame processes, as will be

further highlighted. The increase in NO emissions by a factor 3 for Case B in the LES is close to the experimental value, for which a factor 3.5 is observed. However the trend observed in the experiments is not reproduced in LES for CO. A source of discrepancy might be heat losses, as will be further highlighted in Sec. 9.7.3.

	NO [ppmv]	CO [ppmv]	EINO [g/kg]	EICO [g/kg]
Case A: Experiments	5.0	3.4	0.32	0.20
Case A: LES	3.8	6	0.24	0.37
Case B: Experiments	18	4.4	1.16	0.27
Case B: LES	12	13	0.77	0.80

Table 9.5: SGT-100: Comparison between Case A and Case B for NO and CO emissions at the combustor exit with the experimental data.

Analysis of CO exhaust emission levels

CO is formed in the flame region, where it typically reaches values above equilibrium concentrations. It is further recombined at the end of the flame region and in the post-flame region. The residence time in the combustor must be sufficiently high to achieve low CO emissions, close to equilibrium values at the exhaust. To evaluate CO departure from equilibrium at the combustor outlet, the instantaneous emission index at the combustor exit plane is defined as

$$< \text{EICO} > = 1000 \frac{< \rho u Y_{\text{CO}} >)}{< \rho u Z >} , \tag{9.12}$$

where ρ is the density, u is the axial velocity, and $< \cdot >$ is the spatial averaging operator over the exit plane. It is compared with the emission index obtained with the equilibrium CO mass fraction at the outlet

$$< \text{EICO} >_{eq} = 1000 \frac{< \rho u > Y_{CO}^{eq} \left(T_{outlet}, \mathbf{Y}_{outlet}\right)}{< \rho u Z >} , \tag{9.13}$$

where

$$\mathbf{Y}_{outlet} = \frac{< \rho u \mathbf{Y} >}{< \rho u >} , \tag{9.14}$$

$$T_{outlet} = \frac{< \rho u T >}{< \rho u >} . \tag{9.15}$$

For Case A, the emission index is $< \text{EICO} >= 0.37$ while the emission index based on CO equilibrium concentration is $< \text{EICO} >_{eq}= 0.33$. For Case B, $< \text{EICO} >= 0.8$ and $< \text{EICO} >_{eq}= 0.7$. In both cases, CO levels are only slightly above equilibrium values. It indicates that the residence time in the combustor in both cases is long enough to complete CO oxidation in CO_2. It can be concluded that CO concentrations at the combustor exit are essentially driven by equilibrium values in the LES.

Analysis of NO_x formation

NO formation is analysed by decomposing it into the different chemical pathways, i.e. thermal, N_2O, NNH and prompt pathways as shown in Fig. 9.41 and Fig. 9.42. Results are qualitatively similar between Case A and Case B. The total NO source term intensity in the flame region is similar for the two cases, and in agreement with the behaviour of one-dimensional premixed flames. All the pathways shown have a significant contribution, except prompt NO which is negligible in these lean conditions. In the burnt gases, only N_2O and thermal pathways are significant, and higher in Case B which is directly related to the higher pressure and equivalence ratio, consistently with PSRs calculations detailed in Sec. 9.6.2. The overall absolute and relative contributions are given in Tab. 9.6. Thermal NO is the main contributor for both cases, with an increased contribution in Case B mainly because of higher intensity of this pathway in the burnt gases. Even if the absolute contribution of prompt NO is zero, it might still play an important role, because it is highly coupled with other chemical pathways, as described in Sec. 1.2.2. However the prompt NO contribution evaluated on one-dimensional premixed flames using the subtraction method (Sec. 1.2.2) was also found to play a negligible role in these lean conditions. This allows to conclude that it also has a negligible role in the turbulent flames.

EINO [g/kg]	Case A		Case B	
Pathway contribution	Absolute	Relative	Absolute	Relative
Thermal	0.12	44%	0.55	68%
N_2O	0.07	28%	0.15	20%
NNH	0.07	28%	0.10	12%
Prompt	0	0%	0	0%
Total	0.26	100%	0.8	100%

Table 9.6: SGT-100: Comparison between Case A and Case B: contribution of the different pathways to the total NO production.

The NO production can also be decomposed in terms of fast processes in the flame region (identified via the thickening sensor of the TFLES model) and slow processes in the burnt gases, as already done in Sec. 9.5. This decomposition is given in Tab. 9.7. The trend of both cases is consistent with zero and one-dimensional cases. The absolute contribution of the fast chemical processes is increased by a factor 2 in Case B. This value is rather consistent with the 50 % increase under the effect of higher pressure and equivalence ratio observed on laminar premixed flames. The slow post-flame processes are increased by a factor 4, which is also consistent with the increase of one order of

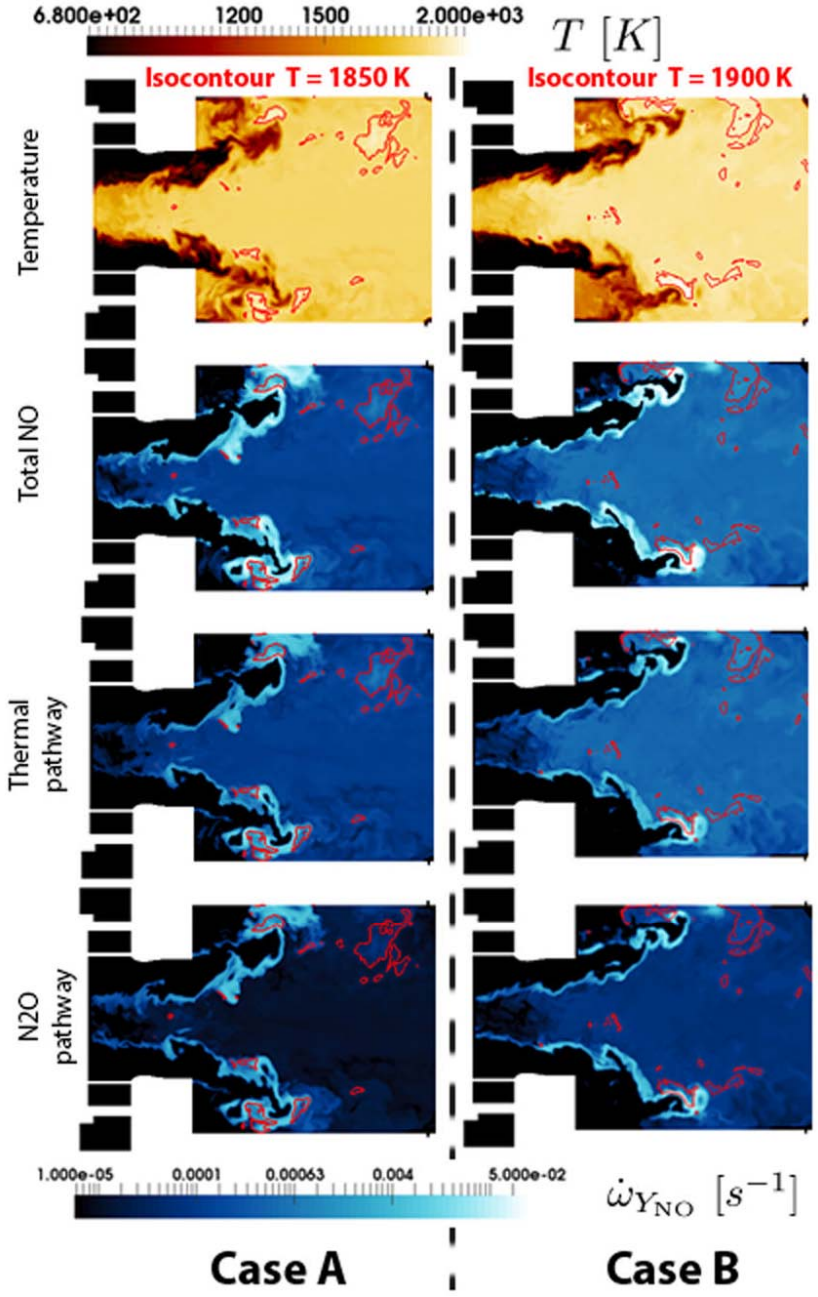

Figure 9.41: SGT-100: Instantaneous fields of temperature, NO source term, thermal and N_2O pathways. Comparison between Case A and Case B.

magnitude of post-flame NO formation expected in Case B from PSRs computations (Sec. 9.6.2).

9.7 Sensitivity to numerical and physical parameters

In this section, the robustness of the LES methodology is assessed by varying several physical and numerical parameters on Case A. The impact of turbulent subgrid scale model is first discussed. Then, the impact of the flame thickening on the flame structure

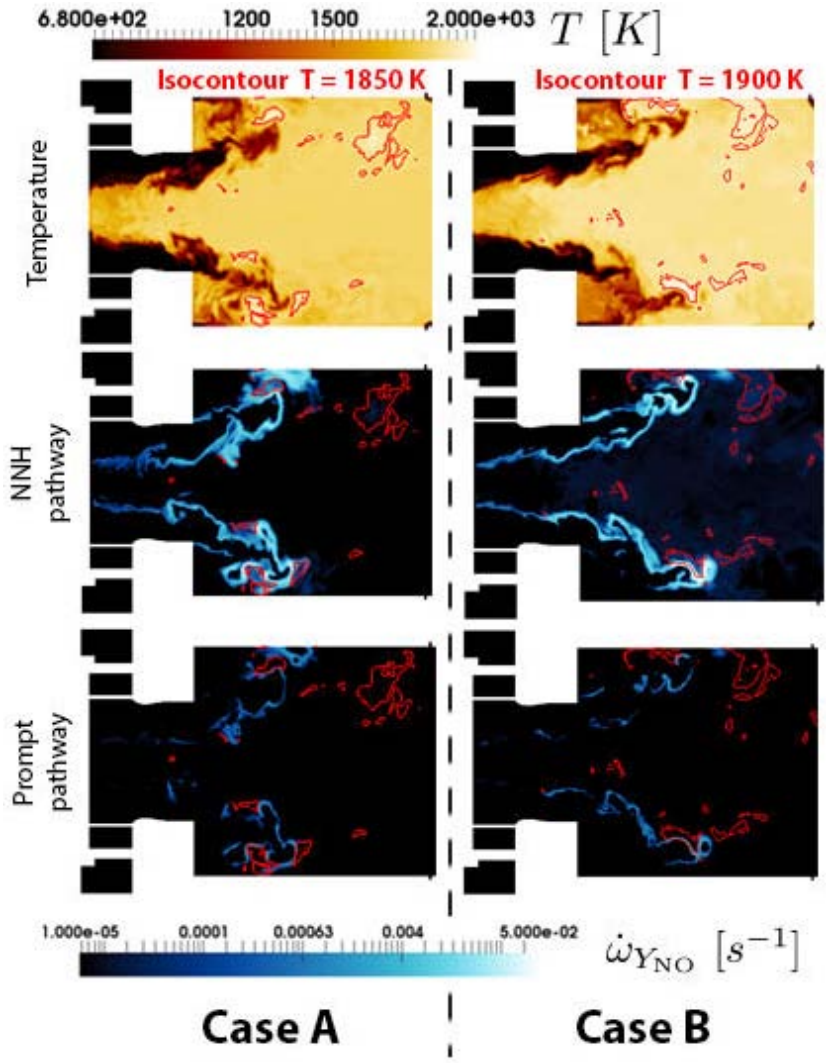

Figure 9.42: SGT-100: Instantaneous fields of temperature, prompt and NNH pathways. Comparison between Case A and Case B.

EINO [g/kg]	Case A		Case B	
	Absolute	Relative	Absolute	Relative
Flame contribution	0.1	40%	0.21	25%
Burnt gases contribution	0.16	60%	0.62	75%

Table 9.7: SGT-100: Comparison between Case A and Case B: contribution of the flame region (fast processes) and burnt gases region (slow processes) to the total NO production.

and pollutant formation is evaluated. Finally, the impact of wall heat transfer is evaluated by comparing LES computation including isothermal walls with the adiabatic reference case. Previous studies [11, 213] suggest that heat losses may significantly impact NO_x formation, given notably the high sensitivity of the thermal pathway on temperature.

9.7.1 Impact of subgrid scale model

To compare with the baseline case for which the SIGMA subgrid scale model is used, LES were also performed with the Dynamic Smagorinsky model and the WALE model. Note that in the Dynamic Smagorinsky case, wall boundaries are modelled with a law-of-the-wall approach rather than the non-slipping formulation because this model yields high non-physical levels of subgrid turbulent viscosity in the highly sheared boundary layer. To compare the three subgrid scale models, the ratio $\mathcal{R}$ is introduced, defined as the ratio of turbulent to laminar viscosity

$$\mathcal{R} = \frac{\nu_t}{\nu_{lam}} \,. \tag{9.16}$$

It is generally considered that sufficient resolution of the turbulent energy spectrum is reached if at least 80% of the total turbulent energy is resolved [165]. A more qualitative criterion is that the resolution of the flow scales are satisfactory if $\mathcal{R} < 20$. The comparison of $\mathcal{R}$ for the three subgrid scale models is shown in Fig. 9.43. The overall intensity is similar, except for the Dynamic Smagorinsky model for which the values are significantly higher in the swirler region. This model is found to be over-dissipative and leads to an underprediction of rms velocities in the swirling jet region. Compared to the SIGMA case, the WALE model leads to subgrid turbulent viscosity levels significantly higher when coherent vortical structures are detected compared to the SIGMA case. Therefore, because of the strong rotational motion of the EVC on the centerline at the combustor exit, the WALE model leads to strong dissipation in that region, significantly higher than the other two models. Typical values of $\mathcal{R} \simeq 15$ are obtained for the SIGMA model whereas $\mathcal{R} \simeq 80$ for the WALE model. This high level of turbulent viscosity leads to a misprediction of the EVC intensity and its spatial extension. This explains why the SIGMA approach with non-slipping walls was finally retained, even if the turbulent boundary layers might be under-resolved, given the grid resolution at the walls, which is in wall units around $y^+ = 40 - 60$ in the swirler vanes, $y^+ = 30 - 40$ in the premixing duct, $y^+ = 10 - 20$ in the dump plane of the combustor and $y^+ = 20 - 30$ in the outer walls of the chamber, which might typically lead to a misprediction of wall fluxes.

9.7.2 Impact of flame thickening

A direct way to evaluate the impact of grid resolution is to vary the grid size, which impacts all flow quantities. To study the flame only, an alternative choice is to vary the parameter $n_{\mathcal{F}}$ which controls the thickening factor applied in the flame front. In this way, the accuracy of the turbulent flow prediction remains unchanged, allowing to isolate the effect of the flame thickening, which may have several impacts:

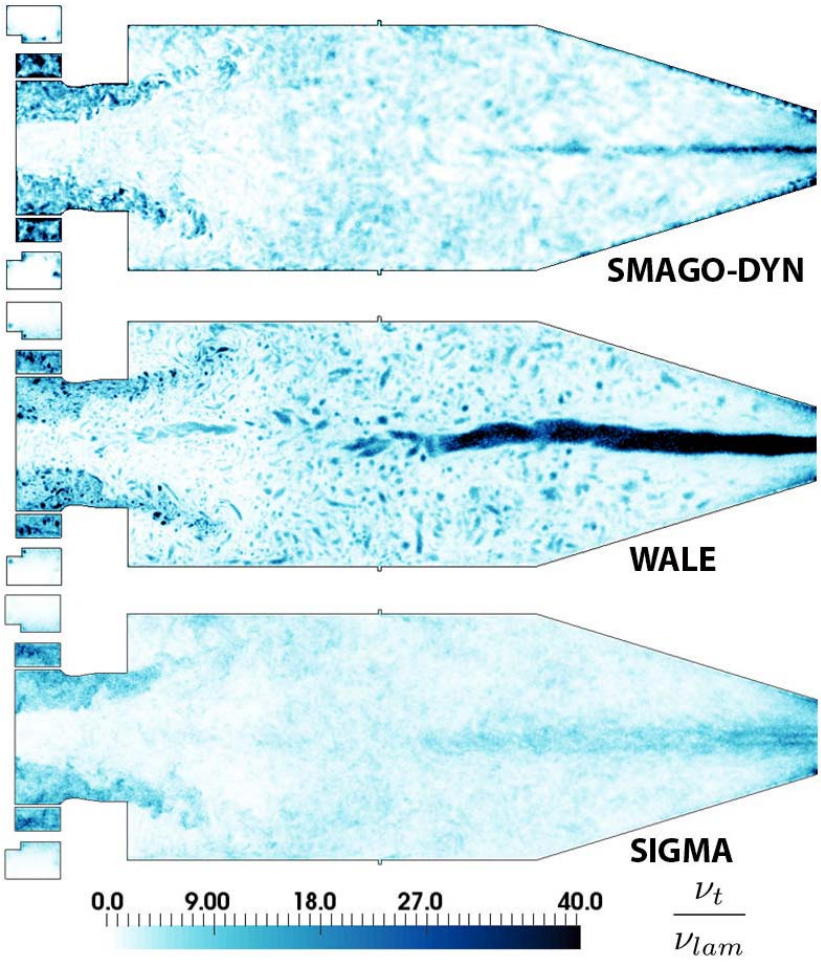

Figure 9.43: SGT-100/Case A: instantaneous fields of turbulent to laminar viscosity ratio $\mathcal{R}$ in the mid-plane of the combustor. Comparison between Dynamic Smagorinsky (top), WALE (middle) and SIGMA (bottom) subgrid scale models.

- The numerical accuracy of the resolution of the flame front depends on the the thickening. In particular, it was shown in Chapter 7 that the choice $n_{\mathcal{F}} = 5$ yields a satisfactory accuracy, even if it was slightly improved with $n_{\mathcal{F}} = 10$.

- The turbulence-flame interaction is also modified. Increased levels of flame thickening tends to reduce flame wrinkling. The flame response to strain may also be modified, as shown in Sec. 9.4.2.2. These effects are modelled via the efficiency function for the flame speed, but the impact for pollutants has to be assessed.

Two additional LES computations were performed with $n_{\mathcal{F}} = 2.5$ and 10 corresponding to typical thickening factor $\mathcal{F} = 6$ and 24, and compared with the baseline case ($n_{\mathcal{F}} = 5$, $\mathcal{F} = 12$). The thickening methodology is briefly validated by comparing the three cases: the filtered sensor used to dynamically thicken the flame should adapt to the flame resolution. The impact of $n_{\mathcal{F}}$ on the thickening sensor is illustrated in

Fig. 9.44 left. As $n_{\mathcal{F}}$ increases, the flame thickening is increased, and the reactive region identified by the unfiltered sensor $\mathcal{S}$ is larger. This can also be seen from the heat release rate fields in Fig. 9.45. Consistently, the filtered sensor $\widehat{\mathcal{S}}$ also gets wider. The sensor covers the strong density/temperature gradient region for the three cases, as shown in Fig. 9.44 right. This confirms that once correctly calibrated, the filtering methodology is able to perform well for a large range of flame thickening.

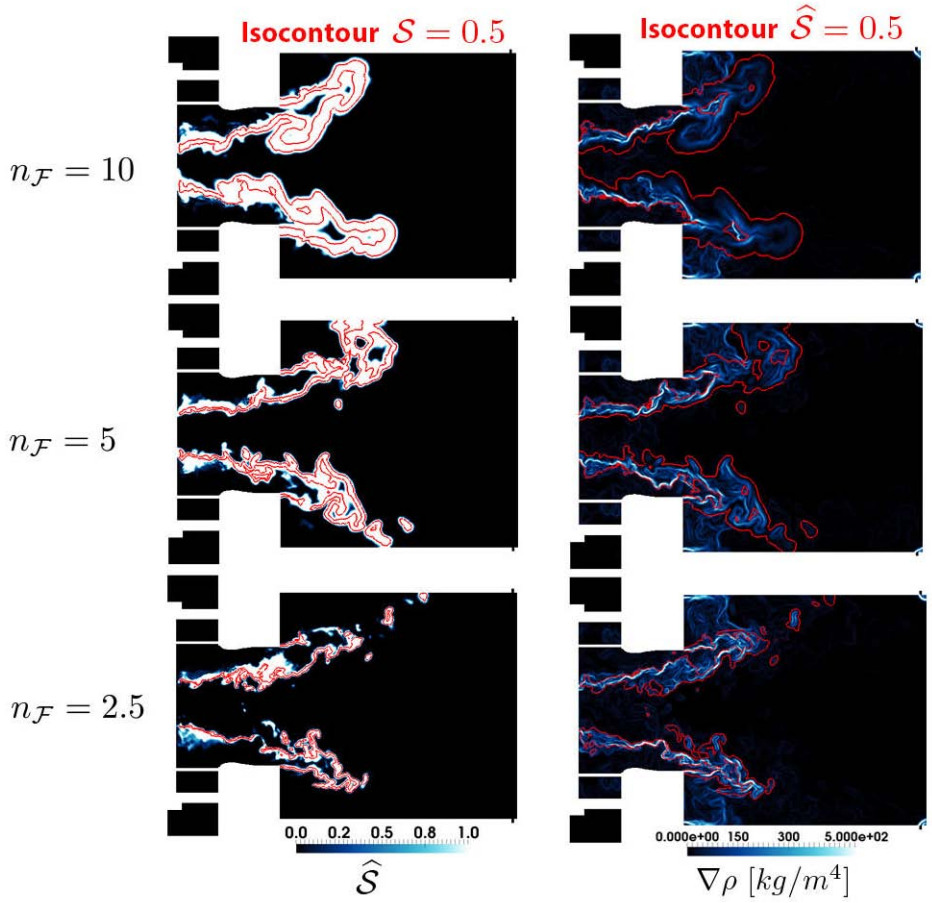

Figure 9.44: SGT-100/Case A: Instantaneous fields from LES in the mid-plane of the combustor, focused on the first half of the combustor. Left: Filtered thickening sensor $\widehat{\mathcal{S}}$. Right: density gradient. Comparison between $n_{\mathcal{F}} = 2.5$ (bottom), $n_{\mathcal{F}} = 5$ (middle, baseline case) and $n_{\mathcal{F}} = 10$ (top).

The impact of the flame thickening on the flame structure is shown in Fig. 9.45. From the temperature field, it can be seen that the small scale structures are damped by high levels of flame thickening, leading to less flame wrinkling, also shown by the heat release rate field. However, the flame shape, stabilisation and length remain similar for the three cases. This is confirmed by the quantitative comparison of transverse profiles of mean temperature and mixture fraction in Fig. 9.46, which are found to be very close for the three cases. As for rms quantities, a slight reduction of mixture fraction

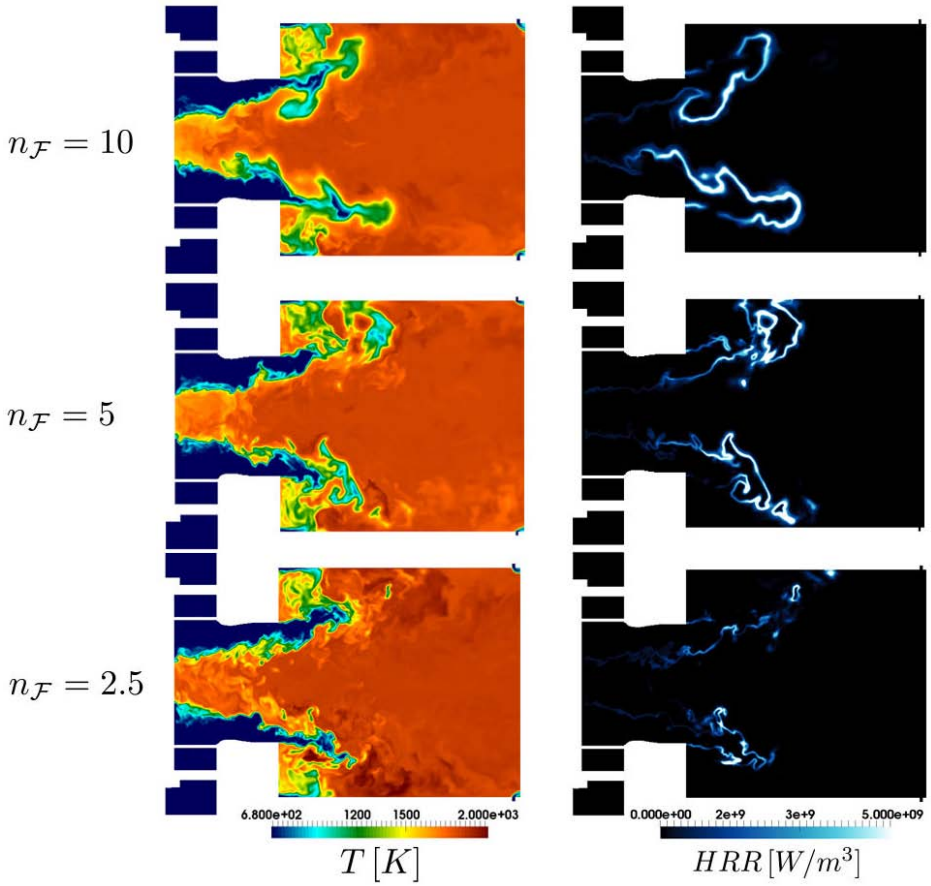

Figure 9.45: SGT-100/Case A: Instantaneous fields from LES in the mid-plane of the combustor, focused on the first half of the combustor. Left: temperature. Right: heat release rate. Comparison between $n_{\mathcal{F}} = 2.5$ (bottom), $n_{\mathcal{F}} = 5$ (middle, baseline case) and $n_{\mathcal{F}} = 10$ (top).

and temperature fluctuations can be observed in Fig. 9.47 in the case $n_{\mathcal{F}} = 10$, also evidenced from the instantaneous temperature fields.

Finally, exhaust emission levels are compared for the three cases in Tab. 9.8. As it was already pointed out, CO exit levels are essentially driven by equilibrium concentrations and are therefore insensitive to the flame resolution. NO formation is slightly impacted by the finer scale fluctuations obtained in the $n_{\mathcal{F}} = 2.5$ case, yielding exhaust NO concentration slightly increased compared to the baseline case and closer to the experimental value. It should be noted that the overall impact is however moderate (about 10% on exhaust NO concentration).

9.7.3 Impact of wall heat transfer

In all cases presented above, heat losses were not taken into account: because of the low flame temperature ($T < 2000\,\mathrm{K}$), radiative heat transfer is expected to have a

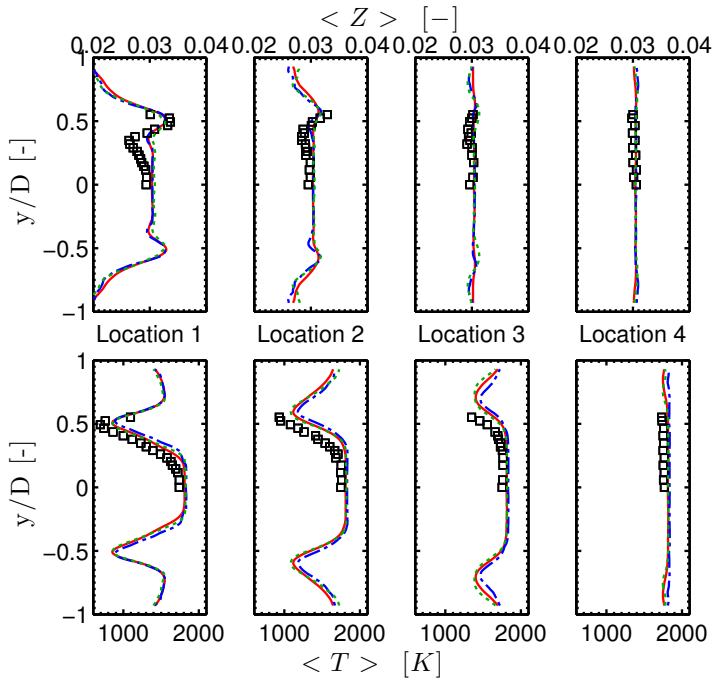

Figure 9.46: SGT-100/Case A: Transverse profiles of mean mixture fraction (top) and temperature (bottom). Comparison between LES with $n_{\mathcal{F}} = 5$ (−), LES with $n_{\mathcal{F}} = 2.5$ (· − ·−), LES with $n_{\mathcal{F}} = 10$ (· · ·) and experiments (□).

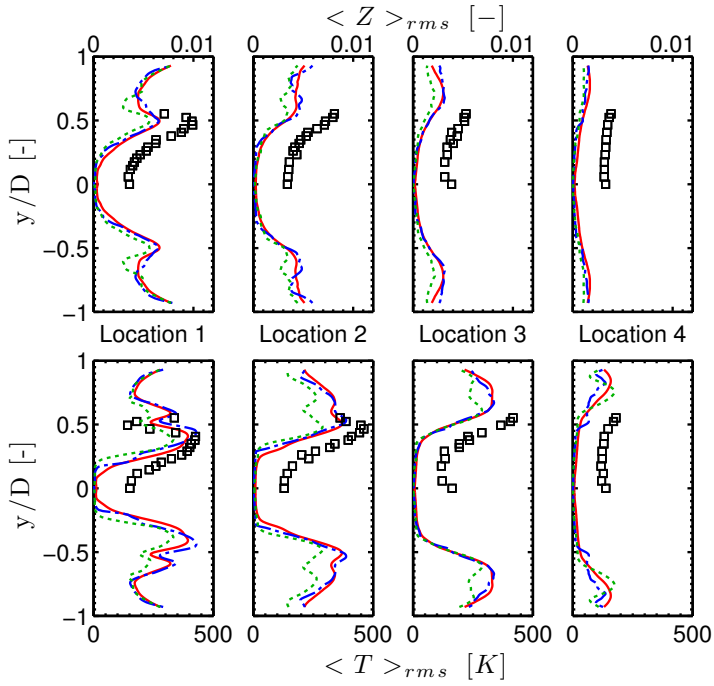

Figure 9.47: SGT-100/Case A: Transverse profiles of rms mixture fraction (top) and rms temperature (bottom). Comparison between LES with $n_{\mathcal{F}} = 5$ (−), LES with $n_{\mathcal{F}} = 2.5$ (· − ·−), LES with $n_{\mathcal{F}} = 10$ (· · ·) and experiments (□).

moderate impact. By including radiative heat losses in the LES computation of this

configuration, *Bulat et al.* showed that it could impact NO and CO prediction. Also, in this configuration, the confined flame results in interactions between reactive regions and walls: this can lead to local quenching. It may impact the flame stabilisation, CO destruction because of incomplete oxidation in CO_2 [111] and NO production because of lower temperatures in the near-wall regions.

This effect is thus evaluated in this subsection by performing LES of Case A with isothermal walls. The imposed wall temperatures are given in Fig. 9.48, and were taken from measurements.

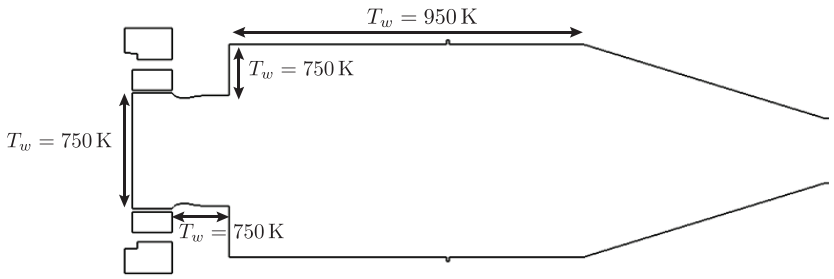

Figure 9.48: SGT-100/Case A: imposed wall temperatures for the isothermal wall case.

From the comparison of instantaneous temperature fields between the adiabatic case and the isothermal case shown in Fig. 9.49, it can be seen that wall heat fluxes have a significant impact in the CRZ region: the temperature levels are much lower for the isothermal case in this region and in the outer shear layer as well. There is also a global reduction of temperature levels in the burnt gases.

The wall heat losses also affect the flame stabilisation at the end corner of the premixing duct, as shown by the heat release rate of Fig. 9.50 left: whereas the flame anchors intermittently to the wall in the adiabatic case, the flame outer branch is completely detached in the isothermal case, under the combined effect of heat losses and high aerodynamic strain that occur in this region. In the side wall region, strong interactions between the flame and the wall occur as well, leading to local quenching: HO_2 normally peaks in reactive region and is zero elsewhere for lean premixed flames, as illustrated in Fig. 9.50 by the strong spatial correlation between heat release rate and HO_2 mass fraction. Yet for the isothermal case, the large spread of HO_2 in the vicinity of the bottom wall indicates that the chemical processes are interrupted in this region, which might significantly affect CO recombination, as will be further highlighted.

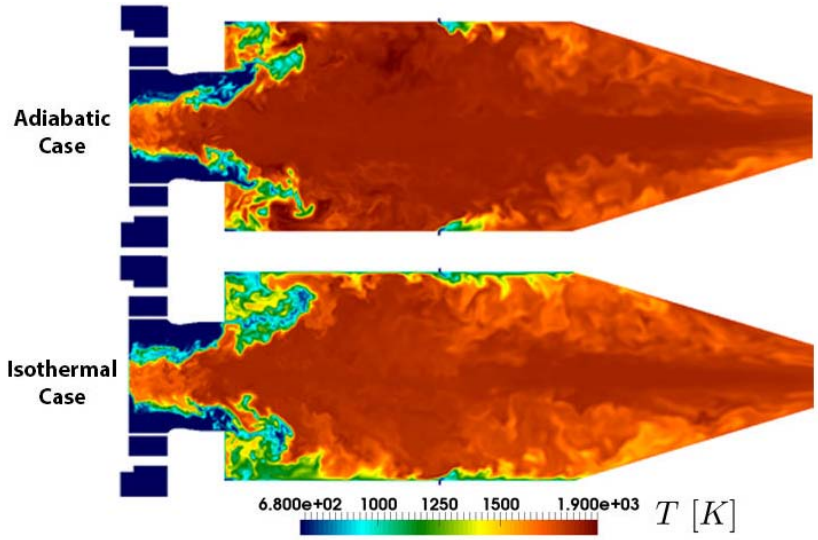

Figure 9.49: SGT-100/Case A: Instantaneous fields of temperature from LES in the mid-plane of the combustor. Comparison between adiabatic case (top) and isothermal case (bottom).

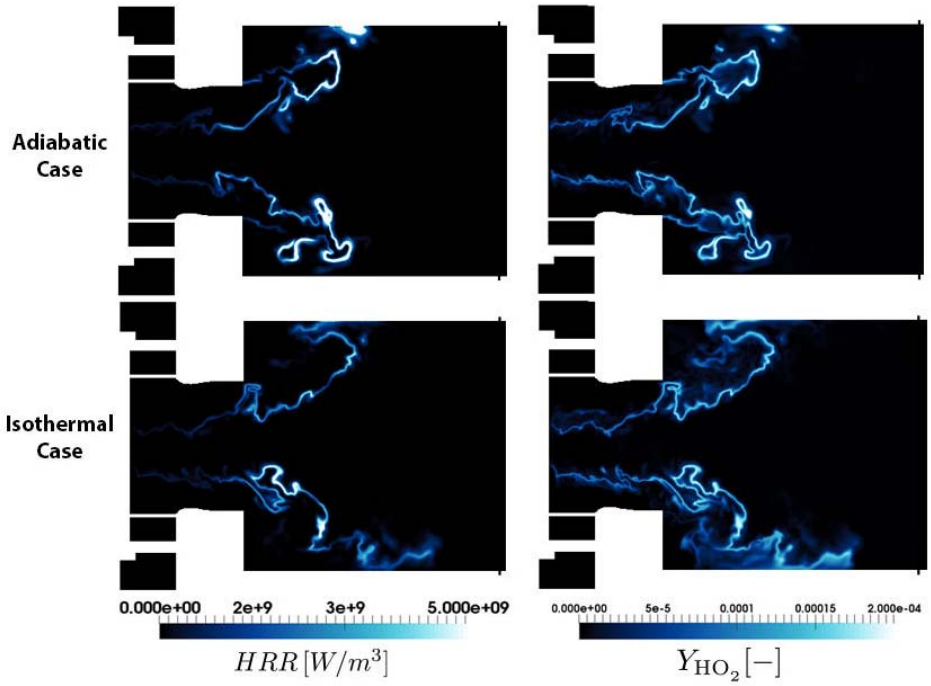

Figure 9.50: SGT-100/Case A: instantaneous fields of heat release rate (left) and HO_2 (right) from LES in the mid-plane of the combustor. Comparison between adiabatic case (top) and isothermal case (bottom).

Impact on mean profiles

As shown by the temperature field of Fig. 9.49, the introduction of heat losses has an impact on the temperature distribution. The comparison of mean temperature profiles of Fig. 9.51 shows that there is a significant reduction of temperature in the outer region for the isothermal wall case. The temperature plateau in the centerline of the

combustor is also significantly impacted at Locations 3 and 4 with a reduction by about 40 K for the isothermal wall case, which falls closer to the experimental values; this is explained by the significant contribution of the wall energy flux to the global energy budget, which represents about 15% of the total heat release rate. At the combustor exit, the mean temperature is reduced from 1740 K for the adiabatic case to to 1670 K for the isothermal case.

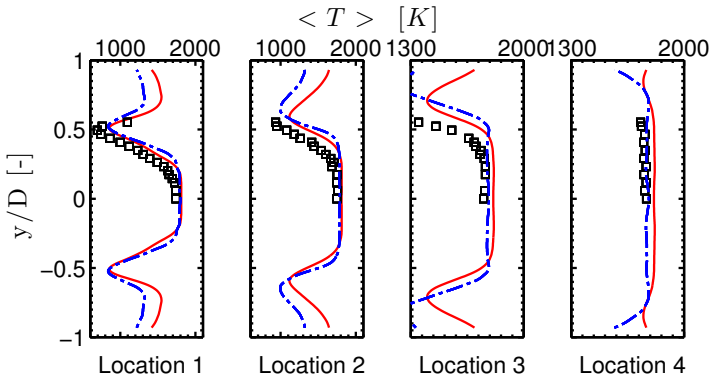

Figure 9.51: SGT-100/Case A: transverse profiles of mean temperature at the four measurement locations. Comparison between adiabatic walls case (baseline), isothermal walls case ($\cdot - \cdot -$) and experiments ($\square$).

Impact on CO formation

The instantaneous fields of CO in Fig. 9.52 reveal a behaviour similar to HO_2 intermediate. Because of the flame-wall interaction at the bottom wall of the combustor, CO recombination is quenched at the flame tip, and delayed further downstream, as indicated by the CO source term of Fig. 9.53. This leads to a large region in the vicinity of the walls having CO high concentration. The downstream recombination is slow but the residence time is long enough so that, in turns, this local quenching does not increase the exhaust CO concentrations, which remain driven by CO equilibrium. For Case A, in the adiabatic case, the emission index is $< \text{EICO} >= 0.18$ whereas the emission index based on CO equilibrium concentration is $< \text{EICO} >_{eq}= 0.16$. For the isothermal wall case considered here, $< \text{EICO} >= 0.08$ whereas $< \text{EICO} >_{eq}= 0.06$. Again CO concentrations at the combustor exit are very close to equilibrium values, which are significantly reduced because of the lower temperature. As shown in Tab. 9.8, this leads to an improved prediction of exhaust CO concentrations compared to the experiments (3 ppmv in LES compared to 3.4 for the experimental value).

Impact on NO formation

Heat losses lead to NO concentrations slightly reduced in the CRZ and close to the walls, because of the reduced temperature levels in these regions. The NO source term

being very sensitive to temperature, this results in a significant reduction of NO production by almost a factor 2 compared to the adiabatic case. Whereas CO prediction is satisfactory for the isothermal wall case, the resulting exhaust NO concentration is lower by a factor 2 compared to the experimental value.

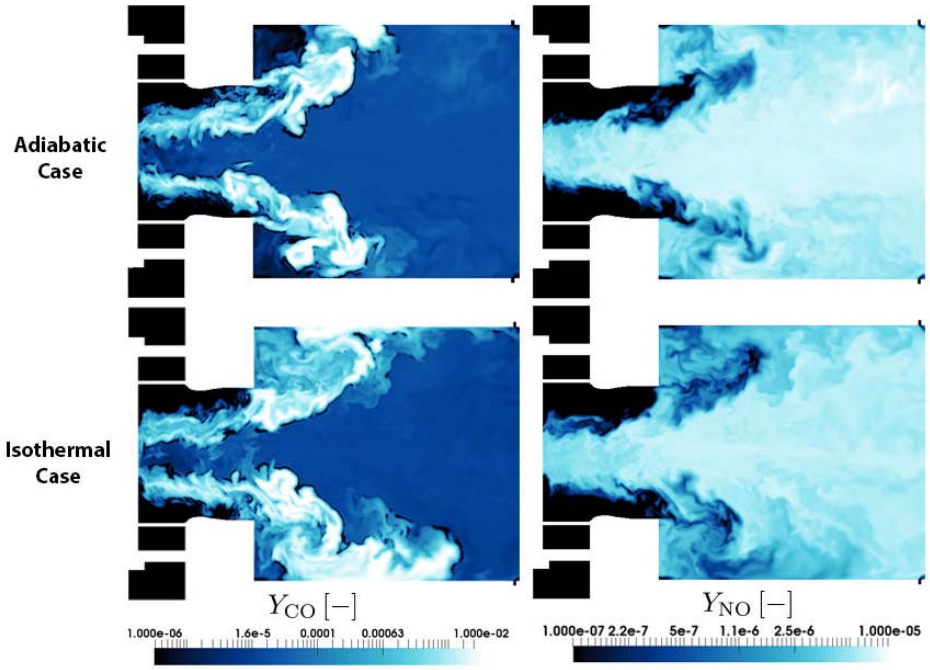

Figure 9.52: SGT-100/Case A: Instantaneous fields of CO mass fraction (left) and NO mass fraction (right, log-scale) from LES in the mid-plane of the combustor. Comparison between adiabatic case (top) and isothermal case (bottom).

	NO [ppmv]	CO [ppmv]
Experiments	5.0	3.4
$n_{\mathcal{F}} = 5$ (baseline case)	3.8	6
$n_{\mathcal{F}} = 2.5$	4.2	7
$n_{\mathcal{F}} = 10$	3.8	6
Isothermal wall case	2.3	3

Table 9.8: SGT-100/Case A: Comparison of NO and CO emissions at the combustor exit between different cases.

Conclusions on heat losses

When including wall heat losses, the agreement of exhaust temperature with the experiments is improved, as well as CO prediction. These findings tend to indicate that the isothermal walls reproduce more accurately the physics of the combustor compared to the adiabatic modelling. NO levels are reduced, which is the expected behaviour given

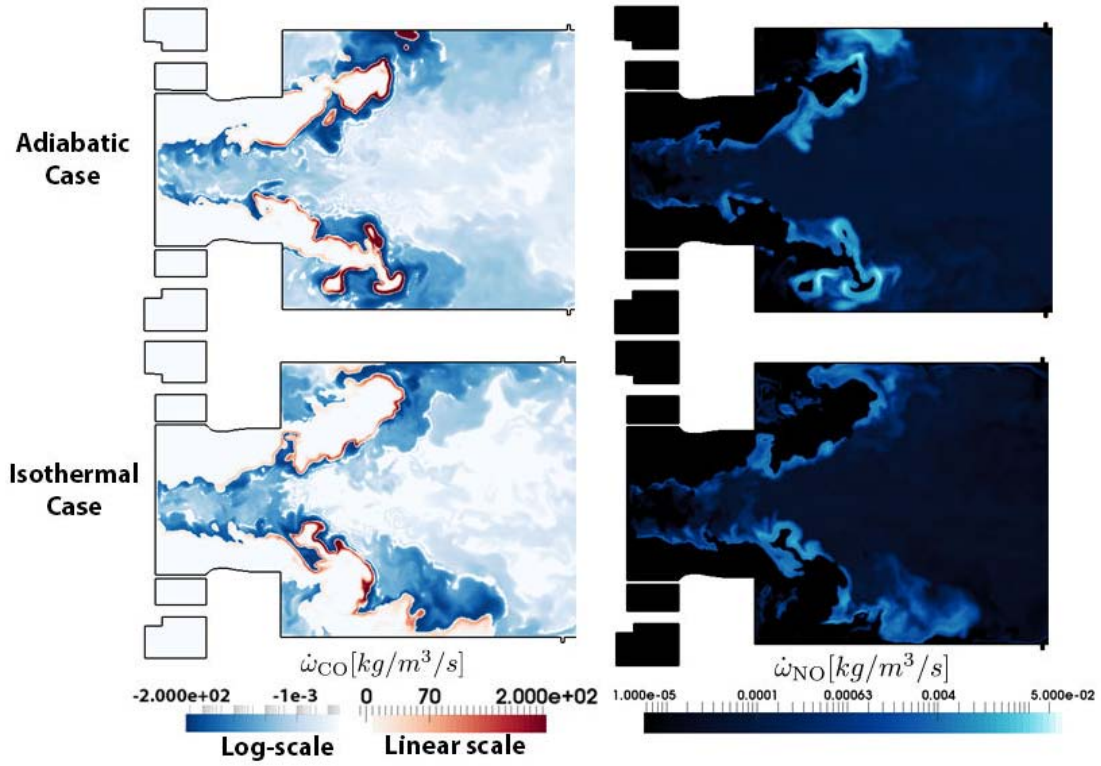

Figure 9.53: SGT-100/Case A: Instantaneous fields of CO source term (left: log-scale for negative values, linear scale for positive values) and NO source term (right - log-scale) from LES in the mid-plane of the combustor. Comparison between adiabatic case (top) and isothermal case (bottom).

the temperature reduction. However, the agreement with experiments is deteriorated. Several factors could explain this discrepancy and would require further investigations. It could be related to a misprediction of unsteady flow features, such as temperature and mixture fraction fluctuations in the flame region, to which NO formation is highly sensitive. It could also be linked to more complex phenomena, such as unsteady flame response or wall interactions, that may not be correctly captured in the LES. Also, the chemical impact of these phenomena might not be well reproduced by the ARC, which was validated only on well-identified canonical cases.

9.8 A few words about CPU time

The CPU times are compared for the different approaches in Tab. 10.4, for simulations run on 15 nodes (360 processors) of the CERFACS in-house NEMO cluster (Intel Haswell architecture). All calculations presented above used the ARC/TFLES model with chemical source terms computed at nodes (ARC @ nodes). The overcost is quite limited, about 30% if compared to the NOMAGT approach, and is essentially due to the higher number of species transport equations solved. The direct chemical source

term evaluation has a limited impact, it represents about 15% of the total calculation time.

Note that source terms computed at cells (ARC @ cells) require more CPU time, the overcost is 100% compared to the NOMAGT case. With 12 additional equations to solve, this overcost still seems reasonable. This allows to conclude that ARCs are a good compromise between CPU cost and accuracy in the present application.

Case	ARC @nodes	ARC @cells	NOMAGT
CPU time for 5 ms of physical time	39 000	62 000	30 000
% of time spent for chemical source terms evaluation	14 %	47 %	[-]

Table 9.9: SGT-100: Comparison of CPU time between the different approaches.

9.9 Conclusions

In this chapter, LES of the SGT-100 combustor was performed at two operating points. An excellent agreement is obtained in the prediction of aerodynamic flow features. The global flame structure and shape are correctly captured as well, and the comparison with laminar cases reveals that the flame structure and pollutant formation is significantly impacted by the effect of turbulence.

In terms of NO_x prediction, an acceptable agreement is obtained between LES and experimental data. In particular, the impact of the operating conditions on NO exhaust concentrations is well captured. The analysis of LES results highlights the contributions of fast flame chemical processes and slower post-flame processes of NO production. The NO_x prediction is found to be robust to the level of flame thickening of the TFLES model, which was initially derived only to correctly account for the subgrid contribution to the flame speed. On the other hand, because of the importance of thermal NO in burnt gases, a significant reduction of exhaust concentrations is observed when wall heat losses are included in the computations, driven by the significant reduction of temperature in the burnt gases ($\simeq 70\,\mathrm{K}$). The ARC/TFLES approach was also compared with the NOMAGT model which is based on tabulated NO_x chemistry: a good qualitative and quantitative agreement is obtained between the two approaches. The NOMAGT model is therefore well-suited for the partially-premixed combustion regime

of this flame.

CO exhaust concentrations are found to be essentially controlled by equilibrium at the combustor exit in the LES. Since CO equilibrium is strongly sensitive to temperature, including wall heat transfer leads to a significant reduction of CO exhaust levels. On Case A, CO exhaust concentration obtained for the isothermal wall case in good agreement with the experimental value, with a reduction by a factor 2 compared to the adiabatic case.

These results demonstrate the capability of the ARC/TFLES methodology to predict NO and CO at a reasonable CPU cost. The chemical response to turbulence-flame interactions and enthalpy losses and its impact on pollutant formation are correctly accounted for by the ARC. Moreover, the additional CPU cost is moderate compared to tabulated approaches.

An in-depth validation of the methodology would require experimental data related to NO_x and CO inside the combustor, which is difficult to obtain due to the inherent complexity of measurements in high pressure and high temperature industrial configurations.

10

LES of the LEMCOTEC prototype combustor

Contents

10.1 Objectives

The prototype of ultra-low NOx combustor currently being developed by SNECMA as part of the LEMCOTEC project (see Sec. 1.3.2) is the target industrial application of this thesis. It is a full annular combustor, with radially staged multipoint injection system. The design issues related to this type of combustor were presented in Sec. 1.3.4.

Experimental campaigns are performed on mono-sector configurations to discriminate between different designs of the injection system, prior to full annular testing, which is the final objective of the project. Numerous campaigns have been conducted by SNECMA to improve the design of low-NO_x injection systems, enabling to evaluate the performance of the injection system for various operating points and fuel-staging. However, given the relatively high temperature and pressure conditions (inlet temperature up to 900 K and pressure up to 30 bars), the optical diagnostics are costly and limited. In this scope, LES provides a better understanding of the driving mechanisms of the overall performance of the combustor, that can be helpful in the optimisation process of the injection system. Previous LES studies of a multipoint injector have been performed by *Jaegle et al.* [91] (TLC project) and *Hannebique et al.* [78] (TECC project), validating and comparing Eulerian and Lagrangian approaches for the description of the dispersed phase. Transverse thermoacoustic instabilities have also been investigated by *Ghani et al.* [68] on a similar configuration as part of the KIAI project. The effect of fuel-split parameter on flame structure and combustor thermoacoustic stability on a similar configuration has also been assessed in the frame of this thesis and can be found in *Bauerheim et al.* [14]. In this chapter, the ARC/TFLES methodology is applied to a mono-sector injection system prototype studied experimentally at ONERA [75] and retained for the LEMCOTEC project. The goal is to demonstrate the applicability of the methodology in complex two-phase flow configurations, and to provide a first evaluation of its capability in terms of NO_x and CO prediction.

To do so, a reduced scheme with NO_x chemistry, based on a detailed mechanism for aeronautical fuel surrogate is derived and validated on canonical cases in Sec. 10.3. Further, the numerical setup is described and the analysis of the LES results allows to demonstrate the applicability of the methodology in Sec. 10.5. Its predictability is assessed by comparing available measurements with numerical results. Note that some details related to the geometry and the operating point are not be provided for confidentiality purposes.

10.2 Description of the configuration

10.2.1 The multipoint injection system

Two global views of the injection system are shown in Fig. 10.1. Because of radial staging, the injection system can be decomposed in two parts:

- **The pilot injection system** includes two co-rotating swirlers and a hollow-cone central injector. The diameter of the pilot exit is 30 mm.

- **The multipoint injection system** surrounds the pilot. It includes a radial swirler with 16 swirler vanes, referred to as multipoint swirler. The fuel is injected through a series of 16 plain holes located on the inner wall downstream of multipoint swirler vanes. The injection of liquid fuel in this swirling environment is expected to promote efficient atomization and rapid mixing between the fuel and the surrounding fresh air, to achieve high level of premixing. The diameter of the multipoint system exit is 60 mm.

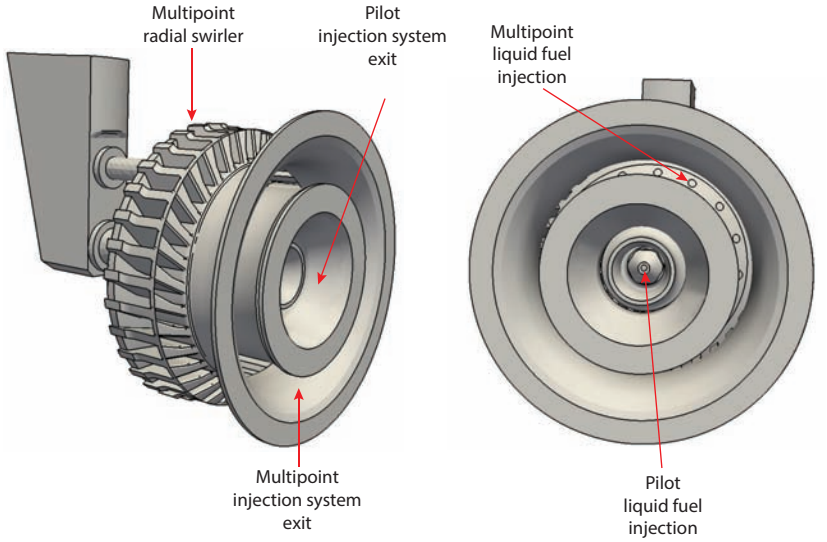

Figure 10.1: LEMCOTEC: Views of the staged multipoint injection system.

10.2.2 The experimental rig

For the experimental study, the injection system was installed in a square-cross section chamber, and connected to an exit convergent, as depicted in Fig. 10.2. The square section has a side length of 50 mm. About 30% of the total air mass flow is used for film cooling to protect the access windows and the rig walls from hot gases. The combustion process occurs in the square part of the combustor prior to acceleration of the flow in the converging section. In the experiments, the convergent is connected to an exhaust pipe, which is not taken into account in the simulation.

10.2.3 Operating point for LES study

The operating point retained for the LES study corresponds to a stabilised operating point of the combustor, with high inlet temperature and pressure. The exact conditions cannot be disclosed, but the combustor pressure is of the order of 10 bars. They are referred to as LEMCOTEC conditions hereafter. The fuel-split parameter α_{split}, defined

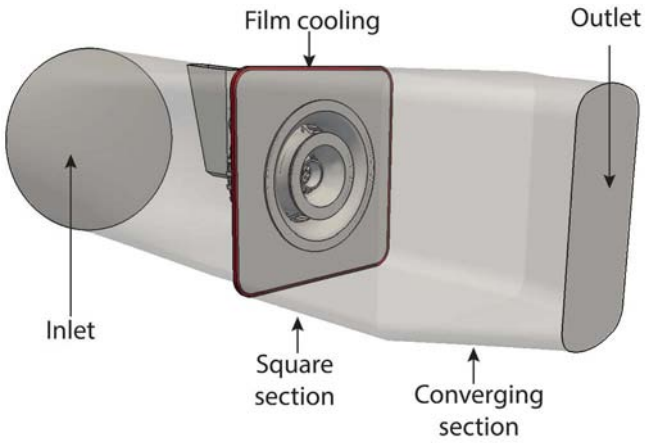

Figure 10.2: LEMCOTEC: View of the experimental rig installed at ONERA.

α_{split}	ϕ_{glob}	Z_{glob}	Z_{st}
11.9%	0.440	0.028	0.062

Table 10.1: LEMCOTEC: Characteristics of the operating point.

as the ratio of pilot fuel mass flow rate to total fuel mass flow rate, is given in Tab. 10.1, along with the global equivalence ratio ϕ_{glob} of the combustor, which is operated in globally lean conditions. Again, the mixture fraction is based on the carbon atom and is taken equal to 0 in the air stream and equal to 1 for pure fuel. The global mixture fraction Z_{glob} and stoichiometric mixture fraction Z_{st} are also provided in Tab. 10.1.

10.3 Derivation of an ARC for aeronautical fuel with NOx chemistry

Kerosene is composed of hundreds of chemical components, and varies significantly. Its exact description is completely out of scope for numerical studies. Therefore, before reducing chemistry, an appropriate surrogate must be determined to describe kerosene-air combustion.

10.3.1 Surrogate fuel and kinetic scheme for kerosene

Commercial kerosenes are typically composed of parrafins, naphthens and aromatics. The average chemical formula ranges from $C_{10.9}H_{20.9}$ to $C_{12}H_{23}$ [42]. They can be generally represented by a surrogate fuel with a limited number of hydrocarbons, that are chosen to suitably reproduce their physical properties (e.g. surface tension, boiling temperature) and chemical properties (e.g. flame speed). Surrogates are typically composed of long hydrocarbon chains, from n-octane to n-hexadecane, along with cyclic hydrocarbons such as methylcyclohexane. Simple surrogates initially consisted

of n-decane only, then other molecules such as aromatics were included to better account for benzene formation. Detailed chemical kinetic schemes for such surrogates are available. For example, the Dagaut mechanism [42] includes 209 species and 1673 reversible reactions, to describe the combustion of a surrogate based on n-decane (74%), n-propylbenzen (15%) and n-propylcyclohexane (11%). The Luche skeletal mechanism derives from the El-Bakali_Ristori detailed kinetic scheme [129] (91 species and 991 reactions), and was also employed to derive a 2-step reduced mechanism for kerosene-air combustion [64].

In this work, the simple surrogate n-dodecane ($nC_{12}H_{26}$) is used. This choice is based on the observation that n-dodecane is one of the main component of surrogates found in the literature [42] for kerosene. It exhibits combustion properties close to kerosene. Its standard enthalpy of combustion $\Delta_c H^0 = 46.4\,\mathrm{MJ/kg}$ is close to kerosene typical values (46.2MJ/kg) and the laminar flame speed is also well reproduced. The skeletal mechanism retained is JetSurf 1.0-l [183], which is a simplified version of JetSurF 1.0 [183]. It features a lumped model for n-alkane cracking and is based on the detailed USC Mech II [204] for the pyrolysis and oxidation of C1-C4 hydrocarbons. It originally includes 120 species and 977 reactions. A reduced mechanism for n-dodecane based on the same detailed mechanism was derived in [200] using methods similar to YARC, yielding a reduced mechanism with a reasonable number (24) of transported species. As the JetSurf 1.0-l does not contain any NO_x chemistry, the one from the Luche mechanism is added (17 additional species and 245 additional reactions).

10.3.2 ARC derivation with YARC

The same methodology as for methane (Sec. 6.2.2) is used to derive an ARC here for kerosene surrogate. The series of flames used for the reduction process consists of three premixed flames with equivalence ratios $\phi = 0.6 - 1.0 - 1.4$ in the target LEMCOTEC operating conditions.

After application of the DRGEP, 47 species remain in the detailed mechanism. Using LOI, QSSA is then applied to 20 species. The retained transported and QSS species in the final ARC_27_JETSURF scheme are provided in Tab. 10.3. The final mechanism contains 452 reactions (forward and backward reactions being counted separately).

10.3.3 Validation on canonical cases

Laminar premixed flames

The ARC_27_JETSURF scheme is validated by performing a series of one-dimensional unstrained premixed flame in the target operating conditions, and for equivalence ratio

Transported species	N_2 H H_2 O OH O_2 H_2O HO_2 CO CH_2O CH_3 CO_2 CH_4 C_2H_6 C_2H_4 CH_2CO C_2H_2 C_3H_6 C_4H_8−1 C_4H_6 C_5H_{10} C_6H_{12} $nC_{12}H_{26}$
Transported NO_x species	NO NO_2 HCN N_2O
QSS species	H_2O_2 CH CH_2 CH_2(S) HCO C_2H_5 C_2H_3 CH_3O HCCO C_2H aC_3H_5 CH_2CHO nC_3H_7 C_4H_7
QSS NO_x species	N NH NCO NH_2 HNCO HNO

Figure 10.3: Transported and QSS species in ARC_27_JETSURF.

in a range that is typically found inside the combustor. The comparison is shown in Fig. 10.4. The results obtained with the reduced mechanism are compared with its detailed scheme (JetSurf), and with the Dagaut mechanism, which has the most refined description of kerosene oxidation and the largest range of validity, thus serving as a reference. The comparison is also performed with the Luche mechanism, from which the NO_x chemistry was extracted. The surrogate employed for Dagaut and Luche mechanisms was previously described (n-decane (74%), n-propylbenzen (15%) and n-propylcyclohexane (11%)). The comparison of adiabatic flame temperature in Fig. 10.4(a) shows the excellent agreement of JetSurf and ARC_27_JETSURF with Dagaut and Luche mechanisms, although different surrogate are employed. The ARC_27_JETSURF slightly underpredicts the laminar flame speed compared to JetSurf in lean conditions, but agrees fairly well with the Dagaut mechanism. On the other hand, the Luche mechanism exhibits significantly higher laminar flame speeds on the rich side. Flame emission indices are defined following Eq. 9.3 and Eq. 9.2. In terms of CO flame emission index, a very good agreement between the three detailed mechanisms and the ARC is obtained. For NO, although the same NO_x chemistry is employed for the three detailed kinetic schemes, the three detailed mechanisms yield different results in the range $\phi = 0.8 - 1.4$, the peak around stoichiometry being significantly lower for JetSurf. This is due to NO formation being highly coupled with the fuel oxidation process. However this is considered acceptable given the uncertainties on NO_x chemistry at these high temperature and pressure conditions. ARC_27_JETSURF agrees well with JetSurf, with a slight overprediction of flame EINO for equivalence ratios in the range $\phi = 0.9 - 1.3$. As flame NO formation is only a part of the total NO production, a validation of burnt gases NO_x chemistry is further performed.

NO_x chemistry in burnt gases

The validity of the ARC_27_JETSURF for NO chemistry in burnt gases is assessed by performing three PSRs computations, for equivalence ratios $\phi = 0.6 - 1.0 - 1.4$ that

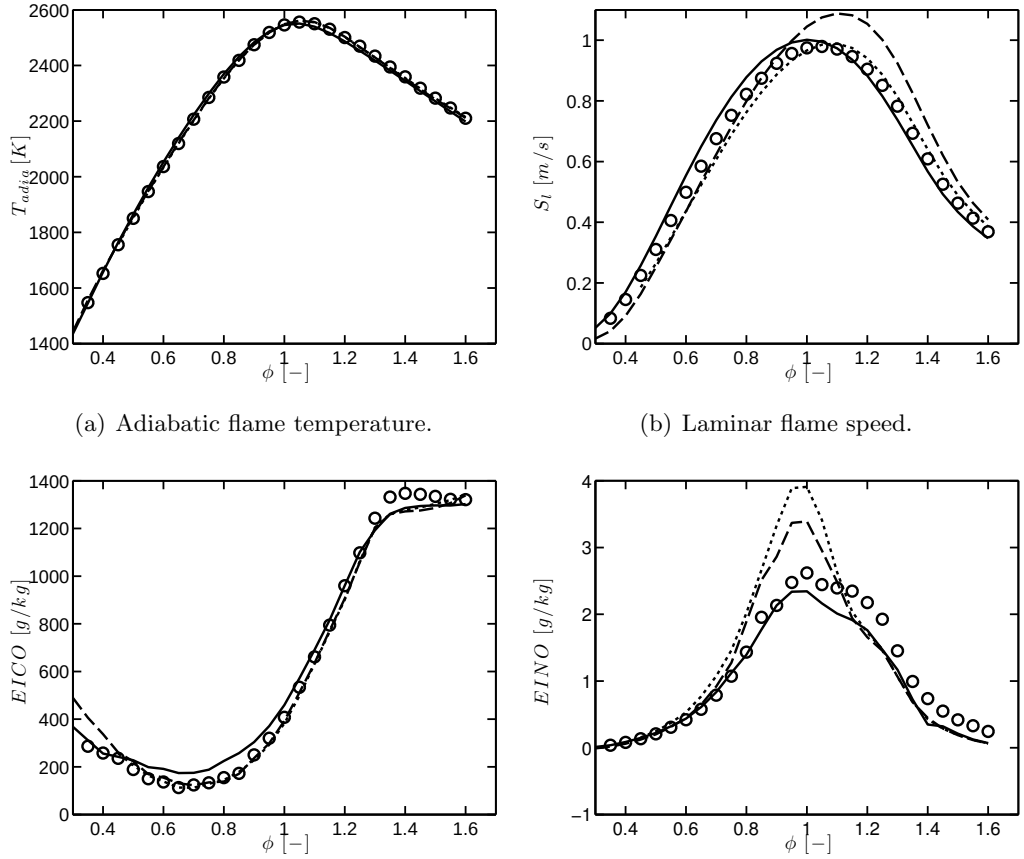

(a) Adiabatic flame temperature.

(b) Laminar flame speed.

(c) Flame EICO.

(d) Flame EINO.

Figure 10.4: Laminar unstrained premixed flames in LEMCOTEC conditions. Comparison of a) adiabatic flame temperature, b) laminar flame speed, c) flame EICO and d) flame EINO between JetSurf mechanism (—), Dagaut mechanism ($\cdots$), Luche mechanism ($--$) and ARC_27_JETSURF ($\circ$).

are representative of the combustor conditions. As in Sec. 5.3.2, the NORA methodology is followed: starting from equilibrium, the chemical composition is perturbed by setting NO concentration of to zero. The trajectory of the NO source term in phase space (Y_{NO}) is extracted and compared in Fig. 10.5 between Luche mechanism and ARC_27_JETSURF. Note that Luche and Dagaut mechanisms yield identical trajectories. An excellent agreement is obtained for the lean and the stoichiometric case (Fig. 10.5(a) and Fig. 10.5(b) respectively), while a slight departure is observed in rich conditions (Fig. 10.5(c)) which stays however largely acceptable.

10.3.4 Stiffness of the ARC_27_JETSURF

Similarly to the ARC validation of Chapter 6, the temporal stiffness of the mechanism is evaluated by extracting the chemical times for the transported species of the mechanism from a one-dimensional premixed flame, at stoichiometric conditions because it is found

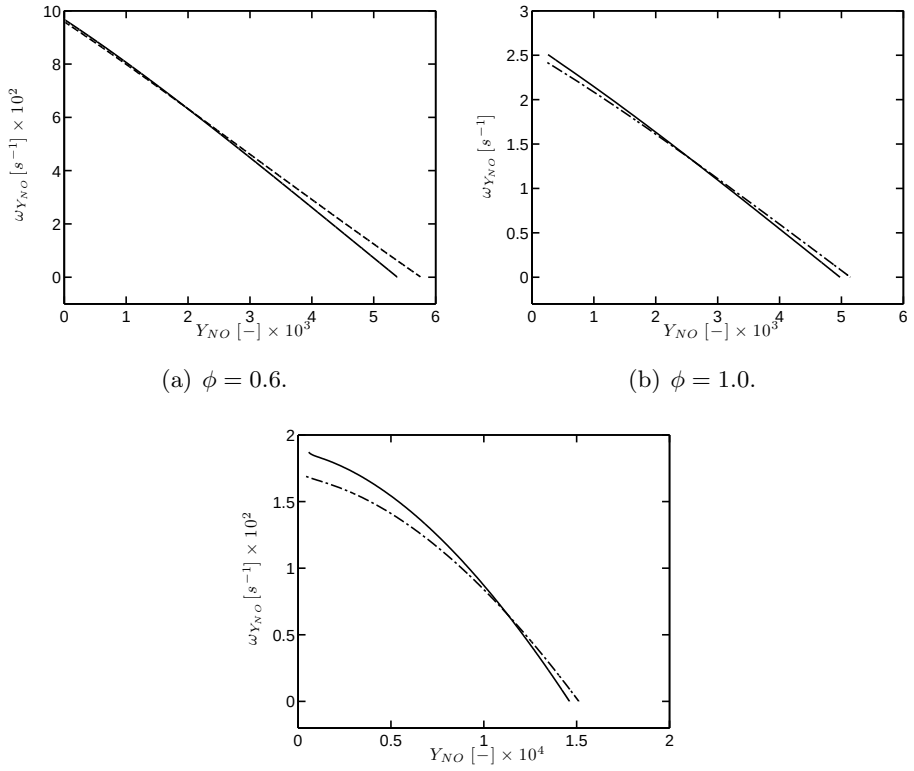

(a) $\phi = 0.6$. (b) $\phi = 1.0$.

(c) $\phi = 1.4$.

Figure 10.5: Evolution of NO source term in phase space extracted from PSR calculations after an initial perturbation of equilibrium composition, for three equivalence ratios. Comparison between Luche mechanism (—) and ARC_27_JETSURF ($\cdot - \cdot$—).

to lead to the lowest chemical times. Figure 10.6 shows that most species have chemical time scales larger than the time-step that will be used in the LES (see Sec. 10.4). Seven species have lower time scales, leading to numerical instabilities, which can be remediated either by subcycling (Sec. 6.5.2) or implicit solving (Sec. 6.5.3). As shown in Fig. 10.6, a large amount of subiterations would be necessary (more than 10) to handle the stiffnesses, which is not computationally efficient. Instead, it was preferred to solve $nC_{12}H_{26}$, H, O and HO_2 implicitly, which was sufficient to remove the numerical instabilities.

10.4 Numerical setup

LES is performed using AVBP, with the TTGC scheme. The same scheme is used for the dispersed phase, which is described by the Eulerian approach introduced in Chapter 3. Turbulent subgrid stresses are modelled with the SIGMA eddy viscosity model [144]. The inlets and the outlet are described by Navier-Stokes characteristic boundary conditions (NSCBC) [160]. The unstructured mesh comprises 86 million

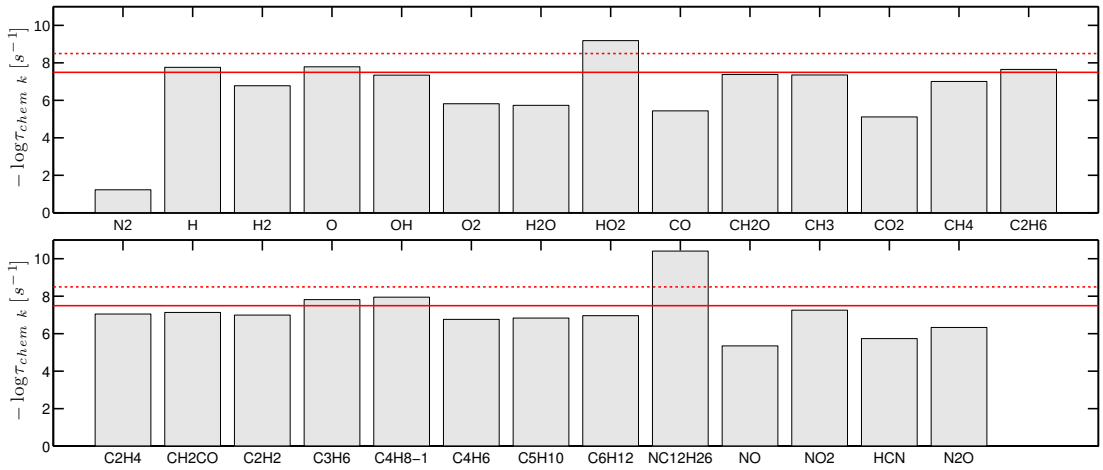

Figure 10.6: Species chemical times extracted from a one-dimensional premixed flame at $\phi = 1.0$ in LEMCOTEC conditions. The continuous line corresponds to the time-step employed in the LES computations ($\Delta t = 3.0 \times 10^{-8}$ s) and the dotted line to the time-step with 10 chemical subiterations ($\Delta t^* = \Delta t/10$).

tetrahedral elements. The grid size distribution is shown in Fig. 10.7. The characteristic grid sizes are $\Delta x = 0.5$ mm in the multipoint swirler vanes, $\Delta x = 0.25$ mm in the pilot swirler vanes and the exit region of the pilot zone and $\Delta x = 0.5$ mm in the multipoint flame region. The grid is coarsened downstream to reach $\Delta x = 0.8$ mm at the exit and in the central recirculation zone. The time-step imposed by the CFL condition is $\Delta t^{CFL} = 40$ ns. However, a smaller time-step of $\Delta t = 30$ ns was required by the stability constraint of the diffusion of species H, which has a high diffusivity ($Sc_{\mathrm{H}} = 0.12$).

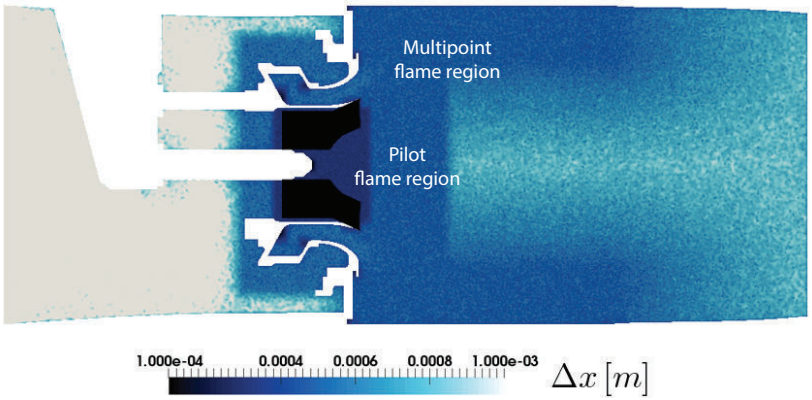

Figure 10.7: Characteristic grid size in the mid-plane of the LEMCOTEC combustor.

10.4.1 Liquid fuel injection

To correctly describe the spray dynamics, the liquid injection of the pilot and the multipoint injectors must be properly defined. The atomisation process can not be simulated

in the present LES and models are used to inject the already formed spray.

Pilot injection: hollow cone spray model

A hollow cone with a half-angle of 30° and Sauter mean diameter (SMD) SMD = 40 µm (from SNECMA data) is defined, following the FIM-UR methodology [175]. It imposes velocity and number of droplets profiles to reproduce the spray issued from a pressure-swirl atomiser. The characteristic axial velocity of the spray is $u_l = 60\,\mathrm{m/s}$, the characteristic radial velocity is $u_l^r = 30\,\mathrm{m/s}$ and the characteristic orthoradial velocity which generates the rotational motion is $u_l^\theta = 10\,\mathrm{m/s}$. The pilot injection inlet is discretised with 15 tetrahedral elements in its diameter.

Multipoint injections: jet in crossflow model

The multipoint injection corresponds to a series of jet-in-crossflow. Such configuration was studied experimentally by *Freitag and Hassa* [66] and *Bellofiore et al.* [15], who identified the main physical parameters governing the liquid jet dynamics. A first governing parameter is the momentum flux ratio between the liquid and the gas phase

$$q = \frac{\rho_l u_l^2}{\rho u^2}\,. \tag{10.1}$$

As shown in Fig. 10.8, this parameter strongly modifies the penetration of the liquid jet. *Jaegle* [89] showed that this could be correctly reproduced by Eulerian and Lagrangian formalisms, as shown in Fig. 10.9. A good agreement of statistical quantities between the Lagrangian polydisperse modelling and the Eulerian monodisperse approach was obtained.

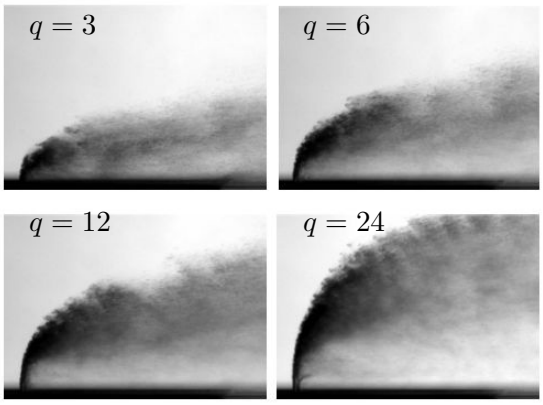

Figure 10.8: Shadowgraphs of liquid jet in crossflow. Effect of momentum flux ratio q. From *Freitag and Hassa* [66].

Note that near the injection hole, the assumption of a dispersed liquid phase does not hold. Indeed, at the exit of the injection hole, a liquid column forms that is further atomised by the entraining air. A dedicated model was developed by *Jaegle* [89] to

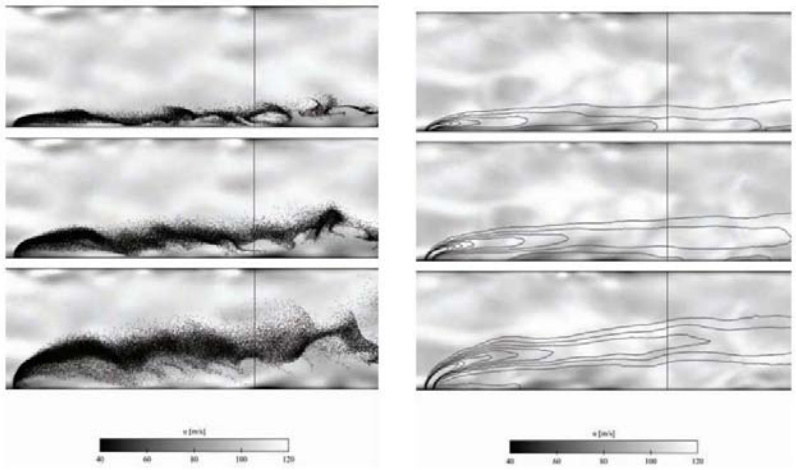

(a) Euler-Lagrange. (b) Euler-Euler.

Figure 10.9: Comparison of Euler-Lagrange and Euler-Euler results on a jet-in-crossflow configuration. From top to bottom: $q = 2$, $q = 6$ and $q = 18$. From [90].

correctly account for this effect. However for low momentum flux ratio ($q < 2$), this column was found to have a negligible impact [66]. In the present study, $q \simeq 1$, thus this effect is neglected. In this regime, the atomisation process is dominated by the aerodynamic forcing. A correlation for SMD was obtained by *Freitag and Hassa* [66]

$$\text{SMD} = 6.9 \times 10^{-4} D^{0.2} \left(\frac{p_{dyn}}{P^{0.45}} \right)^{-0.374} , \tag{10.2}$$

relating the SMD to the multipoint hole diameter D, the gas dynamic pressure $p_{dyn} = 0.5\rho u^2$ and the gas static pressure P. In the present conditions, this correlation gives a SMD of 38 µm. The retained value for the present LES is SMD = 40 µm. A Gaussian-like velocity profile is imposed over each of the 16 multipoint holes, discretised with 20 tetrahedral elements in their diameter. Compared to the actual geometry, the diameter of the holes are multiplied by 4 in the LES ($D^* = 4D$) for resolution purposes. To keep the correct liquid fuel mass flow and momentum flux, the following correction is imposed on the volume fraction boundary value

$$\alpha_l \rightarrow \alpha_l \left(\frac{D}{D^*} \right)^2 . \tag{10.3}$$

Evaporation model

The Spalding model described in Sec. 3.3.2 is employed to model the evaporation source term. The typical evolution of an isolated droplet is shown in Fig. 10.10 for three ambient temperature, with an initial droplet temperature $T_l = 350\,\text{K}$. The ambient temperature strongly influences the evaporation time, which is reduced from $\tau_{evap} = 7.7\,\text{ms}$ for gas temperature corresponding to the inlet temperature $T_g = T_{in}$ to , $\tau_{evap} = 1.7\,\text{ms}$ for

$T_g = 2.6T_{in}$ corresponding roughly to the temperature of the recirculating hot products. These characteristic times are long compared to the convective time from the multipoint fuel injections to the injection system exit and from the multipoint fuel injections to the multipoint flame tip, which are roughly estimated to be respectively 0.25 and 1.0 ms. Thus, the evaporation process starting in the premixing zone is expected to be incomplete in the flame region, which can lead to localised region of high fuel concentrations.

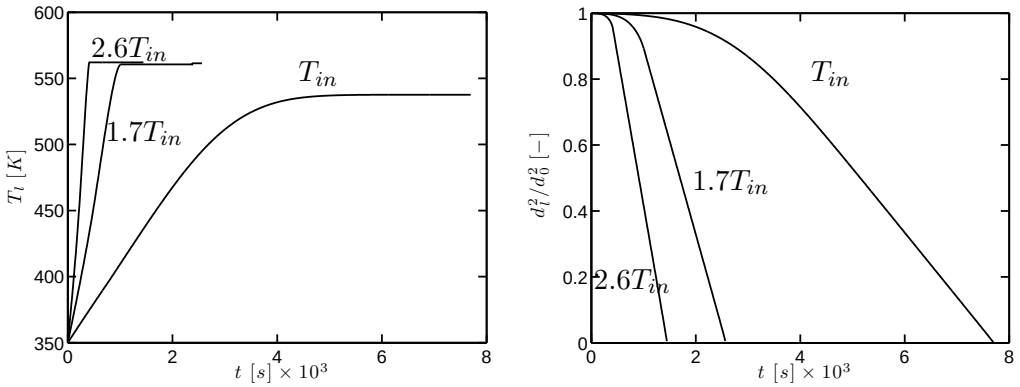

(a) Liquid temperature.

(b) d_l^2 d_0^2.

Figure 10.10: Temporal evolution of a single fuel droplet temperature and the square diameter for three different gas temperatures ($T_g = T_{in} - 1.7T_{in} - 2.6T_{in}$).

10.4.2 TFLES model

The ARC/TFLES methodology described in Sec. 6.4 is employed to dynamically thicken the flame front and is combined with the Charlette efficiency function [34] detailed in Sec. 4.5.2.1. The retained parameters for the sensor detection and filtering are given in Tab. 10.2, and were adjusted so that the sensor correctly encompasses density and temperature gradients in the flame. The threshold value σ (Eq. 6.5) was imposed to 1/10: the evaluation based on the maximum value of the thickening sensor $\sigma = 1/\mathcal{F}_{max}$ (cf. Eq. 6.7) resulted in a sensor which was too sensitive to small fuel source term variations.

α_{cold}	α_{hot}	Sc_ψ	σ
1/100	1/120	0.18	1/10

Table 10.2: LEMCOTEC: Sensor detection and filtering parameters for the TFLES model.

Given the complex flame structure produced by the staged injection system, a wide range of equivalence ratio is encountered locally. The TFLES model requires the evaluation of the flame parameters, namely the laminar flame thickness δ_T, the laminar flame

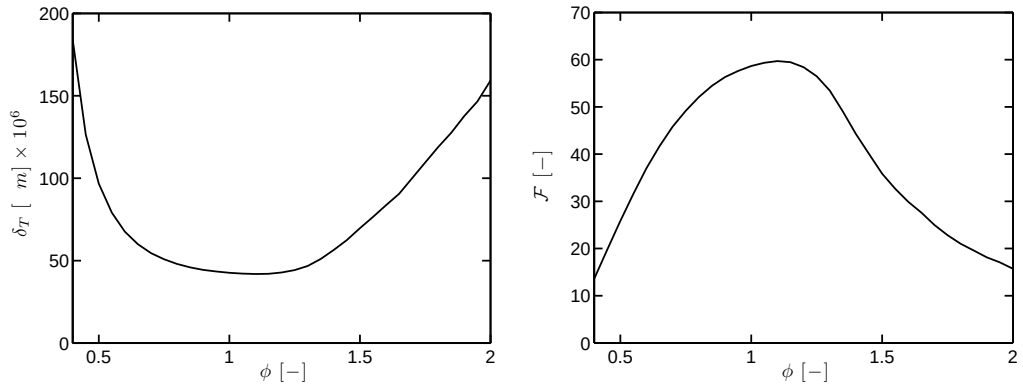

(a) Laminar flame thickness.

(b) Resulting thickening factor.

Figure 10.11: Laminar flame thickness from one-dimensional premixed flame computations in LEMCOTEC conditions and resulting thickening factor vs equivalence ratio ($\Delta x = 0.5\,\mathrm{mm}$ and $n_{\mathcal{F}} = 5$).

speed S_l and the maximum fuel source term $\mid \omega_{\mathrm{nC_{12}H_{26}}} \mid_{1D}^{max}$ to determine the thickening sensor and the flame thickening. These parameters must be evaluated locally, depending on the local equivalence ratio. In practice, they are precomputed as functions of the equivalence ratio ϕ and stored in a table, thus these parameters can be extracted locally in LES computations according to the local equivalence ratio. The variation of the flame thickness with equivalence ratio is shown in Fig. 10.11(a). Fig. 10.11(b) shows how this impacts the thickening factor, which typically ranges between 20 and 60 for a grid size $\Delta x = 0.5\,\mathrm{mm}$ with $n_{\mathcal{F}} = 5$.

10.5 LES results

10.5.1 Aerodynamic fields

Instantaneous velocity fields of axial and tangential (normal to plane) velocities are shown in Fig. 10.12. The high tangential velocity intensity shown in Fig. 10.12 (bottom) reveals that the flow is highly swirled, with opposed swirl orientations between pilot and multipoint regions. This leads to the formation of a large IRZ, revealed by the large region of negative velocity close to the centerline. CRZs are also formed under the effect of the outer shear layer of the multipoint jet. There is also a recirculation zone in the vicinity of the separator between the multipoint and pilot exits (SRZ) that may significantly contribute to the multipoint flame stabilisation. The swirling motion remains significant at the outlet, and its direction is the one of the multipoint swirler, which injects twice as much air in the chamber compared to the pilot injection system.

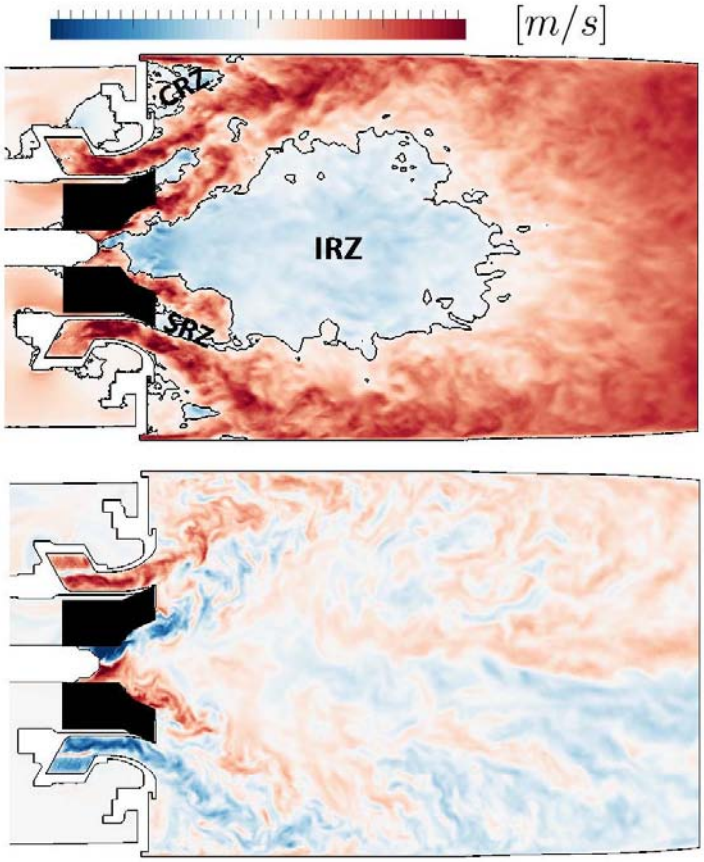

Figure 10.12: LEMCOTEC: Instantaneous fields of axial velocity with zero axial velocity isocontour (top) and tangential velocity (bottom) from LES. CRZ: Corner Recirculation Zone. IRZ: Inner Recirculation Zone. SRZ: Separator Recirculation Zone.

10.5.2 Spray structure

A pressure isosurface in the injector region shown in Fig. 10.13 reveals the presence of a precessing vortex core (PVC), which corresponds to an unstable behaviour of the central vortex core induced by the swirl motion [192]. In the present case, from spectral analysis of pressure probes in this region, the instability occurs at $f = 3850\,\mathrm{Hz}$. This mechanism is likely to promote the dispersion of the liquid spray [145]. Indeed, the stoichiometric liquid volume fraction isosurface shows the spray entrainment, leading to a helicoidal structure.

A global view of the spray in the injection system is shown in Fig. 10.14 left. The liquid multipoint jets follow the strong swirl motion imposed by the gaseous flow. The mass transfer rate indicates that the evaporation tends to increase as the liquid fuel leaves the duct, so that very little liquid fuel remains at the multipoint exit. This leads to conditions close to stoichiometry in the inner shear layer of the multipoint jet, as shown

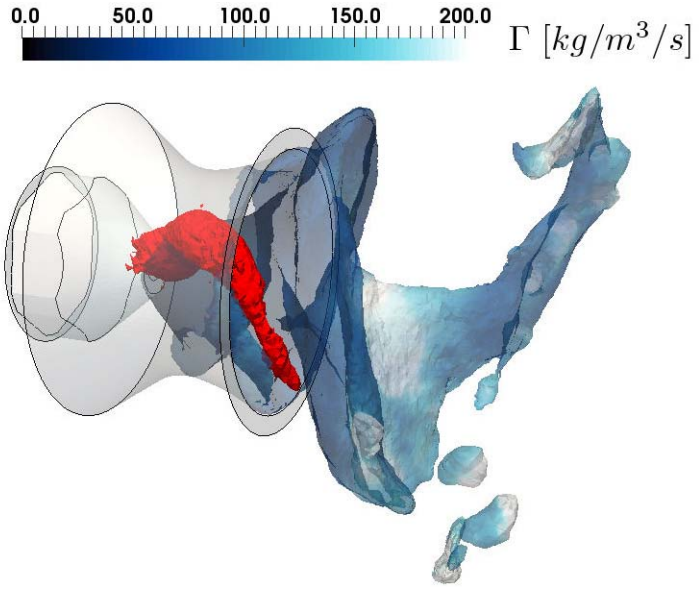

Figure 10.13: LEMCOTEC - Pilot injector region: isosurface of stoichiometric liquid volume fraction coloured by evaporation source term and pressure isosurface (red) highlighting the presence of the PVC.

in Fig. 10.14 right by the isosurface of total (liquid + gas) equivalence ratio. As will be shown later, combustion occurs in that region, with high temperature levels because of conditions close to stoichiometry. It promotes rapid fuel vaporisation, and in turns the overall process is self-sustained.

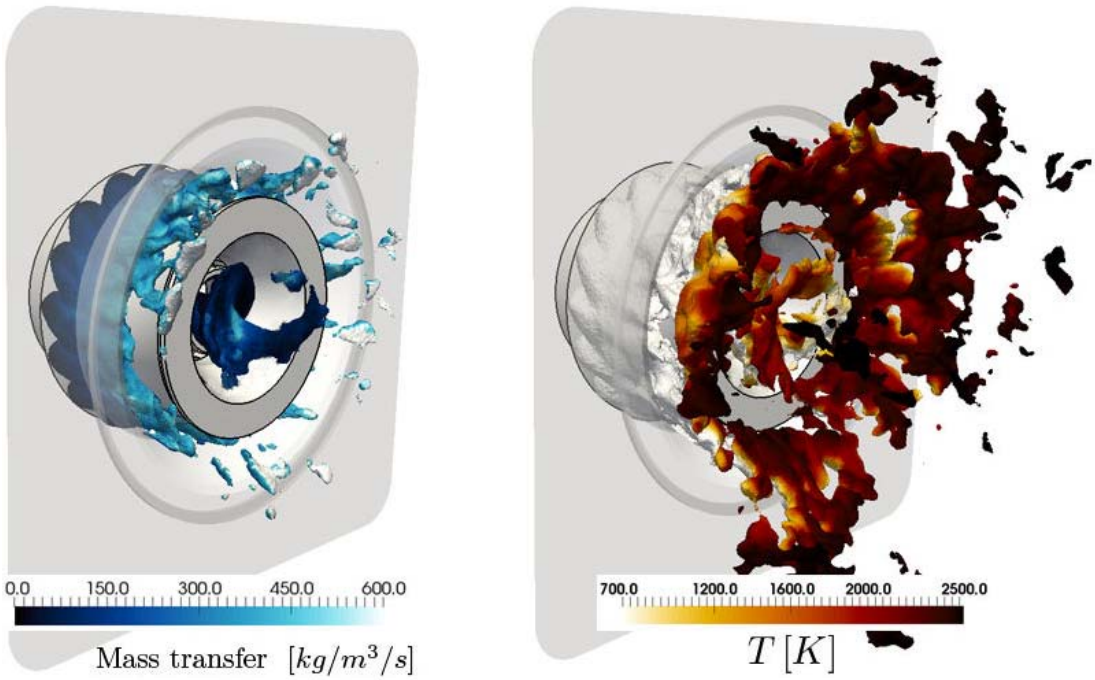

Figure 10.14: LEMCOTEC: Left) isosurface of stoichiometric liquid volume fraction coloured by evaporation source term. Right) isosurface of stoichiometric total (liquid + vapor) equivalence ratio coloured by temperature.

10.5.3 Flame structure

From the mid-plane view of the instantaneous temperature field shown in Fig. 10.15 top, it can be seen that the flame stabilises at the exit of the injection system, in the separation zone between the multipoint and the pilot exits. As shown in Fig. 10.15 bottom, in this region, the mixture fraction is significantly higher than global value ($Z_{glob} = 0.028$) because of the rapid evaporation of the liquid fuel issuing from the multipoint system. In the pilot region, the dispersed phase is partially carried away from the centerline by expansion of the central swirling jet. This leads to the formation of a M-shape flame in

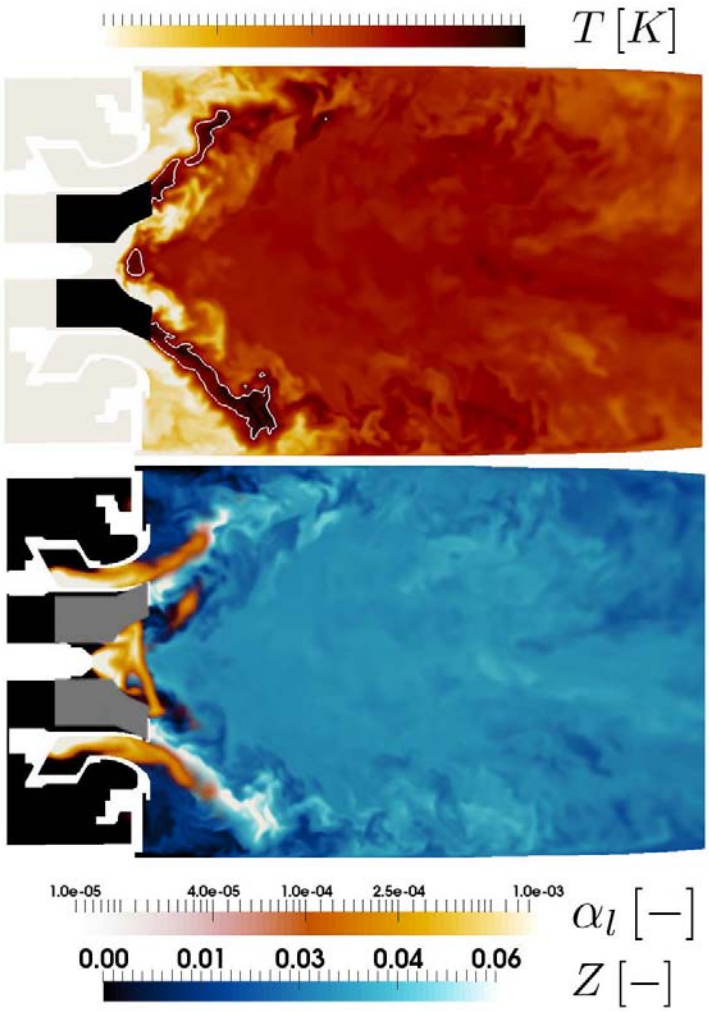

Figure 10.15: LEMCOTEC: Top) instantaneous temperature field with $\phi = 0.8$ isocontour. Bottom) instantaneous field of mixture fraction (blue scale) and superimposed instantaneous field of liquid volume fraction (red scale).

the pilot region. Close to the centerline, the flow stagnates because of the IRZ and high evaporation occurs, leading to a localised region of high equivalence ratio. It results in stronger burning intensity at this location compared to the outer branches of the pilot flame, as shown by the instantaneous fuel consumption rate field in Fig. 10.16. In the

multipoint flame region, the evaporation is located on the cold side of the flame and rather well distributed along the flame basis, leading to a rather homogeneous burning intensity.

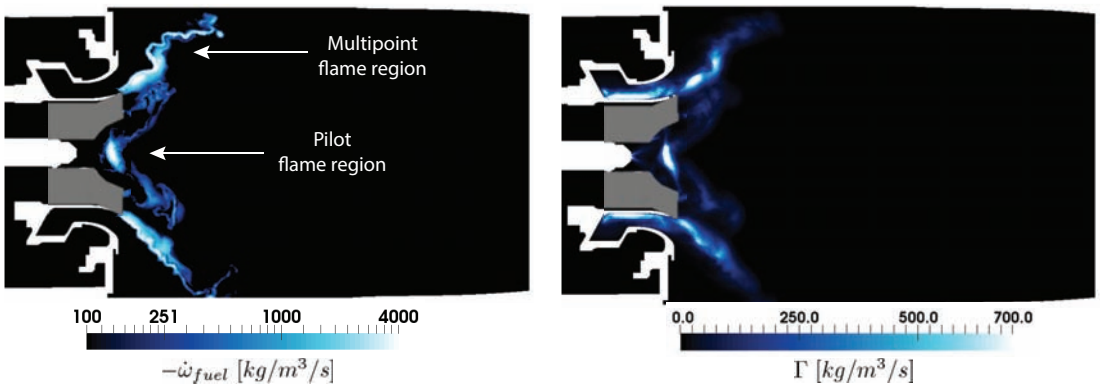

Figure 10.16: LEMCOTEC: Instantaneous fields of left) fuel consumption rate (log-scale) and right) evaporation mass transfer.

Comparison of the flame structure with the experiments

Simultaneous OH and kerosene PLIF visualisations were performed at ONERA [75] through a window restricted to the pilot flame region (Fig. 10.17(right)). Two instantaneous PLIF fields are compared with fuel and OH concentration instantaneous field from LES in Fig. 10.17. A good qualitative agreement is obtained for the flame shape. The main difference appears in the region close to the separator between the pilot and multipoint injection systems, where OH radical is locally higher in the LES. This might be attributed to wall heat losses in this region, which lower the temperature and may lead to flame lift-off.

10.5.4 Analysis of CO formation

CO distribution is first analysed at the exit plane of the combustor on an instantaneous snapshot. Figure 10.18 shows that high CO concentrations are located in the outer very lean regions, where CO equilibrium values are yet the lowest. To assess this effect, CO deviation from equilibrium

$$\Delta Y_{\mathrm{CO}} = Y_{\mathrm{CO}} - Y_{\mathrm{CO}}^{eq}\,, \tag{10.4}$$

is also evaluated in Fig. 10.18, showing that there is indeed significant deviation from equilibrium in these regions.

To assess the impact of this deviation from equilibrium on CO emission levels, three different emission indices are compared on an instantaneous LES field. The first one is the instantaneous emission index over the whole exit plane

$$< \mathrm{EICO} >= 1000\frac{< \rho u Y_{\mathrm{CO}} >}{< \rho u Z >} = 9.1\,, \tag{10.5}$$

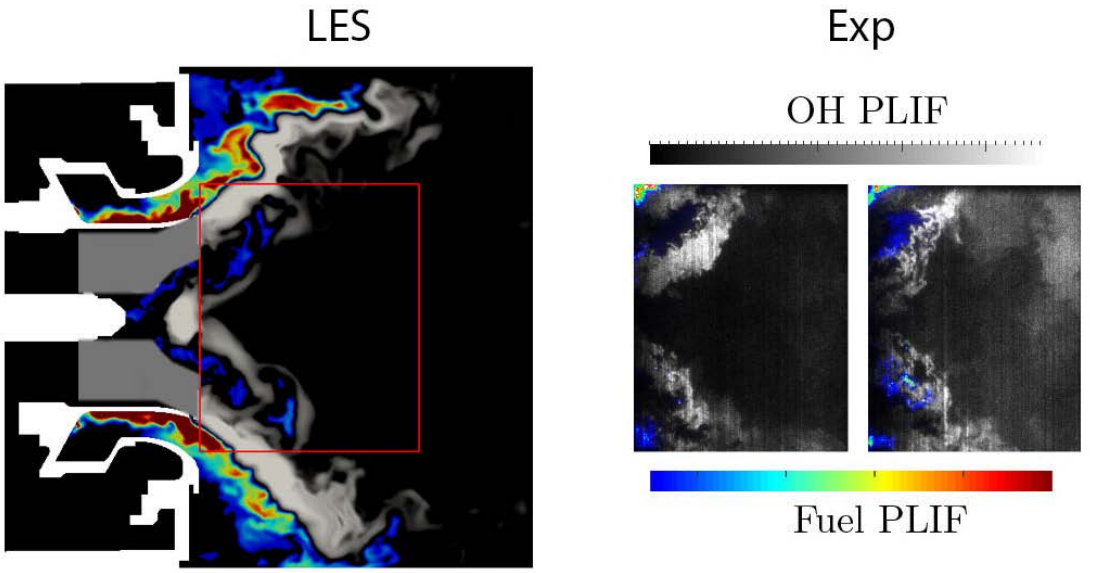

Figure 10.17: LEMCOTEC: Qualitative comparison of instantaneous OH and fuel fields from LES (left) with two instantaneous PLIF fields (right) from ONERA [75].

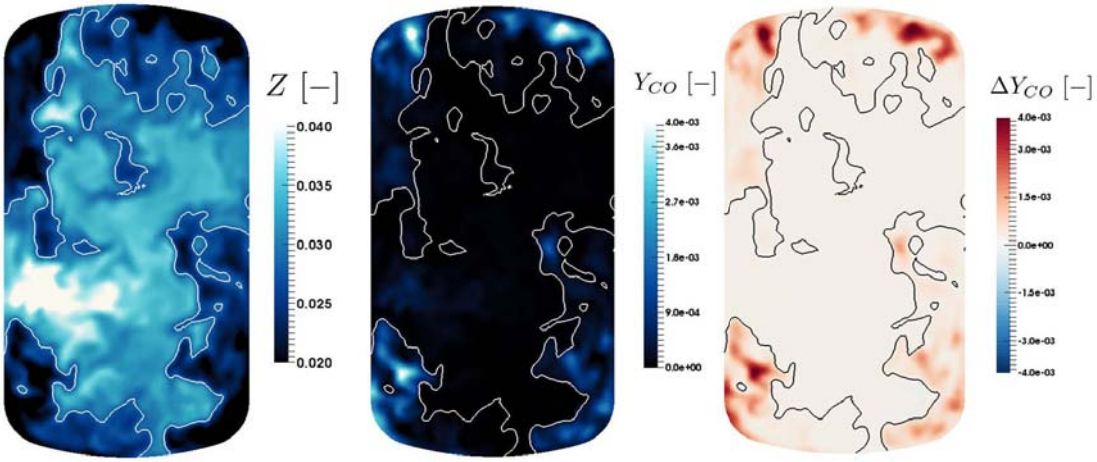

Figure 10.18: LEMCOTEC: Instantaneous LES fields in the exit plane of the combustor. Left: Mixture fraction with isocontour at $Z = Z_{glob}$. Middle: CO mass fraction. Right: CO deviation from equilibrium.

where u is the axial velocity and $< \cdot >$ is the spatial averaging operator over the exit plane. Another index is defined assuming that CO is locally at equilibrium

$$< \text{EICO} >_{eq}^{loc} = 1000 \frac{< \rho u Y_{CO}^{eq}(\mathbf{Y}, T) >}{< \rho u Z >} = 0.61\,, \tag{10.6}$$

where $\mathbf{Y}$ is the local composition and T is the local temperature. The last quantity corresponds to the CO emission index that would be obtained if the mixture was homogeneous and at equilibrium at the outlet

$$< \text{EICO} >_{eq}^{glob} = 1000 \frac{< \rho u > Y_{CO}^{eq}(T_{outlet}, \mathbf{Y}_{outlet})}{< \rho u Z >} = 0.12\,, \tag{10.7}$$

where

$$\mathbf{Y}_{outlet} = \frac{<\rho u \mathbf{Y}>}{<\rho u>}\,, \tag{10.8}$$

$$T_{outlet} = \frac{<\rho u T>}{<\rho u>}\,. \tag{10.9}$$

When considering a uniform mixture at equilibrium at the exit ($<$ EICO $>_{eq}^{glob}$), the emission index is reduced by two orders of magnitude (0.12 instead of 9.1) compared to the real value. When taking into account spatial inhomogeneities while keeping CO at equilibrium ($<$ EICO $>_{eq}^{loc}$), the emission index is marginally increased, but remains significantly lower compared to the real value (0.61 instead of 9.1). This confirms that the CO exhaust levels are mainly driven by non-equilibrium phenomena, contrarily to what was observed for the SGT-100 case in Sec. 9.6.4.

To understand this behaviour, the instantaneous distribution of CO is shown in Fig. 10.19(top). CO concentrations are typically high in the flame region and in the CRZs, with peak values in the hot gases close to the separator. Figure. 10.19(bottom) shows that fast CO production occurs at the flame base. In lean regions, it is followed by a rapid destruction in the flame zone, which continues more slowly in the post-flame region. A closer look at the CO field shows that some pockets of high CO concentration detach from the outer part of the multipoint flame before the fast oxidation process has been achieved. These pockets are convected downstream in the vicinity of the walls, where the mixture fraction is relatively low, as was shown in Fig. 10.15. Because of low associated temperature, this results in CO oxidation rates close to the walls that are too slow compared to the convection time towards the exit, explaining the significant departure from equilibrium observed in the near wall region at the exit plane. The overall process is unsteady and highly intermittent.

10.5.5 Analysis of NO formation

Similarly, NO concentrations are analysed at the combustor exit on an instantaneous field. Figure. 10.20 shows the strong correlation between mixture fraction and temperature, expected as temperature is at equilibrium in the burnt gases. NO concentrations are also strongly correlated to temperature, and high levels of NO concentration are found close to the centerline.

The total fuel consumption and total NO production, extracted from an instantaneous LES field and conditioned on the mixture fraction, are shown in Fig. 10.21. Fuel consumption occurs mainly slightly above the global mixture fraction. The distribution is skewed towards high mixture fractions, under the effect of heterogeneities generated by

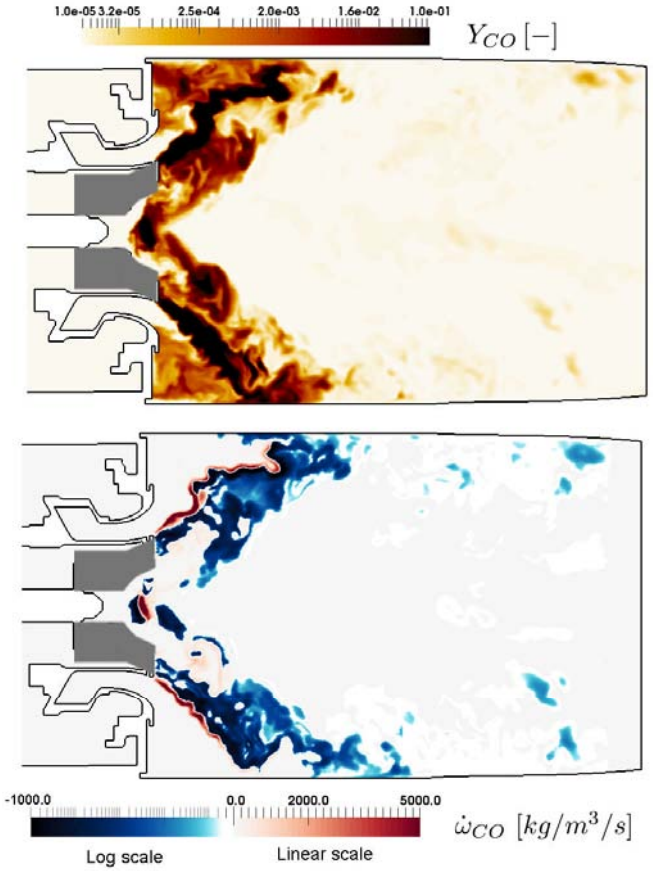

Figure 10.19: LEMCOTEC: Instantaneous fields of CO mass fraction (top) and CO source term (bottom - log-scale for negative values, linear scale for positive values) from LES in the mid-plane of the combustor.

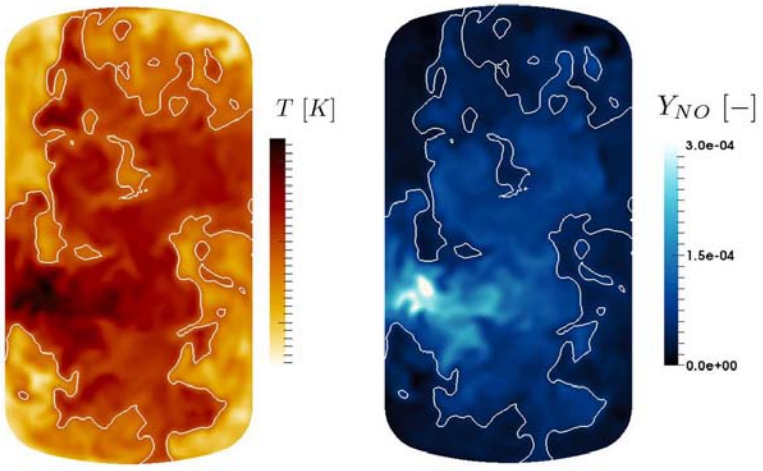

Figure 10.20: LEMCOTEC: Instantaneous LES field in the exit plane of the combustor. Left: temperature field. Right: NO mass fraction field. Mixture fraction isocontour at $Z = Z_{glob}$.

the spray. NO production, also shown in Fig. 10.21, occurs at higher mixture fraction and peaks around stoichiometric conditions, despite fuel consumption being lower at

these mixture fractions. This is consistent with laminar flames (Fig. 10.4(d)), which indicates that flame NO production is higher by one order of magnitude at stoichiometric conditions compared to conditions close to ϕ_{glob}.

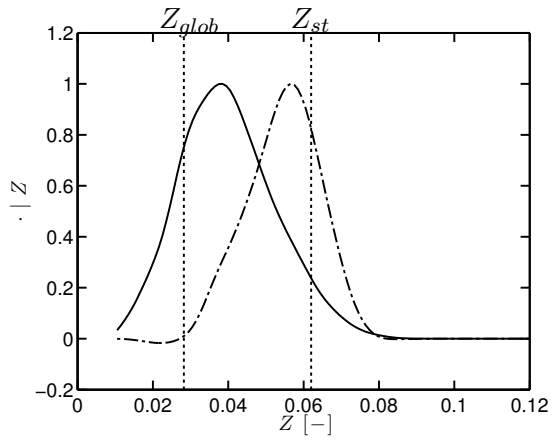

Figure 10.21: LEMCOTEC: Integrated fuel consumption (—) and NO production ($\cdot - \cdot -$) conditioned on the mixture fraction vs mixture fraction. The distributions are normalised by their respective peak value. The vertical lines correspond to the global mixture fraction and the stoichiometric mixture fraction.

Figure 10.22 shows the qualitative decomposition of NO into flame and post-flame contributions. Again, as for the SGT-100 configuration, the flame region is identified via the thickening sensor. Flame NO formation is faster than post-flame formation. In the present case, flame NO formation is also promoted by the mixture fraction levels, which are higher in the flame than in the burnt gases, where the mixing between the fuel, the air from the injection system and the cooling air is almost complete. Thus the contribution of the flame to NO production is very significant for this combustor, and typically varies between 50% to 70% of the total NO production. In the burnt gas region, as previously shown in Fig. 10.15, the mixture fraction is higher close to the centerline, resulting in higher NO production in this region. However this contribution remains limited.

10.5.6 Comparison with exhaust measurements

In the experimental campaign, the emission indices of CO and NO_x are evaluated from exhaust concentration measurements, performed at 6 locations shown in Fig. 10.23. It should be noted that the measurement plane is slightly shifted downstream in the experiments compared to LES. The location of the probes can significantly impact the evaluation of the emission indices, since NO and CO are non-uniform on the exit plane, although the local mass flux is rather uniform (Fig. 10.23). In LES, the emission indices

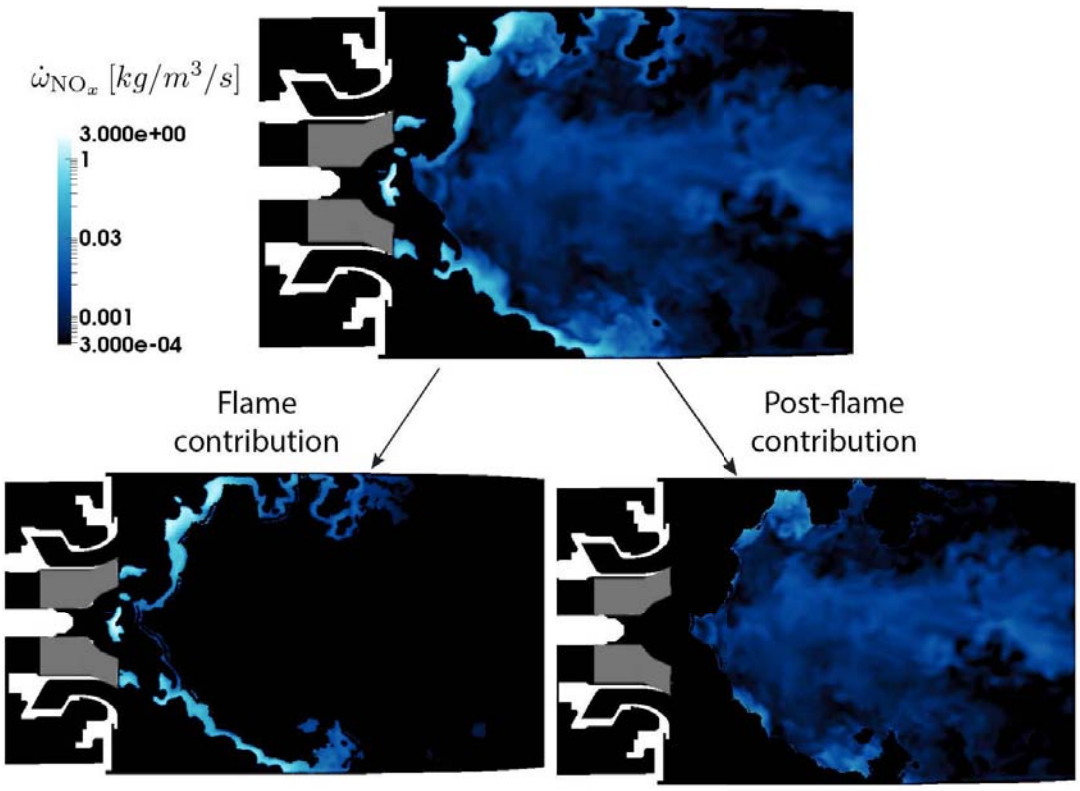

Figure 10.22: LEMCOTEC: Instantaneous NO source term (log-scale) in the mid-plane of the combustor. Decomposition into fast flame and slow post-flame contributions based on the thickening sensor.

EIx^{probes} are evaluated with the same methodology, using time-averaged CO and NO concentrations at the same 6 probes. The statistics were collected for two residence times of the combustor, which is insufficient to achieve full convergence for CO emission index, because of its high amplitude, low-frequency variations.

LES and measured emission indices based on the probes are given in Tab. 10.3. The NO_x emission index includes the contribution of NO and NO_2 as follows

$$\mathrm{EINO}_x^{probes} = W_{\mathrm{NO}_2} \times \left(\mathrm{EINO}/W_{\mathrm{NO}} + \mathrm{EINO}_2/W_{\mathrm{NO}_2}\right) . \tag{10.10}$$

NO_x concentrations at the probes are found to be rather stable whereas strong intermittency is observed again for CO concentrations. By varying the size of the averaging window, the estimated uncertainties on the emission indices is 0.3 for NO_x and 2.5 for CO. The comparison shows that a satisfactory agreement is obtained between measurements and LES for NO_x and CO exhaust emission indices. The emission indices based on integrated mean values at the combustor exit ($< \mathrm{EIx} >_{mean}$) are less sensitive to temporal fluctuations, and are also provided in Tab. 10.3. No significant difference is

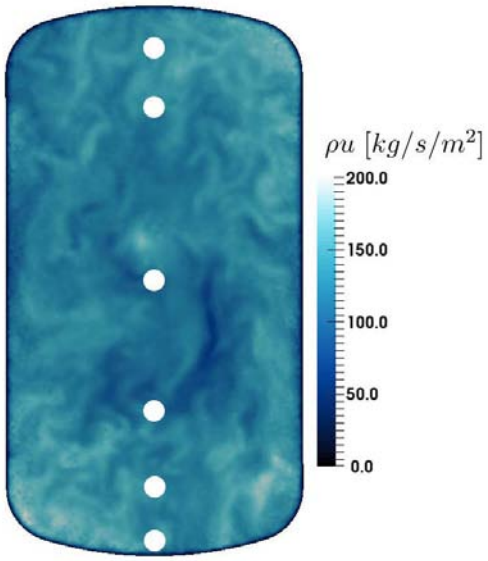

Figure 10.23: LEMCOTEC: Experimental probe locations for exhaust concentration measurements. Color scale: mass flux on an instantaneous snapshot from LES.

observed for NO compared to the probe value. For CO, the difference is more significant because of its strong heterogeneity at the exit.

	Exp	LES
EINO_x^{probes}	4.88	5.4
$< \text{EINO}_x >_{mean}$	[-]	5.3
EICO^{probes}	12.33	8.5
$< \text{EICO} >_{mean}$	[-]	13

Table 10.3: LEMCOTEC: Comparison of exhaust emission indices between LES and experiments.

10.6 A few words about CPU time

The calculations were conducted on 15 nodes (360 processors) of CERFACS NEMO cluster. The CPU cost of the ARC_27_JETSURF, with 41 transported variables, is compared to calculations performed with 2-step chemistry 2S_KERO_BFER, with only 20 transported variables. Consistently with the number of transport equations, the CPU cost is multiplied by 2 for ARC_27_JETSURF. The amount of time spent in the source term evaluation remains acceptable, representing only 18% of the total CPU cost despite the 452 reactions introduced by the ARC_27_JETSURF.

Kinetic scheme	ARC_27_JETSURF	2S_KERO_BFER
CPU time for one convective time	110 000	55 000
% of time spent for source terms evaluation	18 %	[-]

Table 10.4: LEMCOTEC: Comparison of CPU time between the ARC_27_JETSURF scheme and 2S_KERO_BFER.

10.7 Conclusions

In this chapter, the LES of a staged multipoint injection combustor was performed. N-dodecane was retained as a surrogate to describe kerosene-air combustion. An ARC scheme with 27 transported species was derived and showed a satisfactory agreement with reference detailed mechanisms from the literature.

The staged liquid fuel injection leads to a complex flame structure. Qualitative comparison of the flame shape with experiments shows that the pilot flame structure is rather well-reproduced, even if it is likely to be influenced by heat losses at the separator between multipoint and pilot injection systems. Fuel burning occurs on a wide range of equivalence ratios, and in average significantly higher than the global equivalence ratio. This tends to promote NO production which peaks around stoichiometry in the flame region. NO production in the burnt gases occurs at a much lower rate because of much leaner conditions. CO concentrations are found significant at the combustor exit, in particular in very lean regions. This was attributed to CO oxidation being too slow at these very lean conditions to oxidise all the CO that was produced in the flame region. A good quantitative agreement of exhaust concentrations of CO and NO_x was found, showing the capability of the methodology to predict pollutant emissions in real burners.

11

Conclusions and perspectives

This thesis aims at developing a methodology for pollutant prediction applicable to complex industrial geometries. It is based on the use of reduced schemes (ARC), including accurate pollutant chemistry. In this thesis, such schemes are derived using the YARC reduction tool developed by *Pepiot-Dejardins* [149]. Having control over the derivation process allows to derive schemes that are specifically suited for the intended applications in terms of accuracy, numerical cost and stiffness and valid over a wide range of conditions. ARCs are further combined with the thickened flame model [39], to be applied to LES of realistic gas turbine configurations. A thorough numerical validation of the methodology is performed on one-dimensional laminar premixed and non-premixed cases, showing that a satisfactory prediction of the flame structure is obtained with ARCs.

The methodology is then applied to both academic and industrial configurations. A very good agreement of flame structure and pollutant formation is obtained with ARCs on a reference turbulent non-premixed jet flame (Sandia flame D) demonstrating their potential to accurately predict pollutants in turbulent configurations. Interactions between the turbulent flow and the chemistry are captured as well as the pollutant slow formation processes. The sensitivity of the results to the choice of the detailed mechanism is also pointed out, highlighting the need for the development and improvement of detailed mechanisms, for which thorough validations at high pressure and temperature conditions are often lacking, especially for NO_x chemistry. Applying the ARC/TFLES methodology to the LES of the methane-air SGT-100 Siemens burner, a fair agreement is obtained with measurements, in terms of temperature and major species profiles. The chemical structure is found to be significantly impacted by the high strain rates found in the combustor. In addition, the impact of the operating conditions on NO exhaust concentrations is correctly captured. The simulation enable to understand the NO formation processes, by analysing the relative contribution of flame and post-flame processes. CO concentrations at the combustor exit are found to be close to equilibrium values. The LES results also underline the strong sensitivity to wall heat losses, which impacts both CO and NO emissions. Inclusion of heat losses improves the prediction of exhaust CO concentration thanks to a better prediction of exhaust gas temperature but deteriorates the prediction of NO. This is not yet understood and requires further

investigation.

The last application is a low-NO_x kerosene-air staged multipoint injection burner. In this configuration, the level of partial premixing is notably higher compared to the SGT-100, because of the presence of the dispersed phase. The results illustrate the significant impact of partial premixing on pollutant formation. Despite the overall lean conditions, NO production peaks at conditions close to stoichiometry. CO evolution in the post-flame region is intermittent and highly sensitive to mixture stratification, resulting in CO concentrations significantly above equilibrium values at the combustor exit, contrarily to the SGT-100 configuration. In view of the strong impact of stratification, sensitivity to the dispersed phase modelling should be evaluated.

Overall, satisfactory prediction of NO_x and CO is achieved on both the academic and the two industrial configurations considered, which validates the methodology and demonstrates its prediction capability. In the approach, no strong modelling assumption is made about the flame structure and post-flame chemistry, so that including multiphysics effects is straightforward, as exemplified by the direct inclusion of heat losses. Thus, the prediction capability can be easily improved by including the description of multiphysics phenomena occurring in industrial chambers:

- A Lagrangian approach [91] can be employed for the liquid dispersed phase to account for polydispersion effects that may strongly impact the flame structure.
- Wall heat transfer and thermal radiation can be introduced using conjugate heat transfer at walls [92] and Discrete Ordinate Method (DOM) for thermal radiation [162] coupled with the LES [16]. Note that, from the chemistry side, no additional modelling is required to include the effects of heat transfer.

An interesting outcome of the simulations of the turbulent cases is the strong coupling between pollutant formation and turbulence, which may require new developments of the turbulent combustion model. In particular, the strong unsteadiness of turbulent strain may have direct impact on CO and NO_x production. To study this effect, simple canonical cases, such as flame-vortex interaction, would be helpful as it is close to turbulent flames with strain and curvature effects. The turbulent combustion model can be updated with recent developments [202, 203], where the efficiency function is evaluated via a dynamic procedure based on a Germano-like identity [67]. This approach may allow to evaluate the subgrid contribution differently for slow and fast chemical processes, which is of interest, given the large range of Damkohler numbers typically encountered when pollutant species are considered.

The methodology developed in this thesis is applicable to numerous problems. One is the prediction of smoke, which is also a strong concern in industrial combustors. Soot modelling would benefit from the use of ARCs, in which accurate description of gaseous soot precursors can be included and coupled with a dedicated model [110, 139, 167]. Other issues, such as combustion instabilities or flame stabilisation, although not directly linked to chemistry, can be revisited with the use of ARC.

Bibliography

[1] Report of the independent experts on the 2006 NOx review and the establishment of medium and long term technology goals for NOx. 2006. 8, 9, 10

[2] B. Abramzon and W. A. Sirignano. Droplet vaporisation model for spray combustion calculations. *International journal of heat and mass transfer*, 9:1605 1618, 1989. 58

[3] ACARE. http://www.acare4europe.com/. 2013. 9

[4] S. K. Aggarwal, W. A. Sirignano, and A. Y. Tong. A comparison of vaporization models in spray calculations. *AIAA journal*, 22(10):1448 1457, 1984. 55

[5] Airbus. Global market forecast 2015-2034. Technical report, 2015. 8

[6] C. Allouis, F. Beretta, and A. Amoresano. Experimental study of lean premixed prevaporized combustion fluctuations in a Gas Turbine burner. *Combustion Science and Technology*, 180(5):900 909, 2008. 18

[7] C. Angelberger, D. Veynante, F. Egolfopoulos, and T. Poinsot. Large eddy simulations of combustion instabilities in premixed flames. In *Proceedings of the Summer Program*, pages 61 82. Center for Turbulence Research, NASA Ames/Stanford Univ., 1998. 87

[8] S. Baessler, K. G. Mosl, and T. Sattelmayer. NOx emissions of a premixed partially vaporized kerosene spray flame. *Proceedings of the ASME Turbo Expo 2006, Vol 1*, 129(3):191 200, 2006. 15

[9] S. Barbosa, P. Scouflaire, and S. Ducruix. Time resolved flowfield, flame structure and acoustics characterization of a staged multi-injection burner. *Proceedings of the Combustion Institute*, 32(2):2965 2972, 2009. 21

[10] R. S. Barlow and J. H. Frank. Effects of turbulence on species mass fractions in methane/air jet flames. *Symposium (International) on Combustion*, 27(1):1087 1095, 1998. 161, 162

[11] R. S. Barlow, A. N. Karpetis, J. H. Frank, and J. Y. Chen. Scalar profiles and NO formation in laminar opposed-flow partially premixed methane/air flames. *Combustion and Flame*, 127(3):2102 2118, 2001. 12, 111, 145, 146, 147, 227

[12] D. Barré, L. Esclapez, M. Cordier, E. Riber, B. Cuenot, G. Staffelbach, B. Renou, A. Vandel, L. Y. M. Gicquel, and G. Cabot. Flame propagation in aeronautical swirled multi-burners: Experimental and numerical investigation. *Combustion and Flame*, 161(9):2387 2405, 2014. 21, 23

[13] M. Bauerheim. *Theoretical and numerical study of symmetry breaking effects on azimuthal thermoacoustic modes in annular combustors.* PhD thesis, INP Toulouse, 2014. 17

[14] M. Bauerheim, T. Jaravel, L. Esclapez, E. Riber, L. Y. M. Gicquel, B. Cuenot, M. Cazalens, S. Bourgois, and M. Rullaud. Multiphase flow Large Eddy Simulation study of the fuel split effects on combustion instabilities in an ultra-low-NOx annular combustor. *Journal of Engineering for Gas Turbines and Power*, 138(6):061503, nov 2015. 88, 242

[15] A. Bellofiore, A. Cavaliere, and R. Ragucci. Air density effect on the atomization of liquid jets in crossflow. *Combustion Science and Technology*, 179(1-2):319 342, 2007. 250

[16] S. Berger, S. Richard, G. Staffelbach, F. Duchaine, and L. Gicquel. Aerothermal prediction of an aeronautical combustion chamber based on the coupling of Large Eddy Simulation, solid conduction and radiation solvers. In *ASME Turbo Expo 2015: Turbine Technical Conference and Exposition*, 2015. 266

[17] A. Bhargava, D. W. Kendrick, M. B. Colket, W. A. Sowa, and E. Hartford. Pressure effect on NOx and CO emissions in industrial Gas Turbines. *ASME Paper No. 2000-GT-97*, may 2000. 11, 15

[18] F. Biagioli and F. Guthe. Effect of pressure and fuel-air unmixedness on NOx emissions from industrial gas turbine burners. *Combustion and Flame*, 151(1-2):274 288, 2007. 14, 15, 98, 197, 217

[19] R. W. Bilger, S. H. Starner, and R. J. Kee. On reduced mechanisms for methane-air combustion in non-premixed flames. *Combustion and Flame*, 80:135 149, 1990. 69

[20] R. B. Bird, W. E. Stewart, and E. N. Lighfoot. *Transport phenomena.* John Wiley, New York, 1960. 32

[21] M. Boileau. *Simulation aux grandes échelles de l allumage diphasique des foyers aéronautiques.* Phd thesis, INP Toulouse, 2007. 47, 49

[22] C. T. Bowman, M. Frenklach, W. R. Gardiner, and G. Smith. The GRI 3.0 chemical kinetic mechanism, 1999. 12, 74, 111

[23] C. T. Bowman, R. K. Hanson, D. F. Davidson, W. C. Gardiner Jr., V. Lissianski, G. P. Smith, D. M. Golden, M. Frenklach, and M. Goldenberg. GRI-Mech 2.11, 1995. 74, 111

[24] M. P. Boyce. *Gas turbine engineering handbook*. 2011. 17

[25] J. M. Bozelli and A. M. Dean. Direct studies of some elementary steps for the formation and destruction of nitric oxide in the HNO system. *International Journal of Chemical Kinetics*, 1995. 13

[26] J. Buckmaster and G. Ludford. *Theory of laminar flames*. Cambridge University Press, 1982. 66

[27] G. Bulat, W. P. Jones, and A. J. Marquis. NO and CO formation in an industrial gas-turbine combustion chamber using LES with the Eulerian sub-grid PDF method. *Combustion and Flame*, 161(7):1804 1825, feb 2014. 23, 84, 186, 188, 194, 213

[28] S. P. Burke and T. E. W. Schumann. Diffusion flames. *Industrial and Engineering Chemistry*, 20(10):998 1005, 1928. 71

[29] W. Bush and F. Fendell. Asymptotic analysis of laminar flame propagation for general lewis numbers. *Combustion science and technology*, 1:421, 1970. 66

[30] W. K. Bushe and H. Steiner. Conditional moment closure for large eddy simulation of nonpremixed turbulent reacting flows. *Physics of Fluids*, 11(7):1896 1906, 1999. 85

[31] S. M. Candel and T. Poinsot. Flame stretch and the balance equation for the flame surface area. *Combustion science and technology*, 70:1 15, 1990. 65

[32] R. R. Cao and S. B. Pope. The influence of chemical mechanisms on PDF calculations of nonpremixed piloted jet flames. *Combustion and Flame*, 143(4):450 470, 2005. 111, 163, 164, 171

[33] S. Chapman and T. G. Cowling. *The Mathematical Theory of Non-Uniform Gases*. Cambridge University Press, 1939 (digital reprint 1999). 45

[34] F. Charlette, D. Veynante, and C. Meneveau. A power-law wrinkling model for LES of premixed turbulent combustion: Part I - non-dynamic formulation and initial tests. *Combustion and Flame*, 131:159 180, 2002. 86, 87, 190, 252

[35] P. Clavin. Dynamic behavior of premixed flame fronts in laminar and turbulent flows. *Progress in energy and combustion science*, 11:1 59, 1985. 66

[36] R. Clift, J. R. Grace, and M. E. Weber. *Bubbles, Drops, and Particles*. Academic Press, 1978. 48

[37] O. Colin and A. Benkenida. The 3-zones extended coherent flame model (ECFM3Z) for computing premixed/diffusion combustion. *Oil & gas science and technology*, 59(6):593 609, 2004. 97

[38] O. Colin, F. Ducros, D. Veynante, and T. Poinsot. A thickened flame model for large eddy simulations of turbulent premixed combustion. *Physics of Fluids*, 12(7):1843 1863, 2000. 86, 87

[39] O. Colin and M. Rudgyard. Development of high-order taylor-galerkin schemes for unsteady calculations. *Journal of computational physics*, 162(2):338 371, 2000. 40, 164, 265

[40] S. M. Correa. A Review of NOx formation under Gas-Turbine combustion conditions. *Combustion Science and Technology*, 87(1-6):329 362, 1993. 12, 14, 15

[41] B. Cuenot and T. Poinsot. Effects of curvature and unsteadiness in diffusion flames. Implications for turbulent diffusion flames. *Proceedings of the Combustion Institute*, 25:1383 1390, 1994. 73, 74

[42] P. Dagaut and M. Cathonnet. The ignition, oxidation, and combustion of kerosene: A review of experimental and kinetic modeling. *Progress in Energy and Combustion Science*, 32(1):48 92, 2006. 74, 244, 245, 291

[43] S. K. Dhanuka, J. E. Temme, and J. F. Driscoll. Lean-limit combustion instabilities of a lean premixed prevaporized gas turbine combustor. *Proceedings of the Combustion Institute*, 33(2):2961 2966, 2011. 21

[44] S. K. Dhanuka, J. E. Temme, J. F. Driscoll, and H. C. Mongia. Vortex-shedding and mixing layer effects on periodic flashback in a lean premixed prevaporized gas turbine combustor. *Proceedings of the Combustion Institute*, 32 II(2):2901 2908, 2009. 20, 21

[45] P. Domingo, L. Vervisch, and D. Veynante. Large-eddy simulation of a lifted methane jet flame in a vitiated coflow. *Combustion and Flame*, 152(3):415 432, 2008. 83, 93

[46] J. M. Donbar, J. F. Driscoll, and C. D. Carter. Reaction zone structure in turbulent nonpremixed jet flames - from CH-OH PLIF images. *Combustion and Flame*, 122(1-2):1 19, 2000. 179

[47] M. C. Drake, J. W. Ratcliffe, and R. J. Blint. Measurements and modeling of flamefront NO formation and superequilibrium radical concentrations in laminar high-pressure premixed flames. *Symposium (International) on Combustion*, 23(1):387 395, 1991. 13

[48] F. Ducros, F. Nicoud, and T. Poinsot. Wall-adaptating local eddy-viscosity models for simulations in complex geometries. In *ICFD*, pages 293 300. Baines M. J., 1998. 38

[49] T. Echekki and J. H. Chen. Unsteady strain rate and curvature effects in turbulent premixed methane-air flames. *Combustion and Flame*, 106:184 202, 1996. 153, 206, 208

[50] L. Elliott, D. B. Ingham, A. G. Kyne, N. S. Mera, M. Pourkashanian, and C. W. Wilson. Genetic algorithms for optimisation of chemical kinetics reaction mechanisms. *Progress in Energy and Combustion Science*, 30(3):297 328, 2004. 77

[51] B. Enaux, V. Granet, O. Vermorel, C. Lacour, C. Pera, C. Angelberger, and T. Poinsot. Large eddy simulation and experimental study of cycle-to-cycle variations in a spark ignition engine. *Proceedings of the Combustion Institute*, 33:3115 3122, 2011. 88

[52] L. Esclapez. *Numerical study of ignition and inter-sector flame propagation in Gas Turbine*. PhD thesis, INP Toulouse, 2015. 17

[53] C. P. Fenimore. Formation of nitric oxide in premixed hydrocarbon flames. *Symposium (International) on Combustion*, 13(1):373 380, 1971. 12, 13

[54] C. P. Fenimore. Reactions of fuel-nitrogen in rich flame gases. *Combustion and Flame*, 26(C):249 256, 1976. 12

[55] P. Février. *Etude numérique des effets de concentration préférentielle et de corrélation spatiale entre vitesses de particules solides en turbulence homogène isotrope stationnaire*. Phd thesis, INP Toulouse, 2000. 49

[56] P. Février and O. Simonin. Statistical and continuum modelling of turbulent reactive particulate flows. part 2: Application of a two-phase second-moment transport model for prediction of turbulent gas-particle flows. In *Theoretical and Experimental Modeling of Particulate Flows, Lecture Series 2000-06, von Karman Institute for Fluid Dynamics, Rhode Saint Genese (Belgium)*, 2000. 49

[57] B. Fiorina, O. Gicquel, L. Vervisch, S. Carpentier, and N. Darabiha. Approximating the chemical structure of partially premixed and diffusion counterflow flames using FPI flamelet tabulation. *Combustion and Flame*, 140(3):147 160, 2005. 144

[58] B. Fiorina, R. Mercier, G. Kuenne, A. Ketelheun, A. Avdi, J. Janicka, D. Geyer, A. Dreizler, E. Alenius, C. Duwig, P. Trisjono, K. Kleinheinz, S. Kang, H. Pitsch, F. Proch, F. Cavallo Marincola, and A. Kempf. Challenging modeling strategies for LES of non-adiabatic turbulent stratified combustion. *Combustion and Flame*, 2014. 76, 77, 84, 97

[59] B. Fiorina, D. Veynante, and S. Candel. Modeling combustion chemistry in Large Eddy Simulation of turbulent flames. *Flow, Turbulence and Combustion*, 94(1):3 42, dec 2014. 76

[60] B. Franzelli. *Impact of the chemical description on direct numerical simulations and Large Eddy Simulations of turbulent combustion in industrial aero-engines.* PhD thesis, INP Toulouse, 2011. 77, 117, 118, 289

[61] B. Franzelli, B. Fiorina, and N. Darabiha. A tabulated chemistry method for spray combustion. *Proceedings of the Combustion Institute*, 34(1):1659 1666, 2013. 84

[62] B. Franzelli, E. Riber, and B. Cuenot. Impact of the chemical description on a Large Eddy Simulation of a lean partially premixed swirled flame. *Comptes Rendus - Mecanique*, 341(1-2):247 256, 2013. 23, 118

[63] B. Franzelli, E. Riber, L. Y. M. Gicquel, and T. Poinsot. Large Eddy Simulation of combustion instabilities in a lean partially premixed swirled flame. *Combustion and Flame*, 159(2):621 637, 2012. 289

[64] B. Franzelli, E. Riber, M. Sanjosé, and T. Poinsot. A two-step chemical scheme for kerosene-air premixed flames. *Combustion and Flame*, 157(7):1364 1373, 2010. 77, 78, 100, 245, 291

[65] B. Franzelli, E. Riber, M. Sanjosé, and T. Poinsot. A two-step chemical scheme for Large-Eddy Simulation of kerosene-air flames. *Combustion and Flame*, 157(7):1364 1373, 2010. 290

[66] S. Freitag and C. Hassa. Spray characteristics of a kerosene jet in cross flow of air at elevated pressure. *Proceedings ILASS-Europe*, 2008. 250, 251

[67] M. Germano, U. Piomelli, P. Moin, and W. Cabot. A dynamic subgrid-scale eddy viscosity model. *Physics of Fluids*, 3(7):1760 1765, 1991. 38, 266

[68] A. Ghani, T. Poinsot, L. Gicquel, and J. D. Muller. LES Study of transverse acoustic instabilities in a swirled kerosene/air combustion chamber. *Flow, Turbulence and Combustion*, 96(1):207 226, 2016. 242

[69] L.Y.M. Gicquel, G. Staffelbach, and T. Poinsot. Large Eddy Simulations of gaseous flames in gas turbine combustion chambers. *Progress in Energy and Combustion Science*, 38(6):782 817, 2012. 21, 23

[70] O. Gicquel, N. Darabiha, and D. Thévenin. Laminar premixed hydrogen/air counterflow flame simulations using flame prolongation of ILDM with differential diffusion. *Proceedings of the Combustion Institute*, 28:1901 1908, 2000. 76, 94

[71] G. Godel, P. Domingo, and L. Vervisch. Tabulation of NOx chemistry for Large-Eddy Simulation of non-premixed turbulent flames. *Proceedings of the Combustion Institute*, 32(1):1555 1561, 2009. 92

[72] G. A. E. Godsave. Studies of the combustion of drops in a fuel spray. *Fourth Symposium (International) on Combustion*, 4(1):818 830, 1953. 55

[73] P. Gokulakrishnan, M. J. Ramotowski, G. Gaines, C. Fuller, R. Joklik, L. D. Eskin, M. S. Klassen, and R. J. Roby. A novel low NOx lean, premixed, and prevaporized combustion system for liquid fuels. *Journal of engineering for gas turbines and power*, 130(5):51501 51501, 2008. 11, 15

[74] D. Goodwin, N. Malaya, H. Moffat, and R. Speth. Cantera: An object-oriented software toolkit for chemical kinetics, thermodynamics, and transport processes. *Caltech, Pasadena, CA*, 2009. 32, 102

[75] C. Guin and M. Orain. Deliverable D3.2.5 - Detailed Investigation of the selected MSFI configurations. Technical report, LEMCOTEC, 2016. 242, 257, 258

[76] A. K. Gupta, D. G. Lilley, and N. Syred. *Swirl flows*. Abacus Press, 1984. 191

[77] A. Habibi, B. Merci, and D. Roekaerts. Turbulence radiation interaction in Reynolds-averaged Navier-Stokes simulations of nonpremixed piloted turbulent laboratory-scale flames. *Combustion and Flame*, 151(1-2):303 320, 2007. 163

[78] G. Hannebique. *Etude de la structure des flammes diphasiques dans les bruleurs aéronautiques*. PhD thesis, INP Toulouse, 2013. 242

[79] C. M. Heath, Y. R. Hicks, R. C. Anderson, and R. J. Locke. Optical characterisation of a multipoint lean direct injector for gas turbine combustors: velocity and fuel drop size measurements. *Proceedings of the ASME Turbo Expo 2010: Power for land, sea and air*, pages 791 802, 2010. 19

[80] C. Heye, V. Raman, and A. R. Masri. LES/probability density function approach for the simulation of an ethanol spray flame. *Proceedings of the Combustion Institute*, 34(1):1633 1641, 2013. 85

[81] C. Heye, V. Raman, and A. R. Masri. Influence of spray/combustion interactions on auto-ignition of methanol spray flames. *Proceedings of the Combustion Institute*, 35(2):1639 1648, 2015. 85

[82] J. Hirschfelder, C. Curtis, and B. Bird. *Molecular Theory of Gases and Liquids*. John Wiley & Sons, 1954 edition, 1954. 31, 32

[83] Y. Huang and V. Yang. Dynamics and stability of lean-premixed swirl-stabilized combustion. *Progress in Energy and Combustion Science*, 35(4):293 364, 2009. 21

[84] G. L. Hubbard, V. E. Denny, and A. F. Mills. Droplet evaporation: effects of transient and variable properties. *International journal of heat and mass transfer*, 18:1003 1008, 1975. 55

[85] M. Ihme and H. Pitsch. Modeling of radiation and nitric oxide formation in turbulent nonpremixed flames using a flamelet/progress variable formulation. *Physics of Fluids*, 20(5):055110 055110 20, 2008. 22, 76, 77, 84, 96, 97, 163, 165, 172, 182

[86] M. Ihme and H. Pitsch. Prediction of extinction and reignition in nonpremixed turbulent flames using a flamelet/progress variable model. 1. A priori study and presumed PDF closure. *Combustion and Flame*, 155(1-2):70 89, 2008. 163

[87] M. Ihme and H. Pitsch. Prediction of extinction and reignition in nonpremixed turbulent flames using a flamelet/progress variable model: 2. Application in LES of Sandia flames D and E, 2008. 163

[88] H. G. Im, J. H. Chen, and J. Y. Chen. Chemical response of methane/air diffusion flames to unsteady strain rate. *Combustion and Flame*, 118(1-2):204 212, 1999. 65, 127, 165, 179

[89] F. Jaegle. Large eddy simulation of evaporating sprays in complex geometries using Eulerian and Lagrangian methods. *PhD Thesis*, 2009. 250

[90] F. Jaegle. *LES of two-phase flow in aero-engines*. PhD thesis, INP Toulouse, 2009. 251

[91] F. Jaegle, J. M. Senoner, M. García, F. Bismes, R. Lecourt, B. Cuenot, and T. Poinsot. Eulerian and Lagrangian spray simulations of an aeronautical multipoint injector. *Proceedings of the Combustion Institute*, 33(2):2099 2107, 2011. 20, 242, 266

[92] S. Jauré, F. Duchaine, G. Staffelbach, and L.Y.M Gicquel. Massively parallel conjugate heat transfer solver based on large eddy simulation and application to an aeronautical combustion chamber. *Computational Science & Discovery*, 6, 2013. 266

[93] W. P. Jones and R. P. Lindstedt. Global reaction schemes for hydrocarbon combustion. *Combustion and Flame*, 73:222 233, 1988. 77, 213

[94] W. P. Jones and V. N. Prasad. Large Eddy Simulation of the Sandia Flame Series (D-F) using the Eulerian stochastic field method. *Combustion and Flame*, 157(9):1621 1636, sep 2010. 23, 84, 164, 186

[95] W. P. Jones and V. N. Prasad. LES-pdf simulation of a spark ignited turbulent methane jet. *Proceedings of the Combustion Institute*, 33(1):1355 1363, 2011. 84, 85

[96] A. Kaufmann. *Vers la simulation des grandes échelles en formulation Euler/Euler des écoulements réactifs diphasiques*. Phd thesis, INP Toulouse, 2004. 45

[97] K. A. Kemenov and S. B. Pope. Molecular diffusion effects in LES of a piloted methane-air flame. *Combustion and Flame*, 158(2):240 254, 2011. 166

[98] A. Ketelheun, C. Olbricht, F. Hahn, and J. Janicka. NO prediction in turbulent flames using LES/FGM with additional transport equations. *Proceedings of the Combustion Institute*, 33(2):2975 2982, 2011. 96

[99] A. Y. Klimenko and R. W. Bilger. Conditional moment closure for turbulent combustion. *Progress in energy and combustion science*, 25(6):595 687, 1999. 85

[100] V. Knop, A. Nicolle, and O. Colin. Modelling and speciation of nitrogen oxides in engines. *Proceedings of the Combustion Institute*, 34(1):667 675, 2012. 97

[101] E. Knudsen, H. Kolla, E. R. Hawkes, and H. Pitsch. LES of a premixed jet flame DNS using a strained flamelet model. *Combustion and Flame*, 160(12):2911 2927, 2013. 200

[102] A. N. Kolmogorov. The local structure of turbulence in incompressible viscous fluid for very large Reynolds numbers. *C. R. Acad. Sci. , USSR*, 30:301, 1941. 33, 38

[103] A. A. Konnov. Implementation of the NCN pathway of prompt-NO formation in the detailed reaction mechanism. *Combustion and Flame*, 156(11):2093 2105, 2009. 12

[104] K. K. Kuo. *Principles of Combustion*. John Wiley, New York, 1986. 49, 289

[105] N. Lamarque. *Schémas numériques et conditions limites pour la simulation aux grandes échelles de la combustion diphasique dans les foyers d hélicoptère*. Phd thesis, INP Toulouse, 2007. 40

[106] C. K. Law. Unsteady droplet combustion with droplet heating. *Combustion and Flame*, 26(C):17 22, 1976. 55

[107] C. K. Law. *Combustion physics*. 2006. 64, 70

[108] P. D. Lax and B. Wendroff. Systems of conservation laws. *Communications on Pure and Applied mathematics*, 13:217 237, 1960. 40

[109] G. Lecocq. *Approches hybrides combinant chimie complexe, description statistique et densité de surface de flamme pour la simulation aux grandes échelles de l auto-inflammation, l allumage par bougie et la flamme de prémélange dans les moteurs à allumage commandé*. PhD thesis, INSA de Rouen, 2010. 99, 100

[110] G. Lecocq, D. Poitou, I. Herandez, F. Duchaine, E. Riber, and B. Cuenot. A methodology for soot prediction including thermal radiation in complex industrial burners. *Flow, Turbulence and Combustion*, 92(4):947 970, 2014. 267

[111] A. H. Lefebvre. *Gas Turbines Combustion*. Taylor & Francis, 1999. 11, 18, 98, 233

[112] J.-Ph. Légier, T. Poinsot, and D. Veynante. Dynamically thickened flame LES model for premixed and non-premixed turbulent combustion. In *Proceedings of the Summer Program*, pages 157 168. Center for Turbulence Research, NASA Ames/Stanford Univ., 2000. 88

[113] G. Leonard and J. Stegmaier. Development of an aeroderivative gas turbine Dry Low Emissions combustion system. *Journal of Engineering for Gas Turbines and Power*, 116(3):542, 1994. 15

[114] M. Lesieur, O. Métais, and P. Comte. *Large-eddy simulations of turbulence*. 2005. 83

[115] D. C. Leslie and G. L. Quarini. The application of turbulence theory to the formulation of subgrid modelling procedures. *Journal of Fluid Mechanics*, 91(1):65 91, 1979. 38

[116] T. Lieuwen, Y. Neumeier, and B. T. Zinn. The role of unmixedness and chemical kinetics in driving combustion instabilities in lean premixed combustors. *Combustion Science and Technology*, 135(1-6):193 211, 1998. 21

[117] T. C. Lieuwen and V. Yang. *Gas Turbine Emissions*. Cambridge University Press, 2013. 12

[118] D. K. Lilly. The representation of small-scale turbulence in numerical simulation experiments. In *Proceedings of the IBM Scientific Computing Symposium on Environmental Sciences*, Yorktown Heights, USA, 1967. 38

[119] D. K. Lilly. A proposed modification of the germano sub-grid closure method. *Physics of Fluids*, 4(3):633 635, 1992. 38

[120] A. Linan. The asymptotic structure of counterflow diffusion flames for large activation energies. *Acta Astronautica*, 1:1007, 1974. 71

[121] A. N. Lipatnikov and J. Chomiak. Turbulent flame speed and thickness: Phenomenology, evaluation, and application in multi-dimensional simulations. *Progress in Energy and Combustion Science*, 28(1):1 74, 2002. 217

[122] C. Locci, O. Colin, D. Poitou, and F. Mauss. A tabulated, flamelet based no model for large eddy simulations of non premixed turbulent jets with enthalpy loss. *Flow, Turbulence and Combustion*, 94(4):691 729, mar 2015. 22, 77, 163, 182

[123] T. Lovas, P. Amnéus, F. Mauss, and E. Mastorakos. Comparison of automatic reduction procedures for ignition chemistry. *Proceedings of the Combustion Institute*, 29(1):1387 1393, 2002. 82, 112

[124] T. Lovas, D. Nilsson, and F. Mauss. Automatic reduction procedure for chemical mechanisms applied to premixed methane/air flames. *Proceedings of the Combustion Institute*, 28(2):1809 1815, 2000. 82, 112

[125] T. Lu and C. K. Law. A directed relation graph method for mechanism reduction. *Proceedings of the Combustion Institute*, 30(1):1333 1341, 2005. 78, 111

[126] T. Lu and C. K. Law. A criterion based on computational singular perturbation for the identification of quasi steady state species: A reduced mechanism for methane oxidation with NO chemistry. *Combustion and Flame*, 154(4):761 774, 2008. 22, 82, 111, 112, 113

[127] T. Lu, C. K. Law, C. S. Yoo, and J. H. Chen. Dynamic stiffness removal for direct numerical simulations. *Combustion and Flame*, 156(8):1542 1551, 2009. 75, 80, 81

[128] J. Luche. *Elaboration of reduced kinetic models of combustion. Application to a kerosene mechanism.* PhD thesis, LCSR Orleans, 2003. 12, 77, 290

[129] J. Luche, M. Reuillon, J-C. Boettner, and M. Cathonnet. Reduction of large detailed kinetic mechanisms: application to kerosene / air combustion. *Combustion science and technology*, 176:1935 1963, 2004. 245

[130] K. Luo, H. Pitsch, M. G. Pai, and O. Desjardins. Direct numerical simulations and analysis of three-dimensional n-heptane spray flames in a model swirl combustor. *Proceedings of the Combustion Institute*, 33(2):2143 2152, 2011. 84

[131] E. Masi. *Theoretical and numerical study of the modeling of unsteady nonisothermal particle-laden turbulent flows by an Eulerian-Eulerian approach.* PhD thesis, INP Toulouse, 2010. 45

[132] J. A. Miller, M. J. Pilling, and J. Troe. Unravelling combustion mechanisms through a quantitative understanding of elementary reactions. *Proceedings of the Combustion Institute*, 30(1):43 88, 2005. 12

[133] R. K. Mongia, E. Tomita, F. K. Hsu, L. Talbot, and R. W. Dibble. Use of an optical probe for time-resolved in situ measurement of local air-to-fuel ratio and extent of fuel mixing with applications to low NOx emissions in premixed gas turbines. *Symposium (International) on Combustion*, 26(2):2749 2755, 1996. 15

[134] J. B. Moreau. *Modélisation de l écoulement polyphasique à l intérieur et en sortie des injecteurs Diesel.* PhD thesis, INP Toulouse, 2005. 48

[135] J.-B. Mossa. *Extension polydisperse pour la description Euler-Euler des écoulements diphasiques réactifs.* Phd thesis, INP Toulouse, 2005. 45

[136] E. Motheau, F. Nicoud, and T. Poinsot. Mixed acoustic-entropy combustion instabilities in gas turbines. *Journal of Fluid Mechanics*, 749:542 576, 2014. 88

[137] V. Moureau, P. Domingo, and L. Vervisch. From large-eddy simulation to direct numerical simulation of a lean premixed swirl flame: Filtered laminar flame-pdf modeling. *Combustion and Flame*, 158(7):1340 1357, 2011. 121

[138] V. Moureau, G. Lartigue, Y. Sommerer, C. Angelberger, O. Colin, and T. Poinsot. Numerical methods for unsteady compressible multi-component reacting flows on fixed and moving grids. *Journal of computational physics*, 202(2):710 736, 2005. 39

[139] M. E. Mueller and H. Pitsch. Large eddy simulation of soot evolution in an aircraft combustor. *Physics of Fluids (1994-present)*, 2013. 267

[140] R. Mustata, L. Valino, C. Jiménez, W.P. Jones, and S. Bondi. A probability density function Eulerian Monte Carlo field method for large eddy simulations: Application to a turbulent piloted methane/air diffusion flame (Sandia D). *Combustion and Flame*, 145(1-2):88 104, apr 2006. 164

[141] J. Nafe and U. Maas. Modeling of NO formation based on ILDM reduced chemistry. *Proceedings of the Combustion Institute*, 29(1):1379 1385, 2002. 94, 98

[142] S. Navarro-Martinez and A. Kronenburg. LES-CMC simulations of a lifted methane flame. *Proceedings of the Combustion Institute*, 32(1):1509 1516, 2009. 75

[143] S. Navarro-Martinez, A. Kronenburg, and F. Di Mare. Conditional moment closure for large eddy simulations. *Flow, Turbulence and Combustion*, 75(1-4):245 274, 2005. 85

[144] F. Nicoud, H. B. Toda, O. Cabrit, S. Bose, and J. Lee. Using singular values to build a subgrid-scale model for Large Eddy Simulations. *Physics of Fluids*, 23(8), 2011. 39, 164, 189, 248

[145] N. Patel and S. Menon. Simulation of spray turbulence flame interactions in a lean direct injection combustor. *Combustion and Flame*, 153(1-2):228 257, 2008. 254

[146] D. Paulhiac. *Modélisation de la combustion d un spray dans un bruleur aéronautique*. PhD thesis, INP Toulouse, 2015. 88

[147] F. Pecquery. *Développement d un modèle numérique de prédiction des émissions doxydes dazote pour la simulation aux grandes échelles de chambres de combustion aéronautiques*. PhD thesis, Institut National des Sciences Appliquées de Rouen, 2013. 91, 93, 94, 95

[148] F. Pecquery, V. Moureau, G. Lartigue, L. Vervisch, and A. Roux. Modelling nitrogen oxide emissions in turbulent flames with air dilution: Application to LES of a non-premixed jet-flame. *Combustion and Flame*, 161(2):496 509, 2014. 22, 23, 76, 77, 91, 93, 96, 98, 163, 164

[149] P. Pepiot. *Automatic strategies to model transportation fuel surrogates*. PhD thesis, Stanford University, 2008. 79, 110, 111, 265

[150] P. Pepiot-Desjardins and H. Pitsch. An efficient error-propagation-based reduction method for large chemical kinetic mechanisms. *Combustion and Flame*, 154(1-2):67 81, jul 2008. 78, 111

[151] D. W. Pershing and J. O. L. Wendt. Relative contributions of volatile nitrogen and char nitrogen to NOx emissions from pulverized coal flames. *Industrial & Engineering Chemistry Design and Development*, 18(1):60 67, 1979. 13

[152] N. Peters. Local quenching due to flame stretch and non-premixed combustion. *Combustion science and technology*, 30:1 17, 1983. 75

[153] N. Peters. Laminar diffusion flamelet models in non-premixed turbulent combustion. *Progress in energy and combustion science*, 10:319 339, 1984. 75

[154] N. Peters. Laminar flamelet concepts in turbulent combustion. *Symposium (International) on Combustion*, 21(1):1231 1250, 1988. 62

[155] N. Peters. *Turbulent combustion*. Cambridge University Press, 2001. 69

[156] H. Pitsch. FlameMaster v3. 1: A C++ computer program for 0D combustion and 1D laminar flame calculations, 1998. 110

[157] H. Pitsch. Large eddy simulation of turbulent combustion. *Annual review of fluid mechanics*, 38:453 482, 2006. 76

[158] T. Poinsot and S. Lele. Boundary conditions for direct simulations of compressible viscous flows. *Journal of computational physics*, 101(1):104 129, 1992. 39

[159] T. Poinsot and D. Veynante. *Theoretical and Numerical Combustion*. Third Edition (www.cerfacs.fr/elearning), 2011. 65, 66, 67, 70, 72, 135

[160] T. J. Poinsot and S. K. Lele. Boundary conditions for direct simulations of compressible viscous flows. *Journal of Computational Physics*, 101(1):104 129, 1992. 164, 189, 248

[161] T. J. Poinsot, D. Veynante, and S. Candel. Diagrams of premixed turbulent combustion based on direct simulation. In *23rd Symposium (International) on Combustion*, pages 613 619. The Combustion Institute, Pittsburgh, 1990. 67

[162] D. Poitou, J. Amaya, M. El Hafi, and B. Cuénot. Analysis of the interaction between turbulent combustion and thermal radiation using unsteady coupled LES/DOM simulations. *Combustion and Flame*, 159(4):1605 1618, 2012. 266

[163] S. B. Pope. Pdf methods for turbulent reactive flows. *Progress in energy and combustion science*, 19(11):119 192, 1985. 83

[164] S. B. Pope. Lagrangian PDF methods for turbulent flows. *Annual review of fluid mechanics*, pages 23 63, 1994. 84

[165] S. B. Pope. *Turbulent flows*. Cambridge University Press, 2000. 33, 38, 164, 165, 228

[166] F. Proch and A. M. Kempf. Modeling heat loss effects in the large eddy simulation of a model gas turbine combustor with premixed flamelet generated manifolds. *Proceedings of the Combustion Institute*, 35(3):3337 3345, 2014. 77

[167] V. Raman and R. O. Fox. Modeling of fine-particle formation in turbulent flames. *Annual Review of Fluid Mechanics*, 48(1):159 190, 2016. 267

[168] V. Raman, R. O. Fox, and A. D. Harvey. Hybrid finite-volume/transported PDF simulations of a partially premixed methane-air flame. *Combustion and Flame*, 136(3):327 350, 2004. 163

[169] V. Raman and H. Pitsch. A consistent LES/filtered-density function formulation for the simulation of turbulent flames with detailed chemistry. *Proceedings of the Combustion Institute*, 31 II(February):1711 1719, 2007. 164

[170] W. E. Ranz and W. R. Marshall. Evaporation from drops. *Chemical Engineering Progress*, 48(4):173, 1952. 52

[171] J. Réveillon and F. X. Demoulin. Effects of the preferential segregation of droplets on evaporation and turbulent mixing. *Journal of Fluid Mechanics*, 583:273 302, 2007. 15

[172] E. Riber, M. Moreau, O. Simonin, and B. Cuenot. Towards large eddy simulation of non-homogeneous particle laden turbulent gas flows using euler-euler approach. In *11th Workshop on Two-Phase Flow Predictions*, Merseburg, Germany, 2005. 48

[173] M. Rudgyard. Integrated preprocessing tools for unstructured parallel CFD applications. Technical Report TR/CFD/95/08, CERFACS, 1995. 39

[174] P. Sagaut. *Large eddy simulation for incompressible flows.* Springer, 2002. 38

[175] M. Sanjosé, J.M. Senoner, F. Jaegle, B. Cuenot, S. Moreau, and T. Poinsot. Fuel injection model for Euler-Euler and Euler-Lagrange Large Eddy Simulations of an evaporating spray inside an aeronautical combustor. *International Journal of Multiphase Flow*, 37(5):514 529, 2011. 250

[176] R. Sankaran, E. Hawkes, J. Chen, T. Lu, and C. K. Law. Structure of a spatially developing turbulent lean methane air bunsen flame. *Proceedings of the Combustion Institute*, 31:1291 1298, 2007. 23

[177] L. Schiller and A. Nauman. A drag coefficient correlation. *VDI Zeitung*, 77:318 320, 1935. 49

[178] P. Schmitt, T. Poinsot, B. Schuermans, and K. P. Geigle. Large-eddy simulation and experimental study of heat transfer, nitric oxide emissions and combustion instability in a swirled turbulent high-pressure burner. *Journal of fluid mechanics*, 570:17 46, 2007. 77, 165

[179] L. Selle, G. Lartigue, T. Poinsot, R. Koch, K. U. Schildmacher, W. Krebs, B. Prade, P. Kaufmann, and D. Veynante. Compressible large eddy simulation of turbulent combustion in complex geometry on unstructured meshes. *Combustion and Flame*, 137(4):489 505, 2004. 77

[180] M. R. H. Sheikhi, T. G. Drozda, P. Givi, F. A. Jaberi, and S. B. Pope. Large eddy simulation of a turbulent nonpremixed piloted methane jet flame (Sandia Flame D). *Proceedings of the Combustion Institute*, 30(1):549 556, 2005. 163

[181] P. Sierra Sanchez. *Modeling the dispersion and evaporation of sprays in aeronautical combustion chambers.* PhD thesis, INP Toulouse, 2012. 45

[182] W. A. Sirignano. *Fluid dynamics and transport of droplets and sprays.* Cambridge University Press, 1999. 49

[183] B. Sirjean, D. A. Sheen, H. Wang, and E. Dames. JetSurF 1.0-l: Simplified chemical kinetic models for high-temperature oxidation of C5 to C12 n-alkanes. *6th U.S. National Combustion Meeting*, 2009. 245

[184] J. Smagorinsky. General circulation experiments with the primitive equations: 1. the basic experiment. *Mon. Weather Rev.* , 91:99 164, 1963. 38, 48

[185] L. J. Spadaccini and M. B. Colket. Ignition delay characteristics of methane fuels. *Progress in Energy and Combustion Science*, 20(5):431 460, 1994. 217

[186] D. B. Spalding. The combustion of liquid fuels. In *4th Symposium (International) on Combustion*, pages 847 864. The Combustion Institute, Pittsburgh, 1953. 55

[187] G. G. Stokes. On the effect of the inertial friction of fluids on the motions of pendulums. *Trans. Cambridge Phil. Soc.*, 9:8 23, 1851. 49

[188] U. Stopper, M. Aigner, H. Ax, W. Meier, R. Sadanandan, M. Stohr, and A. Bonaldo. PIV, 2D-LIF and 1D-Raman measurements of flow field, composition and temperature in premixed gas turbine flames. *Experimental Thermal and Fluid Science*, 34(3):396 403, 2010. 187

[189] U. Stopper, M. Aigner, W. Meier, R. Sadanandan, M. Stohr, and I. S. Kim. Flow field and combustion characterization of premixed Gas Turbine flames by planar laser techniques. *Journal of Engineering for Gas Turbines and Power*, 131(2):021504, 2009. 187

[190] U. Stopper, W. Meier, R. Sadanandan, M. Stohr, M. Aigner, and G. Bulat. Experimental study of industrial gas turbine flames including quantification of pressure influence on flow field, fuel/air premixing and flame shape. *Combustion and Flame*, 160(10):2103 2118, 2013. 187, 188, 194, 217

[191] C. J. Sung, C. K. Law, and J. Y. Chen. Augmented reduced mechanisms for NO emission in methane oxidation. *Combustion and Flame*, 125(1-2):906 919, 2001. 22, 111, 112, 113, 164, 186

[192] N. Syred. A review of oscillation mechanims and the role of the precessing vortex core in swirl combustion systems. *Progress in energy and combustion science*, 32(2):93 161, 2006. 254

[193] R. Tacina, P. Laing, C. Wey, and A. Mansour. Sector tests of a Low-NOx, Lean-Direct-Injection, MultiPoint integrated module combustor concept. *ASME Turbo Expo*, pages GT 2002 30089, 2002. 19

[194] T. Turanyi, A. S. Tomlin, and M. J. Pilling. On the error of the quasi-steady-state approximation. *The Journal of Physical Chemistry*, 97(1):163 172, 1993. 82

[195] L. Valino. Field Monte Carlo formulation for calculating the probability density function of a single scalar in a turbulent flow. *Flow, Turbulence and Combustion*, 60(2):157 172, 1998. 84

[196] J. A. van Oijen and L. P. H. de Goey. Predicting NO formation with Flamelet Generated Manifolds. *Proceedings of the 4th European Combustion Meeting (ECM 2009)*, pages 1 5, 2009. 92

[197] J. A. van Oijen, F. A. Lammers, and L. P. H. de Goey. Modeling of premixed laminar flames using flamelet generated manifolds. *Combustion science and technology*, 127:2124 2134, 2001. 76

[198] P. E. Vervisch, O. Colin, J. B. Michel, and N. Darabiha. NO Relaxation Approach (NORA) to predict thermal NO in combustion chambers. *Combustion and Flame*, 158(8):1480 1490, 2011. 92, 97, 98

[199] D. Veynante and R. Knikker. Comparison between LES results and experimental data in reacting flows. *Journal of turbulence*, 7(35):1 20, 2006. 83

[200] A. Vié, B. Franzelli, Y. Gao, T. Lu, H. Wang, and M. Ihme. Analysis of segregation and bifurcation in turbulent spray flames: A 3D counterflow configuration. *Proceedings of the Combustion Institute*, 35(2):1675 1683, 2015. 245

[201] A. W. Vreman, B. A. Albrecht, J. A. van Oijen, L. P. H. de Goey, and R. J. M. Bastiaans. Premixed and nonpremixed generated manifolds in large-eddy simulation of Sandia flame D and F. *Combustion and Flame*, 153(3):394 416, 2008. 22, 94, 163, 164, 172, 182

[202] G. Wang, M. Boileau, and D. Veynante. Implementation of a dynamic thickened flame model for large eddy simulations of turbulent premixed combustion. *Combustion and Flame*, 158(11):2199 2213, 2011. 266

[203] G. Wang, M. Boileau, D. Veynante, and K. Truffin. Large eddy simulation of a growing turbulent premixed flame kernel using a dynamic flame surface density model. *Combustion and Flame*, 159(8):2742 2754, 2012. 266

[204] H. Wang, X. You, A. V. Joshi, and S. G. Davis. USC Mech Version II. High-temperature combustion reaction model of H2/CO/C1-C4 Compounds. 2007. 245

[205] L.-P. Wang and M. R. Maxey. Settling velocity and concentration distribution of heavy particles in homogeneous isotropic turbulence. *Journal of fluid mechanics*, 256:27 68, 1993. 49

[206] F. A. Williams. *Combustion Theory*. Benjamin Cummings, Menlo Park, CA, 1985. 64, 65

[207] F. A. Williams. Chemical-kinetic mechanisms for combustion applications, 2003. 12

[208] P. Wolf, G. Staffelbach, R. Balakrishnan, A. Roux, and T. Poinsot. Azimuthal instabilities in annular combustion chambers. In Center for Turbulence Research, editor, *Proceedings of the Summer Program*, pages 259 269, 2010. 88

[209] P. Wolf, G. Staffelbach, L. Gicquel, J-D Muller, and T. Poinsot. Acoustic and large eddy simulation studies of azimuthal modes in annular combustion chambers. *Combustion and Flame*, 159(11):3398 3413, November 2012. 21

[210] J. Xu and S. B. Pope. PDF calculations of turbulent nonpremixed flames with local extinction. *Combustion and Flame*, 123(3):281 307, 2000. 163

[211] A. Yoshizawa. Statistical theory for compressible turbulent shear flows, with the application to subgrid modeling. *Physics of Fluids*, 29(7):2152 2164, 1986. 48

[212] Y. B. Zeldovich. The Oxidation of Nitrogen in Combustion and Explosions. *Acta Physicochimica URSS*, 21(4):218, 1946. 11, 193

[213] B. T. Zoller, J. M. Allegrini, U. Maas, and P. Jenny. PDF model for NO calculations with radiation and consistent NO-NO2 chemistry in non-premixed turbulent flames. *Combustion and Flame*, 158(8):1591 1601, 2011. 22, 77, 96, 97, 163, 165, 172, 182, 227

Appendix A

Two-step GRCs

Methane-air combustion: 2S_CH4_BFER

The GRC has been derived by *Franzelli et al.* [63]. It comprises 6 species, namely N_2, O_2, CH_4, CO, CO_2 and H_2O. The molecular viscosity is obtained via the following power law,

$$\mu(T) = 1.8405 \times 10^{-5} \left(\frac{T}{T_0}\right)^{0.6759} \mathrm{Pa\,s}\,, \tag{A.1}$$

with $T_0 = 300\,\mathrm{K}$. The Prandtl number is $Pr = 0.70$. The species Schmidt numbers are all equal with unity Lewis number assumption. The mechanism comprises two reactions:

$$\text{R1: } CH_4 + 1.5O_2 \longrightarrow CO + 2H_2O\,, \tag{A.2}$$

$$\text{R2: } CO + 0.5O_2 \rightleftharpoons CO_2 \tag{A.3}$$

R1 is fitted to reproduce the laminar flame speed for a large range of pressures (1-10 bars) and temperatures (300-700 K), whereas R2 reproduces the CO-CO_2 equilibrium to obtain the correct burnt gas temperature on the rich side. The reaction rates are expressed as

$$r_1 = f_1(\phi)\, k_1 [CH_4]^{0.5} [O_2]^{0.65} \exp\left(-\frac{E_{a,1}}{RT}\right) \tag{A.4}$$

$$r_2^f = f_2(\phi)\, k_2 [CO][O_2]^{0.5} T^{0.7} \exp\left(-\frac{E_{a,2}}{RT}\right) \tag{A.5}$$

$$r_2^b = f_2(\phi)\, \frac{k_2}{K_{eq,2}(T)} [CO_2] T^{0.7} \exp\left(-\frac{E_{a,2}}{RT}\right) \tag{A.6}$$

where $K_{eq,2}(T)$ is the equilibrium constant [104] of the reaction R2 and

$$k_1 = 4.9 \times 10^9\,\text{cgs units}\,, \tag{A.7}$$

$$k_2 = 2 \times 10^8\,\text{cgs units}\,, \tag{A.8}$$

$$E_{a,1} = 35500\,\text{cal/mol}\,, \tag{A.9}$$

$$E_{a,2} = 12000\,\text{cal/mol}\,. \tag{A.10}$$

$f_1(\phi)$ and $f_2(\phi)$ are two functions depending on the local equivalence ratio which correct the pre-exponential factor to correctly reproduce the flame properties for rich conditions [60]. The 2S_CH4_BFER scheme is evaluated in SGT-100 Case A conditions in terms of adiabatic flame temperature and laminar flame speed in Fig. A.1. The

adiabatic temperature predicted by the 2-step GRC agrees fairly with the ARC and the detailed kinetics scheme, whereas a stronger departure is observed for the laminar flame speed which remains however acceptable.

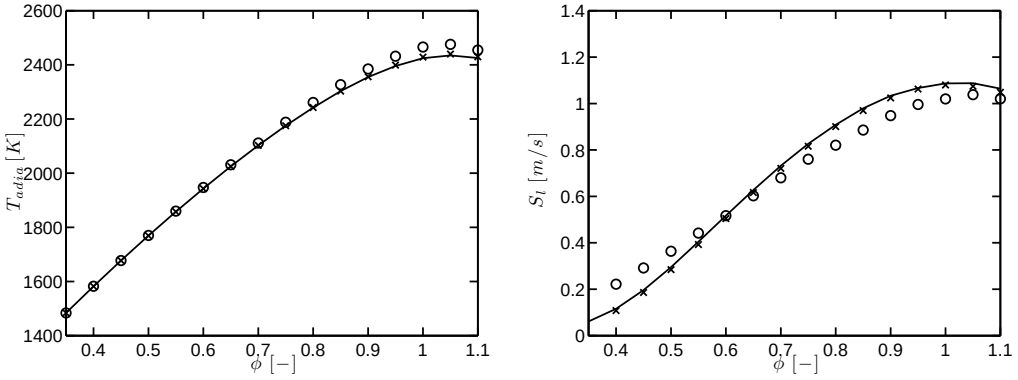

(a) Adiabatic flame temperature.

(b) Laminar flame speed.

Figure A.1: One-dimensional unstrained premixed methane-air laminar flames in the SGT-100 Case A conditions. Comparison between GRI 2.11 detailed mechanism (—), ARC_22_GRI211 (×) and 2S_CH4_BFER scheme (○) for a) adiabatic flame temperature and b) laminar flame speed.

Kerosene-air combustion: 2S_KERO_BFER

The GRC was derived by *Franzelli et al.* [65]. It comprises 6 species, namely N_2, O_2, KERO, CO, CO_2 and H_2O. The molecular viscosity is obtained via the following power law,

$$\mu(T) = 2.5034 \times 10^{-5} \left(\frac{T}{T_0}\right)^{0.6695} \mathrm{Pa\,s}\,, \tag{A.11}$$

with $T_0 = 473\,\mathrm{K}$. The Prandtl number is $Pr = 0.739$. The species Schmidt numbers are all equal with unity Lewis number assumption. The mechanism comprises two reactions:

$$\text{R1: } \mathrm{KERO} + 10\mathrm{O_2} \longrightarrow 10\mathrm{CO} + 10\mathrm{H_2O}\,, \tag{A.12}$$

$$\text{R2: } \mathrm{CO} + 0.5\mathrm{O_2} \rightleftharpoons \mathrm{CO_2}\,. \tag{A.13}$$

R1 is fitted to reproduce the laminar flame speed for a large range of pressures (1-12 bars) and temperature (300-700 K), whereas R2 reproduces the CO-CO_2 equilibrium to obtain the correct burnt gas temperature for rich mixtures based on Luche [128] and

Dagaut [42] detailed mechanisms. The reaction rates are expressed as

$$r_1 = f_1(\phi)\, k_1 [\mathrm{KERO}]^{0.55} [\mathrm{O_2}]^{0.9} \exp\left(-\frac{E_{a,1}}{RT}\right), \tag{A.14}$$

$$r_2^f = f_2(\phi)\, k_2 [\mathrm{CO}][\mathrm{O_2}]^{0.5} \exp\left(-\frac{E_{a,2}}{RT}\right), \tag{A.15}$$

$$r_2^b = f_2(\phi)\, \frac{k_2}{K_{eq,2}(T)} [\mathrm{CO_2}] \exp\left(-\frac{E_{a,2}}{RT}\right), \tag{A.16}$$

where $K_{eq,2}(T)$ is the equilibrium constant of the reaction R2 and

$$k_1 = 8 \times 10^{11}\,\text{cgs units}, \tag{A.17}$$

$$k_2 = 4.5 \times 10^{10}\,\text{cgs units}, \tag{A.18}$$

$$E_{a,1} = 41500\,\text{cal/mol}, \tag{A.19}$$

$$E_{a,2} = 20000\,\text{cal/mol}. \tag{A.20}$$

$f_1(\phi)$ and $f_2(\phi)$ are two functions depending on the equivalence ratio which correct the pre-exponential factor to correctly reproduce the flame properties for rich conditions [64].

Appendix B

Transport coefficients for ARCs

The transport coefficients are extracted from one-dimensional premixed flame computations at stoichiometric conditions in burnt gases obtained with Cantera. The dynamic viscosity is obtained via a power law.

ARC_22_GRI211 and ARC_22_GRI30

The molecular viscosity is obtained via the following power law,

$$\mu(T) = 1.8405 \times 10^{-5} \left(\frac{T}{T_0}\right)^{0.6759} \text{Pa s}, \tag{B.1}$$

with $T_0 = 300\,\text{K}$. The Prandtl number is $Pr = 0.70$. The species Schmidt numbers are given Tab. B.1.

	CH_4	H	H_2	O	O_2	OH	H_2O	H_2O_2	HO_2	CO	CH_2O
Sc	0.69	0.13	0.21	0.49	0.75	0.50	0.55	0.76	0.75	0.76	0.87
	CH_3	CH_3OH	C_2H_2	N_2	C_2H_6	C_2H_4	CO_2	NO	HCN	NO_2	N_2O
Sc	0.68	0.89	0.90	0.74	0.99	0.90	0.96	0.77	0.86	0.86	0.94

Table B.1: Transport coefficients for ARC_22_GRI211 and ARC_22_GRI30.

ARC_27_JETSURF

The molecular viscosity is obtained via the following power law,

$$\mu(T) = 2.5034 \times 10^{-5} \left(\frac{T}{T_0}\right)^{0.6695} \text{Pa s}, \tag{B.2}$$

with $T_0 = 473\,\text{K}$. The Prandtl number is $Pr = 0.70$. The species Schmidt numbers are given Tab. B.2.

	N_2	H	, H_2	O	OH	O_2	H_2O	HO_2	CO	CH_2O
Sc	0.70	0.12	0.20	0.48	0.49	0.74	0.55	0.74	0.75	0.85
	CH_3	CO_2	CH_4	C_2H_6	C_2H_4	CH_2CO	C_2H_2	C_3H_6	$C_4H_8{-}1$	C_4H_6
Sc	0.67	0.95	0.67	0.97	0.89	1.01	0.88	1.25	1.41	1.40
	C_5H_{10}	C_6H_{12}	$nC_{12}H_{26}$	NO	NO_2	HCN	N_2O			
Sc	1.54	1.70	2.53	0.75	0.84	0.85	0.93			

Table B.2: Transport coefficients for ARC_27_JETSURF.

Appendix C

Validation of the ARC_22_GRI211 scheme in SGT-100-Case B conditions

Using the same methodology as for Case A, the ARC_22_GRI211 is compared to the GRI 2.11 scheme on strained premixed methane-air flames in SGT-100/Case B conditions. Figure C.1 shows that again, a good agreement is obtained between the detailed and the reduced mechanism. Again CO and NO are much more sensitive to strain than the fuel consumption.

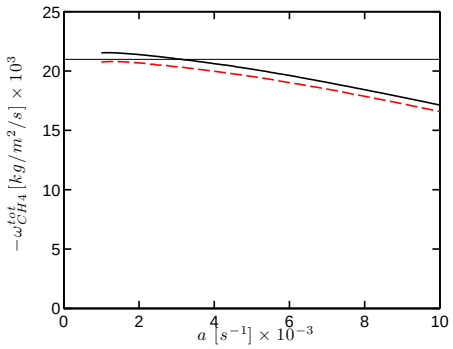

(a) CH_4 total consumption.

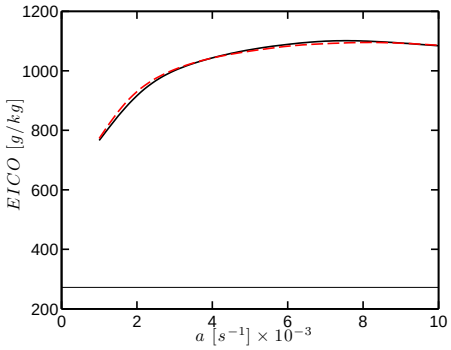

(b) Flame EICO.

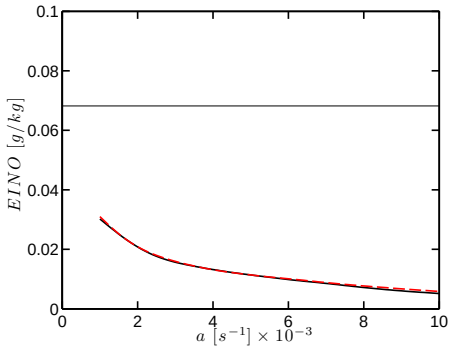

(c) Flame EINO.

Figure C.1: One-dimensional strained premixed methane-air flames in SGT-100/Case B conditions at $\phi = 0.52$. Comparison of the response to strain of global quantities between GRI 2.11 (—), ARC_22_GRI211 (−−). The horizontal lines correspond to the unstrained values.

C. VALIDATION OF THE ARC_22_GRI211 SCHEME IN SGT-100-CASE B CONDITIONS

Appendix D

Impact of NO concentration on the structure of strained premixed flames

In Chapter 9, it was pointed out that the structure of NO in strained premixed flame depends on the NO concentration that is imposed on the burnt gas side. This is illustrated in Fig. D.1, where scatter data from LES is compared with the response of a strained premixed flame for which the imposed NO concentration on the burnt gas side is varied. Figure D.1(a) shows that varying the burnt gases concentration Y^b_{NO} directly impacts the NO concentration found in the flame region. In the present case, the scatter data from LES is closer to the strained premixed flame with $Y^b_{\mathrm{NO}} = 7 \times 10^{-6}$. This disparity of NO concentrations in the flame region significantly affects the structure of the $\mathrm{NO_x}$ source term, as shown in Fig. D.1(b). Note that the NO mass fractions chosen here are at least two order of magnitudes lower than the equilibrium value.

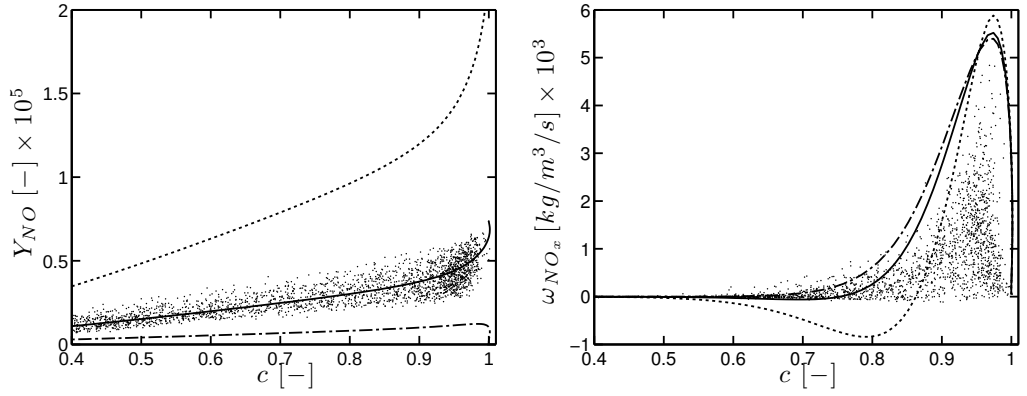

(a) NO mass fraction. (b) $\mathrm{NO_x}$ source term.

Figure D.1: SGT-100 Case A: Scatter plot (·) of a) NO **mass fraction and b)** $\mathrm{NO_x}$ **source term conditioned on the mixture fraction** Z_{glob}**. Comparison with strained laminar premixed methane-air flame at global strain rate** $a = 2000\,\mathrm{s}^{-1}$ **for** $Y^b_{\mathrm{NO}} = 0.0$ **(**$\cdot-\cdot-$**),** $Y^b_{\mathrm{NO}} = 7\times10^{-6}$ **(—) and** $Y^b_{\mathrm{NO}} = 3\times10^{-5}$ **(**$\cdots$**) . The equilibrium value is** $Y^{eq}_{\mathrm{NO}} = 3 \times 10^{-3}$**.**

D. IMPACT OF NO CONCENTRATION ON THE STRUCTURE OF STRAINED PREMIXED FLAMES